Efficient Raman Amplifiers and Lasers in Optical Fibers and Silicon Waveguides: New Concepts

Vom Promotionsausschuss der
Technischen Universität Hamburg-Harburg
zur Erlangung des akademischen Grades
Doktor-Ingenieur (Dr.-Ing.)
genehmigte Dissertation

von

Michael Krause

aus Hamburg

2007

1. Gutachter: Prof. Dr. Ernst Brinkmeyer, TU Hamburg-Harburg
2. Gutachter: Prof. Dr. Klaus Petermann, TU Berlin
3. Gutachter: Prof. Dr. Klaus Schünemann, TU Hamburg-Harburg

Tag der mündlichen Prüfung: 6. Februar 2007

Uniform Resource Name (URN): urn:nbn:de:gbv:830-tubdok-5769

Danksagung

Diese Arbeit ist an der Technischen Universität Hamburg-Harburg während meiner Tätigkeit als wissenschaftlicher Mitarbeiter in der Arbeitsgruppe „Optische Kommunikationstechnik“ entstanden. Ganz herzlich danken möchte ich zunächst dem Leiter dieser Arbeitsgruppe, Herrn Prof. Dr. Ernst Brinkmeyer, für die Möglichkeit zur Mitarbeit und Promotion, die umfassende Betreuung und die Unterstützung sämtlicher meiner Vorhaben.

Zu größtem Dank verpflichtet bin ich weiterhin Hagen Renner für die unzähligen Gelegenheiten zum äußerst ergiebigen fachlichen und nicht-fachlichen Diskutieren und Ideenfinden sowie schließlich für das Korrekturlesen dieser Arbeit.

Bei Sven Cierullies möchte ich mich für die ergebnisreiche Zusammenarbeit auf dem Gebiet der Raman-Faserlaser und die immer angenehme Stimmung im gemeinsamen Büro bedanken.

Weiterhin danke ich Raimonda Stanslovaityte, Robert Draheim, Yi Han und Heiko Fimpel, die im Rahmen ihrer Studien- und Diplomarbeiten hilfreiche Beiträge zu meiner Arbeit geliefert haben.

Auch allen übrigen Mitarbeitern und Studenten der Arbeitsgruppe sei gedankt für ihren Beitrag zu einer gelungenen Arbeitsumgebung; Jörg Voigt danke ich für die Beratung bei praktisch-experimentellen Fragen und Frank Knappe für vielerlei Hilfestellungen. Vielen Dank an Alexander Harke vom Arbeitsbereich „Mikrosystemtechnik“ für die Zusammenarbeit und die Diskussionen beim Frühstück.

Herrn Prof. Bahram Jalali sowie Sasan Fathpour, Varun Raghunathan und Dimitri Dimitropoulos von der University of California in Los Angeles danke ich für die inspirierende und fruchtbare Zusammenarbeit auf dem Gebiet der Raman-Verstärkung in Silizium.

Schließlich danke ich von ganzem Herzen meiner Familie und meinen Freunden für ihren Rückhalt.

Hamburg, im Mai 2007
Michael Krause

Contents

1. Introduction

Raman amplifiers and lasers in fiber-optic communications

Optical amplifiers are key elements of any fiber-optic communication system. Even though modern optical fibers have losses below 0.2 dB/km, a repeated amplification of the transmitted signal to its original strength becomes necessary at long enough distances. One solution for signal regeneration is the conversion of the optical signal into the electrical domain and subsequent re-conversion into a fresh optical signal. However, purely optical amplifiers are usually preferred. They simply amplify the electromagnetic field of the signal via stimulated emission or stimulated-scattering processes in a certain optical frequency range. The amplification process is essentially independent of the details of the spectral channel layout, modulation format or data rate of the transmission span, thus permitting the system operator to later re-configure these parameters without having to upgrade the amplifiers.

For a distributed Raman fiber amplifier (RFA), power is provided by optical pumping of the transmission fiber; the pump wavelength is shorter than the wavelength to be amplified by an amount that corresponds to an optical frequency difference of about 13.2 THz. The signal then experiences gain due to Stimulated Raman Scattering (SRS), a nonlinear optical process in which a pump photon is absorbed and immediately re-emitted in the form of a phonon and a signal photon, thus amplifying the signal. Fig. 1.1

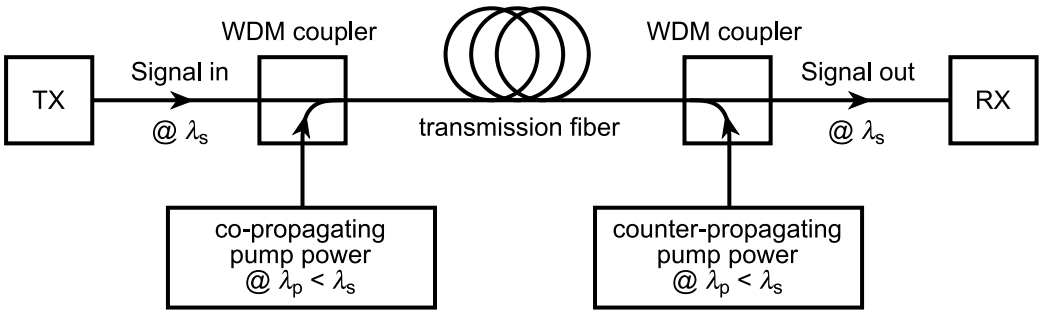

Figure 1.1.: Schematic of a Raman fiber amplifier. The pump power at wavelength λ_p, often provided by Raman fiber lasers, may be co- or counter-propagating (or both) with the signal to be amplified at λ_s.

shows a schematic view of a Raman-amplifed transmission link [1, 2].

RFAs had been investigated already in the 1980s, but the relatively large required pump powers were not conveniently available at that time, so that RFAs were deemed impractical. During the 1990s, the erbium-doped fiber amplifier (EDFA) was the favored and well-established practical alternative. With the advent of high-power semiconductor lasers, however, the RFA could finally be considered for employment in practical transmission systems. This was desirable because RFAs have several advantages over EDFAs, such as better noise performance and increased spectral flexibility—in fact, Raman amplification is possible throughout the entire transparency range of fibers (provided suitable 13.2-THz-shifted pump sources are available), while EDFAs are limited by the emission spectrum of the erbium ions. By 2000, communications equipment incorporating Raman technology was commercially available.

Soon after that, in 2003, Jalali's group at the University of California in Los Angeles could demonstrate a Raman amplifier in a silicon waveguide. While in optical fibers lengths of several hundreds of meters are required to achieve significant Raman gain, in silicon a waveguide of several centimeters is sufficient because of the much larger Raman-gain coefficient of silicon. This being the first time that an optical amplifier could be demonstrated in silicon, the result marked a milestone in the development of the field of silicon-based photonics, which has recently seen significant progress in other areas as well. Today, silicon photonics can provide most of the functionality required for integrated optics [3, 4].

Silicon-based optical-communications components are so widely researched because they have the potential of being mass-produced at low cost, by making use of the existing infrastructure of the electronics industry. A high demand for such components may arise in environments where low cost is more important than ultimate performance, such as in the context of emerging optical access networks. On-chip Raman amplifiers could compensate for silicon-waveguide losses and make possible the realization of complex passive photonic circuitry in a compact form [4].

Finally, the pump sources for RFAs are often Raman fiber lasers (RFLs), which make use of the stimulated Raman effect just like the amplifier itself. RFLs, too, have been researched since the 1980s [1, 2]. In silicon, on the other hand, the first continuous-wave Raman laser was demonstrated only very recently, in 2005, by Paniccia's research group at Intel Corporation, thus setting yet another silicon-photonics milestone.

Thus, with Raman fiber amplifiers and lasers already well-established in state-of-the-art long-haul transmission links, Raman-based silicon components may one day be a key element of low-cost fiber-optic communications equipment, too.

Overview of this thesis

The aim of this thesis was to develop, model and optimize novel concepts for Raman amplifiers and lasers both in fibers and silicon waveguides that have the potential of improving the performance of fiber-optic communication systems.

The starting chapter 2 derives the equations required for the modeling of Raman amplifers and lasers in optical waveguides, especially in fibers. The following two chapters present new designs for Raman fiber lasers: while chapter 3 concentrates on their power efficiency and spectral flexibility, chapter 4 investigates stability properties of RFLs.

Chapter 5 prepares for the second part of the thesis by summarizing the material properties of silicon and extending the RFL model to include the nonlinear absorption effects significant in silicon waveguides. In chapter 6, fundamental properties of silicon Raman amplifiers are derived and several new designs of amplifiers with improved characteristics are proposed. The last chapter 7 analyzes the basic behavior of silicon Raman lasers and finally proposes new designs with increased efficiency. Chapter 8 concludes the thesis.

Details about the mode-solving software that was written for the simulations in chapters 6 and 7 are given in the appendix, followed by a list of the author's publications and the references.

References

[1] M. N. Islam, editor. *Raman Amplifiers for Telecommunications 1 & 2.* Springer-Verlag, 2004.

[2] C. Headley and G. P. Agrawal, editors. *Raman Amplification in Fiber Optical Communication Systems.* Elsevier, 2005.

[3] L. Pavesi and G. Guillot, editors. *Optical Interconnects – The Silicon Approach.* Springer-Verlag, 2006.

[4] B. Jalali, M. Paniccia and G. Reed. Silicon Photonics. *IEEE Microwave Magazine*, 7(3):58–68, June 2006.

2. Stimulated Raman scattering in optical waveguides

This introductory chapter forms the foundation for the remainder of this thesis. Section 2.1 gives an introduction to the Raman effect, which all of the devices analyzed in this thesis are based on. Section 2.2 derives the nonlinear Schrödinger equations (NLSEs) that model the propagation of guided waves coupled by a third-order nonlinearity. Finally, section 2.3 specializes the model to the case of Raman amplification in optical fibers, thus preparing for chapters 3 and 4.

2.1. The Raman effect

Spontaneous Raman scattering is a nonlinear optical process in which a photon, called the "pump" photon, is absorbed by a material while simultaneously a photon of a different energy is emitted. The difference in photon energy is compensated by a change of the vibrational state of the material [Sto04].

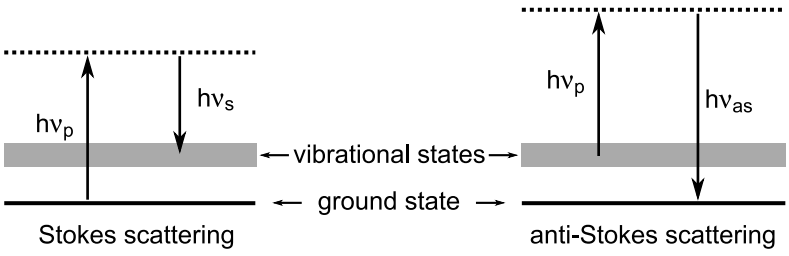

Figure 2.1.: Illustration of spontaneous Stokes and anti-Stokes Raman scattering.

Fig. 2.1 illustrates the two basic types of spontaneous Raman scattering. In so-called Stokes scattering (Fig. 2.1a), a pump photon of energy $h\nu_p$ is absorbed, and a Stokes photon of energy $h\nu_s < h\nu_p$ is emitted, while the material undergoes a transition to a higher vibrational energy state. On the other hand, Anti-Stokes scattering can occur when the material already is in an excited vibrational state. Then, a pump photon of energy $h\nu_p$ is absorbed, and a quantum of vibrational energy is added to that energy to

yield an anti-Stokes photon of higher energy $h\nu_{as} > h\nu_p$, see Fig. 2.1b. The anti-Stokes process is much weaker than the Stokes process, so it is usually neglected in the modeling of Raman amplifiers and lasers [Agr01, HA05].

Stimulated Raman scattering (SRS) occurs when photons at the Stokes wavelength are already present in addition to the pump photons, e. g., when deliberately injecting both a pump and a Stokes beam into the material. Then the rate of the Stokes processes illustrated in Fig. 2.1a is increased: the more Stokes photons are already present, the faster additional Stokes photons are added. In other words, the Stokes beam is amplified [Sto04]. The evolution of the Stokes intensity I_s along the propagation direction z due to SRS can be written in the form

$$\frac{\mathrm{d}I_s}{\mathrm{d}z} = g_R I_p I_s, \tag{2.1}$$

where I_p is the pump intensity—the Raman gain per unit length experienced by the Stokes wave is proportional to the pump intensity and to the Raman-gain constant g_R, which is a property of the nonlinear material. In many cases of practical interest, the Stokes powers are large enough such that SRS dominates and the small effect of spontaneous Raman scattering can be neglected as in Eq. (2.1). SRS can then be described mathematically as a third-order nonlinear effect in terms of a nonlinear susceptibility $\chi^{(3)}$, see section 2.2.

Finally, the Raman-gain constant depends on the optical frequency difference between the pump and Stokes beams. As Fig. 2.1 shows, significant Stokes scattering and thus SRS gain is only obtained when the pump-Stokes frequency difference corresponds to the energy of a vibrational excitation of the material. On the one hand, in crystalline materials such as silicon the vibrational energies are very well defined; the Raman-gain maximum in silicon occurs at a frequency which is 15.6 THz below that of the pump beam, and the gain linewidth is about 100 GHz, see section 5.2.1. On the other hand, in optical fibers based on fused silica the vibrational energy levels are spread over a broad range of frequencies due to the amorphous structure of the material. Here, the gain maximum occurs at a frequency shift of 13.2 THz, but the gain is significant over a range of 6 THz, see Fig. 2.3 on page 20. The effective width of the gain spectrum can even be increased further by pumping Raman fiber amplifiers with several closely spaced pump wavelengths [HA05].

2.2. Mathematical model of nonlinear wave coupling

The models describing amplifiers and lasers in this thesis are based on the formalism of coupled nonlinear Schrödinger equations (NLSEs), which are differential equations

describing the evolution of spatially and temporally varying field envelopes of optical beams propagating inside the waveguide, which are coupled through the waveguide nonlinearity. The absolute square of these field envelopes gives the instantaneous powers of the various beams, which are the quantities of primary interest in the discussions in later chapters.

In this section, the derivation of the NLSEs from Maxwell's equations will be sketched. For clarity, we restrict ourselves to the special case of a waveguide inside which forward- and backward-propagating beams at only two center wavelengths are propagating. Many types of Raman amplifiers and lasers can be successfully described by such a model, where the two wavelengths correspond to the pump and Stokes wavelengths. Eqs. (2.38) and (2.39) will be the main results of this section.

The derivation of the coupled NLSEs sketched in sections 2.2.1–2.2.4 basically follows that of [SdSE02], although we treat the nonlinear polarization in the frequency domain as in [PV86] and we consider the specific case of both co- and counterpropagating beams at two center frequencies.

An extension of this model to the case of more than two wavelengths is straightforward, however, and will be briefly summarized at the appropriate points in later chapters. Also, we will not deal with the effect of Free-Carrier Absorption here—for this we need to take into account the optical generation of charge carriers and their influence on the light propagating inside the waveguide; this effect will be incorporated in the model in Sect. 5.4.

2.2.1. Overview

We consider a longitudinally invariant waveguide, such as an optical fiber (for chapters 3 and 4) or a silicon waveguide (for chapters 6 and 7). Light is coupled into the waveguide the intensity of which is so strong that there will be a significant nonlinear material response influencing the light propagation. The evolution of the electromagnetic field is described by Maxwell's equations,

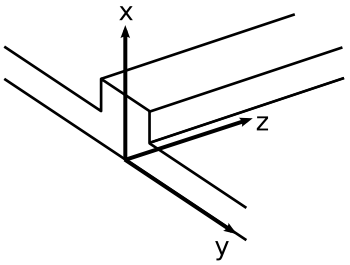

Figure 2.2.: Coordinate system used throughout this thesis. The waveguide is oriented along the z axis.

$$\nabla \times \tilde{\mathbf{E}} = -\mu_0 \frac{\partial \tilde{\mathbf{H}}}{\partial t}, \qquad \nabla \times \tilde{\mathbf{H}} = \frac{\partial}{\partial t}(\epsilon_0 n^2 \tilde{\mathbf{E}} + \tilde{\mathbf{P}}) + \tilde{\mathbf{J}}, \tag{2.2}$$

$$\nabla \cdot (\epsilon_0 n^2 \tilde{\mathbf{E}} + \tilde{\mathbf{P}}) = \tilde{\rho}, \qquad \nabla \cdot \tilde{\mathbf{H}} = 0 \tag{2.3}$$

for the electric and magnetic fields $\tilde{\mathbf{E}}(\mathbf{r},t)$ and $\tilde{\mathbf{H}}(\mathbf{r},t)$, where $\mathbf{r}=(x,y,z)$ is a vector, and the tilde denotes a time-domain function. Fig. 2.2 shows the coordinate system used here. The fields are prescribed over certain surfaces, e. g., at one end of the waveguide, where optical power is coupled in, and we want to know how the fields evolve inside the waveguide.

In this chapter, we assume that there are no free carriers in the waveguide, such that the charge and current densities are zero, $\tilde{\rho}=0$ and $\tilde{\mathbf{J}}=0$. Later in chapter 5, the effect of Free-Carrier Absorption will be included, which will be treated only for the CW case and in the ambipolar approximation, i. e., the excess hole and electron densities are equal at each point such that again $\tilde{\rho}=0$, and there is no net electric current ($\tilde{\mathbf{J}}=0$), see section 5.4.1. We will therefore assume $\tilde{\rho}=0$ and $\tilde{\mathbf{J}}=0$ throughout this thesis.

The refractive-index profile $n(x,y)$ of the waveguide does not vary along the waveguide axis z. The polarization $\tilde{\mathbf{P}}(\mathbf{r},t)$ represents the nonlinear response of the material. The materials considered here (amorphous fused silica or crystalline silicon) have no significant second-order nonlinearity due to their centrosymmetry [Agr01, Boy03]. We therefore consider third-order nonlinearities of the form [Boy03, Mil98]

$$\tilde{P}^i(\mathbf{r},t)=\epsilon_0\iiint_0^\infty \tilde{\chi}^{(3)}_{ijkl}(\tau_1,\tau_2,\tau_3)\tilde{E}^j(\mathbf{r},t-\tau_1)\tilde{E}^k(\mathbf{r},t-\tau_2)\tilde{E}^l(\mathbf{r},t-\tau_3)\,\mathrm{d}\tau_1\,\mathrm{d}\tau_2\,\mathrm{d}\tau_3, \quad (2.4)$$

where the superscripts $i,j,k,l=x,y,z$ denote cartesian field components, and we have used the Einstein notation for writing the products involving the fields and the nonlinear susceptibility tensor $\tilde{\chi}^{(3)}_{ijkl}$, i. e., a summation over $j,k,l=x,y,z$ is implicit on the right-hand side. The third-order nonlinear polarization at a time t given by Eq. (2.4) depends on the electric field at all earlier times and along all cartesian directions according to the response function $\tilde{\chi}^{(3)}_{ijkl}(\tau_1,\tau_2,\tau_3)$, which is zero for negative time lags $\tau_{1,2,3}$ due to causality. Expression (2.4) is sufficiently general that it can describe effects such as stimulated Raman scattering (SRS), two-photon absorption (TPA), self-phase modulation (SPM), cross-phase modulation (XPM), and four-wave mixing (FWM).

The coupled NLSEs, which will be derived during the rest of this chapter, are an approximate reformulation of Eqs. (2.2)–(2.4) which is easier to handle. The basic assumption is that the electromagnetic field in the waveguide can be thought of as consisting of one or only a few beams centered spectrally around specific center frequencies and propagating in specific waveguide modes. These beams will interact inside the waveguide through its nonlinearity, which can in principle result in the generation of light at any optical frequency and in any waveguide mode. However, often these new components can build up significantly only if certain phase-matching conditions are fulfilled, which is generally not the case unless the waveguide is specifically designed for that purpose.

Using the NLSE approach requires one to make a reasonable assumption about what optical frequencies and waveguide modes are significant in the problem at hand.

In the rest of this chapter we will assume that light propagates only in the vicinity of two frequencies, ω_p (pump) and ω_s (Stokes) in our waveguide. Taking into account the two propagation directions, we have four beams in total (forward- and backward-propagating waves at ω_p and ω_s, respectively). We will derive four coupled NLSEs that describe the evolution of these waves along the waveguide, see Eqs. (2.38)–(2.39). They form the basis for the description of all Raman amplifiers and laser in later chapters.

2.2.2. Modal description of light propagation

Fourier-transform conventions

Throughout this thesis, the Fourier transform of any function of time $\tilde{\Psi}(t)$, such as any cartesian component of the electric and magnetic fields $\tilde{\mathbf{E}}(\mathbf{r},t)$ and $\tilde{\mathbf{H}}(\mathbf{r},t)$, is defined according to the convention in [Fli91],

$$\Psi(\omega) = \int_{-\infty}^{+\infty} \tilde{\Psi}(t) e^{-j\omega t}\,\mathrm{d}t, \tag{2.5}$$

such that the inverse Fourier transform is given by

$$\tilde{\Psi}(t) = \frac{1}{2\pi}\int_{-\infty}^{+\infty} \Psi(\omega) e^{j\omega t}\,\mathrm{d}\omega. \tag{2.6}$$

As we are only dealing with real time signals, we have $\Psi(-\omega) = \Psi^*(\omega)$.

Fourier transformation and modal decomposition of Maxwell's equations

The first step to an approximate solution of Eqs. (2.2)–(2.3) with $\tilde{\rho} = 0$ and $\tilde{\mathbf{J}} = 0$ is a Fourier transformation, leading to Maxwell's equations in the frequency domain,

$$\nabla \times \mathbf{E} = -j\omega\mu_0\mathbf{H}, \qquad \nabla \times \mathbf{H} = j\omega(\epsilon_0 n^2\mathbf{E} + \mathbf{P}), \tag{2.7}$$

$$\nabla \cdot (\epsilon_0 n^2\mathbf{E} + \mathbf{P}) = 0, \qquad \nabla \cdot \mathbf{H} = 0, \tag{2.8}$$

The transverse fields (the x and y components) of the solution of Eqs. (2.7)–(2.8) (for any nonlinear polarization $\mathbf{P}$) can be expanded in the complete set of forward- (+) and backward-propagating (−) normal modes of the linear ($\mathbf{P} = 0$) waveguide [SL83],

$$\mathbf{E}^t(\mathbf{r},\omega) = \sum_m \left[A_m^+(z,\omega)e^{-j\beta_m(\omega)z} + A_m^-(z,\omega)e^{j\beta_m(\omega)z}\right]\mathbf{e}_m^{+,t}(x,y,\omega), \tag{2.9}$$

$$\mathbf{H}^t(\mathbf{r},\omega) = \sum_m \left[A_m^+(z,\omega)e^{-j\beta_m(\omega)z} - A_m^-(z,\omega)e^{j\beta_m(\omega)z}\right]\mathbf{h}_m^{+,t}(x,y,\omega), \tag{2.10}$$

where the fields $\mathbf{e}_m^+$ and $\mathbf{h}_m^+$ are the forward-propagating modes of the linear waveguide with propagation constants β_m. The superscript t denotes the transverse part of the corresponding vector, and we are using the convention that the forward- and backward-propagating mode fields are related as

$$\mathbf{e}_m^+ = \mathbf{e}_m^{+,t} + e_m^{+,z}\hat{\mathbf{z}}, \qquad \mathbf{h}_m^+ = +\mathbf{h}_m^{+,t} + h_m^{+,z}\hat{\mathbf{z}}, \tag{2.11}$$

$$\mathbf{e}_m^- = \mathbf{e}_m^{+,t} - e_m^{+,z}\hat{\mathbf{z}}, \qquad \mathbf{h}_m^- = -\mathbf{h}_m^{+,t} + h_m^{+,z}\hat{\mathbf{z}}, \tag{2.12}$$

and the transverse electric fields $\mathbf{e}_m^{\pm,t}$ are chosen real [SL83]. The summations over m in Eqs. (2.9)–(2.10) are understood to represent the summation over the finite number of guided modes and the integration over all propagating and evanescent radiation modes.

Using the conjugated reciprocity theorem [SL83, SF03], one can show that the expansion coefficients $A_m^\pm(z,\omega)$ occuring in Eqs. (2.9)–(2.10) are related to the perturbing polarization $\mathbf{P}(\mathbf{r},\omega)$ through the coupled-mode equations[1]

$$\frac{\partial A_m^\pm(z,\omega)}{\partial z} = \mp j\frac{\omega}{4N_k(\omega)}e^{\pm j\beta_m(\omega)z}\int \mathbf{e}_m^{\pm *}(x,y,\omega)\cdot\mathbf{P}(x,y,z,\omega)\,\mathrm{d}A, \tag{2.13}$$

with the mode normalization

$$N_k(\omega) = \frac{1}{2}\int\left[\mathbf{e}_k^+(x,y,\omega)\times\mathbf{h}_k^{+*}(x,y,\omega)\right]\cdot\hat{\mathbf{z}}\,\mathrm{d}A. \tag{2.14}$$

The frequency-domain polarization $\mathbf{P}(\mathbf{r},\omega)$ occuring in Eq. (2.13) is obtained upon Fourier-transforming Eq. (2.4) as

$$P^i(\mathbf{r},\omega) = \frac{\epsilon_0}{4\pi^2}\iint_{-\infty}^{+\infty}\chi^{(3)}_{ijkl}(\omega_1,\omega_2,\omega-\omega_1-\omega_2) \cdot E^j(\mathbf{r},\omega_1)E^k(\mathbf{r},\omega_2)E^l(\mathbf{r},\omega-\omega_1-\omega_2)\,\mathrm{d}\omega_1\,\mathrm{d}\omega_2, \tag{2.15}$$

where the frequency-dependent $\chi^{(3)}_{ijkl}$ tensor is the Fourier-transformed response function,

$$\chi^{(3)}_{ijkl}(\omega_1,\omega_2,\omega_3) = \iiint_{-\infty}^{+\infty}\tilde{\chi}^{(3)}_{ijkl}(\tau_1,\tau_2,\tau_3)e^{-j(\omega_1\tau_1+\omega_2\tau_2+\omega_3\tau_3)}\,\mathrm{d}\tau_1\,\mathrm{d}\tau_2\,\mathrm{d}\tau_3. \tag{2.16}$$

The expression for the polarization, Eq. (2.15), explicitly shows that the nonlinearity can couple different frequency components of the field — on the other hand, in a linear waveguide all frequency components would propagate independently.

[1] Strictly speaking, Eq. (2.13) is only valid for modes with a real propagation constant β_m; the modification necessary for evanescent modes is not given here, as their contribution to our effects is so weak that we may neglect them.

Longitudinal electric-field component

Eq. (2.9) only gives the transverse electric field in the waveguide. In order to calculate the induced nonlinear polarization from Eq. (2.15), we also need the longitudinal electric-field component $E^z(\mathbf{r},\omega)$. It is obtained from the z-component equation of the right-hand one of Eqs. (2.7) as

$$E^z(\mathbf{r},\omega) = \frac{(\nabla\times\mathbf{H})^z - j\omega P^z(\mathbf{r},\omega)}{j\omega\epsilon_0 n^2}. \tag{2.17}$$

Inserting the transverse magnetic field (2.10) into Eq. (2.17) and making use of the fact that $(\nabla\times\mathbf{h}_m^{+,t})^z = j\omega\epsilon_0 n^2 e_m^{+,z}$, we obtain [SdSE02]

$$E^z(\mathbf{r},\omega) = \sum_m \left[A_m^+(z,\omega)e^{-j\beta_m(\omega)z} - A_m^-(z,\omega)e^{j\beta_m(\omega)z}\right] e_m^{+,z}(x,y,\omega) - \frac{P^z(\mathbf{r},\omega)}{\epsilon_0 n^2}. \tag{2.18}$$

Eqs. (2.9), (2.12) and (2.18) can be combined to give the full electric field in the waveguide in the short form

$$\mathbf{E}(\mathbf{r},\omega) = \bar{\mathbf{E}}(\mathbf{r},\omega) - \frac{P^z(\mathbf{r},\omega)}{\epsilon_0 n^2}\hat{\mathbf{z}}, \tag{2.19}$$

where $\hat{\mathbf{z}}$ is the unit vector in z direction, and we have defined

$$\bar{\mathbf{E}}(\mathbf{r},\omega) = \sum_m \left[A_m^+(z,\omega)e^{-j\beta_m(\omega)z}\mathbf{e}_m^+(x,y,\omega) + A_m^-(z,\omega)e^{j\beta_m(\omega)z}\mathbf{e}_m^-(x,y,\omega)\right]. \tag{2.20}$$

Explicit nonlinear polarization

The next step in the derivation of the NLSEs is obtaining an explicit expression for the nonlinear polarization induced by the electric field in the waveguide. The polarization is given by Eq. (2.15) as a function of the electric field, but the electric field itself depends on the polarization through Eq. (2.19).

An approximate explicit expression for the polarization $\mathbf{P}(\mathbf{r},\omega)$ can be obtained from a perturbation expansion [Nay73] of the polarization (2.15) and the electric field (2.19), keeping only the first-order term. The resulting expression for the polarization is

$$P^i(\mathbf{r},\omega) = \frac{\epsilon_0}{4\pi^2}\iint_{-\infty}^{+\infty}\chi^{(3)}_{ijkl}(\omega_1,\omega_2,\omega-\omega_1-\omega_2) \cdot \bar{E}^j(\mathbf{r},\omega_1)\bar{E}^k(\mathbf{r},\omega_2)\bar{E}^l(\mathbf{r},\omega-\omega_1-\omega_2)\,\mathrm{d}\omega_1\,\mathrm{d}\omega_2, \tag{2.21}$$

with $\bar{\mathbf{E}}$ defined in Eq. (2.20). Eqs. (2.21) and (2.20) now explicitly give the nonlinear polarization in terms of the spectral envelope functions $A_m^\pm(z,\omega)$. The second-order term in the perturbation expansion, which we neglect here, would be quintic in the spectral envelopes. For consistency, this effective quintic nonlinearity must be taken into account

as soon as one includes the physical quintic $\chi^{(5)}$ response of the material in the nonlinear polarization Eq. (2.4) [SdSE02].

Finally, for the cases of interest in this thesis, the frequencies of the light propagating in the structure span at most one octave. The expression for the nonlinear polarization, Eq. (2.21), can then be simplified so as to include only integrations over positive frequencies:

$$P^i(\mathbf{r},\omega) = P^{i*}(\mathbf{r},-\omega) = \frac{3\epsilon_0}{4\pi^2}\iint_0^\infty \chi^{(3)}_{ijkl}(\omega_1,\omega_2,\omega-\omega_1-\omega_2) \cdot \bar{E}^j(\mathbf{r},\omega_1)\bar{E}^k(\mathbf{r},\omega_2)\bar{E}^{l*}(\mathbf{r},\omega_1+\omega_2-\omega)\,\mathrm{d}\omega_1\,\mathrm{d}\omega_2 \quad (\text{for } \omega>0), \quad (2.22)$$

where we have made use of the intrinsic permutation symmetry of the nonlinear susceptibility tensor $\chi^{(3)}_{ijkl}$ [Boy03] and the reality of the time signals. Physically, this simplification means neglecting the possibility of sum-frequency generation which is usually not phase matched [Agr01, Boy03].

2.2.3. Nonlinear coupling of spectral envelopes

Single-mode approximation

As discussed at the end of Sect. 2.2.1, we will assume that light is propagating in the waveguide only in the vicinity of the frequencies ω_p and ω_s. Furthermore, we assume that the field in the waveguide is well represented by a single waveguide mode of the linear waveguide, i. e., we assume that the waveguide nonlinearity changes only the amplitude and the phase of the mode during propagation but does not significantly excite other normal modes. Following Eq. (2.20), the electric field contributing to the nonlinear polarization in Eq. (2.22) is thus given by two contributions,

$$\bar{\mathbf{E}}(\mathbf{r},\omega) = \mathbf{E}_p(\mathbf{r},\omega) + \mathbf{E}_s(\mathbf{r},\omega), \quad (2.23)$$

where the pump and Stokes fields $\mathbf{E}_p$ and $\mathbf{E}_s$, respectively, are significantly non-zero only around the center frequencies ω_p and ω_s, respectively, and do not overlap spectrally. They are defined as

$$\mathbf{E}_p(\mathbf{r},\omega) = A_p^+(z,\omega)e^{-j\beta_p(\omega)z}\mathbf{e}_p(x,y,\omega) + A_p^-(z,\omega)e^{j\beta_p(\omega)z}\mathbf{e}_p^*(x,y,\omega), \quad (2.24)$$

$$\mathbf{E}_s(\mathbf{r},\omega) = A_s^+(z,\omega)e^{-j\beta_s(\omega)z}\mathbf{e}_s(x,y,\omega) + A_s^-(z,\omega)e^{j\beta_s(\omega)z}\mathbf{e}_s^*(x,y,\omega), \quad (2.25)$$

where we have made use of the relation $\mathbf{e}_m^+ = \mathbf{e}_m = (\mathbf{e}_m^-)^*$ valid for propagating modes. The pump and Stokes modes with propagation constants $\beta_p(\omega)$ and $\beta_s(\omega)$ may be the same or entirely different modes of the structure, with mode fields $\mathbf{e}_p(x,y,\omega)$ and $\mathbf{e}_s(x,y,\omega)$, respectively. Finally, $A^\pm_{p,s}(z,\omega)$ are the spectral envelopes of the forward- and backward-propagating pump and Stokes waves.

Contributions to nonlinear coupling

The evolution of the spectral envelopes $A^{\pm}_{p,s}(z,\omega)$ occuring in Eqs. (2.24)–(2.25) is determined by the nonlinear polarization as shown in Eq. (2.13). We thus have to evaluate the nonlinear polarization, Eq. (2.22), near the center frequencies of the two beams, ω_p and ω_s. Inserting Eq. (2.23) into Eq. (2.22), the polarization at frequencies near ω_s is seen to consist of three contributions,

$$P^i(\omega \approx \omega_s) = \frac{3\epsilon_0}{4\pi^2} \iint_0^\infty \chi^{(3)}_{ijkl}(\omega_1, \omega_2, \omega - \omega_1 - \omega_2) \Big[E^j_s(\omega_1) E^k_s(\omega_2) E^{l*}_s(\omega_1 + \omega_2 - \omega) + E^j_s(\omega_1) E^k_p(\omega_2) E^{l*}_p(\omega_1 + \omega_2 - \omega) + E^j_p(\omega_1) E^k_s(\omega_2) E^{l*}_p(\omega_1 + \omega_2 - \omega) \Big] \mathrm{d}\omega_1 \, \mathrm{d}\omega_2, \quad (2.26)$$

where we have simplified the notation by suppressing the explicit dependence on $\mathbf{r}$. The first term represents the action of the Stokes light on itself. The last two terms represent the action of the pump light on the Stokes light, and they are identical due to the intrinsic permutation symmetry of $\chi^{(3)}$. We can thus shorten Eq. (2.26) slightly and write

$$P^i(\omega \approx \omega_s) = \frac{3\epsilon_0}{4\pi^2} \iint_0^\infty \chi^{(3)}_{ijkl}(\omega_1, \omega_2, \omega - \omega_1 - \omega_2) \cdot \Big[E^j_s(\omega_1) E^k_s(\omega_2) E^{l*}_s(\omega_1 + \omega_2 - \omega) + 2 E^j_s(\omega_1) E^k_p(\omega_2) E^{l*}_p(\omega_1 + \omega_2 - \omega) \Big] \mathrm{d}\omega_1 \, \mathrm{d}\omega_2. \quad (2.27)$$

Inserting Eqs. (2.24)–(2.25) into Eq. (2.27) results, upon multiplying out the terms cubic in E, in a rather lengthy expression with 16 terms of the form

$$P^i_{a\sigma_a, b\sigma_b, c\sigma_c}(\omega) = \frac{3\epsilon_0}{4\pi^2} \iint_0^\infty \chi^{(3)}_{ijkl}(\omega_1, \omega_2, \omega - \omega_1 - \omega_2) \cdot A^{\sigma_a}_a(\omega_1) e^{-j\sigma_a \beta_a(\omega_1) z} e^{\sigma_a, j}_a(\omega_1) \cdot A^{\sigma_b}_b(\omega_2) e^{-j\sigma_b \beta_b(\omega_2) z} e^{\sigma_b, k}_b(\omega_2) \cdot [A^{\sigma_c}_c(\omega_1 + \omega_2 - \omega)]^* e^{+j\sigma_c \beta_c(\omega_1 + \omega_2 - \omega) z} e^{-\sigma_c, l}_c(\omega_1 + \omega_2 - \omega), \quad (2.28)$$

where $a, b, c = p, s$ denote center frequencies, and $\sigma_a, \sigma_b, \sigma_c = \pm 1$ indicate propagation directions. The contributions shown in Eq. (2.28) oscillate rapidly along z at a rate determined by the exponential functions in the integral. After inserting these contributions into Eq. (2.13) to finally obtain the spatial rate of change of the spectral envelopes $A^{\pm}_s(z,\omega)$, we make the slowly-varying-amplitude approximation [Boy03]. That is, we only keep the synchronous terms (those without an explicit oscillatory z dependence) and assume that the remaining terms oscillate sufficiently rapidly along z such that their contribution effectively averages to zero over sufficiently short distances and can be left out from the equations.

For example, the rate of change of the forward-propagating Stokes amplitudes has four phase-synchronous contributions:

$$\frac{\partial A_s^+(z,\omega)}{\partial z} = -j\frac{\omega}{4N_s(\omega)}e^{j\beta_s(\omega)z}\int e_s^{i*}(\omega)\big[P^i_{s+,s+,s+}(\omega) + 2P^i_{s+,s-,s-}(\omega) + 2P^i_{s+,p+,p+}(\omega) + 2P^i_{s+,p-,p-}(\omega)\big]\,\mathrm{d}A, \quad (2.29)$$

where the factor of 2 in front of the contribution $P^i_{s+,s-,s-}$ arises from the fact that $P^i_{s-,s+,s-}$ is also a phase-synchronous contribution, which, however, is equal to $P^i_{s+,s-,s-}$ due to intrinsic permutation symmetry. Equations similar to Eq. (2.29) for the backward-propagating Stokes wave and for the two pump waves are obtained analogously.

2.2.4. Nonlinear Schrödinger Equation for temporal envelopes

The model for nonlinear wave coupling derived so far, see Eq. (2.29), is in terms of the spectral envelopes of the forward- and backward-propagating pump and Stokes waves. For the cases considered in this thesis, a time-domain formulation is more desirable, which we will derive now.

Introduction of temporal envelopes

We define the complex temporal envelope functions $a_d^{\sigma_d}(z,t)$ of the forward- ($\sigma_d = +1$) and backward-propagating ($\sigma_d = -1$) pump ($d = p$) and Stokes ($d = s$) waves as

$$a_d^{\sigma_d}(z,t) = \frac{1}{\pi}\sqrt{\hat{N}_d}\int_0^\infty A_d^{\sigma_d}(z,\omega)e^{-j\sigma_d[\beta_d(\omega)-\hat{\beta}_d]z}e^{j(\omega-\omega_d)t}\,\mathrm{d}\omega, \quad (2.30)$$

where we have defined the mode-field normalizations and propagation constants at the center frequency as $\hat{N}_d = N_d(\omega_d)$ and $\hat{\beta}_d = \beta_d(\omega_d)$. In the following we assume that the beams are spectrally so narrow that the mode fields at the pump and Stokes wavelengths do not vary significantly in the corresponding wavelength range, and we simply use the mode fields at the center wavelengths, i. e., $\{\mathbf{e},\mathbf{h}\}_d(x,y,\omega) = \{\mathbf{e},\mathbf{h}\}_d(x,y,\omega_d) =: \{\mathbf{e},\mathbf{h}\}_d$.

Under these assumptions, the absolute square of the temporal envelope gives the instantaneous, longitudinally and temporally varying total power $P_d^{\sigma_d}(z,t)$ of the corresponding wave on a time scale long compared to $2\pi/|\omega_p - \omega_s|$,

$$P_d^{\sigma_d}(z,t) = |a_d^{\sigma_d}(z,t)|^2. \quad (2.31)$$

Dispersive and nonlinear contributions to the NLSE

The nonlinear Schrödinger equation is now obtained by differentiating the temporal envelope, Eq. (2.30), with respect to z, yielding upon application of the chain rule

$$\frac{\partial a_d^{\sigma_d}(z,t)}{\partial z} = \frac{1}{\pi}\sqrt{\hat{N}_d}\left\{ -j\sigma_d \int_0^\infty [\beta_d(\omega) - \hat{\beta}_d] A_d^{\sigma_d}(z,\omega) e^{-j\sigma_d[\beta_d(\omega)-\hat{\beta}_d]z} e^{j(\omega-\omega_d)t}\,\mathrm{d}\omega, \right. \\ \left. + \int_0^\infty \frac{\partial A_d^{\sigma_d}(z,\omega)}{\partial z} e^{-j\sigma_d[\beta_d(\omega)-\hat{\beta}_d]z} e^{j(\omega-\omega_d)t}\,\mathrm{d}\omega \right\}. \quad (2.32)$$

The first term on the right-hand side of Eq. (2.32) describes group velocity and its dispersion: by replacing the first occurrence of $\beta_d(\omega)$ with its Taylor expansion, $\beta_d(\omega) = \hat{\beta}_d + \beta_d'(\omega-\omega_d) + \beta_d''(\omega-\omega_d)^2/2 + \cdots$, the entire dispersive contribution can be written

$$\left.\frac{\partial a_d^{\sigma_d}(z,t)}{\partial z}\right|_{\text{dispersion}} = -\sigma_d \left[\beta_d' \frac{\partial a_d^{\sigma_d}(z,t)}{\partial t} + j\frac{\beta_d''}{2}\frac{\partial^2 a_d^{\sigma_d}(z,t)}{\partial t^2} + \cdots \right] \quad (2.33)$$

to any desired order. The second integral of Eq. (2.32) consists, after inserting the differential equation (2.29) for the spectral envelopes, of contributions of the form

$$Q_{d\sigma_d,a\sigma_a,b\sigma_b,c\sigma_c} = -\frac{\sigma_d}{4\pi\sqrt{\hat{N}_d}} e^{j[\sigma_d\hat{\beta}_d z-\omega_d t]} \int_0^\infty j\omega e^{j\omega t} \int e_d^{-\sigma_d,i}(\omega) P^i_{a\sigma_a,b\sigma_b,c\sigma_c}(\omega)\,\mathrm{d}A\,\mathrm{d}\omega, \quad (2.34)$$

where $e_j^{\sigma_j,i}$ denotes the i-th cartesian component of the electric field of the forward- ($\sigma_j = +1$) or backward-propagating ($\sigma_j = -1$) mode $j = p, s$. Now the expression for $P^i_{a\sigma_a,b\sigma_b,c\sigma_c}(\omega)$, Eq. (2.28), is inserted into Eq. (2.34). The nonlinear susceptibility tensor $\chi^{(3)}_{ijkl}$ occuring in Eq. (2.28) is approximated by its value at the center wavelengths of the respective beams, which is appropriate assuming that the spectra of the pump and Stokes beams are much narrower than the Raman-gain spectrum of the material.[2] Then, Eq. (2.34) can be written

$$Q_{d\sigma_d,a\sigma_a,b\sigma_b,c\sigma_c} = \frac{-3\sigma_d\epsilon_0\Gamma_{d\sigma_d,a\sigma_a,b\sigma_b,c\sigma_c}}{16\pi^3\sqrt{\hat{N}_d}} e^{j[\sigma_d\hat{\beta}_d z-\omega_d t]} \iiint_0^\infty j\omega e^{j\omega t} A_a^{\sigma_a}(\omega_1) e^{-j\sigma_a\beta_a(\omega_1)z} \\ \cdot A_b^{\sigma_b}(\omega_2) e^{-j\sigma_b\beta_b(\omega_2)z} [A_c^{\sigma_c}(\omega_1+\omega_2-\omega)]^* e^{+j\sigma_c\beta_c(\omega_1+\omega_2-\omega)z}\,\mathrm{d}\omega_1\,\mathrm{d}\omega_2\,\mathrm{d}\omega, \quad (2.35)$$

where $\Gamma_{d\sigma_d,a\sigma_a,b\sigma_b,c\sigma_c}$ is an overlap integral defined as

$$\Gamma_{d\sigma_d,a\sigma_a,b\sigma_b,c\sigma_c} = \int \chi^{(3)}_{ijkl}(\omega_a,\omega_b,-\omega_c) e_d^{-\sigma_d,i} e_a^{\sigma_a,j} e_b^{\sigma_b,k} e_c^{-\sigma_c,l}\,\mathrm{d}A, \quad (2.36)$$

[2] This requirement can be relaxed and then leads to the occurrence of convolutional integrals containing a Raman response function in Eq. (2.37).

where the nonlinear susceptibility tensor $\chi^{(3)}$ may be a function of the transverse coordinates. For example, in the case of silicon waveguides where only the silicon core is significantly nonlinear, the integration in Eq. (2.36) will extend only over the core of the waveguide. Finally, we use the definition of the temporal envelopes, Eq. (2.30), to express Eq. (2.35) in its final form in terms of the temporal envelopes,[3]

$$Q_{d\sigma_d,a\sigma_a,b\sigma_b,c\sigma_c} = \frac{-j3\sigma_d\epsilon_0\omega_d\Gamma_{d\sigma_d,a\sigma_a,b\sigma_b,c\sigma_c}}{16\sqrt{\hat{N}_a\hat{N}_b\hat{N}_c\hat{N}_d}}\left(1-\frac{j}{\omega_d}\frac{\partial}{\partial t}\right)\left[a_a^{\sigma_a}\cdot a_b^{\sigma_b}\cdot(a_c^{\sigma_c})^*\right]. \tag{2.37}$$

As we are dealing with beams whose spectra are much narrower than their center wavelengths, we can neglect the second term involving the time derivative in Eq. (2.37).

Coupled NLSEs for pump and Stokes beams

The final coupled NLSEs for the forward- and backward-propagating pump and Stokes envelopes $a_{p,s}^{\pm}(z,t)$ are [SdSE02]

$$\pm\frac{\partial a_p^{\pm}}{\partial z}+\frac{1}{v_p}\frac{\partial a_p^{\pm}}{\partial t} = \left(\Gamma_{p\pm p\pm}|a_p^{\pm}|^2+2\Gamma_{p\pm p\mp}|a_p^{\mp}|^2+2\Gamma_{p\pm s+}|a_s^{+}|^2+2\Gamma_{p\pm s-}|a_s^{-}|^2\right)a_p^{\pm}, \tag{2.38}$$

$$\pm\frac{\partial a_s^{\pm}}{\partial z}+\frac{1}{v_s}\frac{\partial a_s^{\pm}}{\partial t} = \left(\Gamma_{s\pm s\pm}|a_s^{\pm}|^2+2\Gamma_{s\pm s\mp}|a_s^{\mp}|^2+2\Gamma_{s\pm p+}|a_p^{+}|^2+2\Gamma_{s\pm p-}|a_p^{-}|^2\right)a_s^{\pm}, \tag{2.39}$$

where we have included only the phase-synchronous contributions and neglected group-velocity dispersion (see discussion in the next subsection). The $\Gamma_{a\sigma_a b\sigma_b}$ occurring in Eqs. (2.38)–(2.39),

$$\Gamma_{a\sigma_a b\sigma_b} = -j\frac{3\epsilon_0\omega_a}{16\hat{N}_a\hat{N}_b}\Gamma_{a\sigma_a,a\sigma_a,b\sigma_b,b\sigma_b}, \tag{2.40}$$

are overlap integrals of the mode fields with the nonlinear susceptibility tensor of the waveguide material defined in Eq. (2.36), and $v_p = 1/\beta_p'(\omega_p)$ and $v_s = 1/\beta_s'(\omega_s)$ are the group velocities of the pump and Stokes modes, respectively.

The nonlinear susceptibility tensor $\chi^{(3)}$ in the materials considered in this thesis is the sum of two contributions: one describing the electronic contribution that leads to FWM, SPM, XPM and two-photon absorption; and another one describing the nuclear contribution responsible for Raman scattering [SB65, Hel77]. As Eq. (2.40) is linear in the $\chi^{(3)}$, we can treat these two contributions to the various terms in the NLSEs (2.38)–(2.39) separately.

[3] For phase-mismatched contributions (those not occurring in Eq. (2.29)), an additional phase factor $\exp[j(\sigma_d\hat{\beta}_d-\sigma_a\hat{\beta}_a-\sigma_b\hat{\beta}_b+\sigma_c\hat{\beta}_c)z]$ (which is unity for the phase-synchronous contributions considered here) must be added to Eq. (2.37).

Longitudinal evolution of pump and Stokes powers

In writing the NLSEs, Eqs. (2.38)–(2.39), we have not included any terms describing group-velocity dispersion (GVD). This approximation permits us to describe the wave propagation simply in terms of the instaneous powers $P^{\pm}_{p,s}(z,t)$ defined in Eq. (2.31) instead of the complex temporal envelopes $a^{\pm}_{p,s}(z,t)$. From Eqs. (2.31) and (2.38)–(2.39), the pump and Stokes power $P^{\pm}_{p,s}(z,t)$ obey

$$\pm\frac{\partial P_p^{\pm}}{\partial z}+\frac{1}{v_p}\frac{\partial P_p^{\pm}}{\partial t}=2P_p^{\pm}\,\mathrm{Re}\left(\Gamma_{p\pm p\pm}P_p^{\pm}+2\Gamma_{p\pm p\mp}P_p^{\mp}+2\Gamma_{p\pm s+}P_s^{+}+2\Gamma_{p\pm s-}P_s^{-}\right), \quad (2.41)$$

$$\pm\frac{\partial P_s^{\pm}}{\partial z}+\frac{1}{v_s}\frac{\partial P_s^{\pm}}{\partial t}=2P_s^{\pm}\,\mathrm{Re}\left(\Gamma_{s\pm s\pm}P_s^{\pm}+2\Gamma_{s\pm s\mp}P_s^{\mp}+2\Gamma_{s\pm p+}P_p^{+}+2\Gamma_{s\pm p-}P_p^{-}\right), \quad (2.42)$$

where the various Γ's, defined in Eq. (2.40), are overlap integrals of the mode fields with the nonlinear susceptibility tensors $\chi^{(3)}_{ijkl}$.

2.2.5. Bulk nonlinear coefficients and effective areas

Eqs. (2.41)–(2.42) describe the evolution of the powers of the forward- and backward-propagating pump and Stokes waves along the waveguide. We now rewrite the contributions to these equations in a form that is more useful for optimizing waveguides with regards to nonlinearities.

Consider, for example, the contribution Γ_{s+p+} to Eq. (2.42), which describes how the forward-propagating pump wave influences the forward-propagating Stokes wave. In the CW case, where $\partial P^{\pm}_{p,s}/\partial t = 0$, this contribution can be written

$$\frac{\mathrm{d}P_s^{+}}{\mathrm{d}z}=(4\,\mathrm{Re}\,\Gamma_{s+p+})\cdot P_p^{+}P_s^{+}, \quad (2.43)$$

where, using Eqs. (2.40) and (2.36),

$$4\,\mathrm{Re}\,\Gamma_{s+p+}=\frac{3\epsilon_0\omega_s}{4\hat{N}_s\hat{N}_p}\,\mathrm{Im}\int\chi^{(3)}_{ijkl}(\omega_s,\omega_p,-\omega_p)e_s^{i*}e_s^{j}e_p^{k}e_p^{l*}\,\mathrm{d}A. \quad (2.44)$$

We can call $(4\,\mathrm{Re}\,\Gamma_{s+p+})$ the *modal* gain coefficient. Eq. (2.44) shows that it depends both on the waveguide structure (through the Stokes and pump mode fields $\mathbf{e}_s$ and $\mathbf{e}_p$) and on the material properties (through the tensor $\chi^{(3)}_{ijkl}$).[4]

[4] In the following we assume that only one of the materials constituting the waveguide is nonlinear (such as the silicon core in an SOI waveguide), or the nonlinear properties are independent of the transverse coordinate (such as in silica fibers). The $\chi^{(3)}_{ijkl}$ tensor appearing in Eq. (2.44) can then be assumed to be spatially non-varying, while the integration is possibly restricted to a certain region.

It is often desirable to separate the waveguide and material influences by writing the modal gain coefficient as

$$4\,\mathrm{Re}\,\Gamma_{s+p+} = \frac{g}{A_{\mathrm{eff}}}, \tag{2.45}$$

where the *bulk* gain coefficient g (to be defined below) is a material constant, and the effective area A_{eff} describes the influence of the waveguide geometry in terms of a compact formula (to be derived) involving only the mode fields and the waveguide shape. Such a formulation has the advantage that once the material parameter g is known, we can calculate the actual modal gain for any waveguide by simply inserting its mode fields in the effective-area formula, which encapsulates all the information on the tensorial structure of the nonlinearity. A waveguide can then be optimized with regards to nonlinear effects by optimizing the value of the effective area, without having to consider any tensors.

Bulk gain coefficient

In order to derive expressions for the effective areas, we first need to find the relation between the bulk gain constant g and the nonlinear-susceptibility tensor $\chi^{(3)}_{ijkl}(\omega_s, \omega_p, -\omega_p)$. The bulk gain coefficient g is defined in terms of the intensities I_p and I_s of homogeneous plane pump and Stokes waves, respectively, that propagate through the bulk nonlinear medium without any waveguide structure, such that the intensity of the Stokes wave obeys

$$\frac{\mathrm{d}I_s}{\mathrm{d}z} = g(\hat{\mathbf{s}}, \hat{\mathbf{p}}) I_p I_s, \tag{2.46}$$

where $\hat{\mathbf{s}}$ and $\hat{\mathbf{p}}$ are the polarization directions for the Stokes and pump waves. An expression for g can be found from the results of the coupled-mode formalism developed so far by inserting the electromagnetic fields of plane waves instead of waveguide modes in the overlap integrals defined in Eq. (2.36). As the coupled-mode formalism was developed for "modes" with a real transverse electric field, we can here only derive a result for the case where the pump and Stokes plane waves are linearly polarized, which however will be sufficient for our purposes.

We first assume that the plane waves extend over an arbitrary cross-sectional area A, such that their total power is $P^+_{p,s} = AI_{p,s}$. Inserting the latter relation into Eq. (2.43) gives

$$\frac{\mathrm{d}I_s}{\mathrm{d}z} = (4\,\mathrm{Re}\,\Gamma_{s+p+}) A I_p I_s. \tag{2.47}$$

A comparison of Eqs. (2.46) and (2.47) shows that the bulk gain constant g is the product of A and the modal gain coefficient $(4\,\mathrm{Re}\,\Gamma_{s+p+})$. The latter is obtained from Eq. (2.44), where due to the homogeneity of the waves, the integration over the transverse area can

now be replaced by a simple multiplication with A. The pump and Stokes fields can be written $\mathbf{e}_p = |\mathbf{e}_p|\hat{\mathbf{p}}$ and $\mathbf{e}_s = |\mathbf{e}_s|\hat{\mathbf{s}}$, respectively, where $\hat{\mathbf{p}}$ and $\hat{\mathbf{s}}$ are real transverse unit vectors along the polarization directions of the Stokes and pump beams. The $\hat{N}$'s appearing in Eq. (2.44) can be evaluated using Eq. (2.14) and the plane-wave relation $\mathbf{h}_{p,s} = \hat{\mathbf{z}} \times \mathbf{e}_{p,s} \cdot (n_{p,s}/Z_0)$, where Z_0 is the free-space impedance, and n_s and n_p are the (linear) refractive indices of the nonlinear material at the Stokes and pump wavelengths, respectively. The arbitrarily chosen A cancels out, giving the final result that the bulk gain g is related to the nonlinear susceptibility tensor $\chi^{(3)}_{ijkl}$ through

$$g(\hat{\mathbf{s}}, \hat{\mathbf{p}}) = \frac{3\omega_s \mu_0}{n_s n_p} \operatorname{Im}\left[\chi^{(3)}_{ijkl}(\omega_s, \omega_p, -\omega_p)\hat{s}^{i*}\hat{s}^j\hat{p}^k\hat{p}^{l*}\right]. \tag{2.48}$$

Effective area

Now that the bulk gain constant is known, see Eq. (2.48), we can derive an expression for the effective area, which quantifies the influence of the waveguide geometry on the modal gain. By Eq. (2.45), the effective area is defined as the ratio of the bulk gain constant (typically reported in measurements) to the modal gain constant given in Eq. (2.44).

There remains the question which bulk constant to use — as Eq. (2.48) shows, the bulk constant in general depends on the polarization states. A suitable reference bulk constant for the media in this thesis is that where the pump and Stokes fields are co-linearly polarized along the y axis, so we will prepare the expression for the effective area assuming this case. The general expression for the effective area is then the ratio of Eq. (2.48) for $\hat{\mathbf{s}} = \hat{\mathbf{p}} = \hat{\mathbf{y}}$ and Eq. (2.44),

$$A_{\text{eff}} = \frac{g(\hat{\mathbf{y}}, \hat{\mathbf{y}})}{4 \operatorname{Re} \Gamma_{s+p+}} = \frac{4Z_0^2 \hat{N}_s \hat{N}_p}{n_s n_p} \frac{\operatorname{Im} \chi^{(3)}_{yyyy}(\omega_s, \omega_p, -\omega_p)}{\operatorname{Im} \int \chi^{(3)}_{ijkl}(\omega_s, \omega_p, -\omega_p) e_s^{i*} e_s^j e_p^k e_p^{l*} \, \mathrm{d}A}. \tag{2.49}$$

For a specific nonlinearity, what remains to be done now is to make use of the structure of the corresponding $\chi^{(3)}_{ijkl}$ tensor to convert Eq. (2.49) into the final effective-area formula. This will be done for SRS in fibers in section 2.3, and in chapter 5 for the various nonlinear effects occurring in silicon.

We have in this entire section concentrated on the contribution Γ_{s+p+} in Eq. (2.42). The other contributions can be similarly decomposed into a bulk coefficient and an effective area. One obtains results very similar to Eq. (2.48) and Eq. (2.49), where the only differences are the frequency arguments for the nonlinear susceptibility tensor, the conjugation of some of the electric fields when backward-propagating waves are involved, and occasionally a factor of two in the denominator of the expression for the bulk coefficient. However, several of the potentially 16 different bulk constants and

effective areas will turn out to be identical due to the high symmetry of the materials considered in this thesis — see, e. g., Eqs. (5.11), (5.12), (5.22) and (5.32).

2.3. Raman amplification in optical fibers

In this section, we will apply the theory developed so far to write down the final set of equations that is going to be used in chapters 3 and 4 to model Raman amplifiers and lasers in optical fibers.

Eqs. (2.41)–(2.42) describe the evolution of the powers of the forward- and backward-propagating pump and Stokes waves in a general waveguide. One simplification that can be made for fibers is that the only nonlinear contribution to the right-hand sides of those equations is due to Stimulated Raman Scattering (SRS), such that only the contributions $\Gamma_{p\pm s\pm}$ and $\Gamma_{s\pm p\pm}$ remain. The otherwise significant nonlinear effects of SPM and XPM, described by the real part of the $\chi^{(3)}$, do not appear in Eqs. (2.41)–(2.42) as we are concerned with powers only, and two-photon absorption in silica fibers is negligible [Agr01].

2.3.1. Raman amplification in polarization-maintaining fibers

We start by treating the simple case of a single-mode fiber in which the pump and Stokes fields are linearly polarized along the same direction over the entire length of the fiber. This can be practically realized by using a polarization-maintaining fiber and injecting the pump and Stokes light such that they are polarized along a symmetry axis of the fiber. Then the field inside the fiber is well described by a single pump mode and a single Stokes mode, and the theory of section 2 can be applied.

Bulk Raman-gain constant

The bulk Raman-gain constant, Eq. (2.48), in general depends on the polarization of the pump and Stokes beams. In silica glass, only the relative orientation of the polarizations is relevant due to isotropicity. In isotropic materials, any component of a third-order nonlinear-susceptibility tensor can be expressed in terms of three independent components as

$$\chi^{(3)}_{ijkl} = \chi^{(3)}_{xxyy}\delta_{ij}\delta_{kl} + \chi^{(3)}_{xyxy}\delta_{ik}\delta_{jl} + \chi^{(3)}_{xyyx}\delta_{il}\delta_{jk}. \tag{2.50}$$

Inserting Eq. (2.50) into Eq. (2.48) and choosing an arbitrary real transverse unit vector $\hat{\mathbf{s}} = \hat{\mathbf{p}}$ (corresponding to identical linear polarizations for the pump and Stokes beams),

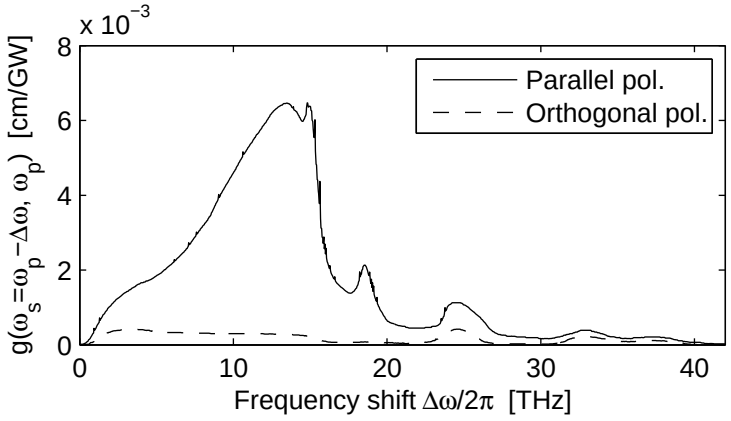

Figure 2.3.: Raman-gain spectrum of fused silica glass for a pump wavelength of $\lambda_p = 1450\,\mathrm{nm}$ (after [Sto04]), where the pump and Stokes waves are polarized identically (solid curve) or orthogonally (dashed curve).

one always obtains the same co-polarized gain,

$$g(\omega_s, \omega_p)_{\parallel} = \frac{3\omega_s \mu_0}{n_s n_p} \operatorname{Im} \chi^{(3),\mathrm{SRS}}_{yyyy}(\omega_s, \omega_p, -\omega_p), \tag{2.51}$$

independent of the actual polarization direction. In Eq. (2.51) we have defined

$$\chi^{(3),\mathrm{SRS}}_{yyyy} = \chi^{(3),\mathrm{SRS}}_{xxyy} + \chi^{(3),\mathrm{SRS}}_{xyxy} + \chi^{(3),\mathrm{SRS}}_{xyyx}. \tag{2.52}$$

The solid curve in Fig. 2.3 shows the measured co-polarized Raman-gain spectrum $g(\omega_s, \omega_p)_{\parallel}$ of bulk silica glass for a pump wavelength of 1450 nm [Sto04]. The maximum Raman gain of about $g = 0.65 \times 10^{-2}\,\mathrm{cm/GW}$ occurs at a frequency shift of 13.2 THz, i. e., at a Stokes wavelength of 1550 nm. The FWHM of the gain curve is as broad as 6 THz.

Effective areas

We have already derived the form of the effective area for the contribution Γ_{s+p+} to Eq. (2.42), which represents stimulated Raman scattering from the forward-propagating pump mode to the forward-propagating Stokes mode, see Eq. (2.49). For the case of optical fibers considered here, however, it can be simplified further. As fibers are weakly guiding waveguides, light propagation can be well described by modes which are uniformly polarized throughout the entire fiber cross section and whose longitudinal components can be neglected [SL83]. Assuming that the pump and Stokes modes are both linearly polarized along the same direction (due to the isotropicity of silica, we can

arbitrarily chose this to be the y direction), the effective area (2.49) reads

$$A_{\text{eff}}|_{s+p+} = \frac{g_{\parallel}}{4\,\text{Re}\,\Gamma_{s+p+}} = \frac{\int |e_p|^2\,\text{d}A \int |e_s|^2\,\text{d}A}{\int |e_p|^2 |e_s|^2\,\text{d}A}, \tag{2.53}$$

where $g_{\parallel}$ is the co-polarized gain given by Eq. (2.51), and in evaluating the mode-field normalizations $\hat{N}_{p,s}$ we have made use of the plane-wave relation $\mathbf{h}_{p,s} = \hat{\mathbf{z}} \times \mathbf{e}_{p,s}/Z$, which is valid for the mode fields of weakly guiding fibers [SL83].

Eq. (2.53) is the well-known expression for the effective core area of optical fibers [Agr01]. It can be directly used to optimize fibers for their Raman-gain properties. One simply needs to find a waveguide structure that minimizes the effective area given by Eq. (2.53). Then, the modal Raman-gain constant ("Stokes gain per unit length per unit pump power") given in Eq. (2.45) is maximized.

It is easily seen that the effective areas describing the contributions Γ_{s-p+} and $\Gamma_{s\pm p-}$ are equal to the effective area just derived, i. e.,

$$A_{\text{eff}}|_{s-p+} = \frac{g_{\parallel}}{4\,\text{Re}\,\Gamma_{s-p+}} = A_{\text{eff}}|_{s\pm p-} = \frac{g_{\parallel}}{4\,\text{Re}\,\Gamma_{s\pm p-}} = A_{\text{eff}}|_{s+p+} =: A_{\text{eff}}, \tag{2.54}$$

such that the longitudinal evolution of the Stokes powers is given by

$$\pm \frac{\partial P_s^{\pm}}{\partial z} + \frac{1}{v_s}\frac{\partial P_s^{\pm}}{\partial t} = \frac{g_{\parallel}}{A_{\text{eff}}}(P_p^{+} + P_p^{-})P_s^{\pm}. \tag{2.55}$$

Finally, the longitudinal evolution of the pump powers can be written

$$\pm \frac{\partial P_p^{\pm}}{\partial z} + \frac{1}{v_p}\frac{\partial P_p^{\pm}}{\partial t} = -\frac{g_{\parallel}}{A_{\text{eff}}}\frac{\lambda_s}{\lambda_p}(P_s^{+} + P_s^{-})P_p^{\pm}, \tag{2.56}$$

where we have made use of the symmetry relation [SB65]

$$\chi_{ijkl}^{(3),\text{SRS}}(\omega_p, \omega_s, -\omega_s) = \left[\chi_{ijkl}^{(3),\text{SRS}}(\omega_s, \omega_p, -\omega_p)\right]^{*}. \tag{2.57}$$

The factor $\lambda_s/\lambda_p > 1$ occurring in Eq. (2.56) expresses photon-number conservation: by SRS, one photon is lost from the pump wave and added to the Stokes wave. As the pump photon has a higher energy than the Stokes photon, the corresponding pump-power loss is larger by a factor of $h\nu_p/h\nu_s = \lambda_s/\lambda_p$ compared to the Stokes-power gain, see Eqs. (2.55)–(2.56).

2.3.2. Raman amplification in standard single-mode fibers

In section 2.3.1 we have considered polarization-maintaining fibers in which the pump and Stokes fields are co-linearly polarized. In contrast, when the pump and Stokes

waves are orthogonally polarized, one obtains from Eqs. (2.48) and (2.50) a different bulk Raman gain constant,

$$g(\omega_s, \omega_p)_\perp = \frac{3\omega_s \mu_0}{n_s n_p} \operatorname{Im} \chi^{(3),\mathrm{SRS}}_{xxyy}(\omega_s, \omega_p, -\omega_p). \tag{2.58}$$

This gain is plotted as the dashed curve in Fig. 2.3. In the interesting region near the Raman-gain peak at 13.2 THz, the cross-polarized gain is less than 10% of the co-polarized gain.

The fact that cross- and co-polarized gains in silica differ by a factor of more than ten is significant for Raman amplification in optical fibers, because the relative polarizations of pump and Stokes waves change randomly during propagation as a result of birefringence fluctuations that lead to polarization-mode dispersion (PMD). Effectively, the Raman gain experienced by the Stokes wave will lie somewhere between the cross- and co-polarized gain. It will depend on the relative polarizations of the pump and Stokes waves that are launched into the fiber, a phenomenon called polarization-dependent gain (PDG). To make things even worse, the PDG can also fluctuate over time. Therefore, the polarization of the pump is often deliberately scrambled in practical Raman amplifiers.[5] It has been shown both experimentally [EMN00, KFH02] and theoretically [LA03] that this effectively suppresses PDG. The Raman gain seen by the Stokes wave is then simply the average of the cross- and co-polarized gains.

2.3.3. Summary of the model

Finally, by phenomenologically introducing the linear fiber losses α_p and α_s at the pump and Stokes wavelength, respectively, and taking into account the discussion in section 2.3.2, the power-evolution equations of section 2.3.1 can be written in the following compact form [Agr01, HA05],

$$\pm\frac{\partial P_p^\pm}{\partial z} + \frac{1}{v_p}\frac{\partial P_p^\pm}{\partial t} = \left[-\alpha_p - \tilde{g}\frac{\lambda_s}{\lambda_p}(P_s^+ + P_s^-)\right] P_p^\pm, \tag{2.59}$$

$$\pm\frac{\partial P_s^\pm}{\partial z} + \frac{1}{v_s}\frac{\partial P_s^\pm}{\partial t} = \left[-\alpha_s + \tilde{g}(P_p^+ + P_p^-)\right] P_s^\pm, \tag{2.60}$$

where the Raman-gain coefficient $\tilde{g}$ of the fiber is defined as

$$\tilde{g} = \begin{cases} \frac{g_\parallel}{A_{\mathrm{eff}}} & \text{for HiBi fibers with co-linear pump and Stokes polarizations,} \\ \frac{g_\parallel + g_\perp}{2A_{\mathrm{eff}}} & \text{for non-polarization-maintaining single-mode fibers.} \end{cases} \tag{2.61}$$

[5] Many pump lasers, such as some fiber lasers, already emit unpolarized light such that often there is no need for deliberately depolarizing them.

Typical values for the $\tilde{g}$ of non-polarization-maintaining fibers are between 0.3 /Wkm for standard single-mode fibers and 2.2 /Wkm for special high-Raman-gain fibers. Recent research highlights the possibilities of using holey fibers [TPT05] or heavily germania-doped fibers [D$^+$05] for achieving even higher gain coefficients.

2.4. Chapter summary

In this chapter, we have derived the nonlinear Schrödinger equations (NLSEs) that describe the longitudinal and temporal evolution of the pump and Stokes powers inside a general waveguide under the influence of third-order nonlinear effects. The NLSEs have been formulated such that they are particularly useful for the later chapter 5, where they will be adapted to the case of silicon waveguides. In section 2.3 we have specialized the equations such that they describe stimulated Raman scattering in silica fibers, which forms the basis for the following two chapters.

3. Designs for efficient and tunable Raman fiber lasers

In this chapter and and in the following one, new designs for Raman fiber lasers (RFLs) for the use as pump sources in Raman fiber amplifiers (RFAs) are proposed and discussed. The basic characteristics and the modeling of RFLs will be explained in the introductory section 3.1. Section 3.2 then introduces the double-cavity RFL which offers more design freedom than a simple RFL. Finally, section 3.3 introduces a design for widely tunable RFLs.

The results of this chapter have been published in [CKRB03, KCRB03, KR05b].

3.1. Basics of Raman fiber lasers

3.1.1. History and applications

The first continuous-wave Raman laser based on an optical fiber has been demonstrated in 1976 by Hill et al. [HKJ76]. Extended designs that were tunable and also incorporated several cascaded Stokes resonators were developed in the following years [Sto80a]. However, all of these lasers incorporated bulk optics for realizing the cavity reflectors and tunable elements. In 1988, the first Raman fiber laser based on fiber Bragg gratings (FBGs) has been demonstrated [KSS$^+$88]. Since then, RFLs have been widely investigated as efficient all-fiber wavelength converters for use in optical communication systems. For example, they are now often used as pump lasers for Raman fiber amplifiers (RFAs), see Fig. 1.1 [CHB04].

The Stokes generation process in RFLs can be cascaded—in 1994, the first all-fiber cascaded Raman laser was shown [GEM$^+$94], in which a pump laser at 1060 nm is converted to 1240 nm via two auxiliary resonators with an efficiency of 50%. In 2000, a multi-wavelength RFL was developed which emitted two closely spaced wavelengths [CLJ$^+$00]. Using such RFLs, the gain profile of RFAs can be widened considerably. More recent designs even emit six wavelengths simultaneously [LBL$^+$02]. An RFL which emitted two

wavelengths spaced by an entire Raman shift of 13.2 THz in a controlled manner was successfully used in 2002 as a dual-order RFA pump [BBR+02].

3.1.2. Geometry and working principle

Fig. 3.1 shows the schematic of a basic Raman fiber laser. The resonator is formed by an optical fiber of length L and two fiber Bragg gratings reflecting at the Stokes wavelength λ_s, with reflectivities R_l and R_r at the left-hand and right-hand fiber ends, respectively. The laser is pumped optically at the left-hand side at the wavelength λ_p. An optional pump-wavelength reflector R_p at the right-hand end of the fiber can reflect unused pump power back into the cavity, thus further increasing the efficiency of the device. In this chapter, we also call the arrangement shown in Fig. 3.1 a single-cavity RFL (SC-RFL), in order to avoid confusion with the double-cavity RFL (DC-RFL) to be introduced in Sect. 3.2.

The operation principle of the laser is simple: when the pump laser is switched on, spontaneous Raman scattering will generate light at new wavelengths (see Fig. 2.3), the most intense peak being generated at the Stokes wavelength corresponding to an optical frequency downshifted by about 13.2 THz from the pump frequency (for example, if the pump laser is an Ytterbium fiber laser emitting at 1060 nm as in the experiments performed at TUHH [Cie05], the Stokes wavelength will be 1112 nm). Furthermore, the spontaneously generated Stokes light in the cavity will be amplified through the effect of stimulated Raman scattering — it will experience Raman gain proportional to the amount of pump power. When reaching the ends of the waveguide, part of the Stokes light leaves the waveguide (forming the output beam), and part of it is reflected back into the waveguide. When the pump power is high enough, this feedback plus the amplification through stimulated Raman scattering leads to an increasing buildup of optical power at the Stokes wavelength. Eventually, a steady state is reached in which the laser continuously converts the pump radiation at λ_p to Stokes radiation at λ_s.

In the case of $R_p = 0$, i. e., an RFL with single-pass pumping (SPP), the pump power launched at the left-hand side of the RFL passes the fiber only once, and the unused pump power leaves the fiber at the right-hand side. On the other hand, in the case of double-pass pumping (DPP), i. e., $R_p > 0$, the pump power reaching the right-hand fiber end is reflected back and passes the fiber a second time. The use of DPP as opposed to SPP thus increases the effective length of Raman interaction between pump and Stokes light. As a consequence, DPP setups typically employ shorter fibers than SPP setups, even though they can have similar conversion efficiencies (see the results in Sect. 3.2.3).

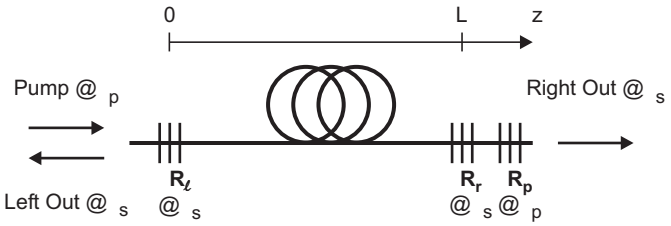

Figure 3.1.: Schematic of a basic single-cavity Raman fiber laser (SC-RFL).

3.1.3. Modeling, simulation, and typical characteristics

Following Sect. 2.3, we model the continuous-wave operation of a single-cavity, non-cascaded RFL (as shown in Fig. 3.1) by the differential equations for the forward- (+) and backward-propagating (−) pump ("p") and Stokes ("s") waves $P_p^{\pm}$ and $P_s^{\pm}$, respectively,

$$\pm\frac{1}{P_p^{\pm}}\frac{\mathrm{d}P_p^{\pm}}{\mathrm{d}z} = -\alpha_p - g\frac{\lambda_s}{\lambda_p}(P_s^+ + P_s^-), \tag{3.1}$$

$$\pm\frac{1}{P_s^{\pm}}\frac{\mathrm{d}P_s^{\pm}}{\mathrm{d}z} = -\alpha_s + g(P_p^+ + P_p^-). \tag{3.2}$$

The reflections at the FBGs and the pump-power injection are taken into account by the boundary conditions

$$P_s^+(0) = R_l P_s^-(0), \qquad P_s^-(L) = R_r P_s^+(L), \tag{3.3}$$

$$P_p^+(0) = P_0, \qquad P_p^-(L) = R_p P_p^+(L). \tag{3.4}$$

Here, z denotes the position along the fiber, L is the fiber length, and $R_{l,r,p}$ are the power reflectivities of the three FBGs shown in Fig. 3.1. Finally, P_0 is the input pump power at $z = 0$ — for simplicity of the description, the pump power is coupled in from the left-hand side for each RFL configuration throughout this section. The reflectors R_l and R_r are assumed to be lossless, and the left-hand and right-hand Stokes output powers of this RFL are then given as

$$P_l = P_s^-(0)(1 - R_l), \qquad P_r = P_s^+(L)(1 - R_r). \tag{3.5}$$

The present model was first used by AuYeung and Yariv to discuss the characteristics of RFLs in 1979 [AY79]. It was later extended to a model for cascaded and multi-wavelength RFLs [RCD00, JM01, CRB03].

All RFLs analyzed in this section are pumped at the wavelength $\lambda_p = 1060\,\mathrm{nm}$ and have FBGs at the Stokes wavelength $\lambda_s = 1112\,\mathrm{nm}$, corresponding to the frequency difference of 13.2 THz where the Raman gain is maximal, see Fig. 2.3. We assume a

fiber with Raman gain constant $g = 1.2\,(\mathrm{W}\cdot\mathrm{km})^{-1}$ and fiber loss coefficients of $\alpha_p = 0.8\,\mathrm{dB/km}$ and $\alpha_s = 0.66\,\mathrm{dB/km}$ for the pump and Stokes wavelengths, respectively. The results obtained here for this specific fiber can easily be rescaled to other fibers [RCK03].

Numerical solution

An explicit analytic solution of the boundary-value problem (BVP) given by Eqs. (3.2)–(3.4) is not known. However, a solution can be readily obtained numerically using a collocation method [AMR88] for two-point BVPs which is available as the function `bvp4c` in MATLAB.

An example of the result of such a numerical simulation is shown in Fig. 3.2, where the steady-state longitudinal distribution of the pump and Stokes powers inside an RFL is plotted. It has left-hand and right-hand Stokes reflectivities of $R_l = 99\%$ and $R_r = 51.2\%$, respectively, no pump backreflector ($R_p = 0$), and the result is shown for a pump power of $P_0 = 4\,\mathrm{W}$. The pump power injected at the left-hand side (at $z = 0$) decreases towards larger z, because it loses power to the forward- and backward-propagating Stokes waves through SRS; also, it experiences linear losses. The forward-propagating Stokes wave grows towards larger z as it experiences Raman gain. When it reaches the right-hand end of the fiber, 51.2% of it is reflected by the FBG, forming the backward-propagating Stokes wave (the part of the Stokes power not reflected at the right-hand FBG forms the output power). Upon propagating back to the left-hand end of the fiber, the backward-propagating Stokes wave, too, is amplified by SRS. Finally, 99% of the backward-propagating Stokes power are reflected to form the forward-propagating Stokes wave, which finishes the round-trip.

The thick solid line in Fig. 3.6 shows the characteristics of this RFL. When the pump power exceeds the threshold power of 1.17 W, the output power grows monotonously.

Lasing threshold

Even though a general analytic solution of Eqs. (3.2)–(3.4) is not known, the threshold power P_{th} can be given in closed form [AY79].

By integrating the differential equations (3.2) describing the longitudinal evolution of the Stokes powers over the entire fiber, one obtains the two relations

$$P_s^+(L) = GP_s^+(0), \qquad P_s^-(0) = GP_s^-(L), \tag{3.6}$$

where

$$G = \exp\left\{\int_0^L -\alpha_s + g[P_p^+(z) + P_p^-(z)]\,\mathrm{d}z\right\} \tag{3.7}$$

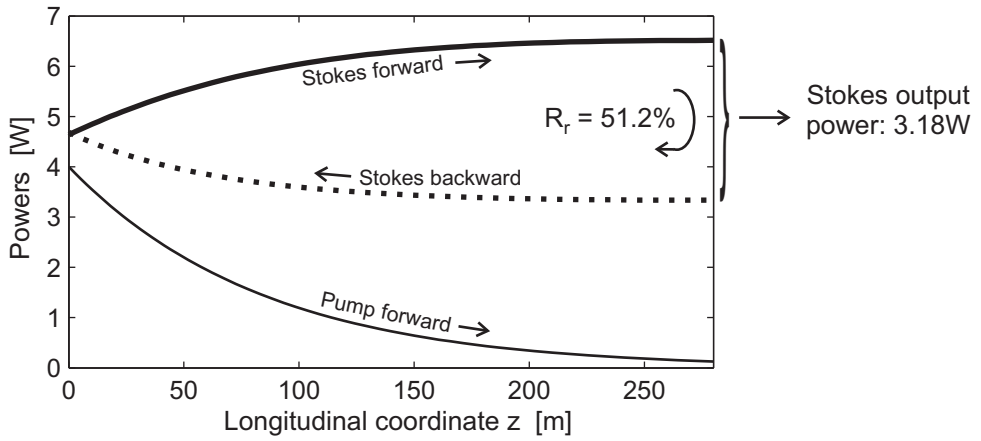

Figure 3.2.: Longitudinal pump- and Stokes-power distribution inside a Raman fiber laser.

is the single-pass gain experienced by both the forward- and backward-propagating Stokes waves. By then making use of the boundary conditions (3.3), one obtains the statement

$$P_s^+(0) \cdot (1 - R_l R_r G^2) = 0, \tag{3.8}$$

which must always be fulfilled by any solution of our model, no matter how large the pump power. If the laser is beyond threshold, $P_s^+(0) > 0$ and Eq. (3.8) shows that then the round-trip condition

$$R_l R_r G^2 = 1 \tag{3.9}$$

must be fulfilled. At the lasing threshold, the depletion of the pump power by the Stokes waves can be neglected, and the longitudinal pump-power distribution is a simple exponential decay due to the linear losses, see Eq. (3.1). Thus, G can be evaluated explicitly. Inserting this into the round-trip condition (3.9) and rearranging for the pump power, one obtains the threshold pump power for arbitrary pump backreflectors R_p,

$$P_{\mathrm{th}} = \frac{\alpha_p}{g} \cdot \frac{\alpha_s L - \frac{1}{2}\ln(R_l R_r)}{(1 - e^{-\alpha_p L})(1 + R_p e^{-\alpha_p L})}. \tag{3.10}$$

For $R_p = 0$, this formula reduces to that derived in Ref. [AY79].

3.1.4. Conversion efficiency versus threshold

In this section, we show that the threshold power and the conversion efficiency at large pump powers can not be designed independently in SC-RFLs as shown in Fig. 3.1. Later in Sect. 3.2, the concept of DC-RFLs is introduced, which does not have such a restriction. For the sake of simplicity, we concentrate on RFLs with single-pass pumping only

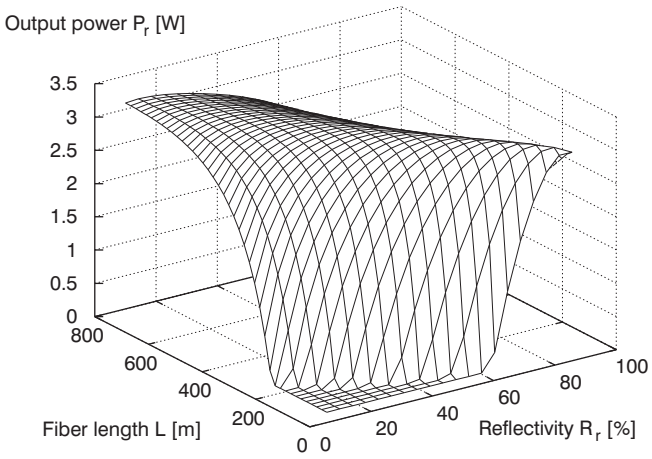

Figure 3.3.: The right-hand output power P_r of a single-cavity Raman fiber laser as a function of the right-mirror reflectivity R_r and the fiber length L. The left-mirror reflectivity is $R_l = 99\%$, and the pump power is $P_0 = 4\,\mathrm{W}$.

($R_p = 0$). Qualitatively, however, RFLs behave the same for $R_p > 0$ (see Sect. 3.2.3).

We start by calculating the output power of various SC-RFLs for a fixed input pump power of $P_0 = 4\,\mathrm{W}$, launched from the left-hand fiber end. As usually done in practically realized RFLs [HBM+02], we choose a mirror for the Stokes wavelength with high reflectivity (HR), $R_l = 99\%$, at the same end of the fiber, so that light is coupled out essentially only at the right-hand side of the RFL (Fig. 3.1). In order to find a configuration that is optimal in the sense that it emits maximum output power, we vary the two remaining free parameters, namely the right-hand reflectivity R_r and the fiber length L.

Fig. 3.3 shows the calculated right-hand output power P_r as a function of R_r and L. At $R_r = 51.2\%$ and $L = 280\,\mathrm{m}$, P_r has its maximum value of 3.18 W. However, this maximum is not very pronounced and its exact location can not be made out clearly in the graph. In fact, there is a relatively large range of parameters R_r and L that yield an RFL with almost maximal conversion efficiency [KST+01]. However, we will show next that all these near-optimal lasers have a similar threshold pump power, i. e., it is not possible to find an RFL that has near-maximal conversion efficiency and at the same time a considerably lower threshold pump power.

To this aim, we pose the (arbitrary) requirement that the RFL to be designed have an output power not below 99% of the maximum obtainable output power 3.18 W. We thus restrict ourselves to a certain allowed range for the parameters R_r and L. This range is shown in Fig. 3.4 by the longish grey area in the R_r–L plane, where the black dot indicates the maximum-output-power configuration. Also included in Fig. 3.4 are the

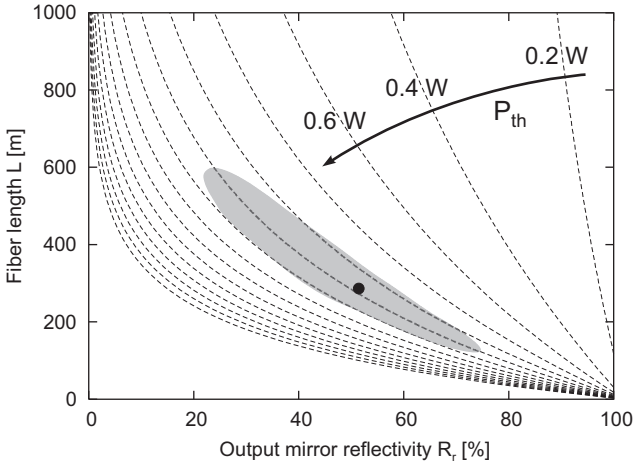

Figure 3.4.: Lines of constant threshold power P_{th} for a single-cavity, single-pass-pumped Raman fiber laser separated by steps of 0.2 W, in the plane of the right-mirror reflectivity R_r and the fiber length L. At $P_0 = 4\,\mathrm{W}$, the right-hand output power of the configurations inside the grey area is greater than 99% of the maximum output power of 3.18 W, which is obtained for $R_r = 51.2\%$ and $L = 280\,\mathrm{m}$ (black dot).

lines of constant threshold power, calculated from (3.10) with $R_p = 0$. As can be seen, the allowed parameter range is oriented just along the lines of constant threshold power, with the result that the threshold power of the maximum-output-power RFL (which is $P_{\mathrm{th}} = 1.17\,\mathrm{W}$) can be lowered at most by 0.2 W by choosing another configuration from the right upper edge of the grey area. The threshold power can be lowered further only at the expense of considerably reduced conversion efficiency at $P_0 = 4\,\mathrm{W}$. This demonstrates the collision of the two optimization criteria "large output power" and "low threshold power".

In order to further illustrate the collision of the two requirements "large output power" and "low threshold power" in SC-RFL designs, we now consider a variety of RFLs with a much lower, fixed threshold power of $P'_{\mathrm{th}} = 0.2\,\mathrm{W}$ (in contrast, the maximum-output-power RFL found at the beginning of this section had a threshold power of $P_{\mathrm{th}} = 1.17\,\mathrm{W}$) and look at their output powers when pumped with $P_0 = 4\,\mathrm{W}$. Suitable parameters R_r and L for the desired low-threshold RFLs can be found directly from Eq. (3.10) and correspond to the dashed line labeled "0.2 W" in Fig. 3.4. Note that each of the low-threshold RFLs can be uniquely identified by its fiber length L. In Fig. 3.5, the output power at $P_0 = 4\,\mathrm{W}$ is plotted versus the length L of the considered low-threshold RFLs. The maximum output power achievable with the low-threshold RFLs at $P_0 = 4\,\mathrm{W}$ is about 1.1 W, while that of the maximum-output-power RFL is 3.18 W, for which we posed no restrictions on the threshold power.

The results of this section show clearly that one has to find a trade-off between the threshold power and the conversion efficiency when designing an SC-RFL. The same situation arises in many conventional lasers. The reason is that a low threshold requires low cavity round-trip losses, i. e., cavity mirrors with a high reflectivity, see Eq. (3.10). However, a high reflectivity implies low transmission, so that for mirror reflectivities approaching 100% (which would result in the lowest possible threshold), the Stokes power actually coupled out of the cavity is becoming ever lower and vanishes for the case where the threshold pump power is lowest.

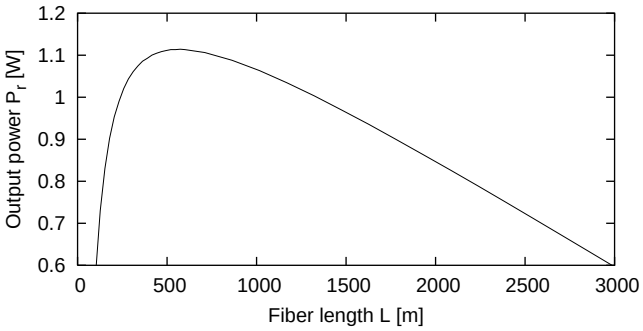

Figure 3.5.: Output power for a pump power $P_0 = 4\,\mathrm{W}$ of single-cavity Raman fiber lasers with the same threshold power of 0.2 W versus the fiber length L.

3.1.5. Comparison of left-hand- and right-hand-output RFLs

It is important for the double-cavity designs discussed later that we compare the single-cavity RFLs considered so far with their "reversed" counterparts, i. e., we exchange the left-hand (highly reflective in Sect. 3.1.4) and right-hand (moderately reflective in Sect. 3.1.4) mirrors. Now, the laser light is coupled out at the same fiber end at which the pump power is coupled in. We will see that such an output reversal only weakly influences the input-output characteristics of the RFL.

The input-output characteristic of the RFL marked with a black dot in Fig. 3.4 is plotted as a thick solid line in Fig. 3.6. The corresponding reversed (left-hand output) RFL has been obtained by exchanging R_r and R_l in the optimized design and considering the left-hand side of the RFL as the output now. The resulting characteristic is plotted as a thick dashed curve. The difference between the two curves is very small and hardly noticable. The respective threshold powers are even exactly the same, as predicted by Eq. (3.10).

For further illustration of the smallness of the effect of interchanging the reflectivities, the characteristics of two other (non-optimized) setups with arbitrarily chosen R_r and

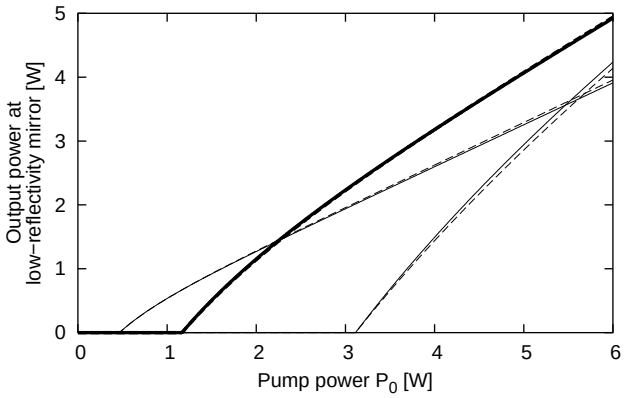

Figure 3.6.: Input-output characteristics of single-cavity Raman fiber lasers. The thick solid and dashed curves (almost indistinguishable) correspond to the SC-RFL optimized in Sect. 3.1.4 and the one obtained by interchanging the mirror reflectivities R_l and R_r, respectively. The remaining two pairs of curves represent additional arbitrary setups, illustrating the small effect of interchanging the reflectivities.

L and their reversed counterparts have been plotted. The two curves with a threshold of 3.1 W correspond to a setup with $R_r = 35\%$ and $L = 150\,\mathrm{m}$, and the two curves with a threshold of 0.5 W correspond to a setup with $R_r = 60\%$ and $L = 700\,\mathrm{m}$. Again, the behavior of the reversed setups is very close to that of the original, non-reversed ones. These examples show that left-hand-output configurations are practically equivalent to right-hand-output configurations. This will be illustrated again by the results of Sect. 3.2.3.

3.2. Double-cavity Raman fiber lasers

In this section, we introduce the concept of double-cavity Raman fiber lasers. We demonstrate that the threshold and the conversion efficiency can be optimized independently in these devices. The results of this section have been published in [KR05b].

Motivation

When an RFL is designed for use as an amplifier pump source, it is usually optimized for maximum conversion efficiency, i. e., such that it provides as much output power as possible at the maximum available input pump power. On many occasions, however, other criteria may be more important for the design of an RFL. For example, applications that require switching between several power levels, such as a measurement test source or a dynamically configurable optical amplifier [CKRB04, BGL04], could profit from an

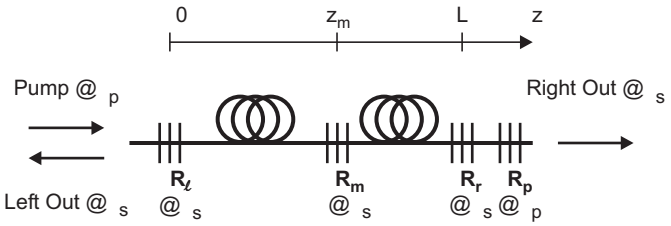

Figure 3.7.: Schematic of a double-cavity Raman fiber laser (DC-RFL).

RFL that has both a low threshold pump power and a high conversion efficiency at large pump powers.

In a conventional single-cavity RFL (SC-RFL), the output wavelength (Stokes) cavity is formed by two FBGs at the ends of an optical fiber, see Sect. 3.1. In such devices, the two optimization criteria "high conversion efficiency" (at large pump powers) and "low threshold pump power" collide with each other, as shown in Sect. 3.1.4. A high conversion efficiency can usually only be achieved at the cost of a high threshold, so that a trade-off has to be found in the design of the device if both of these properties are desirable.

On the other hand, we show here that the introduction of a third FBG into the Stokes cavity, resulting in a double-cavity RFL (DC-RFL), can lead to a significantly different behavior of the input-output characteristics compared to a conventional single-cavity RFL. In particular, the threshold pump power of an RFL and its conversion efficiency at large pump powers can be optimized independently. A totally different application of DC-RFLs—the reduction of pump-to-Stokes transfer of relative intensity noise—will be discussed in Sect. 4.3.

3.2.1. Geometry and model

We consider the setup shown in Fig. 3.7. It represents a double-cavity RFL (DC-RFL) which differs from usual single-cavity RFLs only in that the cavity contains one more Stokes reflector R_m in the middle of the cavity in addition to the left-hand and right-hand Stokes reflectors R_l and R_r and the pump reflector R_p. Thus, two concatenated cavities ($R_l \leftrightarrow R_m$ and $R_m \leftrightarrow R_r$) are formed for the Stokes laser line instead of only one as in conventional single-cavity RFLs. For the moment, we set $R_p = 0$.

The DC-RFL shown in Fig. 3.7 can be numerically simulated in a manner very similar to SC-RFLs, the model of which was described in Sect. 3.1.3. One merely has to take into account that in a DC-RFL, the values of the forward- and backward-propagating Stokes waves before and behind the new intra-cavity FBG are coupled through the two

new boundary conditions

$$P_s^+(z_m^+) = T_m P_s^+(z_m^-) + R_m P_s^-(z_m^+), \tag{3.11}$$

$$P_s^-(z_m^-) = T_m P_s^-(z_m^+) + R_m P_s^+(z_m^-), \tag{3.12}$$

where z_m^- and z_m^+ indicate longitudinal positions directly at the left-hand and right-hand sides of the intra-cavity reflector with reflectivity R_m and transmittivity T_m, respectively. When using the `bvp4c` function in MATLAB, the new boundary conditions (3.11) and (3.12) are easily incorporated in an existing program for the simulation of SC-RFLs. In the following examples, this reflector is assumed to be lossless ($T_m = 1 - R_m$), which is a reasonable assumption for FBGs inscribed directly into the Raman fiber.

The boundary conditions (3.11) and (3.12) are based on the assumption of incoherent superposition of the reflected and transmitted powers. Thus, this formalism is only applicable as long as the spatial separation of the Stokes reflectors is larger than the coherence length of the Stokes light; otherwise interference effects would have to be taken into account [RCK03]. The typical spectral width of the RFL output is typically in the order of a nanometer [KSS+88, PKU00, KCDP00, BDB+00, APT+01, MHB+01], corresponding to a coherence length in the order of millimeters, which is well below the usual spatial separation of the Stokes reflectors of tens to thousands of meters.

3.2.2. Input-output characteristics

As a first example, we choose a DC-RFL with the same fiber as in Sect. 3.1 and the new parameters $R_l = 74\%$, $R_m = 99\%$, $R_r = 99\%$, $R_p = 0$, $z_m = 150\,\mathrm{m}$ and $L = 270\,\mathrm{m}$, where z_m and R_m are the position and the reflectivity of the newly introduced intra-cavity Stokes reflector in between R_l and R_r, respectively. Note that for now, we restrict the discussion to the case when only R_l is moderately reflective, and the remaining reflectors R_m and R_r are highly reflective. Other combinations will be discussed in Sect. 3.2.3.

Fig. 3.8 shows the numerically calculated left-hand and right-hand output characteristics of our DC-RFL as the thick solid and dotted curves, respectively. A threshold power of 0.203 W is found,[1] above which the left-hand output power increases with a relatively small slope. This slope is initially increasing, but at pump powers above 2 W it decreases again. The right-hand output power also exhibits an unusual behavior, as it is not monotonically increasing everywhere. It increases until it reaches its maximum at a pump power of $P_0 = 1.02\,\mathrm{W}$, above which it decreases again. These results should be contrasted to the fact that the input-output characteristics of SC-RFLs are always

[1] An analytic relation for the threshold pump power of double-cavity RFLs can be found in [KR05b].

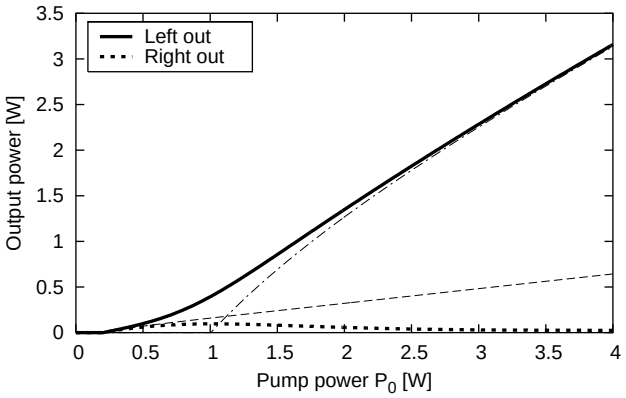

Figure 3.8.: Input-output characteristics of a double-cavity Raman fiber laser. The thick solid and dotted curves represent left-hand and right-hand output power, respectively. The thin dashed and dashed-dotted curves represent the left-hand outputs of SC-RFLs corresponding to the individual right-hand and left-hand cavities, respectively.

numerically observed to be both monotonically increasing and concave, i. e., the slopes of the curves are monotonically decreasing with increasing P_0 (see the curves in Fig. 3.6).

The most notable feature of these characteristics is, however, the high conversion efficiency observed for large pump powers at the left-hand output, in spite of a low threshold power. The presented configuration has an output power of $P_l = 3.16\,\mathrm{W}$ at $P_0 = 4\,\mathrm{W}$ and a threshold power of $0.2\,\mathrm{W}$. Such characteristics have been shown above to be impossible to be achieved with an SC-RFL: in Sect. 3.1.4 we showed that no right-hand output SC-RFL with a threshold power of $0.2\,\mathrm{W}$ based on the same fiber can give more than $1.1\,\mathrm{W}$ of output power when pumped with $4\,\mathrm{W}$ (see Fig. 3.5). (From the results in Sect. 3.1.5, we conclude a similar limitation for left-hand output SC-RFLs.) By introducing the concept of the double-cavity RFL, we have thus eliminated the incompatibility of the two optimization criteria "low threshold power" and "high conversion efficiency".

Asymptotic input-output characteristics

In order to see the reason for the particular behavior of the input-output characteristics of DC-RFLs, we consider separately the two cavities that constitute the DC-RFL. It follows from Eq. (3.10) with $R_p = 0$ that an SC-RFL made up of the right-hand cavity ($R_m \leftrightarrow R_r$) alone would have a lower threshold than an SC-RFL consisting of the left-hand cavity ($R_l \leftrightarrow R_m$). This is due to the larger feedback of the HR mirrors R_m and R_r. In fact, the exact threshold powers can be calculated from Eq. (3.10); they are $1.00\,\mathrm{W}$ and $0.199\,\mathrm{W}$ for SC-RFLs constituted by the left-hand and right-hand cavities,

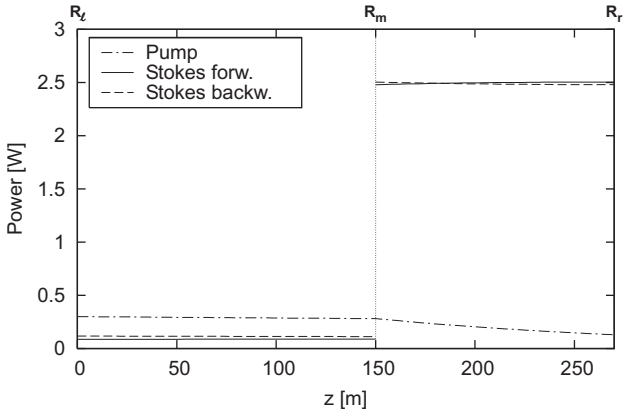

Figure 3.9.: Longitudinal pump and Stokes power distributions for a DC-RFL just above threshold ($P_0 = 0.3\,\mathrm{W}$).

respectively.

A simplifying description is now given for the operating principle of the DC-RFL and the reason for its particular characteristics (Fig. 3.8). If we consider the DC-RFL at a pump power of $P_0 = 0.3\,\mathrm{W}$, this pump power is not sufficient to put the left-hand cavity alone into the lasing state, because the latter has a threshold power of 1.00 W. Because of this, the pump beam passes the left-hand, non-lasing cavity, while being depleted slightly only by linear fiber losses. It then reaches the right-hand cavity, for which the threshold power of 0.199 W is clearly exceeded. This cavity is thus lasing. Part of the backward Stokes power leaves the fiber at the left-hand side through the reflectors R_m and R_l, giving the observed non-zero left-hand output power of the DC-RFL. Fig. 3.9 shows the pump and Stokes power distributions along the fiber of the DC-RFL at $P_0 = 0.3\,\mathrm{W}$. The position z_m of the intra-cavity mirror can be easily identified, because the two cavities differ considerably in the powers circulating inside them.

As explained in the previous paragraph and shown in Fig. 3.9, the operation of the present DC-RFL in the low-power regime is dominated by the right-hand low-loss cavity, with some minor feedback from the left-hand cavity. Consequently, the characteristic of the DC-RFL should be expected to remain essentially unchanged for low pump powers when we recalculate it with $R_l = 0$, i. e., ignoring the influence of the left-hand reflector. This characteristic is plotted as the dashed curve in Fig. 3.8. We see that there is in fact a close agreement with the characteristic of the full DC-RFL around threshold.

We now consider the behavior of the DC-RFL for large pump powers. Fig. 3.10 shows the longitudinal pump and Stokes power distributions for an input pump power of $P_0 = 4\,\mathrm{W}$. The pump is depleted almost completely within the left-hand cavity. Because of that, the right-hand cavity plays virtually no role and the left-hand output characteristic of the DC-RFL is expected to reduce to that of the SC-RFL constituted by the left-hand cavity ($R_l \leftrightarrow R_m$) alone. The dashed-dotted curve in Fig. 3.8 shows

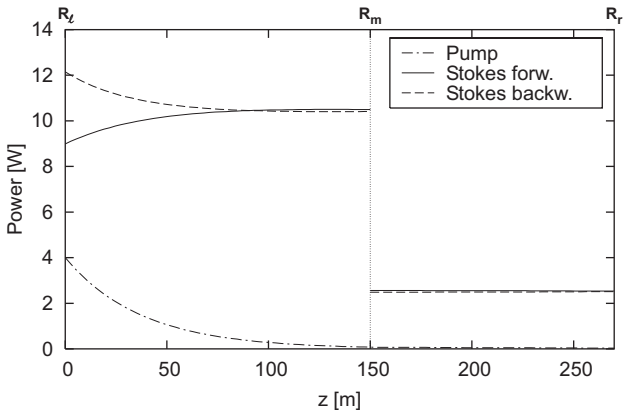

Figure 3.10.: Longitudinal pump and Stokes power distributions for a DC-RFL at a large pump power of $P_0 = 4\,\mathrm{W}$.

the characteristic of the left-hand-cavity SC-RFL, i. e., the DC-RFL with $R_r = 0$, which shows the expected agreement with the characteristic of the full DC-RFL for large pump powers.

In summary, two operating regimes can be identified for the DC-RFL in dependence on the pump power P_0. At low pump powers, the behavior of the left-hand output characteristic is determined by the right-hand cavity, because it has the lower round-trip losses. In particular, the threshold power is mainly determined by this cavity. At large pump powers, the right-hand cavity practically stops contributing and the input-output characteristic is governed almost fully by the left-hand cavity.

Threshold reduction for SC-RFLs using an additional reflector

The considerations of Sect. 3.2.2 lead to the following procedure for lowering the threshold of any given SC-RFL. Suppose we have an SC-RFL design that has been optimized for maximum conversion efficiency or some other criterion other than the threshold power, and we want to lower its threshold power by using the double-cavity concept.

For a successful application of the double-cavity concept, the RFL has to use the left-hand side as the Stokes output, i. e., the pump side. So, if the original design uses the right-hand side as the output, we first need to exchange the left and right reflectors. As we showed in Sect. 3.1.5, this step scarcely modifies the input-output characteristic.

The resulting RFL with an HR FBG at the right-hand end of the fiber is now further optimized by adding another piece of fiber to the right-hand end of the existing cavity and terminating it by a second HR FBG. This step determines the threshold of the new DC-RFL, but does not modify significantly the behavior of the original SC-RFL at large pump powers. Referring to a diagram like Fig. 3.4 or directly to Eq. (3.10), one can easily identify the parameters for the HR cavity that lead to the desired low threshold, chosen independently from the behavior at large pump powers.

Setup	L_{opt}	$R_{\mathrm{out,opt}}$	$P_{\mathrm{out,4W}}$	P_{th}
SC, SPP, Out R	280 m	51.2%	3.18 W	1.17 W
SC, SPP, Out L	289 m	51.2%	3.18 W	1.14 W
SC, DPP, Out R	165 m	50.2%	3.40 W	0.980 W
SC, DPP, Out L	168 m	50.1%	3.40 W	0.967 W
DC, SPP, Out R	no right-hand cavity		0.677 W	0.199 W
DC, SPP, Out L	349 m	56.9%	3.20 W	0.207 W
DC, DPP, Out R	no right-hand cavity		1.27 W	0.192 W
DC, DPP, Out L	305 m	47.6%	3.29 W	0.201 W

Table 3.1.: Optimization results for eight possible non-cascaded Raman fiber laser schemes. "Out R" and "Out L" mean laser output at the right-hand or left-hand fiber ends, respectively. The optimization result for the double-cavity right-hand-output configurations (DC, Out R) is that they give maximum output power when there is no right-hand cavity at all.

3.2.3. Comparison of optimized DC-RFLs and SC-RFLs

So far, we have discussed three basic setup options for non-cascaded RFLs. The first option is whether the Stokes output shall be at the left-hand side (where pump power is coupled in) or at the right-hand side, where it is usually located. Second, one can choose whether to use single-pass or double-pass pumping. Third, one can decide on a single-cavity or a double-cavity design. The resulting eight setup schemes will be compared with regard to optimizability in this section, so that the characteristic features of each become apparent.

All RFLs considered in this section are optimized to yield maximum Stokes output power at a pump power of $P_0 = 4\,\mathrm{W}$. For the DC-RFLs, the threshold power can be chosen nearly freely, because the configuration of the HR cavity is an additional degree of freedom compared to SC-RFLs. We choose a low threshold of 0.2 W for the DC-RFLs considered in this section. When designing such a DC-RFL, one could vary the reflectivities and positions of the Stokes reflectors until both the threshold power and the conversion efficiency exactly reach their desired values. In the following, however, we simply choose the length of the HR cavity such that this cavity on its own has a threshold of exactly 0.2 W. The threshold of the overall DC-RFL is then close to that desired value, and a tedious iterative design process is avoided. Finally, in all of the RFLs, each reflector except the output reflector has a reflectivity of 99%. The results of the numerical optimizations are summarized in Table 3.1.

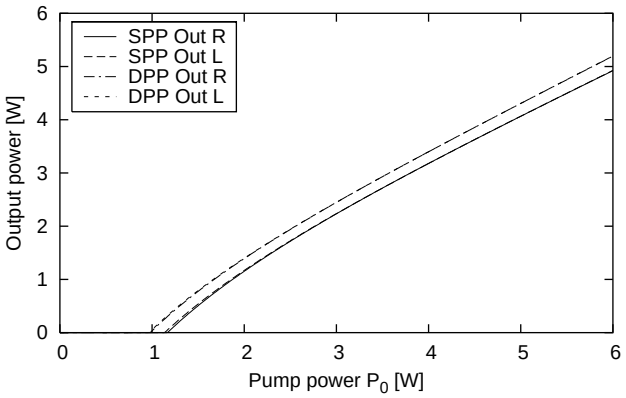

Figure 3.11.: Input-output characteristics of four optimized single-cavity Raman fiber lasers from Table 3.1. The curves for the left-hand- and right-hand-output double-pass pumped (DPP) setups coincide (upper curves), as the curves for the left-hand- and right-hand-output single-pass pumped (SPP) setups (lower curves) do.

Optimized single-cavity RFLs

Fig. 3.11 shows the input-output characteristics of the four SC-RFLs. The curves can be separated into two groups, one group for the configurations with SPP and one group with DPP. The two curves within each group correspond respectively to the left-hand- and right-hand-output configurations, optimized separately (i. e., not obtained by a simple reversal as described in Sect. 3.1.5). These curves are hardly distinguishable, which demonstrates again the practical equivalence of left-hand- and right-hand-output coupling for SC-RFLs.

We also see that the optimized RFLs with DPP provide more Stokes output power than the optimized RFLs with SPP for all pump powers. As expected from the discussion in Sect. 6.2.1, the optimized DPP setups have shorter fibers than the SPP setups (compare the L_{opt} column in Table 3.1). Thus, the effect of fiber losses is lower in the DPP setups, which consequently can provide more output power.

A practical complication for a left-hand-output design can be that the outgoing Stokes power has to be separated from the incoming pump power by means of a wavelength-selective element, as in [BDB$^+$00, CKRB03], otherwise it would be guided into the pump laser. A right-hand-output design, on the other hand, yields an RFL whose output can be spliced directly to other components of a fiber system, thus avoiding potential losses.

Optimized double-cavity RFLs

The DC-RFLs listed in Table 3.1 were designed by first choosing the length of the highly reflective cavity so that it has the desired low threshold pump power of about 0.2 W. For

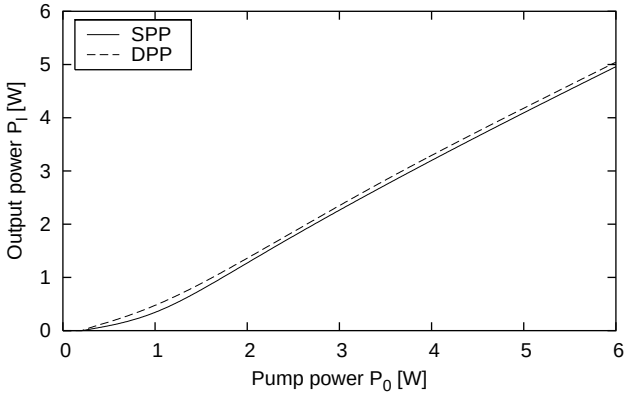

Figure 3.12.: Input-output characteristics of two optimized double-cavity Raman fiber lasers with left-hand output from Table 3.1.

DC-RFLs with SPP, the required length of the HR cavity was found from Eq. (3.10) to be 120 m, for DC-RFLs with DPP 33 m. Then, the overall fiber length of the DC-RFL and the reflectivity of the output reflector were optimized such that the device delivers maximum output power at $P_0 = 4\,\mathrm{W}$. The pump backreflector R_p is always kept at the right-hand fiber end, regardless of the location of the Stokes output mirror.

We first discuss the right-hand-output DC-RFLs. In these setups, the HR cavity is located at the left-hand side, where the pump is also coupled in. This cavity determines the threshold power of the DC-RFL, because at low pump powers, only this cavity can lase (the right-hand cavity is still below threshold). For large pump powers, the pump power is depleted within the first cavity, so that again only the HR cavity is lasing. In summary, the HR cavity determines the characteristics of right-hand-output DC-RFLs for both low and large pump powers, so that it can not be expected that the threshold power and the conversion efficiency at large pump powers can be optimized independently. In fact, Table 3.1 shows that the optimized right-hand-output RFLs yield maximum output power at the right-hand side if there is no right-hand cavity at all. Thus, the DC-RFL concept, as discussed here with R_l and R_m being highly reflective to constitute a low-loss left-hand cavity, is not interesting for right-hand-output RFLs.

We now turn to the optimized left-hand-output DC-RFLs. Fig. 3.12 shows the input-output characteristics corresponding to the SPP (solid line) and DPP (dashed line) setups. As in the case of single-cavity RFLs (Sect. 3.2.3), the DPP setup can deliver slightly more power than the SPP setup. This can again be ascribed to the shorter length of the fiber in the former case (see the L_{opt} column in Table 3.1).

A comparison of Figures 3.11 and 3.12 shows that the concept of double-cavity RFLs makes it possible to lower the threshold of RFLs considerably while still retaining the op-

timizability for high conversion efficiency at large pump powers. We have demonstrated this property of DC-RFLs only in the case of a few arbitrarily selected configurations. However, the results can be scaled to an infinite number of different fibers [RCK03].

Alternative double-cavity setups

So far we have only considered double-cavity RFLs where two of the three Stokes reflectors are highly reflective. In this section we finally discuss some more general DC-RFL schemes.

We divide the choice of the reflectivities R_l, R_m and R_r into the two categories "low or moderate reflectivity" (L) and "high reflectivity" (H). This results in eight ways to configure a DC-RFL. Of these, we have mainly analyzed the LHH configuration in this paper, i. e., the one with R_l moderately reflective, and R_m and R_r highly reflective. This is the configuration that enables independent optimization of the threshold power and the conversion efficiency at large pump powers. We have also briefly considered the HHL configuration (right-hand-output DC-RFL) in Sect. 3.2.3 and found no advantages over conventional SC-RFLs.

Besides the HHL and LHH configurations, six other schemes are possible. We comment on the HLL and LLH configurations next. These are modifications of the configurations already considered, where the middle reflector R_m is now moderately instead of highly reflecting. We numerically examined several HLL configurations, and found no advantage over ordinary SC-RFLs in their input-output characteristics. For LLH configurations, a lowering of the threshold pump power could be achieved in comparison to SC-RFLs. However, the effect was not as pronounced as in the case when choosing a high-reflectivity mirror R_m (an LHH configuration). Furthermore, it turns out that it is no longer possible to estimate the threshold power of such configurations with sufficient accuracy by considering only a single cavity. All the reflectors contribute in a significant manner to the threshold of the DC-RFL, which makes the design process more difficult.

The HLH and HHH configurations are not very promising, because their conversion efficiencies are rather small. Due to the high reflectivity of both of their output reflectors, not much power is coupled out. Finally, the LHL and LLL configurations can be used to realize double-cavity RFLs with characteristics that allow the suppression of relative-intensity-noise transfer from the pump laser to the Stokes. These devices will be discussed in Sect. 4.3.

3.3. Widely tunable cascaded Raman fiber lasers

In this section, we show how a tunable Raman fiber laser (RFL) can be designed such that a wide continuous spectral tuning range spanning several Stokes orders is achieved and the lasing of undesired parasitic resonators is suppressed. The results of this section have been published in [KCRB03].

3.3.1. Motivation

Widely tunable RFLs are potentially useful as measurement test sources or as flexible pump sources for use in Raman fiber amplifiers. For example, it has been suggested to pump a Raman fiber amplifier in a counter-propagating configuration (see Fig. 1.1), where the pump wavelength is periodically swept across a certain wavelength range. This can effectively increase the amplification bandwidth [WSZ02]. Another application of a tunable RFL is the possibility to dynamically reconfigure the RFA pump wavelength which may be required when the channel load in an RFA changes as WDM channels are added to or removed from the system.

A tunable RFL with a continuous tuning range of 113 nm (25 THz) has been experimentally demonstrated by the Optical Communications Technology group at TUHH in 2003 [CKRB03]. Except for the tunable element, the concept exclusively employs all-fiber components, which makes it more efficient than all-bulk-optical setups such as [JLSA77], and the achieved tunable frequency range was more than three times wider than that of the most recently reported tunable all-fiber RFL [RHT01] at that time. In this section, we report details on the design of the widely tunable RFL from [CKRB03] and present a new design for an RFL which is continuously tunable from 1300 to 1650 nm.

The principal design problem is the occurrence of spectral gaps in the tunable range, where laser operation of the tunable resonator is interrupted. These gaps are due to undesired parasitic resonators formed by the fiber Bragg gratings (FBGs) of the auxiliary resonators, by fiber-end reflections, and by Rayleigh backscattering. We will show in the following how tunable RFLs can be designed such that a wide continuous tuning range without spectral gaps is achieved.

3.3.2. Geometry and design considerations

A schematic of the considered tunable RFL design is shown in Fig. 3.13. First of all, an all-fiber cascade of fixed-wavelength auxiliary resonators (ARs) formed by high-reflectivity FBGs at wavelengths $\lambda_{\mathrm{AR},i}$ is formed. This is the principle of cascaded

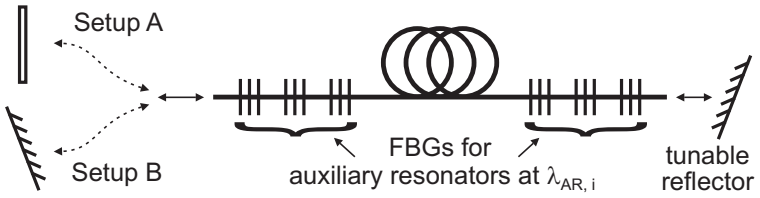

Figure 3.13.: Two possible designs for tunable Raman fiber lasers with a bulk-optical tuning element. A: broadband reflector on one side. B: wavelength-selective reflectors on both sides.

resonators introduced for non-tunable RFLs in [GEM+94]. It is illustrated in Fig. 3.14. The Stokes light generated by the pump laser in the first cavity (labeled "auxiliary resonator 1" in Fig. 3.14) acts itself as the pump for the next cavity, labeled "auxiliary resonator 2". This process is repeated until the desired output wavelength is reached. Optical conversion efficiencies (from the pump wavelength to the output wavelength) greater than 50% can be achieved in such lasers [GEM+94]. Cascaded RFLs are also commercially available. (In Sect. 7.4, we will show that this concept can also be useful for silicon Raman lasers.)

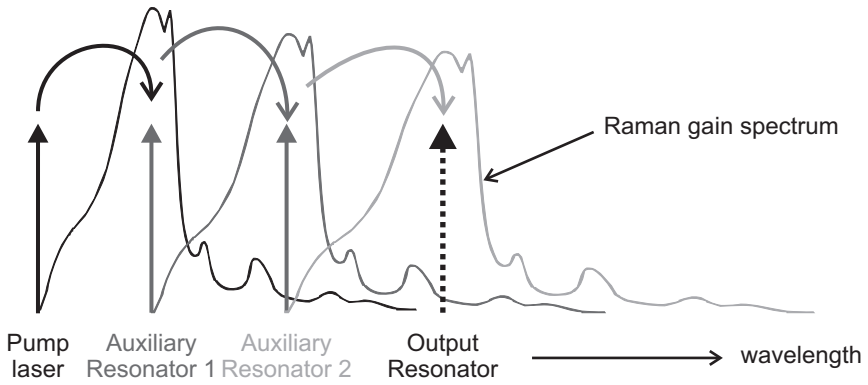

Figure 3.14.: Illustration of the principle of cascaded Raman lasers. In this example, successive resonators are always placed in the Raman-gain maximum of the previous stage, which is actually not optimal if the cascade serves as the foundation for a tunable RFL, see discussion in the main text.

The cascade of auxiliary resonators (ARs) shown in Fig. 3.14 makes Raman gain available at all wavelengths in the range of interest, without introducing high losses. In our tunable RFL (see Fig. 3.13), an additional tunable resonator is formed by a bulk-optical tunable reflection grating on one side, while on the other side we can either place a broadband mirror (setup A) or another reflection grating (setup B). Setup A, inspired by [JLSA77], has the advantage of lower overall losses and easier alignment, but the problem of parasitic resonators is more critical (see below). Setup B was used in the

experiment published in [CKRB03], where actually the output beams of both fiber ends have been directed to the same reflection grating.

Parasitic resonators

The primary design goal is to avoid spectral gaps in the tunable range caused by competition of the tunable resonator (TR) with parasitic resonators (PRs). PRs are unwanted resonators formed by reflecting elements such as fiber-end faces, FBGs of long-wavelength auxiliary resonators not needed for short tuned wavelengths, the broadband mirror in case of setup A, and Rayleigh backscattering. A PR is fatal if it starts to lase at a sufficiently high power level while depleting the TR, possibly stopping the TR to lase at all, and thus causing zero tuned output power. Whether a PR is critical depends not only on the setup, but also on the shape of the cascaded Raman gain spectrum and thus on the pump power. The behaviour described in this section was observed both experimentally [CKRB03] and in numerical simulations.

The most obvious PRs are ARs at wavelengths longer than the tuned wavelength. These ARs are not required, because they do not provide Raman gain to the tuned wavelength. If the TR is spectrally close to one of the undesired ARs, the low-loss AR might start to lase at the expense of the relatively high-loss TR. Therefore, depending on the tuned wavelength, some of the long-wavelength ARs must be switched off. An AR can be switched off by detuning one of its FBGs by about one width of its reflectivity spectrum. In case of setup A, though, the broadband mirror on the left-hand side in Fig. 3.13 can still form a low-loss PR with the right-side FBG of the "switched-off" AR. It turned out that, in addition, a reduction of the reflectivity of the FBG itself may be necessary in this case (which is not required for setup B).

We have observed that other broadband-reflecting elements such as fiber-end faces and even Rayleigh backscattering can also form PRs at wavelengths corresponding to the Raman gain maxima of other resonators lasing at shorter wavelengths. Using setup A, we observed this even when the right-side fiber end was immersed in an index-matched liquid, from which we conclude that Rayleigh backscattering can indeed be significant for the formation of PRs.

In setup B, even though there is no broadband mirror, the FBGs of switched-off ARs and the fiber-end faces can form PRs at the AR wavelengths $\lambda_{\mathrm{AR},i}$. The problem of these fiber-end PRs is weakened when an AR does not spectrally coincide with the Raman gain maximum of its short-wavelength neighbour (this latter, non-optimal case is shown in Fig. 3.14). Instead, the ARs should be spaced closer together on the wavelength axis. In any case, it is advisable to have tilted fiber-end faces so as to reduce their reflectivities.

Successive ARs must be placed spectrally closer to each other also in order to prevent the occurrence of tuned-wavelength intervals with too low cascaded Raman gain for the tunable resonator (due to the roughly triangular shape of the Raman gain curve, see Fig. 2.3).

In summary, the design of tunable RFLs according to our concept consists in choosing the optimum wavelengths $\lambda_{\mathrm{AR},i}$ of the ARs (while minimising the total number of required ARs), determining at which wavelength the ARs must be switched on when sweeping through the tuning range, and deciding whether the AR FBGs need to be adjusted in their reflectivities (as opposed to be merely detuned).

3.3.3. Modeling

The model describing Raman amplification in optical fibers summarized in section 2.3 takes into account beams only at two wavelengths, namely the pump and the Stokes wavelength. However, the model can be easily extended to take into account an arbitrary number of laser lines, resulting in a widely used model for cascaded and multi-wavelength Raman fiber lasers [JM01, CRB03]. We thus model the tunable RFLs using the differential equations

$$\pm \frac{\mathrm{d}P_i^{\pm}}{\mathrm{d}z} = \left[-\alpha_i + \sum_{j=1}^{N} g_{j,i}(P_j^+ + P_j^-) \right] P_i^{\pm} + S\alpha_i P_i^{\mp}, \tag{3.13}$$

where the $P_i^{\pm}(z)$ $(i = 1 \ldots N)$ are the powers of the forward $(+)$ and backward $(-)$ propagating laser lines[2], α_i are the constants of attenuation due to Rayleigh scattering, S is the Rayleigh backscattering capture fraction, and the $g_{j,i}$ describe the stimulated Raman interaction. At the left-hand and right-hand fiber ends z^- and z^+, respectively, the Stokes lines $(i \geq 2)$ fulfil the boundary conditions $P_i^{\pm}(z^{\mp}) = R_i(z^{\mp})P_i^{\mp}(z^{\mp})$, where R_i are the reflectivities of the reflecting elements. For the pump line, $P_1^+(z^-) = P_0$, where P_0 is the pump power (we consider single-pass-pumped RFLs here). The right-hand output power of line i is $P_{\mathrm{out},i} = P_i^+(z^+) - P_i^-(z^+)$. Only those wavelengths are included in the simulation at which we can expect lasing operation of ARs, PRs and the TR from the discussion above. In our simulation, we allow for one pump line, a number n_{AR} of ARs, $n_{\mathrm{AR}} + 1$ fiber-end PRs in the gain maxima of both the pump and the ARs, and the TR. In setups where an AR is switched off by detuning one of its FBGs, it is necessary to include two laser lines for a switched-off AR in the simulation,

[2] The detailed spectral line shapes of the resonator emissions are not resolved in this model, we consider only the total power contained in each laser line, see the discussion in Sect. 4.4.1.

corresponding to resonators at the center wavelengths of the two detuned FBGs of the switched-off AR.

Numerical solution

As explained in section 3.1.3, we solve the boundary-value problem (BVP) describing the RFL using the collocation method `bvp4c` available in MATLAB. In the simulation of tunable RFLs, where the model includes a large number of laser lines at different wavelengths (as opposed to only two wavelengths in section 3.1.3), it becomes increasingly difficult to find an approximate initial solution of the BVP. Such a solution is required by the collocation method—the closer this initial solution guess is to the exact solution of the boundary-value problem, the faster the method converges. If the initial solution guess is too different from the desired exact solution, the method may converge to an entirely different, mathematically possible but non-physical solution (such as one with negative powers).

We avoid this problem by first solving the model for a pump power of $P_0 = 0$. Guessing the solution for this case is easy—all the powers are identical to zero over the entire length of the fiber. We then successively solve the BVP for slowly increasing pump powers, each time using the existing solution as the solution guess for the next iteration, where the pump power is slightly increased, until the solution for the desired pump power is reached. Finally, to avoid the non-physical, "trivial" solutions of the BVP where the Stokes lines are exactly zero even though the laser is above threshold, we include additional auxiliary terms in the equations for each line that could be interpreted as representing an increase of the line's power due to spontaneous Raman scattering [KCR03]. However, these terms are included only as a tool for finding the desired solution of the BVP; it is checked that they do not perceptibly influence that solution.

Alternative algorithms for solving the BVP have been developed in [Cie05], where suitable initial guesses for the collocation solver are obtained through approximate analytical solutions of the BVP, which have been recently discovered also by other authors [BGL05, MTS+05].

3.3.4. Design results

The solid curve in Fig. 3.15 shows the simulated output power versus the tuned wavelength for a tunable RFL according to setup B. It has a continuous tuning range of 350 nm without spectral gaps. The RFL is pumped at a wavelength of 1250 nm, and ARs are introduced at longer wavelengths in intervals of 9.7 THz (in contrast, the Ra-

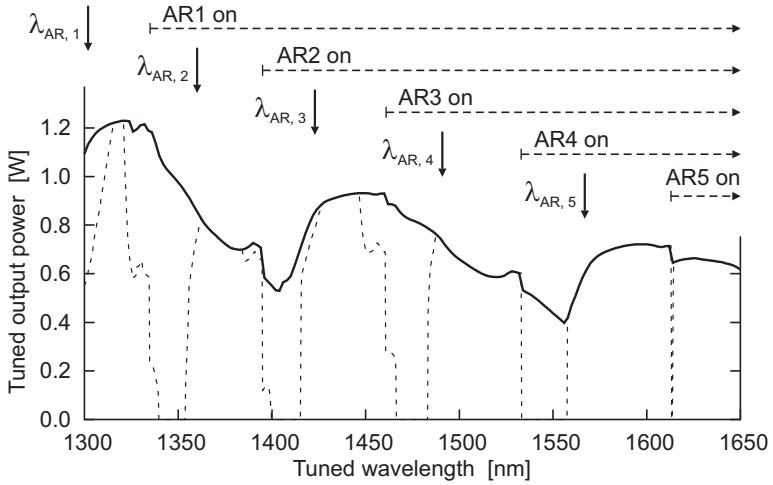

Figure 3.15.: Simulated tuned output power versus tuned wavelength of an RFL according to setup B. Fiber-end reflectivities are 0.2% for the solid curve, and 4% for the dashed curve.

man gain maximum is at 13.2 THz) by FBGs with reflectivities of 95% on both sides. An AR is only switched on when the tuned wavelength exceeds the wavelength $\lambda_{\mathrm{AR},i}$ of the AR by an amount corresponding to 5.5 THz. The pump power is held constant at 3 W. The reflectivity of the tunable grating is 30%, and the reflectivities of both tilted fiber ends are 0.2%. The design is for 600 m of FiberLogix High Raman Gain fiber with a specified peak Raman gain constant of $g = 2.3\,(\mathrm{Wkm})^{-1}$ at 1550 nm, and $\alpha(1550\,\mathrm{nm}) = 0.4\,\mathrm{dB/km}$. For other pump wavelengths, the peak gain is assumed to scale as $1/\lambda_s$ [Sto80b]. The Raman gain spectrum used in the simulations is shown as the solid curve in Fig. 2.3. The fiber attenuation has been assumed to scale as $1/\lambda^4$ (corresponding to a fiber with only Rayleigh scattering), and the capture fraction is $S = 2 \times 10^{-3}$. In spite of a rather conservative choice of parameters, this design has been found to be robust against parameter changes. For example, fiber length variations of ± 100 m are tolerated, without introducing gaps in the tunable range.

The dashed curve in Fig. 3.15 shows the results for the same setup with the fiber-end faces non-tilted (4% reflectivity). This change is sufficient for some of the switched-off ARs to start lasing for certain tuned wavelengths, resulting in spectral gaps in the tunable range. The output power breaks down around 1347, 1408, 1475, 1545 and 1613 nm. This shows that is essential to suppress fiber-end reflections in our tunable RFL.

Finally, we note that it is, in principle, possible to achieve the same wide continuous tuning range even with setup A. If we assume that the reflectivity of the bulk-optical broadband mirror is 60%, we obtain a tunable range without gaps provided that ARs are

switched off by reducing the corresponding FBG reflectivities from 95% to less than 5% (merely detuning their center wavelengths is not sufficient). However, it is questionable whether the FBG reflectivity can be reduced non-destructively to such low values.

Further setups for tunable RFLs have been explored experimentally and theoretically in [Cie05], where the bulk-optical tuning element still present in the design shown in Fig. 3.13 could be replaced by widely tunable FBGs.

3.4. Chapter summary

After an introduction to single-cavity, non-cascaded Raman fiber lasers and their inherent limitations with respect to optimizability, we have introduced in this chapter the double-cavity RFL, which can be designed such that it simultaneously has a low threshold pump power and a high conversion efficiency at large pump powers. On the other hand, we have proposed a scheme for widely tunable RFLs and explained how spectral gaps in the tunable range due to the presence of parasitic resonators can be avoided, concluding with a practical design that is continuously tunable over 350 nm, thus spanning the full optical-communications wavelength range.

4. Stability of Raman fiber lasers

This chapter is concerned with the stability of Raman fiber lasers. Section 4.1 gives details on the modeling of pump-to-Stokes transfer of relative intensity noise (RIN). Sections 4.2 and 4.3 show two methods how RFLs can be optimized for low-RIN operation, thus increasing their potential for use in co-pumped Raman fiber amplifiers, and section 4.4 shows how the power-dependent line broadening in RFLs can stabilize multi-wavelength RFLs.

Parts of the results of this chapter have been published in [KCR03, KCRB04, KR04, KSC+05, KCRB06].

4.1. Pump-to-Stokes RIN transfer in RFLs

In this section, we present measurements of the RIN spectra of an RFL and its pump laser. A model for the transfer of RIN from the pump laser to the RFL output is then developed, which can qualitatively explain the experimental results [KCRB04,KCRB06].

4.1.1. Significance of relative intensity noise in RFLs

A particularly attractive application of Raman fiber lasers (RFLs) is as pump sources for distributed Raman fiber amplifiers (RFAs). On the one hand, RFLs can easily provide the required optical powers at almost arbitrary wavelengths, which may not be available from semiconductor laser diodes [Hea05]. Furthermore, multiple output wavelengths necessary for a flat broad-band RFA gain can be generated within a single compact device [Hea05].

In order to obtain the best possible tradeoff between signal-to-noise ratio and signal nonlinear distortions in a distributed RFA, it is preferable to inject pump power into both sides of a transmission span, such that part of the pump power is co-propagating with the signal [BBT+03]. Also, the tilt of the optical signal-to-noise ratio across the WDM signal bandwidth in an RFA pumped by multiple wavelengths can be reduced by co-pumping the shorter wavelengths [KEN+01]. However, any undesired temporal

variations in the pump power are transferred to the amplified signal due to the short response time of the stimulated Raman effect.

This pump-to-signal transfer of relative intensity noise (RIN) is relatively insignificant in counter-pumped RFAs, where the pump and the signal are propagating in opposite directions, because the pump-power fluctuations "seen" by the signal are strongly averaged out along the fiber even at very low frequencies. In co-pumped RFAs, the pump and the signal light propagate in the same direction, and the only pump-noise averaging is due to the dispersion-induced walk-off between pump and signal, which becomes significant only at relatively high frequencies [FHM01, MHB02, MBH03]. Thus, sources for co-propagating pump light must have especially low RIN [SWR05].

While there have been several successful attempts at reducing the RIN of RFLs by using novel setups [MLB+04, LMB+05, BFC+06], results on the actual origins of the RIN of ordinary RFLs are scarce in the literature. In [CHB04] it was noted from experimental RIN spectra that the pump-laser RIN is transferred to the output of an RFL. A mathematical model for this pump-to-Stokes RIN transfer was first presented in [KCRB04], on which the results in this Chapter are based. Further work on the RIN of cascaded RFLs has been done by a group at the Russian Academy of Sciences [BCK05a, BCK+05b, BCF+05, FBC+05].

4.1.2. Experimental RIN spectra

Fig. 4.1 shows our experimental setup. The Raman fiber laser consists of a spool of single-mode fiber of length $L = 5\,\mathrm{km}$. It is composed of two fiber Bragg gratings at the Stokes wavelength of $\lambda_s = 1110\,\mathrm{nm}$, one highly reflecting and one with a peak reflectivity of about 40%. The RFL is pumped by an Ytterbium fiber laser emitting at a wavelength of $\lambda_p = 1060\,\mathrm{nm}$. In order to measure the RIN spectrum, the output power of the RFL at the Stokes wavelength is detected by a photodetector, the signal of which is led to an oscilloscope and to a spectrum analyzer. The RIN spectrum is obtained from the measured data as $\mathrm{RIN}(f) = S_{\mathrm{el}}(f)/\bar{P}_{\mathrm{el}}$, where $S_{\mathrm{el}}(f)$ and $\bar{P}_{\mathrm{el}}$ are the power spectral density and average power of the electrical signal, respectively. The electrical spectrum analyzer (model Advantest R9211A) has an upper frequency limit of 100 kHz, which prevented measurements of RIN at higher frequencies.

The measured RIN spectrum of our RFL is shown in Fig. 4.2a. We observe resonances at integer multiples of the inverse cavity round-trip time, $f = v_g/2L = 20\,\mathrm{kHz}$, where $v_g = 2 \times 10^8\,\mathrm{m/s}$ is the group velocity of light in the fiber. Furthermore, the average value of the RIN spectrum as well as its contrast are clearly decreasing with increasing pump power. In contrast, the RIN spectrum of the Ytterbium pump laser, shown in

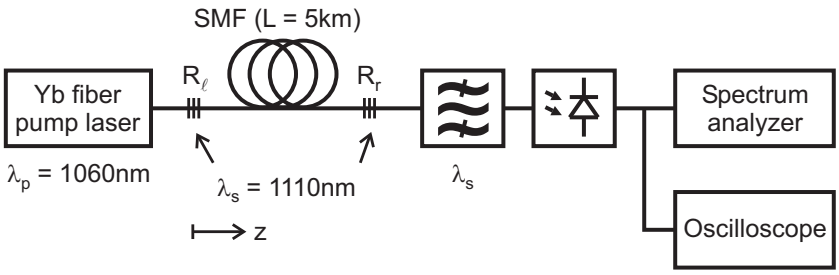

Figure 4.1.: Schematic of the setup to measure the RIN of a Raman fiber laser.

Fig. 4.2b, is fundamentally different. The spectrum is essentially flat, apart from a slight tilt towards higher frequencies, and it is practically independent of output power.

In the next section we will show that the RIN spectrum of the RFL, shown in Fig. 4.2a, can be explained as simply being due to the transfer of RIN from the Ytterbium pump laser to the output of the RFL.

4.1.3. Modeling of pump-to-Stokes RIN transfer

Mathematical model

The RIN spectrum of the Raman fiber laser (see Fig. 4.2a) can be explained in the framework of the usual model of Raman fiber lasers summarized in Sect. 2.3. The partial differential equations

$$\pm \frac{\partial P_i^{\pm}}{\partial z} + \frac{1}{v_i}\frac{\partial P_i^{\pm}}{\partial t} = \left[-\alpha_i + \sum_j g_{j,i}(P_j^+ + P_j^-)\right] P_i^{\pm} \tag{4.1}$$

describe the temporal evolution of the functions $P_{p,s}^{\pm}(z,t)$, which denote the forward $(+)$ and backward $(-)$ propagating optical powers at the pump (p) and Stokes (s) wavelengths. The coefficients $g_{j,i}$ describe the transfer of power from wave j to wave i due to stimulated Raman scattering, the α_i are the fiber attenuation constants, and v_i is the group velocity at wavelength λ_i. The two FBGs for the Stokes wavelength are located at $z = 0$ and $z = L$ and have reflectivities R_l and R_r, respectively, and are described by the two boundary conditions

$$P_s^-(L,t) = R_r P_s^+(L,t), \tag{4.2}$$

$$P_s^+(0,t) = R_l P_s^-(0,t). \tag{4.3}$$

As there is no pump backreflector at $z = L$ in our setup, $P^-(z,t) = 0$. The boundary condition for the pump wave is simply

$$P_p^+(0,t) = P_0(t), \tag{4.4}$$

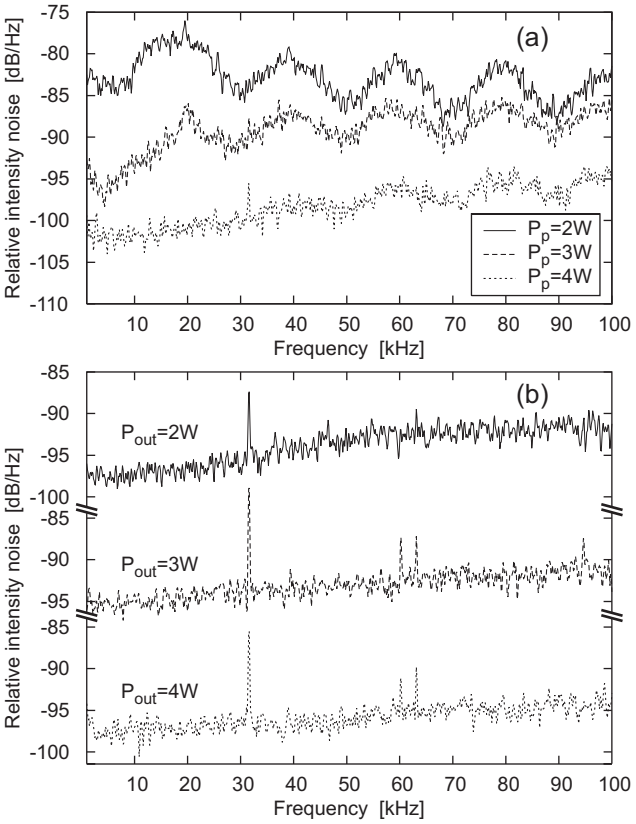

Figure 4.2.: (a) measured output RIN of the Raman fiber laser (1110 nm) from Fig. 4.1 for various pump powers P_p, (b) measured RIN of the Ytterbium (1060 nm) laser used to pump the RFL, for various output powers P_{out} (the three curves have been displaced vertically so they can be clearly distinguished).

where $P_0(t)$ is the prescribed time-varying pump power. The output power of the RFL is given by

$$P_{\text{out}}(t) = P_s^+(L,t) \cdot (1 - R_r) = P_s^+(L,t) - P_s^-(L,t), \tag{4.5}$$

where we have assumed that the reflectors R_l and R_r are lossless. The boundary-value problem (BVP) consisting of Eqs. (4.1)–(4.4) can be solved numerically to yield the temporal evolution of the output power $P_{\text{out}}(t)$, given the pump-power $P_0(t)$ [JM01, CKRB04, CKRB05, BGL04].

In our case, the pump power varies only slightly around its steady-state value $\bar{P}_0$,

$$P_0(t) = \bar{P}_0 + p_0(t), \tag{4.6}$$

where $p_0(t)$ characterizes the noise of the pump laser, and $|p_0(t)| \ll \bar{P}_0$. Thus, we are only interested in small deviations from the steady state of the RFL. In particular, the output power is expected to vary around its steady-state value $\bar{P}_{\text{out}}$ as

$$P_{\text{out}}(t) = \bar{P}_{\text{out}} + p_{\text{out}}(t), \tag{4.7}$$

where $|p_{\text{out}}(t)| \ll \bar{P}_{\text{out}}$. The solution process can thus be sped up considerably by linearizing the BVP around its steady-state solution. We thus make the small-signal

ansatz for all powers at all positions z,

$$P_i^{\pm}(z,t) = \bar{P}_i^{\pm}(z) + p_i^{\pm}(z,t), \tag{4.8}$$

where the small-signal powers $p_i^{\pm}(z,t)$ represent the deviation from the steady-state solution $\bar{P}_i^{\pm}(z)$. The latter satisfies the time-independent BVP corresponding to Eqs. (4.1)–(4.4),

$$\pm\frac{\mathrm{d}\bar{P}_i^{\pm}}{\mathrm{d}z} = \left[-\alpha_i + \sum_j g_{j,i}(\bar{P}_j^{+} + \bar{P}_j^{-})\right]\bar{P}_i^{\pm}, \tag{4.9}$$

$$\bar{P}_s^{-}(L) = R_r\bar{P}_s^{+}(L), \tag{4.10}$$

$$\bar{P}_s^{+}(0) = R_l\bar{P}_s^{-}(0), \tag{4.11}$$

$$\bar{P}_p^{+}(0) = \bar{P}_0. \tag{4.12}$$

Inserting Eq. (4.8) into Eq. (4.1), using Eqs. (4.9)–(4.12), and neglecting products of small-signal powers leads to the linear partial differential equations

$$\pm\frac{\partial p_i^{\pm}}{\partial z} + \frac{1}{v_i}\frac{\partial p_i^{\pm}}{\partial t} = \left[-\alpha_i + \sum_j g_{j,i}(\bar{P}_j^{+} + \bar{P}_j^{-})\right]p_i^{\pm} + \left[\sum_j g_{j,i}(p_j^{+} + p_j^{-})\right]\bar{P}_i^{\pm}, \tag{4.13}$$

where the steady-state solution $\bar{P}_i^{\pm}(z)$ appears as coefficients on the right-hand side. Inserting Eq. (4.8) into the boundary conditions (4.2)–(4.4), we obtain the boundary conditions for the small-signal powers,

$$p_s^{-}(L,t) = R_r p_s^{+}(L,t), \tag{4.14}$$

$$p_s^{+}(0,t) = R_l p_s^{-}(0,t), \tag{4.15}$$

$$p_p^{+}(0,t) = p_0(t). \tag{4.16}$$

As the BVP (4.13)–(4.16) is linear in $p_i^{\pm}$, we can perform a Fourier transform,

$$\tilde{p}_i^{\pm}(z,\omega) = \int_{-\infty}^{+\infty} p_i^{\pm}(z,t)\exp(-j\omega t)\,\mathrm{d}t, \tag{4.17}$$

to eliminate the temporal derivatives. This finally leads to the ordinary differential equations

$$\pm\frac{\mathrm{d}\tilde{p}_i^{\pm}}{\mathrm{d}z} = \left[-\tilde{\alpha}_i + \sum_j g_{j,i}(\bar{P}_j^{+} + \bar{P}_j^{-})\right]\tilde{p}_i^{\pm} + \left[\sum_j g_{j,i}(\tilde{p}_j^{+} + \tilde{p}_j^{-})\right]\bar{P}_i^{\pm}, \tag{4.18}$$

where $\tilde{\alpha}_i = \alpha_i + j\omega/v_i$, and the boundary conditions are

$$\tilde{p}_s^{-}(L,\omega) = R_r\tilde{p}_s^{+}(L,\omega), \tag{4.19}$$

$$\tilde{p}_s^{+}(0,\omega) = R_l\tilde{p}_s^{-}(0,\omega), \tag{4.20}$$

$$\tilde{p}_p^{+}(0,\omega) = \tilde{p}_0(\omega). \tag{4.21}$$

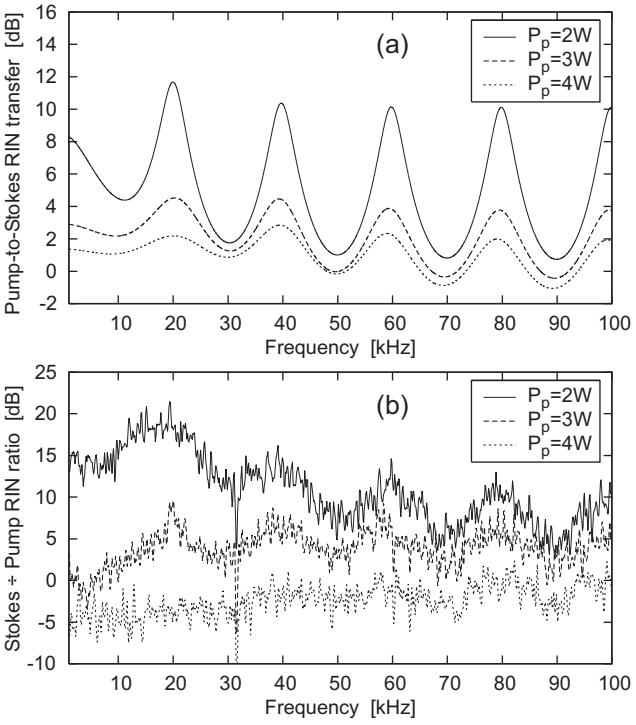

Figure 4.3.: (a) calculated pump-to-Stokes RIN transfer function for a Raman fiber laser with parameters corresponding to the experimental RFL from Fig. 4.1 for various pump powers P_p, (b) measured ratio of Stokes RIN to pump RIN (difference between Figs. 4.2a and 4.2b), for various pump powers P_p. The resonance peaks and the decrease of average RIN and RIN contrast with increasing pump power are in good agreement.

As can be seen from Eq. (4.18), the steady-solution has to be calculated only once for a given RFL from Eqs. (4.9)–(4.12), as it does not depend on the modulation frequency ω. The response of the RFL to a sinusoidal modulation of the frequency ω can then be easily obtained by solving the linear BVP (4.18)–(4.21) for $\tilde{p}_{\text{out}}(\omega) = \tilde{p}_s^+(L,\omega) - \tilde{p}_s^-(L,\omega)$. This immediately gives the modulation transfer function (MTF),

$$H(\omega) = \frac{\tilde{p}_{\text{out}}(\omega)}{\tilde{p}_0(\omega)} = \frac{\tilde{p}_s^+(L,\omega) - \tilde{p}_s^-(L,\omega)}{\tilde{p}_0(\omega)}, \tag{4.22}$$

or, equivalently, the desired RIN transfer function,

$$H_{\text{RIN}}(\omega) = \left[\frac{|\tilde{p}_{\text{out}}(\omega)|/\bar{P}_{\text{out}}}{|\tilde{p}_0(\omega)|/\bar{P}_0}\right]^2 = \left[\frac{\bar{P}_0}{\bar{P}_{\text{out}}}|H(\omega)|\right]^2. \tag{4.23}$$

Comparison with experimental results

Fig. 4.3a shows the calculated RIN transfer function $10\log H_{\text{RIN}}(\omega)$ for an RFL with parameters corresponding to the experimental RFL from Fig. 4.1. We have used a Raman gain constant of $g = g_{p,s} = -(\lambda_p/\lambda_s)g_{s,p} = 0.8\,(\text{Wkm})^{-1}$, attenuation constants $\alpha_p = 1.8\,\text{dB/km}$ and $\alpha_s = 1.5\,\text{dB/km}$, FBG reflectivities $R_l = 90\%$ and $R_r = 40\%$, and equal group velocities for both pump and Stokes waves, $v_p = v_s = 2\times10^8\,\text{m/s}$ (dispersion has a negligible effect, as discussed at the end of this subsection).

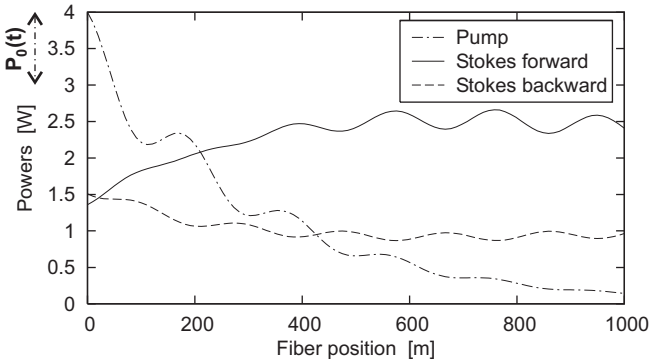

Figure 4.4.: Longitudinal distribution of the pump and Stokes powers inside a Raman fiber laser under sinusoidal modulation $P_p(t) = [3.5 + \cos(2\pi ft)/2]\,\mathrm{W}$ with $f = 10.5\,\mathrm{FSR}$ (off-resonance modulation). The figure shows a snapshot at a time where the pump power is maximal.

A comparison of the theoretical RIN transfer function, Fig. 4.3a, with the measured ratio of the Stokes and pump RIN, Fig. 4.3b, shows that the qualitative features are in good agreement. In particular, the resonance frequencies agree excellently, and the decrease of average RIN and of the RIN contrast with increasing pump power is clearly observed both experimentally and numerically. We conclude from this that pump-to-Stokes RIN transfer has a significant effect on the output RIN of the RFL.

In the calculation above, and in all results presented in the remainder of this chapter, we have assumed equal group velocities for the pump and Stokes waves, $v_p = v_s$. After that, we have repeated all calculations assuming a typical value for the group-velocity dispersion of $D = -20\,\mathrm{ps/(nm \cdot km)}$ at $\lambda = 1100\,\mathrm{nm}$. Taking $v_s = 1/[(\lambda_s - \lambda_p)D + 1/v_p]$ and $v_p = 2 \times 10^{-8}\,\mathrm{m/s}$, we found no significant effect of dispersion on the results.

Illustration of RIN transfer

To conclude this section, we briefly illustrate the occurrence of the resonance peaks in the RIN spectrum or in the MTF. The two numerical examples shown in Figs. 4.4 and 4.5 correspond to a different RFL than above, because the effect is more clearly visible here. Its length is $L = 1000\,\mathrm{m}$, such that the inverse cavity round-trip time or free spectral range (FSR) is $v_g/2L = 100\,\mathrm{kHz}$. The results in this section have been obtained from the small-signal BVP (4.18)–(4.21).

Fig. 4.4 shows the longitudinal distribution of the pump and Stokes powers inside the RFL under sinusoidal modulation with a frequency of 10.5 times the FSR. The pump power oscillates between 3 and 4 W, and the figure shows a snapshot at a time when the pump power is maximal, i. e., 4 W. There is a weak modulation of the Stokes wave, which is most pronounced in the forward-propagating Stokes wave at the right-hand side of the

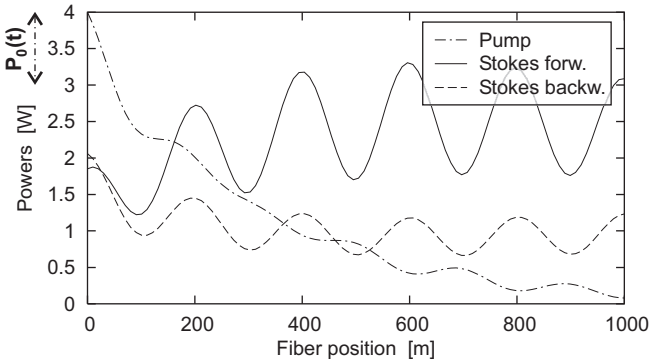

Figure 4.5.: Longitudinal distribution of the pump and Stokes powers inside a Raman fiber laser under sinusoidal modulation $P_p(t) = [3.5+\cos(2\pi ft)/2]\,\mathrm{W}$ with $f = 10\,\mathrm{FSR}$ (on-resonance modulation). The figure shows a snapshot at a time where the pump power is maximal.

cavity. However, at the left-hand side of the cavity, where the pump is coupled in, the Stokes-wave modulation is out of phase by 180 degrees with respect to the pump-power modulation. This corresponds to the case of off-resonance modulation.

In contrast, Fig. 4.5 shows the resonant case. The modulation frequency is now exactly 10.0 times the FSR. Now, the Stokes modulation wavelength can be seen to fit inside the round-trip length $2L$ exactly ten times. Both the Stokes modulation and the pump modulation are seen to have a peak at the same time at the left-hand side of the cavity. The modulation is in phase and thus the system in resonance, and there is an efficient transfer of modulation from the pump wave to the Stokes wave.

It is clear that by sweeping the modulation frequency, one alternately passes through non-resonant and resonant states, the latter corresponding to the modulation frequencies where the corresponding modulation wavelength fits into twice the cavity length ($2L$) an integer number of times.

4.2. Optimization of RFLs for low-noise co-pumped Raman amplifiers

We now turn to the problem of designing an RFL as a pump source for a co-pumped Raman amplifier such that the performance degradation of the transmission span due to RIN transfer in the amplifier is minimized. The results presented here form part of [KCRB06]. It will be assumed in the following that the RIN of the considered RFLs stems exclusively from pump-to-Stokes RIN transfer, see section 4.1.

4.2.1. Overview of the optimization task

Assuming that the noise on the RFA's pump laser (the RFL to be designed) can be treated as Gaussian and neglecting the noise on "0" bits in the signal stream, the penalty dBQ in the signal-quality factor Q can be estimated as [FHM01]

$$\begin{aligned} \mathrm{dB}Q &= 10 \log \sqrt{1 + Q_S^2 \int_0^\infty r_S(f)\,\mathrm{d}f} \\ &= 10 \log \sqrt{1 + Q_S^2 \int_0^\infty r_{\mathrm{RFL}}(f) H_A(f)\,\mathrm{d}f}, \end{aligned} \tag{4.24}$$

where $r_S(f)$ is the RIN of the signal at the receiver due to RIN transfer in the amplifier, and equals the product of the RIN spectrum $r_{\mathrm{RFL}}(f)$ of the pumping RFL and the RIN transfer function $H_A(f)$ of the amplifier. The latter is modelled as a low-pass filter,

$$H_A(f) = \frac{H_A(0)}{1 + f^2/f_c^2}, \tag{4.25}$$

and we assume a cut-off frequency of $f_c = 5\,\mathrm{MHz}$ and a DC RIN transfer of $H_A(0) = 5\,\mathrm{dB}$, corresponding to a Raman amplifier with an on-off gain of 7.72 dB [FHM01]. The signal quality at the receiver without Raman-induced RIN is taken as $Q_S = 7$, corresponding to a bit-error ratio (BER) of 1.3×10^{-12}.

We now assume that the RIN spectrum $r_{\mathrm{RFL}}(f)$ of the RFA's pump laser (the RFL to be designed) is exclusively due to transfer of RIN from the RFL's pump laser to the output of the RFL. Thus, $r_{\mathrm{RFL}}(f) = r_0 H_{\mathrm{RFL}}(f)$, where r_0 is the RIN of the pump laser of the RFL (assumed constant, $r_0 = -95\,\mathrm{dB/Hz}$, compare Fig. 4.2b), and $H_{\mathrm{RFL}}(f)$ is the RIN transfer function of the RFL to be designed. We aim at optimizing $H_{\mathrm{RFL}}(f)$ such that dBQ is minimized.

What we do below can be summarized as follows. We pick a certain RFL configuration and, from the BVP (4.9)–(4.12), we calculate the steady-state solution at the given pump power. From the BVP (4.18)–(4.21), the RIN transfer function of the RFL is then calculated at a sufficiently large number of frequencies between $f = 0$ and $f = f_{\max}$, where $f_{\max}$ is set to a sufficiently large value so that a further increase does not change the final results (we have used $f_{\max} = 200\,\mathrm{MHz}$, which is well above the cut-off frequency of the low-pass filter of the RIN transfer function of the amplifier). The calculated RIN transfer function is then multiplied with r_0 and with $H_A(f)$ and then integrated from $f = 0$ to $f = f_{\max}$, yielding the integral in Eq. (4.24) and thus the Q-factor penalty dBQ induced by the RIN of the particular RFL under consideration.

Note that the case of a counter-pumped Raman amplifier can be modeled by a low-pass filter similar to Eq. (4.25) with a much lower cut-off frequency $f_c < 10\,\mathrm{kHz}$ [FHM01,

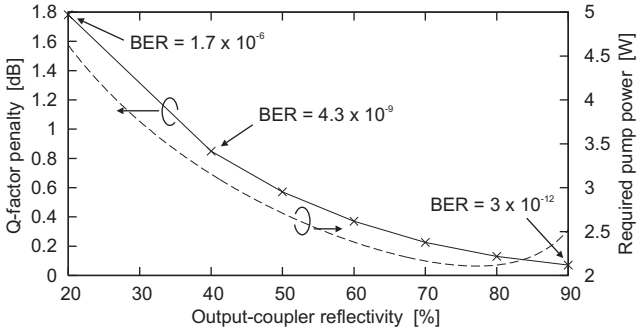

Figure 4.6.: Q-factor penalty introduced by a noisy Raman fiber laser in a Raman-amplified transmission span, as a function of the output-coupler reflectivity R_r of the RFL. The pump power is adjusted such that the output power is constant for all RFLs.

MHB02, MBH03]. Consequently, resulting Q-factor penalties are much lower, and the RIN requirements on a counter-pumping RFL are much less critical.

4.2.2. Dependence of Q penalty on RFL parameters

Fig. 4.6 shows the variation of Q-factor penalty dBQ with the reflectivity R_r of the output coupler of an RFL. The remaining parameters of the RFL are a moderate Raman gain of $1.5\,(\mathrm{Wkm})^{-1}$, pump and Stokes wavelengths of $\lambda_p = 1060\,\mathrm{nm}$ and $\lambda_s = 1110\,\mathrm{nm}$, respectively, fiber attenuation constants of $\alpha_p = 0.91\,\mathrm{dB/km}$ and $\alpha_s = 0.76\,\mathrm{dB/km}$, fiber length $L = 150\,\mathrm{m}$, group velocities $v_p = v_s = 2 \times 10^8\,\mathrm{m/s}$, and a left-hand FBG reflectivity of $R_l = 99\%$. The steady-state pump power $\bar{P}_0$ is adjusted such that the output power of all compared RFLs is $\bar{P}_{\mathrm{out}} = 1.5\,\mathrm{W}$.

Fig. 4.6 shows clearly that a high-reflectivity output coupler is advantageous for low-noise operation of a co-pumped Raman-amplified transmission span. For example, the BER of the system can be reduced by three orders of magnitude simply by using a 90% FBG instead of a 40% one. However, the required pump power for the RFL also depends on the reflectivity of the output coupler. The reflectivity required for maximum conversion efficiency is evidently not the same as the one required for optimal noise performance, so there is a tradeoff between pump power and noise performance.

For the results shown in Fig. 4.7, the output-coupler reflectivity is kept fixed at $R_r = 60\%$, and only the Raman-gain coefficient of the fiber used for the RFL is varied. The results show clearly that a high Raman gain leads to a lower BER of the co-pumped transmission system, and it also reduces the pump power required to obtain the desired 1.5 W of output power.

Finally, Fig. 4.8 shows the dependence of the Q-factor penalty on the length of the

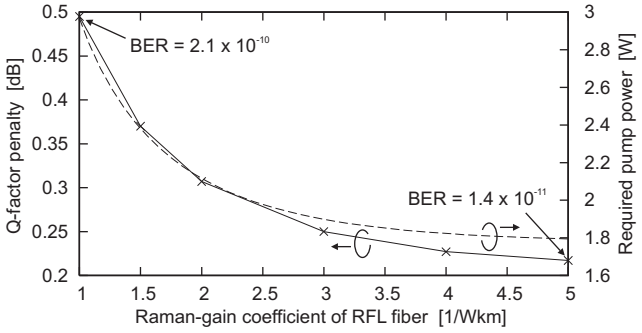

Figure 4.7.: Q-factor penalty introduced by a noisy Raman fiber laser in a Raman-amplified transmission span, as a function of the Raman-gain coefficient g of the fiber used for the RFL. The pump power is adjusted such that the output power is constant for all RFLs.

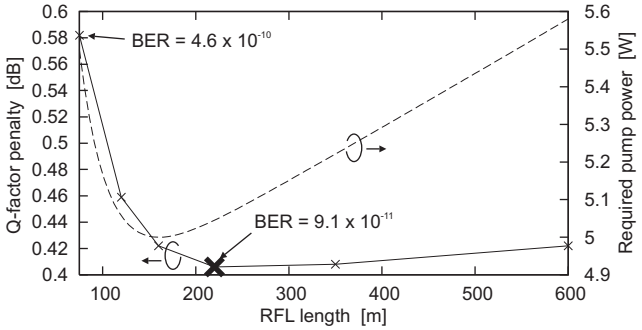

Figure 4.8.: Q-factor penalty introduced by a noisy Raman fiber laser in a Raman-amplified transmission span, as a function of the length L of the RFL. The pump power is adjusted such that the output power is constant for all RFLs.

fiber used in the RFL, while all other parameters are kept fixed. In contrast to above, we now use an output-coupler reflectivity of $R_r = 25\%$, a high-Raman-gain fiber with a gain constant of $g = 4\,(\mathrm{Wkm})^{-1}$, and the output power of the RFL is kept fixed at $\bar{P}_{\mathrm{out}} = 4.5\,\mathrm{W}$. The results show that there is an optimal value for the fiber length both in terms of noise performance as well as conversion efficiency. However, the optimal lengths are different, so again there is a tradeoff. For the sake of completeness, Fig. 4.9 shows the RIN spectrum of the RFL with the length chosen such that noise performance in the transmission system is optimal (marked with the thick cross in Fig. 4.8).

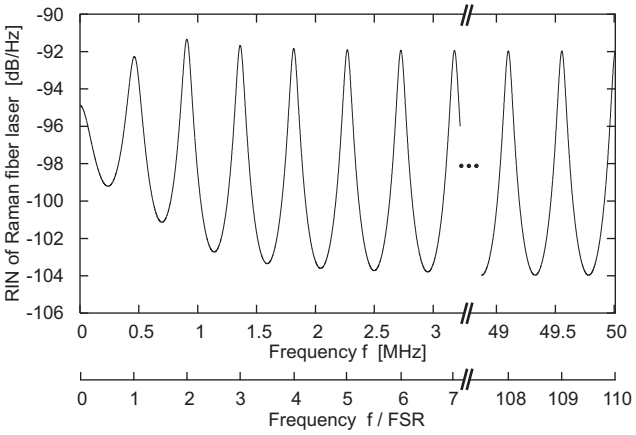

Figure 4.9.: RIN spectrum of the optimum RFL from Fig. 4.8 (marked with the thick cross). The lower axis shows the frequency in units of the free spectral range (FSR).

4.3. Suppression of low-frequency RIN transfer in double-cavity RFLs

In this Section, we further investigate the concept of the double-cavity RFL with three fibre Bragg gratings (FBGs) at the Stokes wavelength, introduced in Sect. 3.2. In the discussion of the various design possibilities in Sect. 3.2.3 we have postponed a discussion of the LxL configurations, i. e., those with a low left-hand and a low right-hand output reflectivity. We show here by simple numerical simulations that the input-output characteristics of those DC-RFLs can exhibit a pump power level at which the slope efficiency $\mathrm{d}P_{\mathrm{out}}/\mathrm{d}P_{\mathrm{pump}}$ is zero. At this operating point, the output power is independent of the pump power and low-frequency pump power variations are not transferred to the RFL output, thus suppressing low-frequency RIN caused by pump-to-Stokes RIN transfer. Furthermore, the low-noise operating point is tunable by merely varying the reflectivity of one of the FBGs [MHB+01], thus providing a continuously power-tunable low-noise Stokes output for use as a pump source in co-pumped RFAs. The theoretical results of this section have been published in [KR04].

4.3.1. Geometry and model

Fig. 3.7 shows the setup of a double-cavity Raman fibre laser (DC-RFL). It contains three FBGs reflecting at the Stokes wavelength λ_s, at fibre positions $z = 0$, $z = z_m$ and $z = L$, where L is the fibre length. Thus two concatenated cavities ($R_l \leftrightarrow R_m$ and $R_m \leftrightarrow R_r$) are formed for the Stokes laser line instead of only one as in conventional single-cavity RFLs, see Sect. 3.1.

The significantly different behaviour of such DC-RFLs as compared to single-cavity RFLs is studied by numerical simulations based on the standard RFL model, which is modified to take into account the incoherent superposition of reflected and transmitted powers at the intra-cavity Stokes reflector with reflectivity R_m and transmittivity T_m, see Sect. 3.2.1. We have assumed the lossless case $T_m = 1 - R_m$ here. The DC-RFL considered here is pumped at the wavelength $\lambda_p = 1060\,\mathrm{nm}$, and the Stokes wavelength is $\lambda_s = 1112\,\mathrm{nm}$. We assume a fibre of length $L = 600\,\mathrm{m}$ with Raman gain constant $g = 1.2\,(\mathrm{Wkm})^{-1}$ and fibre loss coefficients of $\alpha_p = 0.8\,\mathrm{dB/km}$ and $\alpha_s = 0.66\,\mathrm{dB/km}$ for the pump and Stokes lines, respectively. The reflectivities of the left-hand, intra-cavity, and right-hand FBGs are $R_l = 40\%$, $R_m = 95\%$ and $R_r = 30\%$, respectively. The intra-cavity reflector is located at $z_m = 100\,\mathrm{m}$.

4.3.2. Theoretical characteristics

Fig. 4.10 shows the numerically calculated input-output characteristics of our DC-RFL. While the left-hand output power is monotonically increasing with the pump power, the right-hand output power initially increases, but reaches a maximum at $P_{\mathrm{pump}} = 4.3\,\mathrm{W}$. When the laser is operated at this pump power, low-frequency pump power variations (e. g., due to RIN of the pump laser) are not transferred to the right-hand output, leading to the desired suppression of the low-frequency RIN output spectrum due to pump-to-Stokes RIN transfer.

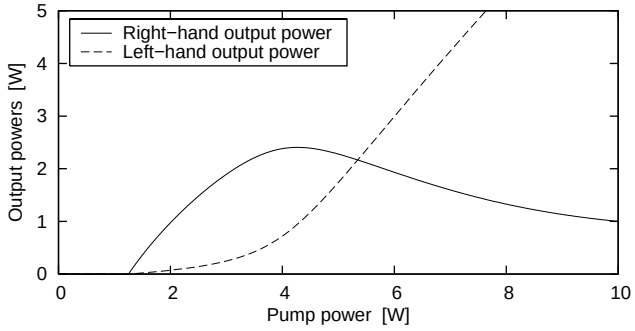

Figure 4.10.: Input-output characteristics of a DC-RFL.

The reason for the special behaviour of DC-RFLs becomes particularly clear by considering an "idealized" DC-RFL, whose intra-cavity FBG reflectivity is $R_m = 100\%$ instead of just 95% as in Fig. 4.10. Because no Stokes power can be exchanged between the left-hand and right-hand cavities through the intra-cavity Stokes reflector at z_m, the idealized DC-RFL simply corresponds to a longitudinal concatenation of two independent single-cavity RFLs, the right-hand one of which ($R_m \leftrightarrow R_r$) is pumped by the

residual pump power of the left-hand RFL ($R_l \leftrightarrow R_m$).

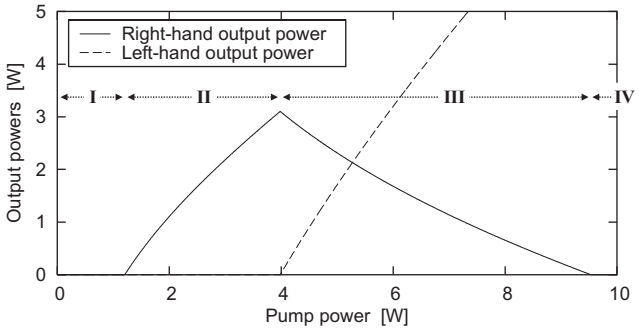

Figure 4.11.: Input-output characteristics of the DC-RFL from Fig. 4.10 with $R_m = 100\%$. Four operating regimes I–IV are indicated.

The characteristics of the idealized DC-RFL are plotted in Fig. 4.11. There are now four clearly separated operating regimes. In the first regime ($P_{\mathrm{pump}} < 1.20\,\mathrm{W}$), the pump power is below the threshold of the left-hand cavity $P_{\mathrm{th},1} = 3.98\,\mathrm{W}$, and the pump is attenuated only by linear fibre losses. Consequently, the pump power of the right-hand cavity is $P_{\mathrm{pump2}} = P_{\mathrm{pump}} \exp(-\alpha_p z_m) = 0.982 P_{\mathrm{pump}}$, which is below the threshold of the right-hand cavity $P_{\mathrm{th},2} = 1.18\,\mathrm{W}$, too. As a result, the DC-RFL produces neither left-hand nor right-hand output power.

In the second regime ($1.20\,\mathrm{W} < P_{\mathrm{pump}} < 3.98\,\mathrm{W}$), the pump power is still below the threshold of the left-hand cavity. However, the right-hand cavity is above threshold now, so it starts lasing, producing the observed right-hand output power. The third regime, ($3.98\,\mathrm{W} < P_{\mathrm{pump}} < 9.54\,\mathrm{W}$) is characterized by the simultaneous lasing of both cavities. Note that for an increase of the pump power, the output power of the left-hand cavity increases, as expected for any single-cavity RFL. However, due to the resulting depletion of the pump power in the left-hand cavity, the pump power P_{pump2} available for the right-hand cavity is reduced, leading to a decrease of the right-hand output power of the DC-RFL.

Finally, in the fourth regime ($P_{\mathrm{pump}} > 9.54\,\mathrm{W}$), the residual pump power at the end of the left-hand cavity P_{pump2} is below the threshold of the right-hand cavity, which consequently does not lase.

We now switch back to the more realistic case where the intra-cavity FBG reflectivity R_m is smaller than 100%. Comparing Fig. 4.11 (idealized DC-RFL with $R_m = 100\%$) with Fig. 4.10 (realistic DC-RFL with $R_m = 95\%$) shows that reducing the value of R_m "smoothes out" the laser characteristics. When one of the cavities of a realistic DC-RFL is lasing, part of its power leaks through R_m to the opposite output of the DC-RFL, so that above threshold, both output powers are always non-zero as opposed to the case of

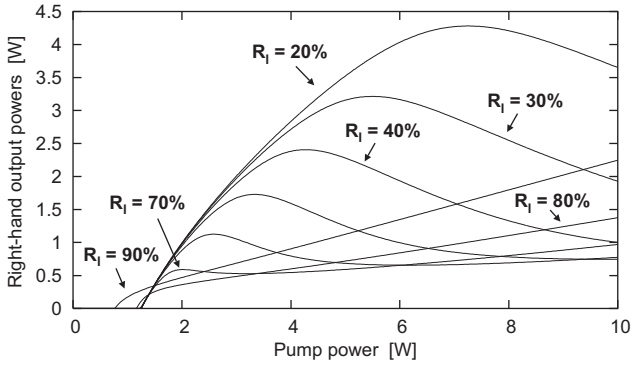

Figure 4.12.: Input-output characteristics of several DC-RFLs with the left-hand reflectivity R_l varying between 20% (upper curve) and 90% in steps of 10%.

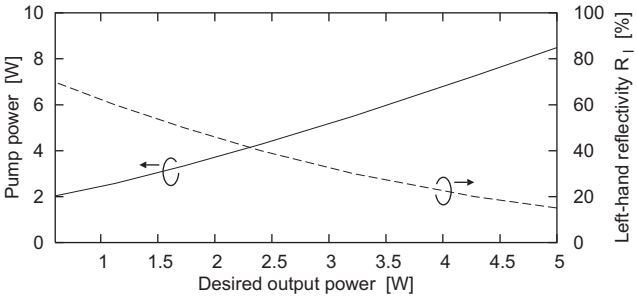

Figure 4.13.: Required pump power P_{pump} and left-hand reflectivity R_l for low-noise operation of a DC-RFL at a desired output power.

the idealized DC-RFL. For the same reason, the transition between regimes II and III is now smooth. The curvature of the right-hand output characteristics at the zero-slope point is the higher the larger R_m is chosen.

Tunability

From the discussion above it is clear that by increasing R_l, the left-hand cavity starts lasing for lower pump powers so that the third regime sets in earlier and the zero-slope point moves to lower pump powers. Fig. 4.12 shows the right-hand output characteristics of our DC-RFL with $R_m = 95\%$ for eight different left-hand FBG reflectivities R_l. It is seen that by varying R_l, the zero-slope-efficiency point can be tuned across a broad output-power range. This makes the DC-RFL suitable as a power-tunable low-noise RFA pump source. Fig. 4.13 shows how low-noise operation at desired output powers down to 0.6 W can be achieved by adjusting the pump power and the left-hand reflectivity.

4.3.3. Experimental characteristics

In our experimental DC-RFL (see Fig. 4.14) [Sta06], the right-hand cavity for the Stokes line is formed by 600 m of Fiberlogix high-Raman-gain fiber (HRGF) and two FBGs at a center wavelength of 1111 nm, with peak reflectivities of 96% and 31%, respectively, and FWHMs of about 0.1 nm. The left-hand cavity is formed by 2 km of standard single-mode fiber (SSMF), by the 96% grating just mentioned and by the broadband left-hand

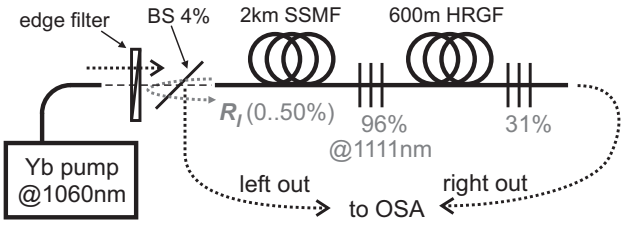

Figure 4.14.: Experimental setup of a double-cavity Raman fiber laser incorporating a bulk-optically tuned left-hand reflector.

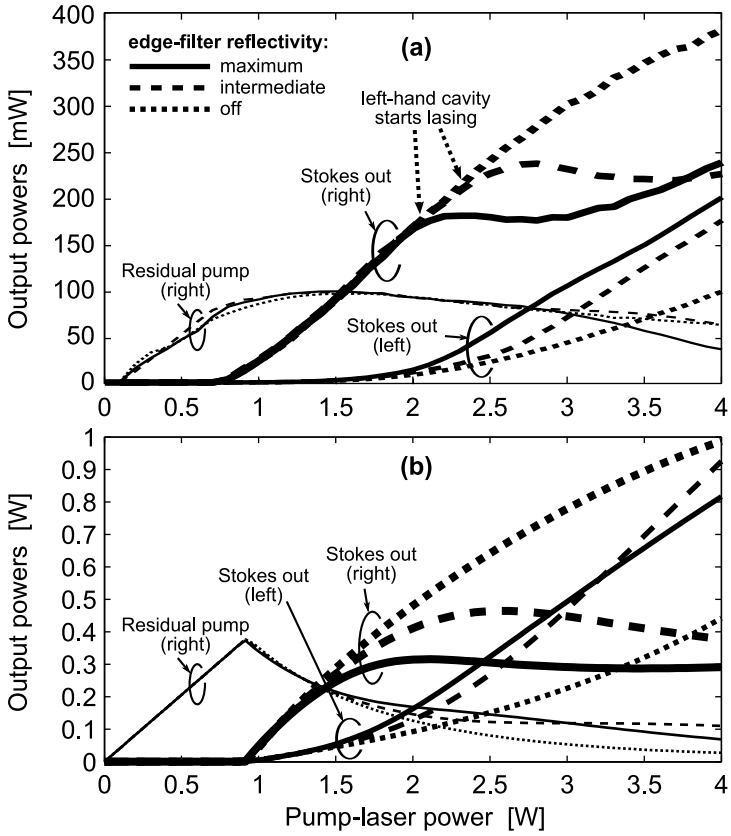

Figure 4.15.: *(a)* measured and *(b)* simulated characteristics of a double-cavity Raman fiber laser with a tunable low-noise operating point.

reflector R_l, which is an edge filter that reflects a tunable amount of the Stokes light back into the fiber. It also serves as a multiplexer for the injection of pump light generated by the Yb fiber laser at 1060 nm. More details about the employed components can be found in [Cie05, Sta06]. Fig. 4.15a shows the measured characteristics of the DC-RFL for three settings of the left-hand reflector R_l. The FWHM of the Stokes line was about 0.5 nm. No lasing at higher Stokes orders was observed.

The characteristics shown in Fig. 4.15a are essentially those expected from theory (compare Fig. 4.15b): the right-hand cavity has a lower threshold than the left-hand one and thus starts lasing first when pump-laser power is increased from zero. Eventually, the threshold of the left-hand cavity is reached. When the latter starts lasing (marked by the dotted arrows in Fig. 4.15a), less pump power is passed on to the right-hand cavity, the output power of which therefore saturates and decreases, leading to the desired

local maximum in the characteristics. At such an operating point, a change in pump power (e.g., due to RIN on the pump laser) is not transferred to the Stokes output. Furthermore, this operating point is tunable by merely varying the reflectivity of the left-hand reflector R_l.

For the simulations we used the following parameters: for the SSMF, $\alpha_p = \alpha_s = 0.7\,\mathrm{dB/km}$ and $g = 0.3\,/\mathrm{Wkm}$. For the HRGF, $\alpha_p = \alpha_s = 1.5\,\mathrm{dB/cm}$ (scaled from the manufacturer's data according to $1/\lambda^4$) and $g = 3.5\,/\mathrm{Wkm}$ (scaled from the manufacturer's data according to $1/\lambda$). The effective FBG reflectivites are $R_l = 60$, 40 or 0.5% for the three settings of the edge filter, $R_m = 85\%$ and $R_r = 30\%$. We assume that 70% of the pump-laser power is actually coupled into the double-cavity RFL.

4.4. Stabilizing effect of line broadening

We now show phenomenologically that power-dependent Stokes line broadening can stabilize Raman fiber lasers (RFLs) against undesired pump power changes. The results of this section have been published in [KCR03].

4.4.1. Overview

The need for Raman amplifiers that provide a flattened gain over a large bandwidth [PW02, RK98] has raised the need for light sources with configurable simultaneous power output at two or more closely spaced wavelengths. Recently developed multi-wavelength Raman fiber lasers (MWRFLs) meet these requirements well [CLJ+00, LBL+02, CHB04]. In multi-wavelength RFLs, one laser pumps several Stokes resonators simultaneously, as illustrated in the adjacent figure.

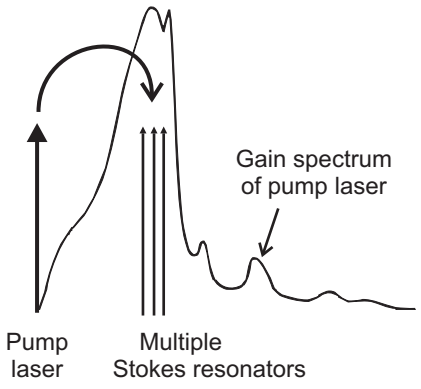

In conventional RFL models (such as those used so far in this thesis), the total power of a laser line is usually treated as being concentrated at one wavelength, namely the center wavelength of the FBG that comprises the corresponding laser-line cavity. The finite non-zero linewidth of the laser lines in practical RFLs is neglected. This leads to simple, spectrally discrete equations and boundary conditions determining the pump and Stokes power distributions in an RFL, see Eqs. (3.1)–(3.4).

We show in the following that these simple RFL models (relying on power-independent laser linewidths) predict a significant instability of the laser line powers in MWRFLs. For example, a change of the input pump power in the order of one percent can cause one

or more laser lines to be suppressed. On the other hand, power-dependent line broadening has been observed in various experiments [KCDP00, PKJU00, PKC01, LWS80] and is usually attributed to four-wave mixing [BCI+06]. We demonstrate that RFLs, in particular MWRFLs are significantly stabilized when the effective reflectivities of the fiber Bragg gratings (FBGs) forming the Stokes resonators are permitted to decrease with increasing incident power due to the spectral broadening of the Stokes lines.

4.4.2. Power-dependent effective reflectivities

Standard boundary conditions

In the conventional model for RFLs (see section 3.1.3), the boundary conditions for an RFL with reflecting elements such as FBGs at the fiber ends are

$$P_1^+(0) = P_p \qquad \text{(input pump power)}, \tag{4.26}$$

$$P_i^+(0) = P_i^-(0) \cdot R_{\mathrm{L}i} \qquad (i = 2 \ldots n), \tag{4.27}$$

$$P_i^-(L) = P_i^+(L) \cdot R_{\mathrm{R}i} \qquad (i = 1 \ldots n), \tag{4.28}$$

where $R_{\mathrm{L}i}$ and $R_{\mathrm{R}i}$ denote the reflectivities of the FBGs at the left-hand and right-hand fiber ends for line i, respectively, and line 1 corresponds to the pump power.

Usually, the FBGs at the pump side (left-hand side here) are highly reflecting, and a few of the right-hand FBGs are moderately reflecting in order to couple out laser light. The output power of line i is

$$P_{\mathrm{out},i} = P_i^+(L) - P_i^-(L) = P_i^+(L)(1 - R_{\mathrm{R}i}). \tag{4.29}$$

Due to the assumption of Stokes lines with zero spectral width, the reflectivities used in the boundary conditions (4.27) and (4.28) are usually taken to be the maxima of the FBG reflectivity spectra, and the detailed shapes of the latter are irrelevant for these models. We will now relax this assumption.

Introduction of power-dependent effective reflectivities

It has been observed experimentally that the spectral linewidth of the Stokes output of a Raman fiber laser increases with increasing output power [KCDP00, PKJU00, PKC01, LWS80]. This behavior is usually attributed to the $\chi^{(3)}$ nonlinear effects in the fiber, such as self-phase modulation and four-wave mixing (see, e. g., [BCI+06]). However, we do not need to know the exact physical mechanism of line broadening. Our results are simply based on the reasonable generalization of well-known experimental results

that not only the Stokes output line but also the corresponding intra-cavity Stokes line broadens monotonically with increasing power carried by it. Making this simple phenomenological assumption, we avoid the need for a spectrally resolved model of the RFL.

We consider the influence of the spectral width of a Stokes line on the total power reflected from an FBG with the reflectivity spectrum $R(\lambda)$. The ratio of the total reflected power P_{refl} to the total incident power P_{inc} represents an effective reflectivity R_{eff} of the FBG,

$$R_{\text{eff}} = \frac{P_{\text{refl}}}{P_{\text{inc}}}\,, \tag{4.30}$$

where the total powers

$$P_{\text{inc}} = \int S_{\text{inc}}(\lambda)\,\mathrm{d}\lambda \tag{4.31}$$

and

$$P_{\text{refl}} = \int S_{\text{refl}}(\lambda)\,\mathrm{d}\lambda = \int R(\lambda) S_{\text{inc}}(\lambda)\,\mathrm{d}\lambda \tag{4.32}$$

are calculated as the integrals of the incident and reflected spectral power densities of the corresponding laser lines $S_{\text{inc}}(\lambda)$ and $S_{\text{refl}}(\lambda)$, respectively, over the wavelength λ.

It is obvious that for most practical FBGs (for which the reflectivity $R(\lambda)$ is essentially monotonically decreasing for increasing detuning from the center wavelength), a broader incident spectrum leads to a lower effective reflectivity. Since the spectrum broadens with increasing power, it is physically reasonable to assume that the effective reflectivity R_{eff} of an FBG decreases with increasing incident Stokes power P_{inc}. This is the phenomenological assumption on which the results of this paper are based.

The reduction of the effective reflectivity by a non-zero Stokes linewidth can simply be illustrated by assuming the reflectivity $R(\lambda)$ of the FBG and the power density $S_{\text{inc}}(\lambda)$ of the Stokes lines to have Gaussian spectra $R(\lambda) = \hat{R}\exp\left[-(\lambda-\lambda_B)^2/w_R^2\right]$ and $S_{\text{inc}}(\lambda) = \hat{S}\exp\left[-(\lambda-\lambda_B)^2/w_S^2\right]$, respectively, where $\hat{R}$ and $\hat{S}$ are the corresponding maximum values, and λ_B is the center or Bragg wavelength of the FBG. The effective reflectivity obtained from Eq. (4.30),

$$R_{\text{eff}} = \frac{\hat{R}}{\sqrt{1+(w_S/w_R)^2}}\,, \tag{4.33}$$

thus decreases with an increasing ratio w_S/w_R, where w_S and w_R are the spectral widths of the Stokes line and of the grating reflectivity spectrum, respectively. If now the Stokes line broadens (and w_S increases) due to an increase of its power P_{inc}, the effective reflectivity R_{eff} must decrease.

In the following we show that RFLs can be more stable against undesired changes of the pump power than predicted by models assuming power-independent linewidths. The underlying principle is simple: an increase of the Stokes power in any cavity increases the corresponding spectral linewidth. This reduces the effective reflectivity of the FBGs of the cavity and thus increases the total cavity loss. The latter counteracts the power increase and thus stabilizes the RFL. We show phenomenologically by numerical simulations that the characteristics of multi-wavelength RFLs can be strongly affected by taking this effect into account.

4.4.3. Stabilizing effect on single-wavelength RFLs

In this section we consider a simple single-wavelength RFL and illustrate how the power-dependent line broadening decreases the sensitivity of the intra-cavity Stokes power against changes of the pump power P_p. In Section 4.4.4 we show a dramatic effect on the stability of multi-wavelength RFLs.

All the RFLs in this paper are based on a fiber with an attenuation $\alpha(\lambda) = \bar{\alpha} \cdot \bar{\lambda}^4/\lambda^4$ ($\bar{\alpha} = 0.4\,\mathrm{dB/km}$, $\bar{\lambda} = 1550\,\mathrm{nm}$) caused by Rayleigh scattering. The pump wavelength is $\lambda_p = 1060\,\mathrm{nm}$. There is no pump backreflector at the fiber end in our examples, but the behavior is similar for backreflected pumps.

The specific RFL in this example has one Stokes line at $\lambda_2 = 1120\,\mathrm{nm}$. The fiber has the length $L = 200\,\mathrm{m}$, and the Raman gain coefficient is $g = 1 \times 10^{-3}/\mathrm{Wm}$ [Agr01]. Let us suppose that at a pump power of $\bar{P}_p = 4\,\mathrm{W}$, the Stokes spectra are such that the effective FBG reflectivities are $R_{\mathrm{L2,eff}}|_{\bar{P}_p} = 99\%$ on the left-hand side and $R_{\mathrm{R2,eff}}|_{\bar{P}_p} = 50\%$ on the right-hand side (such a setup can be realized practically by writing FBGs with adequate reflection spectra into the fiber). For these parameters, the intra-cavity forward Stokes power of the RFL at the right-hand side is $P_2^+(L)|_{\bar{P}_p} = 4.57\,\mathrm{W}$, as calculated from the conventional model given in section 3.1.3.

We now assume, according to the discussion in section 4.4.2, that the effective reflectivity $R_{\mathrm{R2,eff}}$ of the right-hand (output) FBG decreases with an increase of the incident power $P_2^+(L)$ according to

$$R_{\mathrm{R2,eff}}|_{P_p} = R_{\mathrm{R2,eff}}|_{\bar{P}_p} + R'_{\mathrm{R2,eff}}\big|_{\bar{P}_p} \cdot \left\{ P_2^+(L)\big|_{P_p} - P_2^+(L)\big|_{\bar{P}_p} \right\}, \tag{4.34}$$

where the differential effective reflectivity $R'_{\mathrm{R2,eff}}|_{\bar{P}_p} < 0$ quantifies the strength of the power dependence of the effective reflectivity and depends on the actual Stokes and FBG spectra. In case of Gaussian reflection and power-density spectra, the differential effective reflectivity of an FBG at a certain incident power P_{inc} can be calculated from

Eq. (4.33) as

$$R'_{\mathrm{eff}} = \frac{\mathrm{d}R_{\mathrm{eff}}}{\mathrm{d}P_{\mathrm{inc}}} = -R_{\mathrm{eff}} \frac{w_S}{w_S^2 + w_R^2} \frac{\mathrm{d}w_S}{\mathrm{d}P_{\mathrm{inc}}}. \tag{4.35}$$

From the experimental results in [KCDP00] we estimate using Eq. (4.35) that the differential effective reflectivity R'_{eff} can be as large as $-8\,\%/\mathrm{W}$.

We assume that the left-hand effective reflectivity $R_{\mathrm{L2,eff}}$ remains constant, for example because the reflectivity spectrum of the left-hand FBG is much broader than that of the right-hand FBG (a non-negligible power dependence here would not yield any qualitative changes in the results).

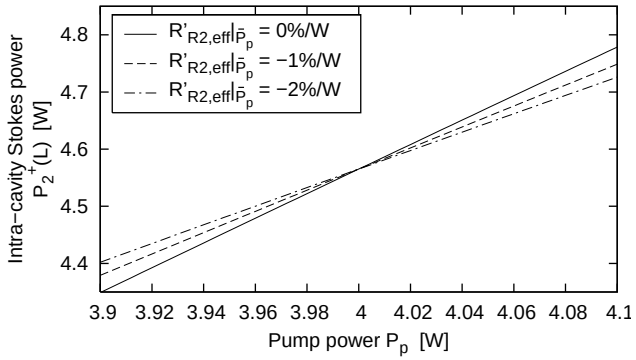

Figure 4.16.: Intra-cavity Stokes power $P_2^+(L)$ versus pump power P_p in a simple single-wavelength Raman fiber laser. Solid curve: power-independent FBG reflectivites. Dashed and dashed-dotted curves: effective right-hand reflectivity $R_{\mathrm{R2,eff}}$ has been assumed to decrease with incident Stokes power according to Eq. (4.34).

If $R'_{\mathrm{R2,eff}}|_{\bar{P}_p} = 0$, i. e., if the line spectra are power-independent, we obtain the characteristic shown as the solid curve in Fig. 4.16. Assuming that the differential effective reflectivities are $R'_{\mathrm{R2,eff}}|_{\bar{P}_p} = -1\,\%/\mathrm{W}$ or $R'_{\mathrm{R2,eff}}|_{\bar{P}_p} = -2\,\%/\mathrm{W}$, the characteristics are the dashed and dashed-dotted curves in Fig. 4.16, respectively. We see that the intra-cavity characteristics of the RFLs with power-dependent effective reflectivities are less sensitive against pump-power changes than those predicted by neglecting the power dependence of the Stokes linewidth. Also, RFLs in which the Stokes line broadens faster with increasing power have a larger value of $R'_{\mathrm{R2,eff}}|_{\bar{P}_p}$, and thus are less sensitive against pump-power changes. The effect as presented up to now is relatively weak, but it is much more pronounced in the multi-wavelength RFLs presented in the next section.

We note that while the intra-cavity characteristics are always stabilized, the output characteristics $P_{\mathrm{out,2}}(P_p)$ can actually become less stable in some cases. This is best illustrated by considering an extreme situation. Imagine that the effective reflectivity of the output FBG is 99% for a specified pump power. An increase of the pump power now

leads to a decrease of this effective reflectivity to, for example, 98%. This 1% change in reflectivity with its relatively small effect on the intra-cavity Stokes power must be contrasted to the change of the transmittivity of the FBG, which is doubled from 1% to 2%. Thus the RFL output power is nearly doubled. Without a change in the FBG reflectivity, the output power would not increase that much.

4.4.4. Stabilizing effect on multi-wavelength RFLs

In this section we show that the stabilizing effect of power-dependent effective reflectivities can be particularly strong in multi-wavelength RFLs.

We first consider an MWRFL with three Stokes lines at the wavelengths $\lambda_2 = 1100\,\text{nm}$, $\lambda_3 = 1110\,\text{nm}$ and $\lambda_4 = 1120\,\text{nm}$, respectively. The fiber length is $L = 500\,\text{m}$. For the sake of a simple modeling, the gain coefficient for stimulated Raman scattering from wavelength λ_p to λ_s is approximated by a triangular profile with a peak value of $1 \times 10^{-3}/\text{Wm}$ at the wavelength difference $\lambda_s - \lambda_p = 60\,\text{nm}$. In the differential equations describing the longitudinal evolution of the pump and various Stokes powers, we take into account all possible SRS interactions between the various lines as in [CRB03]—for example, the lowest-wavelength Stokes line ($i = 2$) can act as a pump for the two higher-wavelength Stokes lines, although with a relatively low gain coefficient, see Fig. 2.3.

Suppose now that the MWRFL is pumped with $\bar{P}_p = 4\,\text{W}$, and its Stokes and FBG spectra are such that the effective reflectivities in this operating state are $R_{\text{L}i,\text{eff}}|_{\bar{P}_p} = 99\%$ for all three Stokes lines $i = 2, 3, 4$, and $R_{\text{R2,eff}}|_{\bar{P}_p} = 80\%$, $R_{\text{R3,eff}}|_{\bar{P}_p} = 18.6\%$ and $R_{\text{R4,eff}}|_{\bar{P}_p} = 4.33\%$. Then, the output power $P_{\text{out},i}(\bar{P}_p)$ of each of the three lines is equal to 0.666 W. The reflectivities have been determined by using the optimization algorithm described in [CRB03]. We consider this design with equalized output powers for visual clarity of the presented figures.

The input-output characteristic of the MWRFL specified above is plotted in Fig. 4.17 for the case of power-independent effective FBG reflectivities, i. e., the Stokes linewidths do not change from their values at $P_p = \bar{P}_p$. It can be seen that this RFL is rather instable: changing the pump power by only about 1% causes one of the Stokes lines to vanish.

If the Stokes linewidths of the MWRFL are permitted to vary with the carried power, however, the situation is quite different. As in Section 4.4.3, we consider what happens when the right-hand effective FBG reflectivities vary with the incident Stokes powers according to

$$R_{\text{R}i,\text{eff}}\big|_{P_p} = R_{\text{R}i,\text{eff}}|_{\bar{P}_p} + R'_{\text{R}i,\text{eff}}\big|_{\bar{P}_p} \cdot \left\{ P_i^+(L)\big|_{P_p} - P_i^+(L)\big|_{\bar{P}_p} \right\} \tag{4.36}$$

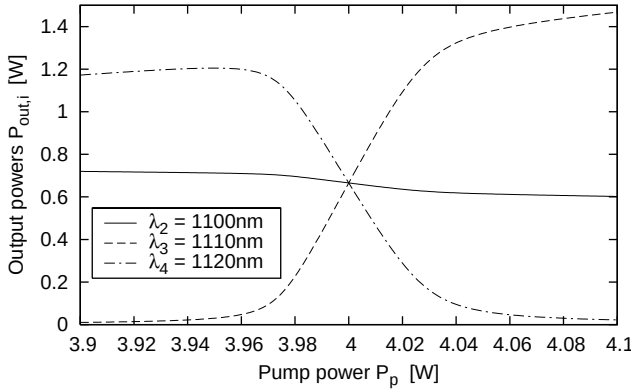

Figure 4.17.: Input-output characteristic of a multi-wavelength RFL obtained from a simulation with power-independent Stokes linewidths.

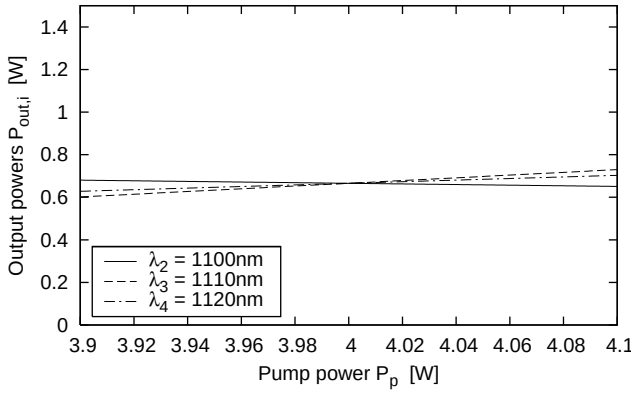

Figure 4.18.: Input-output characteristic of a multi-wavelength RFL whose right-hand effective FBG reflectivities have a differential effective reflectivity of $R'_{\mathrm{R}i,\mathrm{eff}}|_{\bar{P}_p} = -1\,\%/\mathrm{W}$ for $i = 2, 3, 4$ at $P_p = \bar{P}_p = 4\,\mathrm{W}$. Compared to Fig. 4.17, this MWRFL is more stable against pump-power changes.

for $i = 2, 3, 4$. For the sake of simplicity we assume equal differential effective reflectivities $R'_{\mathrm{R}i,\mathrm{eff}}|_{\bar{P}_p}$ for all Stokes lines (in practice, the FBG reflectivity spectra would have to be designed accordingly). The characteristic of this MWRFL is plotted in Fig. 4.18 for $R'_{\mathrm{R}i,\mathrm{eff}}|_{\bar{P}_p} = -1\,\%/\mathrm{W}$ $(i = 2, 3, 4)$. Obviously the stability of this MWRFL is considerably higher than that of the MWRFL with power-independent Stokes linewidths, in accordance with the arguments at the end of Section 4.4.2.

In order to be able to quantify the degree of stability, we define the sensitivity σ of our MWRFL within an interval $[P_<, P_>]$ around a specified pump power $\bar{P}_p$ as the maximum change occuring in the output powers,

$$\sigma = \max_{\substack{2\le i\le 4 \\ P_p\in[P_<,P_>]}} \left| \frac{P_{\mathrm{out},i}(P_p) - P_{\mathrm{out},i}(\bar{P}_p)}{P_p - \bar{P}_p} \right| . \tag{4.37}$$

In the case above, $\bar{P}_p = 4\,\mathrm{W}$ and $[P_<, P_>] = [3.9\,\mathrm{W}, 4.1\,\mathrm{W}]$, and the sensitivity of our MWRFL with $R'_{\mathrm{R}i,\mathrm{eff}}|_{\bar{P}_p} = 0$ is $\sigma = 23.1$, whereas that of the MWRFL with $R'_{\mathrm{R}i,\mathrm{eff}}|_{\bar{P}_p} = -1\,\%/\mathrm{W}$ is only $\sigma = 0.643$.

Finally, we illustrate the improvement of the stability within $[P_<, P_>] = [3.9\,\mathrm{W}, 4.1\,\mathrm{W}]$ for other three-wavelength RFLs with output powers equalized for $P_p = \bar{P}_p = 4\,\mathrm{W}$. Fig. 4.19 shows the sensitivity of MWRFLs without ($R'_{\mathrm{R}i,\mathrm{eff}}|_{\bar{P}_p} = 0$, solid curve) and with line broadening ($R'_{\mathrm{R}i,\mathrm{eff}}|_{\bar{P}_p} = -1\,\%/\mathrm{W}$, dashed curve) as a function of the effective reflectivity $R_{\mathrm{R2,eff}}|_{\bar{P}_p}$ of the right-hand FBG for line $i = 2$ at $P_p = \bar{P}_p$. The line broadening reduces the sensitivity by more than one order of magnitude. The parameter $R_{\mathrm{R2,eff}}|_{\bar{P}_p}$ is varied to model the MWRFL configurations. The required effective reflectivities for Stokes lines 3 and 4 follow from the algorithm described in [CRB03] by requiring equalized output powers in all three Stokes lines at the pump power $P_p = \bar{P}_p$. All other parameters of the RFL besides these reflectivities are the same as in the MWRFL considered at the beginning of this section. Fig. 4.20 shows the corresponding results in dependence of the fiber length L. These results demonstrate that the stabilizing effect of line broadening is a quite general characteristic of such RFLs.

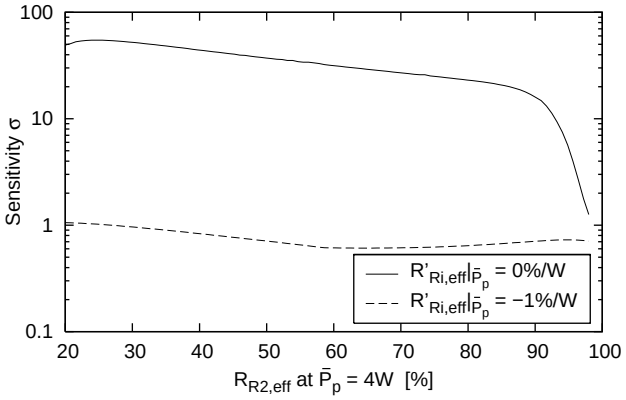

Figure 4.19.: Sensitivity σ of three-wavelength RFLs as a function of the effective reflectivity $R_{\mathrm{R2,eff}}|_{\bar{P}_p}$ of the right-hand FBG for line $i = 2$ at $\bar{P}_p = 4\,\mathrm{W}$. Output powers of the three Stokes lines $i = 2, 3, 4$ are kept equalized for $P_p = \bar{P}_p$. Solid curve: without line broadening ($R'_{\mathrm{R}i,\mathrm{eff}}|_{\bar{P}_p} = 0$). Dashed curve: with line broadening ($R'_{\mathrm{R}i,\mathrm{eff}}|_{\bar{P}_p} = -1\,\%/\mathrm{W}$).

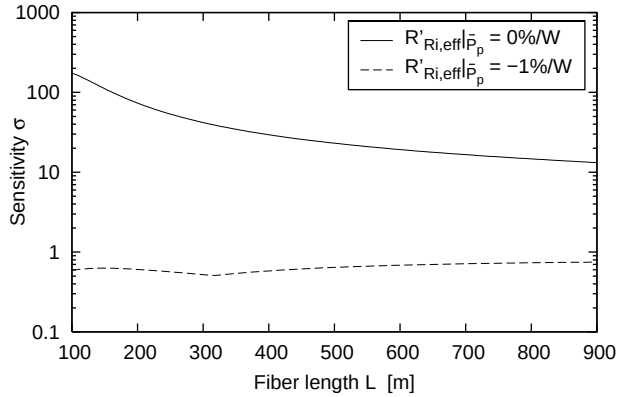

Figure 4.20.: Sensitivity σ of three-wavelength RFLs as a function of the fiber length L. Output powers of the three Stokes lines $i = 2, 3, 4$ are kept equalized at $P_p = \bar{P}_p = 4\,\mathrm{W}$, and $R_{\mathrm{R2,eff}}|_{\bar{P}_p}$ is kept fixed at 80%. Solid curve: without line broadening ($R'_{\mathrm{R}i,\mathrm{eff}}|_{\bar{P}_p} = 0$). Dashed curve: with line broadening ($R'_{\mathrm{R}i,\mathrm{eff}}|_{\bar{P}_p} = -1\,\%/\mathrm{W}$).

4.5. Chapter summary

In this chapter, we have developed a model for the pump-to-Stokes transfer of relative intensity noise in Raman fiber lasers. The model can qualitatively explain the measured output RIN spectra of RFLs. We have then shown how single-cavity RFLs can be optimized such that the degradation of the bit-error rate of a Raman-amplified transmission span by the RIN of the RFL is minimized. Furthermore, we have shown theoretically and experimentally that a double-cavity RFL can be used to realize RFLs that have a local maximum in their characteristics, at which the RFL is stable against low-frequency pump-power fluctuations. Finally, we have shown that the effect of power-dependent line broadening in RFLs significantly improves the stability of multi-wavelength RFLs against pump-power fluctuations, as compared to what the usual model (without line broadening) predicts.

5. Raman gain and nonlinear absorption in silicon waveguides

In Chapter 2 we derived a model describing the interaction between the pump and Stokes powers in a general waveguide, see Eqs. (2.41)–(2.42). This chapter prepares for the remainder of the thesis by adapting this general model to silicon waveguides.

A short overview over silicon waveguides is given in section 5.1. Sections 5.2 and 5.3 are concerned with the effects of Stimulated Raman Scattering (SRS) and Two-Photon Absorption (TPA), respectively, while section 5.4 extends our model to include the important effect of Free-Carrier Absorption (FCA). Section 5.5 summarizes the complete model in a compact form for easy reference.

While at least two detailed derivations of similar models for wave propagation in silicon have recently been published in the literature [CPO06, PL06], several aspects of the results presented here are novel. The existing models do not allow for counter-propagating pump and Stokes waves, but in order to describe lasers they have to be included in the model. Furthermore, the modeling of FCA from section 5.4 makes clear for the first time the precise relationship between the effective free-carrier lifetime τ_{eff} "seen" by the mode and the underlying carrier-diffusion problem. This is particularly important for the modeling of cladding-pumped Raman amplifiers in section 6.4, where the pump and Stokes mode fields may have totally different mode shapes and overlaps with the silicon. Finally, the models for the TPA spectrum and the tensorial structure of

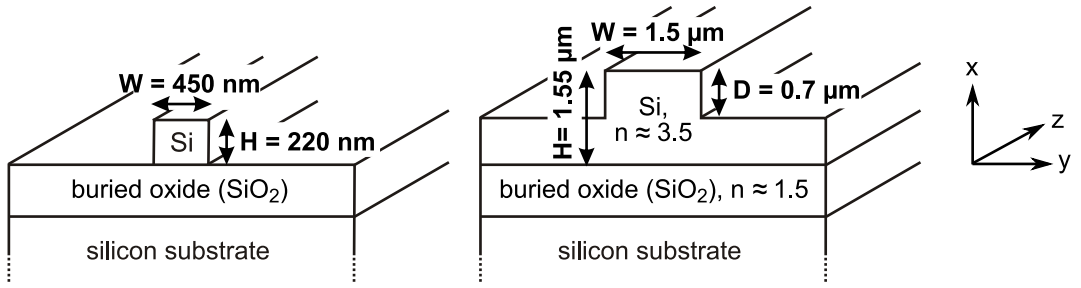

Figure 5.1.: Two typical silicon-waveguide geometries. *left:* strip waveguide as in [EDRMO+04], *right:* rib waveguide as in [RJL+05].

the nonlinear-susceptibility tensor for TPA discussed in section 5.3 are used here for the first time and are required for the realistic modeling of silicon Raman lasers in section 7.4.

5.1. Silicon waveguides

In silicon photonics, practical single-mode waveguides with low propagation losses can be realized in various forms. Strip waveguides or so-called "photonic wires", as shown on the left-hand side of Fig. 5.1, have a silicon core with cross-sectional dimensions on the order of a few hundred nanometers. They are surrounded everywhere by lower-refractive-index material, namely the silica buffer layer below and air or silica above [VM04, BDJ+05, TYF+05]. On the other hand, rib waveguides have a larger core on the order of micrometers, as well as adjacent slabs of silicon on both sides, see the right-hand side of Fig. 5.1. In spite of their large core dimensions, rib waveguides can be designed such that they guide only the fundamental mode, while all higher-order modes are leaky and radiate power through the adjacent slab waveguides [SSP91, JYY+98, CPL+05]. Finally, photonic-crystal waveguides have been demonstrated, where light is guided along a line defect in a photonic-crystal slab [LDVS00, MMV03, BDJ+05].

Of all these waveguide types, rib waveguides pose the weakest requirements on the processing technology due to their relatively large dimensions. Furthermore, coupling light between rib waveguides and optical fibers is relatively easy, and rib waveguides can be designed to have low or even zero birefringence [CPL+05, YXJ+05]. Linear waveguide losses as low as 0.1 dB/cm have been achieved, but due to scattering at the rough waveguide sidewalls the losses tend to increase when the waveguide dimensions are reduced [JPR06].

5.2. Stimulated Raman scattering in silicon waveguides

An accurate modeling of Stimulated Raman scattering in waveguides with a crystalline silicon core is slightly more complex than in the case of optical fibers (see Sect. 2.3) for two reasons: silicon is not an isotropic material, and the mode fields in silicon waveguides can not be assumed to be uniformly polarized across the waveguide cross section, such that the well-known formula for the effective area, Eq. (2.53), is no longer applicable.

In this section, we summarize the symmetry properties of the nonlinear susceptibility

tensor describing SRS in silicon, give an overview over measurements for the bulk Raman-gain constant from the literature, and finally derive an expression for the effective area for SRS in silicon waveguides.

5.2.1. Properties of Raman gain in silicon

Consider a coordinate system $\tilde{x}, \tilde{y}, \tilde{z}$ which is aligned with the crystallographic axes of crystalline silicon. In this coordinate system, the third-order nonlinear-susceptibility tensor $\tilde{\chi}^{(3),\mathrm{SRS}}_{ijkl}(\omega_p, -\omega_p, \omega_s)$ describing stimulated Raman scattering from a pump wave at frequency ω_p to a Stokes wave at ω_s in crystalline silicon is known to have the form [SB65, DHCJ03, LRJ+06]

$$\tilde{\chi}^{(3),\mathrm{SRS}}_{ijkl}(\omega_p, -\omega_p, \omega_s) = \chi_R(\omega_p - \omega_s) \sum_{m=X,Y,Z} (\mathbf{R}^m)_{ij} (\mathbf{R}^m)_{kl}, \tag{5.1}$$

where the matrices $\mathbf{R}^{X,Y,Z}$,

$$\mathbf{R}^X = \begin{pmatrix} 0 & 0 & 0 \\ 0 & 0 & 1 \\ 0 & 1 & 0 \end{pmatrix}, \quad \mathbf{R}^Y = \begin{pmatrix} 0 & 0 & 1 \\ 0 & 0 & 0 \\ 1 & 0 & 0 \end{pmatrix}, \quad \mathbf{R}^Z = \begin{pmatrix} 0 & 1 & 0 \\ 1 & 0 & 0 \\ 0 & 0 & 0 \end{pmatrix}, \tag{5.2}$$

reflect the symmetry properties of the material and of the Raman-active phonons [Lou75, Car82, YC05]. The function $\chi_R(\Omega)$ occuring in Eq. (5.1) has the form

$$\chi_R(\Omega) = \frac{\omega_0 \Delta\omega_0}{\omega_0^2 - \Omega^2 - i\Delta\omega_0 \Omega} \hat{\chi}_R, \tag{5.3}$$

the imaginary part of which is a Lorentzian centered around ω_0 with an FWHM of $\Delta\omega_0$ and a peak value of $\hat{\chi}_R$. By expanding the sums in Eq. (5.1), it is seen that the only non-vanishing tensor components are [JRDB06]

$$\begin{aligned} \tilde{\chi}_{\tilde{x}\tilde{y}\tilde{x}\tilde{y}} = \tilde{\chi}_{\tilde{x}\tilde{y}\tilde{y}\tilde{x}} = \tilde{\chi}_{\tilde{x}\tilde{z}\tilde{x}\tilde{z}} = \tilde{\chi}_{\tilde{x}\tilde{z}\tilde{z}\tilde{x}} = \tilde{\chi}_{\tilde{y}\tilde{x}\tilde{x}\tilde{y}} = \tilde{\chi}_{\tilde{y}\tilde{x}\tilde{y}\tilde{x}} = \tilde{\chi}_{\tilde{y}\tilde{z}\tilde{y}\tilde{z}} = \tilde{\chi}_{\tilde{y}\tilde{z}\tilde{z}\tilde{y}} \\ = \tilde{\chi}_{\tilde{z}\tilde{x}\tilde{x}\tilde{z}} = \tilde{\chi}_{\tilde{z}\tilde{x}\tilde{z}\tilde{x}} = \tilde{\chi}_{\tilde{z}\tilde{y}\tilde{y}\tilde{z}} = \tilde{\chi}_{\tilde{z}\tilde{y}\tilde{z}\tilde{y}} = \chi_R, \end{aligned} \tag{5.4}$$

and they are all identical to χ_R defined in Eq. (5.3). Now that the tensor structure is known, we can use Eq. (2.48) to find the bulk Raman-gain constant as a function of the pump and Stokes polarizations $\hat{\mathbf{p}}$ and $\hat{\mathbf{s}}$:

$$g(\omega_s, \omega_p, \hat{\mathbf{s}}, \hat{\mathbf{p}}) = \frac{3\omega_s \mu_0}{n_s n_p} \operatorname{Im}\left[\tilde{\chi}^{(3),\mathrm{SRS}}_{iklj}(\omega_p, -\omega_p, \omega_s) \hat{s}^{i*} \hat{s}^j \hat{p}^k \hat{p}^{l*}\right], \tag{5.5}$$

where i, j, k, l range over the crystallographic axes $\tilde{x}, \tilde{y}, \tilde{z}$, and we have made use of the intrinsic permutation symmetry of $\tilde{\chi}^{(3)}_{iklj}$ in order to account for the different order of the

frequency arguments in Eq. (5.1) and Eq. (2.48). For example, for pump light polarized along the $\tilde{x}$ axis and Stokes light polarized along $\tilde{y}$, the bulk Raman gain is

$$g_R(\omega_p - \omega_s) = \frac{3\omega_s\mu_0}{n_s n_p} \operatorname{Im} \tilde{\chi}^{(3),\mathrm{SRS}}_{\tilde{y}\tilde{x}\tilde{x}\tilde{y}}(\omega_p, -\omega_p, \omega_s) = \frac{3\omega_s\mu_0}{n_s n_p} \operatorname{Im} \chi_R(\omega_p - \omega_s), \tag{5.6}$$

where χ_R was defined in Eq. (5.3). The same Raman gain is also obtained whenever the pump and Stokes beams are polarized along any two different crystallographic axes of the silicon crystal, as an inspection of Eq. (5.4) shows. On the other hand, for beams co-polarized along the same crystallographic axis the gain becomes zero.

Finally, the Raman-gain spectrum is offset from the pump wavelength by $\omega_0 = 15.6\,\mathrm{THz}$ and has a linewidth $\Delta\omega_0$ of about 100 GHz [CDR+03].

Waveguide orientation

The strong polarization dependence of the Raman gain has implications on the layout of the waveguides on a silicon wafer. Silicon waveguides are usually fabricated on a (100) surface, such that the x coordinate of our waveguide coordinate system defined in Fig. 2.2 coincides with the crystallographic $\tilde{x}$ axis, see Fig. 5.2. The propagation direction can vary in the (100) plane according to the angle θ in Fig. 5.2.

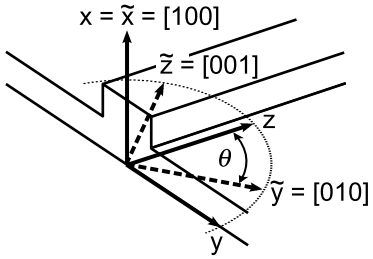

Figure 5.2.: Silicon waveguides are usually fabricated along the [011] direction ($\theta = 45°$) on a (100) surface.

If the waveguide were fabricated such that the propagation direction is the crystallographic $\tilde{z}$ axis ($\theta = 90°$ in Fig. 5.2), the quasi-TE mode would be predominantly polarized along $\tilde{y}$, and the quasi-TM mode would be predominantly polarized along $\tilde{x}$. Following the discussion of Eq. (5.6), a TE pump could amplify only the TM Stokes mode and vice-versa. Practical waveguides, however, are often fabricated along the [011] direction [CDR+03, LRJ+06], corresponding to $\theta = 45°$ in Fig. 5.2. In the crystallographic-axes coordinate system, the polarization vectors for quasi-TE and quasi-TM polarizations are then $\hat{\mathbf{e}}_{\mathrm{TE}} = (0, 1, -1)/\sqrt{2}$ and $\hat{\mathbf{e}}_{\mathrm{TM}} = (1, 0, 0)$, respectively. Using these vectors for $\hat{\mathbf{s}}$ and $\hat{\mathbf{p}}$ in Eq. (5.5), one sees that a TE pump can now equally well amplify both

the TE and TM Stokes modes, and that a TM pump can amplify a TE Stokes mode. Only TM–TM amplification remains impossible [LRJ+06] (when we ignore the slight hybridicity of the quasi-TM modes).

Table 5.1 gives an overview over Raman-gain constants reported in the literature for silicon. Reported values vary between 10 and 80 cm/GW. The reason for such large variations is not clear. One reason may be that several of the employed measurement methods involve fitting to amplifier models in which several other parameters are not known very well either, such as the Two-Photon Absorption constant (see Sect. 5.3). The modeling in the remainder of this thesis will use a conservative value of 20 cm/GW.

Ref.	λ_p (μm)	g (cm/GW)	Method / Notes
[CDJ02]	1.427	70	Extrapolated from spont. data [RC70]
[CDHJ02]	1.427	76	From spontaneous scattering efficiency
[CDR+03]	1.427	37	From spontaneous scattering efficiency
[CDR+03]	1.427	20	CW-amplifier gain in rib waveguide
[EDRMO+04]	1.435	29 ± 4	Pulsed-amplifier gain in strip waveguide
[LRP+04]	1.545	10.5	Pulsed-amplifier gain in rib waveguide
[LRJ+06]	1.548	9.5	Pulsed-amplifier gain in rib waveguide

Table 5.1.: Proposed values for the Raman-gain coefficient g of silicon in the literature.

5.2.2. Co- and counter-propagating effective areas

We now derive the effective areas for stimulated Raman scattering in silicon waveguides. Eq. (2.42) describes the longitudinal evolution of the forward- and backward-propagating Stokes powers in the waveguide in a general way, and we will rewrite the SRS contribution to the four nonlinear interactions described by Γ_{s+p+}, Γ_{s+p-}, Γ_{s-p+} and Γ_{s-p-} as the ratio of the bulk Raman-gain constant and certain effective areas, as illustrated in Sect. 2.2.5. We consider the case where the pump and Stokes frequency difference is such that the Raman gain is maximal, i. e., $\omega_p - \omega_s = \omega_0$.

We consider only silicon waveguides oriented along the [011] direction on a (100) surface, as in these the quasi-TE copolarized gain is maximal, see Sect. 5.2.1. Thus, the nonlinear susceptibility tensor of silicon, Eq. (5.1), must first be transformed from the crystallographic-axes coordinate system $\tilde{x}, \tilde{y}, \tilde{z}$ to the waveguide coordinate system x, y, z (the relation between the two coordinate systems is shown in Fig. 5.2, with $\theta = 45°$),

yielding

$$\chi^{(3),\mathrm{SRS}}_{ijkl}(\omega_p,-\omega_p,\omega_s)=\chi_R(\omega_p-\omega_s)\sum_{m=X,Y,Z}(\mathbf{S}^T\mathbf{R}^m\mathbf{S})_{ij}(\mathbf{S}^T\mathbf{R}^m\mathbf{S})_{kl}, \tag{5.7}$$

where

$$\mathbf{S}=\frac{1}{\sqrt{2}}\begin{pmatrix}\sqrt{2}&0&0\\0&1&1\\0&-1&1\end{pmatrix} \tag{5.8}$$

is the change-of-bases transformation matrix. With the help of the intrinsic permutation symmetry of $\chi^{(3),\mathrm{SRS}}_{ijkl}$ to adjust the order of the frequency arguments, Eq. (5.7) can be inserted into Eq. (2.44) to get the modal gain coefficient for stimulated Raman scattering from the forward-propagating pump wave to the forward-propagating Stokes wave,

$$4\,\mathrm{Re}\,\Gamma_{s+p+}=\frac{3\epsilon_0\omega_s}{4\hat{N}_s\hat{N}_p}\,\mathrm{Im}\left[i\hat{\chi}_R\int(\mathbf{S}^T\mathbf{R}^m\mathbf{S})_{ik}(\mathbf{S}^T\mathbf{R}^m\mathbf{S})_{lj}e_s^{i*}e_s^je_p^ke_p^{l*}\,\mathrm{d}A\right]. \tag{5.9}$$

Following the idea of Sect. 2.2.5, we want to rewrite the modal gain coefficient (5.9) as

$$4\,\mathrm{Re}\,\Gamma_{s+p+}=\frac{g_R(\omega_0)}{A^{(\mathrm{SRS})}_{\mathrm{eff,co}}}, \tag{5.10}$$

where $g_R(\omega_0)$ is the peak bulk gain coefficient, see Eq. (5.6), and $A^{(\mathrm{SRS})}_{\mathrm{eff,co}}$ is the effective area to be derived. Solving Eq. (5.10) for the latter and inserting Eq. (5.7), one obtains

$$A^{(\mathrm{SRS})}_{\mathrm{eff,co}}=\frac{4Z_0^2\hat{N}_p\hat{N}_s}{n_pn_s}\left[\int_{\mathrm{Si}}(e_s^x)^2[(e_p^y)^2-(e_p^z)^2]+(e_s^y)^2[(e_p^x)^2+(e_p^y)^2]+(e_s^z)^2[(e_p^x)^2-(e_p^z)^2]\right.$$
$$\left.+2(e_s^xe_s^ye_p^xe_p^y+e_s^xe_s^ze_p^xe_p^z+e_s^ye_s^ze_p^ye_p^z)\,\mathrm{d}A\right]^{-1}, \tag{5.11}$$

where $\mathbf{e}_{p,s}$ are the pump and Stokes mode fields with real transverse and imaginary longitudinal components (see Eqs. (2.11)–(2.12)), and $\hat{N}_{p,s}$ are the corresponding mode normalizations defined in Eq. (2.14).

We can proceed similarly for the other SRS contributions occurring in Eq. (2.42) and write them as the ratio of the bulk gain given by Eq. (5.6) and an effective area. The result is that the other co-propagating SRS contribution $4\,\mathrm{Re}\,\Gamma_{s-p-}$, describing the gain exerted on the backward-propagating Stokes wave by the backward-propagating pump wave, has the same effective area $A^{(\mathrm{SRS})}_{\mathrm{eff,co}}$ given in Eq. (5.11). The two counter-propagating SRS contributions $4\,\mathrm{Re}\,\Gamma_{s+p-}$ and $4\,\mathrm{Re}\,\Gamma_{s-p+}$, however, share an effective

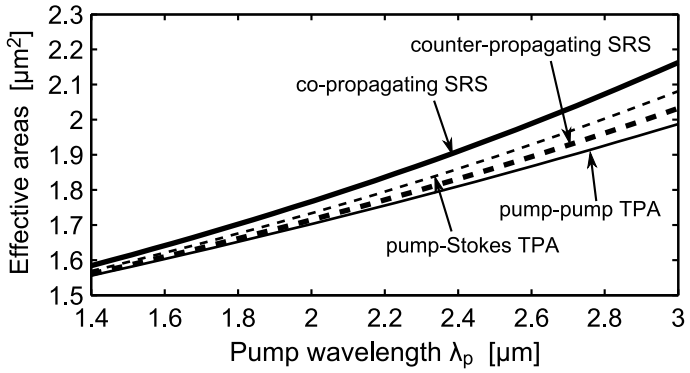

Figure 5.3.: The thick solid and dashed curves show the effective areas $A_{\mathrm{eff,co}}^{(\mathrm{SRS})}$ and $A_{\mathrm{eff,cntr}}^{(\mathrm{SRS})}$ for co- and counter-propagating SRS as a function of the pump wavelength λ_p. The curves correspond to the silicon rib waveguide on the right-hand side of Fig. 5.1. All modes are quasi-TE.

area which differs from Eq. (5.11) in two minus signs:

$$A_{\mathrm{eff,cntr}}^{(\mathrm{SRS})} = \frac{4Z_0^2\hat{N}_p\hat{N}_s}{n_p n_s}\left[\int_{\mathrm{Si}} (e_s^x)^2[(e_p^y)^2-(e_p^z)^2] + (e_s^y)^2[(e_p^x)^2+(e_p^y)^2] + (e_s^z)^2[(e_p^x)^2-(e_p^z)^2] \right. \\ \left. + 2(e_s^x e_s^y e_p^x e_p^y - e_s^x e_s^z e_p^x e_p^z - e_s^y e_s^z e_p^y e_p^z)\,\mathrm{d}A\right]^{-1}. \quad (5.12)$$

In summary, the contribution of SRS to the longitudinal evolution of the forward- and backward-propagating Stokes powers $P_s^{\pm}$ can be written

$$\pm\frac{1}{P_s^{\pm}}\frac{\mathrm{d}P_s^{\pm}}{\mathrm{d}z} = g_R(\omega_0)\left(\frac{P_p^{\pm}}{A_{\mathrm{eff,co}}^{(\mathrm{SRS})}} + \frac{P_p^{\mp}}{A_{\mathrm{eff,cntr}}^{(\mathrm{SRS})}}\right). \quad (5.13)$$

The thick solid and dashed curves in Fig. 5.3 show the effective areas for co- and counter-propagating SRS as a function of the pump wavelength. They have been calculated using a custom-made full-vectorial mode solver (see Appendix A) for the quasi-TE fundamental mode of the waveguide used by Intel [RJL+05], the geometry of which is shown on the right-hand side of Fig. 5.1 (the waveguide is clad on top with silica, which is not shown in the figure). In calculating the effective areas for the various wavelengths, the Stokes wavelength is always offset from the pump wavelength by the Raman shift of ω_0. Fig. 5.3 shows that the difference between the forward- and backward-propagating effective areas can be as large as 5% at $\lambda_p = 3\,\mu$m for this waveguide, while becoming smaller at shorter wavelengths.

So far we have only written the SRS "seen" by the Stokes powers in terms of effective areas, see Eq. (5.13). To complete the description, we must also find corresponding

expressions for the terms that appear in the equations for the longitudinal evolution of the forward- and backward-propagating pump powers, see Eq. (2.41). The result can be written in the form

$$\pm \frac{1}{P_p^{\pm}} \frac{\mathrm{d}P_p^{\pm}}{\mathrm{d}z} = -g_R(\omega_0) \frac{\lambda_s}{\lambda_p} \left(\frac{P_s^{\pm}}{A_{\mathrm{eff,co}}^{(\mathrm{SRS})}} + \frac{P_s^{\mp}}{A_{\mathrm{eff,cntr}}^{(\mathrm{SRS})}} \right), \tag{5.14}$$

which follows from the symmetry relation

$$\tilde{\chi}_{ijkl}^{(3),\mathrm{SRS}}(\omega_p, \omega_s, -\omega_s) = \left[\tilde{\chi}_{ijkl}^{(3),\mathrm{SRS}}(\omega_s, \omega_p, -\omega_p) \right]^*, \tag{5.15}$$

which can be obtained from the theory of [SB65] that has also led to Eq. (5.1). As in section 2.3.1, the factor $\lambda_s/\lambda_p > 1$ occurring in Eq. (5.14) expresses photon-number conservation.

Polarization dependence of the effective areas for SRS

As discussed in section 2.2.5, the effective area is defined such that it encapsulates all the information about the tensorial structure of the nonlinearity, in this case SRS: one simply inserts the pump and Stokes mode fields of the waveguide into the formula. As an example, we have shown in Fig. 5.4 the effective area for co-propagating SRS as a function of the pump wavelength.

There are four curves, each corresponding to a particular combination of pump and Stokes polarizations. The thin solid curve in Fig. 5.4 (also shown in Fig. 5.3 as the thick solid curve) shows the effective area when both the pump and the Stokes powers are guided in the fundamental quasi-TE mode of the waveguide. The other two thin curves in Fig. 5.4 represent the effective areas for the cases when one of the pump and Stokes modes is the quasi-TE mode, and the other one is the quasi-TM mode. The three thin curves in Fig. 5.4 almost coincide and increase slightly towards larger wavelengths due to the decreasing mode confinement.

Finally, the thick solid curve in Fig. 5.4 represents the case where both the pump and the Stokes powers are guided in the fundamental quasi-TM mode of the waveguide. The effective areas are much larger than for the other polarization combinations. Thus SRS is very inefficient, in accordance with the discussion in section 5.2.1. In contrast to the other curves, however, the thick solid curve in Fig. 5.4 decreases towards larger wavelengths. On the one hand, the mode confinement decreases for larger wavelengths and this should increase the effective area. However, at the same time, the hybridicity of the mode becomes stronger—with increasing wavelength, the y and z components of the electric field of the quasi-TM mode become larger, and these components can contribute

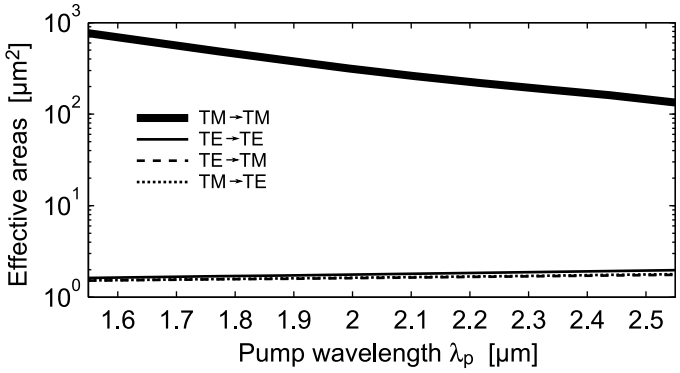

Figure 5.4.: Illustration of the strong polarization dependence of SRS in silicon waveguides: the figure shows the effective areas $A_{\mathrm{eff,co}}^{(\mathrm{SRS})}$ for co-propagating SRS as a function of the pump wavelength. TM–TM amplification (thick solid line) is much less efficient than TE–TE, TE–TM, or TM–TE amplification.

to the amplification of the quasi-TM Stokes mode. As a result, the effective area for TM–TM amplification decreases with increasing wavelength.

5.3. Two-Photon Absorption

Two-Photon Absorption (TPA) is a nonlinear absorption effect that has a significant limiting influence on the operation of Raman amplifiers and lasers based on silicon waveguides. In a TPA process, two photons are absorbed simultaneously, while exciting an electron from the valence band to the conduction band (see Fig. 5.5).

The two absorbed photons can have the same frequency (for example, when they are both taken from the pump wave or both from the Stokes wave), which is the case of degenerate TPA, see Fig. 5.5a. Alternatively, the two photons can have different frequencies (one photon from the pump wave, and one photon from the Stokes wave), which case is called non-degenerate TPA, see Fig. 5.5b. In either case, TPA can only

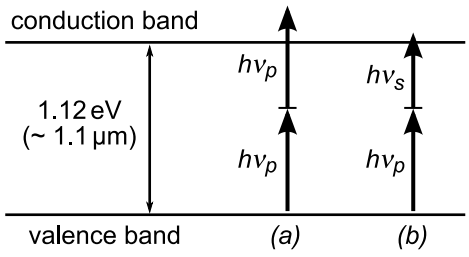

Figure 5.5.: Illustration of *(a)* degenerate and *(b)* non-degenerate Two-Photon Absorption (TPA) in silicon.

Ref.	λ (μm)	β (cm/GW)	Method / Notes
[RM73]	1.06	1.5	pulsed laser; bulk Si ($T = 100\,\mathrm{K}$)
[DQG03]	1.27	0.74 ± 0.11	z-scan; $\langle 110 \rangle$ direction
[RVY04]	1.53	0.9 ± 0.18	pulsed laser; multi-mode strip waveguide
[TWL$^+$02]	1.54	0.45 ± 0.1	pulsed laser; rib waveguide
[DQG03]	1.54	0.79 ± 0.11	z-scan; $\langle 110 \rangle$ direction
[DQG03]	1.54	0.88 ± 0.13	z-scan; $\langle 111 \rangle$ direction
[LT04]	1.547	0.67 ± 0.07	pulsed laser; rib waveguide
[YSC$^+$05]	1.550	0.6	pulsed laser; single-mode strip waveguide
[CDR$^+$03]	1.560	0.44 ± 0.10	pulsed laser; rib waveguide

Table 5.2.: Measurements of the degenerate TPA coefficient $\beta(\lambda)$ of silicon in the literature.

take place when the sum of the energies of the two photons exceeds the indirect-band-gap energy of silicon, $E_{ig} \approx 1.12\,\mathrm{eV}$.

In Sect. 5.3.1 we will summarize the known results for degenerate TPA in silicon and derive an expression for the corresponding effective area. Sect. 5.3.2 then summarizes the few existing results for non-degenerate TPA and the assumptions we use in the remainder of this thesis.

5.3.1. Degenerate TPA

Just as in the case of any other bulk nonlinear coefficient (see Sect. 2.2.5), the coefficients describing the strength of TPA in bulk silicon are defined in terms of plane waves. A single homogeneous CW plane wave with intensity I propagating along z is damped by degenerate TPA according to

$$\frac{\mathrm{d}I}{\mathrm{d}z} = -\beta I^2, \tag{5.16}$$

where β is the bulk degenerate-TPA coefficient, which is in general polarization-dependent. Table 5.2 gives an overview of measurements of β for silicon from the literature, where often the polarization is not clearly specified. Reported values at wavelengths around $1.5\,\mu$m range from 0.4 to 0.9 cm/GW.

Wavelength dependence of the bulk TPA coefficient

For the modeling of cascaded silicon Raman lasers in Sect. 7.4, where the propagating waves span a wide wavelength range ($1.5 \ldots 3.0\,\mu$m), it is important to know the spectral dependence of the TPA coefficient $\beta(\omega)$. The degenerate-TPA coefficient must vanish for $\lambda > 2.2\,\mu$m, where the photon energy is less than half the indirect band gap of

silicon. Indeed, it has been shown experimentally [RSSJ06] that the transmission of a bulk silicon sample saturates with increasing power at a wavelength of 2.09 μm due to TPA, but not at a wavelength of 2.94 μm. However, there are no known experimental results in the literature on the precise dependence of the TPA coefficient on wavelength between 1.5 μm and 2.2 μm.

A recent theoretical paper by Dinu gives the following expression for the spectral dependence of the degenerate-TPA coefficient of silicon [Din03],

$$\beta_{\mathrm{deg}}(\omega) = C \cdot \frac{\left(2\hbar\omega/E_{ig} - 1\right)^4}{\left(2\hbar\omega/E_{ig}\right)^7} \tag{5.17}$$

for frequencies ω above half the band gap, $\omega > E_{ig}/(2\hbar)$, and C is a constant that depends on details of the employed band-structure model of silicon [Din03]. The degenerate-TPA coefficient given by Eq. (5.17) is plotted versus wavelength as the solid curve in Fig. 5.6, where we have chosen C such that $\beta_{\mathrm{deg}}(1427\,\mathrm{nm}) = 0.7\,\mathrm{cm/GW}$ as in [CRDJ04].

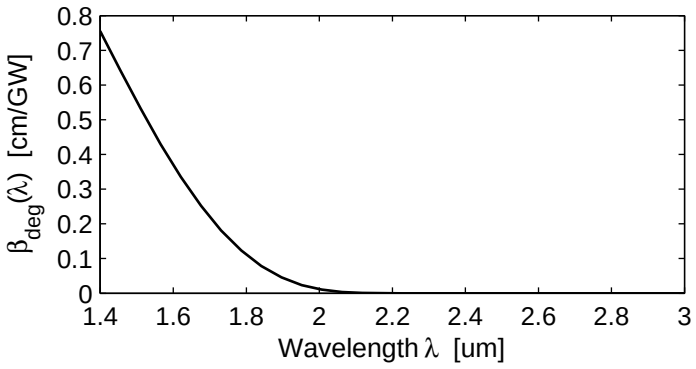

Figure 5.6.: Spectrum of the bulk degenerate-TPA coefficient of silicon according to the theory of [Din03]. The curve is scaled such that $\beta_{\mathrm{deg}}(1427\,\mathrm{nm}) = 0.7\,\mathrm{cm/GW}$.

Form of the nonlinear susceptibility tensor

Because two photons are involved in a TPA process, the two-photon absorption rate given by Eq. (5.16) is quadratic in the optical intensities. Like stimulated Raman scattering, TPA can thus also be described mathematically in terms of its contribution $\tilde{\chi}^{(3),\mathrm{TPA}}_{ijkl}$ to the third-order nonlinear susceptibility. A derivation similar to that performed in Sect. 2.2.5 for a general bulk nonlinear constant gives the following relation between the bulk degenerate-TPA constant occurring in Eq. (5.16) and the TPA tensor $\tilde{\chi}^{(3),\mathrm{TPA}}_{ijkl}$,

$$\beta(\omega, \hat{\mathbf{e}}) = \frac{3\omega\mu_0}{2n^2}\,\mathrm{Im}\left[\tilde{\chi}^{(3),\mathrm{TPA}}_{ijkl}(\omega, \omega, -\omega)\hat{e}^{i*}\hat{e}^{j}\hat{e}^{k}\hat{e}^{l*}\right], \tag{5.18}$$

where n is the (linear) refractive index of silicon at the frequency ω, $\hat{\mathbf{e}} = (\hat{e}^x, \hat{e}^y, \hat{e}^z)$ is a unit vector along the polarization direction, and ω is the optical angular frequency. A knowledge of the structure of the tensor $\chi^{(3),\mathrm{TPA}}_{ijkl}$ describing TPA in silicon is important for the accurate modeling of TPA in waveguides, in particular in small strip waveguides or in higher-order modes of the cladding-pumped structures of Sect. 6.4, where all three cartesian electric-field components are significant.

As silicon has a cubic crystal structure of the m3m class, a general third-order nonlinear susceptibility tensor $\chi^{(3)}_{ijkl}(\omega_1, \omega_2, \omega_3)$ can have at most 21 non-zero elements, of which only 4 are independent [Boy03]. For the degenerate TPA contribution $\tilde{\chi}^{(3),\mathrm{TPA}}_{ijkl}(\omega, \omega, -\omega)$ considered here, the first two frequency arguments are equal, so that intrinsic permutation symmetry even further reduces the number of independent elements to three [Boy03]. The three independent elements of the TPA tensor may in principle be determined experimentally by measuring the bulk TPA coefficient β for three different polarizations [HW94]. Results on this are scarce in the literature, however. Salem et al. [SM04] measured the TPA photocurrent in a silicon photodiode for various polarizations at a wavelength of 1.55 μm, although it is not clear whether the chosen polarization directions are sufficient to fully determine the three independent TPA tensor elements, as the orientation of the crystallographic axes is not given in [SM04]. Nevertheless, as the authors suggest, the results are fully explained when one assumes that (a) the TPA response of silicon at the wavelength of 1.55 μm is isotropic, and (b) that the incremental TPA dichroism parameter [HW94] is $\delta = 1/3$ as in a material satisfying Kleinman symmetry [Boy03]. This is equivalent to assuming that there is only one independent element in the tensor $\tilde{\chi}^{(3),\mathrm{TPA}}_{ijkl}(\omega, \omega, -\omega)$ [HW94]. This assumption is also consistent with the experimental results of Dinu et al. [DQG03], also given in Table 5.2, where the bulk TPA coefficient of silicon was measured to be identical (according to the accuracy of measurement) for two different polarizations.

In conclusion, it is consistent with available experimental data to assume that the degenerate TPA tensor $\tilde{\chi}^{(3),\mathrm{TPA}}_{ijkl}(\omega, \omega, -\omega)$ of silicon has only one independent element $\chi_T(\omega)$, in terms of which the full tensor can be expressed in any cartesian coordinate system as [Boy03]

$$\chi^{(3),\mathrm{TPA}}_{ijkl}(\omega, \omega, -\omega) = \frac{1}{3}\chi_T(\omega)(\delta_{ij}\delta_{kl} + \delta_{ik}\delta_{jl} + \delta_{il}\delta_{jk}), \tag{5.19}$$

where δ_{ij} is the Kronecker delta.

Effective area

Eqs. (2.41) and (2.42) describe the longitudinal evolution of the pump and Stokes powers in a general way. The frequency-degenerate TPA contributions are the first two terms on the right-hand sides of those equations. We want to rewrite these as the ratio of a bulk TPA coefficient and an effective area. This is done the same way as in Sects. 2.2.5 and 5.2.2, with the result that the frequency-degenerate TPA contributions to the equations describing the longitudinal evolution of the pump and Stokes powers can be written in the compact form

$$\pm\frac{1}{P_p^{\pm}}\frac{\mathrm{d}P_p^{\pm}}{\mathrm{d}z} = -\frac{\beta_{pp}}{A_{pp}^{(\mathrm{TPA})}}(P_p^{\pm} + 2P_p^{\mp}), \tag{5.20}$$

$$\pm\frac{1}{P_s^{\pm}}\frac{\mathrm{d}P_s^{\pm}}{\mathrm{d}z} = -\frac{\beta_{ss}}{A_{ss}^{(\mathrm{TPA})}}(P_s^{\pm} + 2P_s^{\mp}), \tag{5.21}$$

where β_{pp} and β_{ss} are the linearly-polarized bulk degenerate-TPA coefficients at the pump and Stokes wavelengths, respectively, and the effective areas are given by

$$A_{ii}^{(\mathrm{TPA})} = \frac{4Z_0^2\hat{N}_i^2}{n_i^2}\left[\frac{1}{3}\int_{\mathrm{Si}} 2|\mathbf{e}_i|^4 + |\mathbf{e}_i\cdot\mathbf{e}_i|^2\,\mathrm{d}A\right]^{-1}, \tag{5.22}$$

where $\mathbf{e}_i$ ($i = p,s$) are the pump and Stokes mode fields, and we have assumed the tensor structure of Eq. (5.19). Note that while the effective areas for SRS depend on whether the relevant pump and Stokes waves are co- or counterpropagating, see Eqs. (5.13)–(5.14), there is no such directional dependence for the TPA process.

The thin solid curve in Fig. 5.3 shows the effective area $A_{pp}^{(\mathrm{TPA})}$ as a function of the pump wavelength for the waveguide shown on the right-hand side of Fig. 5.1. The effective area increases towards longer wavelengths, because the mode field becomes less and less confined such that TPA, like all other nonlinearities, becomes less efficient.

The various effective areas for SRS and TPA shown in Fig. 5.3 for the waveguide of Fig. 5.1b are all quite similar, differing only by a few percent at a given pump wavelength. The difference becomes even smaller for rib waveguides with larger dimensions. In several of the later sections discussing properties of specific silicon Raman amplifiers and lasers we will therefore assume that all the effective areas are exactly equal and simply write A_{eff}, which clarifies the discussion and does not influence qualitatively our results. However, the full model must be used in modeling cladding-pumped silicon Raman amplifiers in Sect. 6.4, because there the mode fields of the pump and Stokes modes have significantly different shapes.

5.3.2. Non-degenerate TPA

Similar to the bulk Raman-gain constant, Eq. (5.5), we can define a bulk non-degenerate-TPA constant by

$$\beta(\omega_s, \omega_p, \hat{\mathbf{s}}, \hat{\mathbf{p}}) = \frac{3\omega_s \mu_0}{2 n_s n_p} \operatorname{Im}\left[\tilde{\chi}^{(3),\mathrm{TPA}}_{ijkl}(\omega_s, \omega_p, -\omega_p) \hat{s}^{i*} \hat{s}^j \hat{p}^k \hat{p}^{l*}\right], \tag{5.23}$$

such that when we have co-propagating homogeneous pump and Stokes plane waves with polarization directions $\hat{\mathbf{s}}$ and $\hat{\mathbf{p}}$ in bulk silicon, the Stokes wave will be attenuated according to

$$\frac{\mathrm{d}I_s}{\mathrm{d}z} = -2\beta(\omega_s, \omega_p, \hat{\mathbf{s}}, \hat{\mathbf{p}}) I_p I_s. \tag{5.24}$$

The corresponding attenuation seen by the pump wave can be written

$$\frac{\mathrm{d}I_p}{\mathrm{d}z} = -2\frac{\lambda_s}{\lambda_p}\beta(\omega_s, \omega_p, \hat{\mathbf{s}}, \hat{\mathbf{p}}) I_p I_s, \tag{5.25}$$

where we have made use of the relation

$$\beta(\omega_p, \omega_s, \hat{\mathbf{p}}, \hat{\mathbf{s}}) I_p I_s = \frac{\lambda_s}{\lambda_p}\beta(\omega_s, \omega_p, \hat{\mathbf{s}}, \hat{\mathbf{p}}) I_p I_s, \tag{5.26}$$

which follows when we assume a symmetry relation similar to Eq. (5.15),

$$\tilde{\chi}^{(3),\mathrm{TPA}}_{ijkl}(\omega_p, \omega_s, -\omega_s) = \left[\tilde{\chi}^{(3),\mathrm{TPA}}_{ijkl}(\omega_s, \omega_p, -\omega_p)\right]^*, \tag{5.27}$$

Similar to the case of SRS, the factor λ_s/λ_p in Eq. (5.25) expresses the fact that frequency-degenerate TPA removes photons from the participating pump and Stokes beams in equal amounts, see the discussion following Eqs. (5.13)–(5.14).

Magnitude of the bulk non-degenerate-TPA constant

To the best of the author's knowledge, there are no measurements of non-degenerate TPA coefficients of silicon in the literature, at least not in the wavelength range of interest here ($\lambda > 1.4\,\mu$m) and for large frequency separations $\omega_p - \omega_s$. Theoretical results, too, are extremely scarce on non-degenerate TPA in silicon [Din03], owing to the fact that silicon is an indirect-gap semiconductor (results on direct-gap semiconductors are available in a large number, see references in [Din03]).

It is suggested in [Din03] to approximate the non-degenerate TPA coefficient $\beta(\omega_s, \omega_p)$ of silicon by the degenerate-TPA coefficient $\beta_{\mathrm{deg}}(\omega)$ (see Eq. (5.17)) evaluated at the mean frequency instead, because this approximation gives good results for direct-gap semiconductors. In our modeling, we therefore use

$$\beta(\omega_s, \omega_p) = \sqrt{\frac{\omega_s}{\omega_p}}\,\beta_{\mathrm{deg}}\left(\frac{\omega_p + \omega_s}{2}\right), \qquad \beta(\omega_p, \omega_s) = \sqrt{\frac{\omega_p}{\omega_s}}\,\beta_{\mathrm{deg}}\left(\frac{\omega_p + \omega_s}{2}\right), \tag{5.28}$$

which is consistent with Eq. (5.26).

Form of the nonlinear susceptibility tensor

We have found in Sect. 5.3.1 that the three potentially different independent elements of the tensor describing *degenerate* TPA in silicon may be assumed to be equal. On the other hand, the tensor describing *non-degenerate* TPA, $\tilde{\chi}^{(3),\mathrm{TPA}}_{ijkl}(\omega_s, \omega_p, -\omega_p)$, can in principle have four different independent elements, see Sect. 5.3.1. As there are neither experimental nor theoretical data available on the polarization dependence of non-degenerate TPA in silicon (see preceding subsection), we assume that, similar to the tensor describing degenerate TPA, also the tensor describing non-degenerate TPA has only a single independent element $\chi_T(\omega_s, \omega_p)$, and that we can write any tensor element in the form

$$\chi^{(3),\mathrm{TPA}}_{ijkl}(\omega_S, \omega_p, -\omega_p) = \frac{1}{3}\chi_T(\omega_s, \omega_p)(\delta_{ij}\delta_{kl} + \delta_{ik}\delta_{jl} + \delta_{il}\delta_{jk}), \tag{5.29}$$

similar to Eq. (5.19).

Effective area

Now that the form of the nonlinear susceptibility tensor for non-degenerate TPA is specified, see Eq. (5.29), we can proceed to evaluate the form of the effective areas following the procedure used already in the case of SRS (Sect. 5.2.2) and degenerate TPA (Sect. 5.3.1). The result is that the contribution of non-degenerate TPA to the longitudinal evolution of the pump and Stokes powers can be written

$$\pm\frac{1}{P_p^{\pm}}\frac{\mathrm{d}P_p^{\pm}}{\mathrm{d}z} = -\frac{\lambda_s}{\lambda_p}\frac{\beta_{sp}}{A_{sp}^{(\mathrm{TPA})}}(2P_s^{+} + 2P_s^{-}), \tag{5.30}$$

$$\pm\frac{1}{P_s^{\pm}}\frac{\mathrm{d}P_s^{\pm}}{\mathrm{d}z} = -\frac{\beta_{sp}}{A_{sp}^{(\mathrm{TPA})}}(2P_p^{+} + 2P_p^{-}), \tag{5.31}$$

where

$$A_{sp}^{(\mathrm{TPA})} = \frac{4Z_0^2\hat{N}_s\hat{N}_p}{n_s n_p}\left[\frac{1}{3}\int_{\mathrm{Si}}|\mathbf{e}_s|^2|\mathbf{e}_p|^2 + |\mathbf{e}_s\cdot\mathbf{e}_p|^2 + |\mathbf{e}_s\cdot\mathbf{e}_p^*|^2\,\mathrm{d}A\right]^{-1}, \tag{5.32}$$

and β_{sp} is the linearly co-polarized non-degenerate bulk TPA coefficient "seen" by the Stokes wave.

5.4. Free-Carrier Absorption

Free-Carrier Absorption (FCA) is a consequence of the effect of Two-Photon Absorption (TPA) which we discussed in Sect. 5.3. While TPA itself causes only a modest amount of

attenuation (see Sect. 6.2.2), the TPA-generated electrons and holes accumulate in the core of a silicon waveguide, increase its conductivity and thus lead to Ohmic losses for any optical wave propagating in the waveguide. This so-called Free-Carrier Absorption can become quite strong, and it is currently the main effect limiting the efficiency of Raman amplifiers and lasers in silicon waveguides, see Sect. 6.2.

In this section, we will extend the wave-propagation model of Sect. 2.2 to include the effect of FCA. As the following Chapters will be concerned only with continuous-wave amplifiers and lasers, we restrict all derivations to the stationary case. We proceed as follows: Sect. 5.4.1 first derives an expression for the carrier density caused by TPA in the waveguide, and Sect. 5.4.2 then determines the attenuation of the optical waves caused by the presence of these carriers. Eq. (5.45) is the main result of this section.

5.4.1. Steady-state charge-carrier density

In this section we derive an expression for the steady-state charge-carrier density inside the silicon waveguide. Carriers are generated by TPA, diffuse through the silicon and recombine both inside the silicon and at the interfaces between silicon and the surrounding cladding materials. The steady-state carrier density is determined by an equilibrium between these processes.

As we are dealing only with optically generated charge carriers without any externally applied electric fields, the diffusion process is well described in the ambipolar approximation [McK66, See91], i. e., the excess electron and hole densities are equal at each position due to the Coulomb attraction of electrons and holes, and the joint diffusion of electrons and holes is described by an ambipolar diffusion constant. Furthermore, we assume that the optical powers in the waveguide vary slowly enough along the propagation direction z such that the carrier-generation rate and thus the steady-state carrier density vary with z only on a scale large compared to the carriers' diffusion length. This reduces the carrier-diffusion problem to a locally two-dimensional process taking place only in the transverse cross-sectional plane (x, y) of the waveguide.

The steady-state carrier density $N(x, y)$ obeys the diffusion equation [McK66]

$$D\,\nabla^2 N + G - \frac{N}{\tau_b} = 0, \tag{5.33}$$

where D is the ambipolar diffusion constant, $G(x, y)$ is the local TPA carrier-generation rate, and τ_b is the bulk carrier lifetime. At the interfaces between silicon and the surrounding waveguide materials, N fulfills the boundary conditions

$$D\,\mathbf{n}\cdot\nabla N = -SN, \tag{5.34}$$

where $\mathbf{n}$ is a unit vector normal to the interface and directed outward, and S is the recombination velocity.

In order to solve Eqs. (5.33)–(5.34) for the carrier density $N(x, y)$, we need to know the local carrier generation rate $G(x, y)$. The spatial distribution and the magnitude of the generation rate $G(x, y)$ will depend on the mode-field shapes and powers of the various forward- and backward-propagating waves. A simple general solution for N can be obtained when we assume that the carrier diffusion is so fast that the steady-state carrier density N is constant, $N(x, y) = \bar{N}$, in those regions of silicon where the mode fields are concentrated (this approximation is often justified [DJC+05]).[1] Consequently, the solution of Eqs. (5.33)–(5.34) does not depend on where exactly the carriers are generated in the waveguide cross section, but only how many of them are generated in total. Mathematically,

$$\bar{N} = M \cdot \int G(x, y)\, \mathrm{d}A = M G_{\mathrm{tot}}, \tag{5.35}$$

where G_{tot} is the total number of carriers generated through TPA in the entire cross section of the waveguide per unit time and per unit waveguide length, and M is a constant of proportionality with unit $\mathrm{s/m^2}$ which depends only on the waveguide geometry and the two material parameters, bulk recombination lifetime τ_b and interface recombination velocity S. An approximate analytical expression for M in rib waveguides has been derived in [DJC+05].

An expression for the total carrier generation rate $G_{\mathrm{tot}}(z)$ is obtained by rewriting the differential equations describing TPA, Eqs. (5.20)–(5.21) and (5.30)–(5.31), in terms of the photon fluxes

$$F^{\pm}_{p,s}(z) = \frac{P^{\pm}_{p,s}(z)}{h\nu_{p,s}}, \tag{5.36}$$

which represent the number of photons flowing through the entire waveguide cross section at z per unit time. In terms of these, Eqs. (5.20)–(5.21) and (5.30)–(5.31) read

$$\pm\frac{1}{F^{\pm}_p}\frac{\mathrm{d}F^{\pm}_p}{\mathrm{d}z} = -\frac{\beta_{pp}}{A^{(\mathrm{TPA})}_{pp}}(F^{\pm}_p + 2F^{\mp}_p)h\nu_p - \frac{\beta_{ps}}{A^{(\mathrm{TPA})}_{ps}}(2F^{+}_s + 2F^{-}_s)h\nu_s, \tag{5.37}$$

$$\pm\frac{1}{F^{\pm}_s}\frac{\mathrm{d}F^{\pm}_s}{\mathrm{d}z} = -\frac{\beta_{ss}}{A^{(\mathrm{TPA})}_{ss}}(F^{\pm}_s + 2F^{\mp}_s)h\nu_s - \frac{\beta_{sp}}{A^{(\mathrm{TPA})}_{ps}}(2F^{+}_p + 2F^{-}_p)h\nu_p. \tag{5.38}$$

Consider now a thin slice Δz of the waveguide. Fig. 5.7 illustrates the photon fluxes entering and leaving this slice. By subtracting the outgoing photon flux from the photon

[1] Another case where a simple general solution for N can be given is when carriers are generated only by the waves at a single wavelength. For example, in an unsatured amplifier the Stokes powers are so small that they do not contribute significantly to carrier generation, and the total generation rate is due only to the pump waves.

flux going into that slice, one obtains the number of photons that are absorbed inside that slice per unit time by TPA. For each two absorbed photons, an electron-hole pair is generated, so that the total carrier-generation rate is given by

$$G_{\mathrm{tot}}(z) = \frac{1}{2}\left(\frac{\mathrm{d}F_p^-}{\mathrm{d}z} + \frac{\mathrm{d}F_s^-}{\mathrm{d}z} - \frac{\mathrm{d}F_p^+}{\mathrm{d}z} - \frac{\mathrm{d}F_s^+}{\mathrm{d}z}\right) \tag{5.39}$$

$$= \frac{\beta_{pp}h\nu_p}{2A_{pp}^{(TPA)}}(F_p^{+2} + F_p^{-2} + 4F_p^+F_p^-) + \frac{\beta_{ss}h\nu_s}{2A_{ss}^{(TPA)}}(F_s^{+2} + F_s^{-2} + 4F_s^+F_s^-)$$

$$+ (F_p^+ + F_p^-)(F_s^+ + F_s^-)\left(\frac{\beta_{ps}h\nu_s}{A_{ps}^{(TPA)}} + \frac{\beta_{sp}h\nu_p}{A_{ps}^{(TPA)}}\right) \tag{5.40}$$

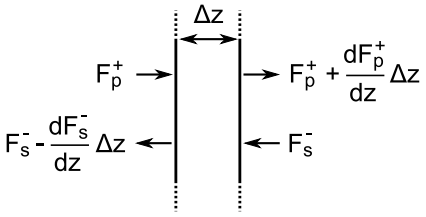

Figure 5.7.: Illustration of the photon fluxes into and out of a slice Δz of the waveguide (analogous contributions of F_s^+ and F_p^- are not shown).

5.4.2. Optical absorption due to free carriers

Now that the steady-state carrier density generated by Two-Photon Absorption is known, see Eq. (5.35), we need to relate it to the loss "seen" by the optical modes.

The dependence of optical losses on the amount of excess charge carriers in silicon has been extensively investigated by Soref et al. in the 1980's [SB86, SB87]. Their results are commonly formulated in a compact form as (see, e. g., p. 289 in [PL04])

$$\Delta\alpha = 8.5 \times 10^{-18}\,\mathrm{cm}^2 \cdot \Delta N_e + 6.0 \times 10^{-18}\,\mathrm{cm}^2 \cdot \Delta N_h, \tag{5.41}$$

where $\Delta N_{e,h}$ are the densities of excess electrons and holes in a silicon sample, and $\Delta\alpha$ is the optical absorption at $1.55\,\mu$m. Refs. [SB86, SB87] are often cited as the source of Eq. (5.41), even though the authors of [SB86, SB87] themselves do not explicitly state this formula. In fact the experimental results in [SB86,SB87] deviate somewhat from the linear relationship given in Eq. (5.41). According to the Drude theory of the absorption due to free carriers, the absorption given in Eq. (5.41) is expected to vary with the square of the wavelength [SB87]. Setting $\Delta N_e = \Delta N_h = N$ (see Sect. 5.4.1), we can thus write Eq. (5.41) as [CRDJ04]

$$\Delta\alpha(\lambda) = \bar{\varphi}\lambda^2 N, \tag{5.42}$$

where we have defined the FCA efficiency as

$$\bar{\varphi} = 6.0 \times 10^{-10}. \tag{5.43}$$

The effect of Free-Carrier Absorption can now be included in the model of Sect. 2.2 by expressing the absorption as the imaginary part of a dielectric constant [Agr01],

$$\Delta\epsilon = i\frac{nc}{\omega}\Delta\alpha, \tag{5.44}$$

and then using this to add the additional perturbing polarization $\mathbf{P}_{\text{FCA}} = \epsilon_0 \Delta\epsilon \bar{\mathbf{E}}$ to the $\mathbf{P}$ in Eq. (2.7). The result is an additional contribution to the equations describing the longitudinal evolution of the pump and Stokes powers,

$$\pm\frac{1}{P_p^{\pm}}\frac{\mathrm{d}P_p^{\pm}}{\mathrm{d}z} = -\eta_p\bar{\varphi}\lambda_p^2\bar{N}, \qquad \pm\frac{1}{P_s^{\pm}}\frac{\mathrm{d}P_s^{\pm}}{\mathrm{d}z} = -\eta_s\bar{\varphi}\lambda_s^2\bar{N}. \tag{5.45}$$

where $\bar{N}$ is the steady-state carrier density given by Eqs. (5.35) and (5.39), and $\eta_{p,s}$ are confinement factors,

$$\eta_{p,s} = \frac{n_{p,s}}{2Z_0\hat{N}_{p,s}}\int_{\text{Si}} |\mathbf{e}_{p,s}|^2 \,\mathrm{d}A. \tag{5.46}$$

5.4.3. The effective carrier lifetime τ_{eff}

In order to complete our model of silicon Raman amplifiers and lasers, we establish in this section a relation between the parameter M defined in Eq. (5.35) and the effective carrier lifetime τ_{eff} that is normally used in the literature to quantify the effect of FCA.

Consider the case where only the forward-propagating pump wave P_p^+ exists and all other powers are zero. From Eqs. (5.20) and (5.45), the longitudinal evolution of the power P_p^+ due to TPA and FCA is then described by the equations

$$\frac{1}{I_p}\frac{\mathrm{d}I_p}{\mathrm{d}z} = -\beta_{pp}I_p - \eta_p\bar{\varphi}\lambda_p^2\bar{N}, \qquad \bar{N} = \frac{M\beta_{pp}A_{pp}^{(\text{TPA})}}{2h\nu_p}I_p^2, \tag{5.47}$$

where $I_p = P_p^+/A_{pp}^{(\text{TPA})}$ is an effective intensity. By defining the effective carrier lifetime as

$$\boxed{\tau_{\text{eff}} = \eta_p A_{pp}^{(\text{TPA})} M,} \tag{5.48}$$

the longitudinal evolution of the effective intensity I inside the waveguide given by Eqs. (5.47) can be rewritten in the form found in simpler models of silicon Raman amplifiers and lasers in the literature [CRDJ04, RLN+04, LRJ+06]

$$\frac{1}{I_p}\frac{\mathrm{d}I_p}{\mathrm{d}z} = -\beta_{pp}I_p - \bar{\varphi}\lambda_p^2 N_{\text{eff}} \quad \text{(a)}, \qquad N_{\text{eff}} = \frac{\tau_{\text{eff}}\beta_{pp}}{2h\nu_p}I_p^2 \quad \text{(b)}. \tag{5.49}$$

Eqs. (5.49) show that the effective carrier lifetime τ_{eff} is "effective" in the sense that a homogeneous plane wave of intensity I_p propagating in bulk silicon with the bulk carrier recombination lifetime of $\tau_b = \tau_{\text{eff}}$ would generate the carrier density N_{eff} given by Eq. (5.49b) and see the total attenuation given by Eq. (5.49a).

Table 5.3 gives an overview over the effective carrier lifetime τ_{eff} of silicon waveguides given in the literature. Typical values are in the order of a few nanoseconds. It has been reported that the effective carrier lifetime τ_{eff} can vary relatively strongly from one waveguide to another waveguide even on the same wafer [LRP+04].

Ref.	τ_{eff} (ns)	Method / Notes
[EDRMO+04]	0.77	strip waveguide; estimated upper bound
[YSC+05]	0.8	strip waveguide; fit to pump transmission
[JRL+05]	1	rib wg + pin; fit to pump transmission & amp gain
[RLJ+05]	1.2	rib waveguide + pin diode; fit to pump transmission
[XAL05]	1.37	strip waveguide; temporal FCA decay after pump off
[LT06]	1.9	He-implanted rib waveguide
[RBJ05]	4	rib waveguide; temporal FCA decay after pump off
[RLN+04]	23	rib waveguide; fit to pump transmission
[RLJ+05]	65	rib waveguide; fit to pump transmission
[RVY04]	150	large strip waveguide

Table 5.3.: Typical values for the effective carrier lifetime τ_{eff} of silicon waveguides from the literature.

5.5. Summary of the model

Combining Eqs. (5.13), (5.14), (5.20), (5.21), (5.30) and (5.31), and including the linear waveguide losses phenomenologically, we obtain the differential equations governing the longitudinal evolution of the powers of forward- (+) and backward-propagating (−) CW pump ("p") and Stokes ("s") waves:

$$\pm\frac{1}{P_p^{\pm}}\frac{\mathrm{d}P_p^{\pm}}{\mathrm{d}z} = -\alpha_p - \frac{\lambda_s}{\lambda_p}g\left(\frac{P_s^{\pm}}{A_{\mathrm{co}}^{(\mathrm{SRS})}} + \frac{P_s^{\mp}}{A_{\mathrm{cntr}}^{(\mathrm{SRS})}}\right) - \beta_{pp}\frac{P_p^{\pm}+2P_p^{\mp}}{A_{pp}^{(\mathrm{TPA})}} - \frac{\lambda_s}{\lambda_p}\beta_{sp}\frac{2P_s^{+}+2P_s^{-}}{A_{sp}^{(\mathrm{TPA})}} - \eta_p\bar{\varphi}\lambda_p^2\bar{N}, \quad (5.50)$$

$$\pm\frac{1}{P_s^{\pm}}\frac{\mathrm{d}P_s^{\pm}}{\mathrm{d}z} = -\alpha_s + g\left(\frac{P_p^{\pm}}{A_{\mathrm{co}}^{(\mathrm{SRS})}} + \frac{P_p^{\mp}}{A_{\mathrm{cntr}}^{(\mathrm{SRS})}}\right) - \beta_{ss}\frac{P_s^{\pm}+2P_s^{\mp}}{A_{ss}^{(\mathrm{TPA})}} - \beta_{sp}\frac{2P_p^{+}+2P_p^{-}}{A_{sp}^{(\mathrm{TPA})}} - \eta_s\bar{\varphi}\lambda_s^2\bar{N}, \quad (5.51)$$

where the five terms on the right-hand sides of Eqs. (5.50)–(5.51) represent, respectively, linear (scattering) losses given by α_p and α_s, SRS, frequency-degenerate TPA, non-degenerate TPA, and FCA. The free-carrier density $\bar{N}$ occurring in Eqs. (5.50) and (5.51) is given by

$$\bar{N} = \frac{M}{2}\left[\frac{\beta_{pp}}{h\nu_p A_{pp}^{(\mathrm{TPA})}}(P_p^{+2}+P_p^{-2}+4P_p^{+}P_p^{-}) + \frac{\beta_{ss}}{h\nu_s A_{ss}^{(\mathrm{TPA})}}(P_s^{+2}+P_s^{-2}+4P_s^{+}P_s^{-}) + \frac{4\beta_{sp}}{h\nu_s A_{sp}^{(\mathrm{TPA})}}(P_p^{+}+P_p^{-})(P_s^{+}+P_s^{-})\right], \quad (5.52)$$

where M is related to the effective carrier lifetime through $M = \tau_{\mathrm{eff}}/(\eta A^{(\mathrm{TPA})})$, where τ_{eff} is the effective lifetime seen by a mode of the waveguide with confinement factor η and TPA effective area $A^{(\mathrm{TPA})}$, see Sect. 5.4.3.

Unless noted otherwise, we will use the following parameters in all simulations in Chapters 6 and 7. The pump and Stokes wavelengths, $\lambda_p = 1427\,\mathrm{nm}$ and $\lambda_s = 1542\,\mathrm{nm}$ as in [CDR+03], respectively, are separated by the silicon Stokes shift of 15.6 THz. We choose a conservative value for the Raman-gain constant of $g = 20\,\mathrm{cm/GW}$ (see Table 5.1). We assume linear losses of $\alpha_p = \alpha_s = 1.0\,\mathrm{dB/cm}$ [JPR06], and an FCA efficiency of $\bar{\varphi} = 6.0 \times 10^{-10}$, see Sect. 5.4.2. In order not to underestimate the effect of TPA, we choose a rather high value for the pump-TPA constant of $\beta_{pp} = 0.7\,\mathrm{cm/GW}$. Following the model discussed in Sect. 5.3, the coefficients for pump-Stokes TPA and Stokes TPA

are $\beta_{sp} = 0.57\,\mathrm{cm/GW}$ and $\beta_{ss} = 0.47\,\mathrm{cm/GW}$. The various effective areas and confinement factors used in our simulations are based on the quasi-TE fundamental mode of the rib-waveguide structure on the right-hand side of Fig. 5.1 and are plotted in Fig. 5.3.

Finally, we note that while many properties of silicon Raman amplifiers and lasers can be understood with less detailed models, the full model as described above will be used to analyze cladding-pumped silicon Raman amplifiers (section 6.4) and cascaded silicon Raman lasers (section 7.4).

5.6. Chapter summary

The general model of nonlinearly coupled wave propagation in waveguides of chapter 2 has been adapted to the special case of silicon waveguides. By incorporating available material data from the literature, compact formulas for the effective areas describing SRS and TPA have been derived. These encapsulate the tensorial structure of the nonlinearities and thus allow for the design and analysis of waveguides optimized with regards to these effects, based on the waveguide mode fields. The effective carrier lifetime describing the influence of FCA has been derived from a carrier-diffusion model. The model developed in this chapter includes co- and counterpropagating waves and is thus suitable for analyzing both Raman amplifiers and lasers in the following two chapters.

6. Analysis and design of silicon Raman amplifiers

This chapter is concerned with the analysis and design of silicon Raman amplifiers (SRAs). Section 6.1 gives a short historical overview of the subject. Fundamental characteristics and limitations of the most basic form of SRAs are discussed in section 6.2. Sections 6.3 and 6.4 introduce the concept of the tapered and the cladding-pumped SRA, respectively, which are shown to be able to deliver more gain than "conventional" SRAs. Finally, section 6.5 analyzes the curvature loss in silicon rib waveguides, which is important as optimal SRAs require rather long waveguide lengths which must be wound up to fit on a silicon chip.

Parts of the results presented in this chapter have been published in [RKB05,KRB06c, RK06, KRB$^+$06b, KRB06a].

6.1. Historical overview

The first observation of spontaneous and stimulated Raman scattering in a silicon waveguide by Claps et al. in 2002 [CDHJ02] and 2003 [CDR$^+$03], respectively, marked the beginning of a worldwide research effort into integrated-optical amplifiers and lasers based on stimulated Raman scattering (SRS) in silicon waveguides.

While Raman amplifiers in glass fibers are several kilometers in length, Raman amplifiers in silicon waveguides can be much shorter, because the Raman gain of crystalline silicon is 10.000 times larger than in silica glass. Furthermore, the core of silicon waveguides can be made much smaller than that of glass fibers — the resulting increased spatial concentration of the optical power will further increase the obtainable gain per unit length. Raman amplifiers based on optical fibers are already well-established in long-haul transmission systems due to their spectral flexibility and low-noise operation. Integrated-optical Raman amplifiers based on silicon, on the other hand, could one day play an important role on the chip scale, where they could compensate for the on-chip losses of an integrated-optical circuit [JPR06].

The fundamental problem in realizing an efficient silicon Raman amplifier or laser is the presence of nonlinear absorption effects that need to be suppressed or mitigated: first, Two-Photon Absorption (TPA) absorbs the pump light and generates free charge carriers. Second, these charge carriers accumulate in the silicon waveguide and lead to substantial optical losses, called Free-Carrier Absorption (FCA).

A significant suppression of FCA has been achieved so far only by two methods: on the one hand, FCA can become insignificant when the waveguide is pumped by pulses only. The maximum pulsed Raman gain demonstrated so far is 20 dB [RBJ05], and the first silicon Raman laser demonstrated in 2004 by Jalali's group at UCLA also operated in a pulsed mode [BJ04]. On the other hand, the TPA-generated carriers can be extracted electrically by means of a transverse p-i-n structure. Using this concept, Intel demonstrated in 2005 a CW silicon Raman amplifier with a net gain of 3 dB [JRL$^+$05], and the first continuous-wave silicon Raman laser [RJL$^+$05]. Recently, it has been suggested to implant helium ions in a silicon waveguide in order to reduce the lifetime of the TPA-generated carriers [LT06].

In the remainder of this thesis, the limitations of existing designs for Raman-based silicon devices will be analyzed and several new designs for more efficient Raman amplifiers and lasers will be proposed and discussed.

6.2. Basic characteristics of silicon Raman amplifiers

In this section, we will discuss the characteristics of the most basic type of continuous-wave silicon Raman amplifier, which has been first experimentally demonstrated in 2003 [CDR$^+$03]. It consists of a straight, longitudinally invariant rib or strip waveguide of length L, see Fig. 6.1. The pump power and the Stokes light to be amplified are injected at one end ($z = 0$), and the amplified Stokes light is measured at the other end of the waveguide.

Sect. 6.2.1 summarizes the model that underlies our analysis. In Sect. 6.2.2, we show that the nonlinear absorption effects TPA and FCA lead to a roll-over in the amplifier characteristics — the amplifier gain can not be increased indefinitely merely by increasing the pump power. Finally, an explicit formula for the maximum possible gain and the required amplifier length and pump power will be derived in Sect. 6.2.3.

6.2.1. Mathematical model

We assume that the amplifier is unsaturated, i. e., the Stokes light to be amplified is so weak that we can neglect the depletion of the pump due to SRS and non-degenerate

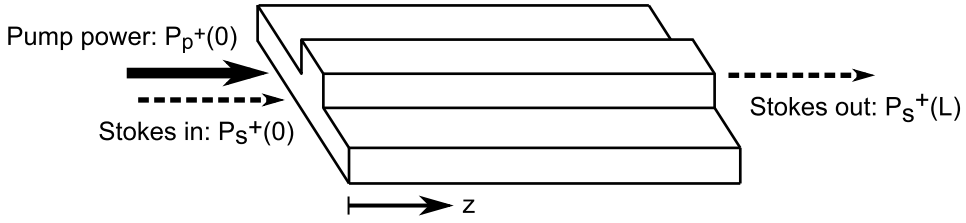

Figure 6.1.: Schematic of a basic silicon Raman amplifier.

TPA with the Stokes wave. This is an assumption often made in the analysis of both fiber-based and silicon-based optical amplifiers [HA05, LRJ+06, CRDJ04], which leads to significant insight into the operation of an amplifier while leaving out the complexities associated with the large-signal regime. Using $S \ll P$ in Eqs. (5.50)–(5.52), we can write the equations describing the longitudinal evolution of the pump and Stokes powers $P(z) = P_p^+(z)$ and $S(z) = P_s^+(z)$ as

$$\frac{1}{P}\frac{\mathrm{d}P}{\mathrm{d}z} = -\alpha_p - \frac{\beta_{pp}}{A_{pp}^{(\mathrm{TPA})}}P - \eta_p\bar{\varphi}\lambda_p^2\bar{N}, \tag{6.1}$$

$$\frac{1}{S}\frac{\mathrm{d}S}{\mathrm{d}z} = -\alpha_s + \left(\frac{g}{A^{(\mathrm{SRS})}} - \frac{2\beta_{sp}}{A_{sp}^{(\mathrm{TPA})}}\right)P - \eta_s\bar{\varphi}\lambda_s^2\bar{N} = \gamma(z), \tag{6.2}$$

where $\gamma(z)$ is the local Stokes gain, and the free-carrier density is given by

$$\bar{N} = M\frac{\beta_{pp}P^2}{2h\nu_p A_{pp}^{(\mathrm{TPA})}}, \qquad M = \frac{\tau_{\mathrm{eff}}}{\eta_p A_{pp}^{(\mathrm{TPA})}}. \tag{6.3}$$

In these equations, $\alpha_{p,s}$ are the linear waveguide losses at the pump and Stokes wavelengths $\lambda_{p,s}$, β_{pp} and β_{sp} are the bulk TPA coefficients for degenerate pump TPA and non-degenerate TPA between the pump and Stokes waves, respectively, g is the bulk Raman-gain coefficient of silicon, and τ_{eff} is the effective carrier lifetime. Finally, the pump and Stokes modes are characterized by the effective areas $A_{pp}^{(\mathrm{TPA})}$ and $A_{sp}^{(\mathrm{TPA})}$ for degenerate pump TPA and non-degenerate pump-Stokes TPA, respectively, by the effective area $A^{(\mathrm{SRS})}$ for co-directional SRS, and by the two confinement factors η_p and η_s.

The two differential equations (6.1)–(6.2) can be solved numerically, where the injected pump power $P(0) = P_0$ and Stokes power $S(0)$ are specified as initial conditions at $z = 0$. The total amplifier gain is obtained from the solution as

$$G = \frac{S(L)}{S(0)} = \exp\left[\int_0^L \gamma(z)\,\mathrm{d}z\right] \quad (\text{usually given as } G|_{\mathrm{dB}} = 10\log_{10}G), \tag{6.4}$$

where L is the amplifier length.

6.2.2. Amplifier characteristics

We base the simulations in this section on the parameters given in Sect. 5.5: linear losses of $\alpha_p = \alpha_s = 1.0\,\mathrm{dB/cm}$, bulk Raman-gain and TPA coefficients of $g = 20\,\mathrm{cm/GW}$ and $\beta_{pp} = 0.7\,\mathrm{cm/GW}$, respectively, pump and Stokes wavelengths of $\lambda_p = 1427\,\mathrm{nm}$ and $\lambda_s = 1542\,\mathrm{nm}$, respectively, and effective areas taken from Fig. 5.3, i. e., for the waveguide shown in Fig. 5.1b. The amplifier has a length of $L = 3\,\mathrm{cm}$.

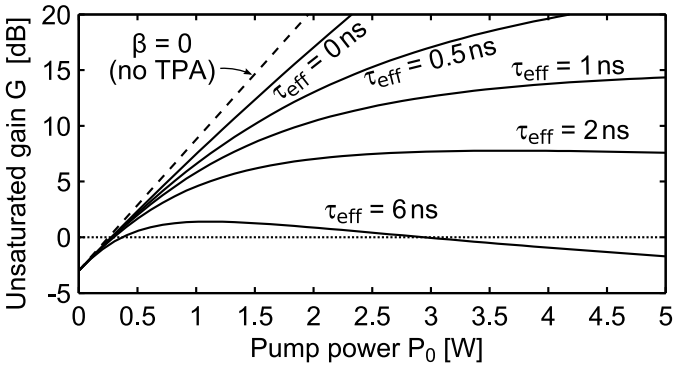

Figure 6.2.: Gain–power characteristics for silicon Raman amplifiers with various effective lifetimes (solid curves). The dashed straight curve shows the case where TPA is absent ($\beta = 0$).

Typical shape of amplifier characteristics

The solid curves in Fig. 6.2 show the amplifier gain G versus pump power P_0 for silicon Raman amplifiers with varying effective carrier lifetimes τ_{eff}, calculated from Eqs. (6.1)–(6.4). It can be observed that for a fixed pump power P_0, the gain G decreases with increasing effective carrier lifetime τ_{eff}. Furthermore, the characteristics for each τ_{eff} exhibit a roll-over point, beyond which a further increase in the pump power decreases the amplifier gain. While these maxima are only clearly visible in Fig. 6.2 for the two curves corresponding to $\tau_{\mathrm{eff}} = 2$ and 6 ns, the other curves with $\tau_{\mathrm{eff}} > 0$ also have maxima which lie beyond the plotting range, however. Fig. 6.2 also shows that the maximal possible gain decreases for increasing effective lifetime τ_{eff}. The overall behavior of silicon Raman amplifiers shown in Fig. 6.2 has been predicted theoretically in 2004 [CRDJ04] and demonstrated experimentally in 2005 [JRL+05].

We now proceed to show why every amplifier in which FCA is present ($\tau_{\mathrm{eff}} > 0$) has a maximum in its gain–power characteristics.

Three regimes for the local Stokes gain

Consider first the *local* Stokes gain $\gamma(z)$ defined in Eq. (6.2). It is an equation quadratic in the local pump power $P(z)$, and there are three regimes. If the local pump power is very low, the linear losses $-\alpha_s$ dominate. On the other hand, if the local pump power is very high the negative quadratic term due to FCA dominates. Between these two regimes, there exists a maximum local Stokes gain

$$\gamma_{\max} = -\alpha_s + \left(g \frac{A_{pp}^{(\mathrm{TPA})}}{A^{(\mathrm{SRS})}} - 2\beta_{sp} \frac{A_{pp}^{(\mathrm{TPA})}}{A_{sp}^{(TPA)}} \right)^2 \frac{\eta_p}{\eta_s} \frac{h\nu_p}{2\bar{\varphi}\lambda_s^2 \tau_{\mathrm{eff}} \beta_{pp}} \tag{6.5}$$

that is obtained only at the local pump power

$$P|_{\gamma=\gamma_{\max}} = \left(g \frac{A_{pp}^{(\mathrm{TPA})}}{A^{(\mathrm{SRS})}} - 2\beta_{sp} \frac{A_{pp}^{(\mathrm{TPA})}}{A_{sp}^{(TPA)}} \right) \frac{\eta_p}{\eta_s} \frac{h\nu_p}{\bar{\varphi}\lambda_s^2 \tau_{\mathrm{eff}} \beta_{pp}} A_{pp}^{(\mathrm{TPA})}. \tag{6.6}$$

Note that the maximum local Stokes gain given by Eq. (6.5) must be positive if one wants to realize an amplifier,

$$\gamma_{\max} > 0. \tag{6.7}$$

If the material parameters are such that condition (6.7) is not fulfilled, the local Stokes gain will never exceed zero no matter how much pump power is applied, and it is impossible to realize an amplifier with the given waveguide technology.

The solid curve in Fig. 6.3 shows schematically how the local pump power $P(z)$ decays along the waveguide in a silicon Raman amplifier. The longitudinal evolution of the local pump power is governed by Eq. (6.1), where all the contributions on the right-hand side have a negative sign, resulting in an attenuation of the pump power. The local pump power $P(z)$ is thus a monotonously decreasing function of z.

The dashed curve in Fig. 6.3 shows the longitudinal evolution of the corresponding local Stokes gain $\gamma(z)$, which is directly related to the local pump power by Eq. (6.2).

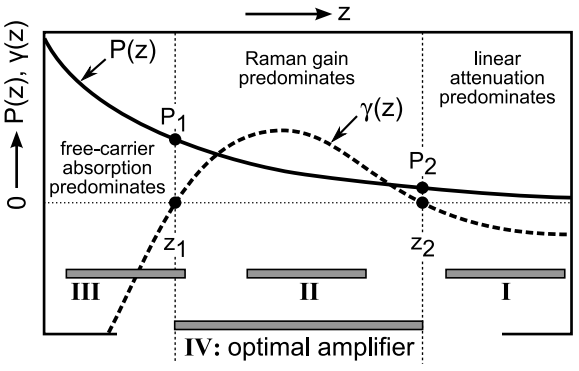

Figure 6.3.: Schematic distribution of the pump power $P(z)$ (solid) and local gain $\gamma(z)$ (dashed) along the waveguide in a silicon Raman amplifier. The shape of the two curves depends only on the material parameters. The optimal amplifier (IV) experiences only positive local gain and thus extends from z_1 to z_2.

As the pump power $P(z)$ is monotonously decreasing along z, the local Stokes gain $\gamma(z)$ passes sequentially through the three regimes discussed at the beginning of this subsection — on the left-hand side of Fig. 6.3, the pump power is so large that the local Stokes gain is negative due to the dominant quadratic FCA term in Eq. (6.2). In the middle of Fig. 6.3, the pump power is moderate and Raman gain dominates, while on the right-hand side, the pump power is so low that only the linear losses $-\alpha_s$ remain.

Now that the qualitative shape of the local-Stokes-gain distribution is known, we can discuss the behavior of the total gain G of the amplifier, which is the integral over the local Stokes gain along the waveguide, see Eq. (6.4).

Roll-over of amplifier characteristics

To understand why any silicon Raman amplifier has a gain maximum, consider the longitudinal distribution of the local pump power and Stokes gain in Fig. 6.3. When the pump power of the amplifier is changed, the solid and dashed curves in Fig. 6.3 simply shift to the left or right without changing their shapes. This is because the pump-power evolution is described by a first-order differential equation with constant coefficients, see Eq. (6.1), the solution of which depends only on the initial value at a given z. In other words, any given amplifier "sees" a certain region of the dashed local-Stokes-gain curve in Fig. 6.3, depending on its pump power and length, while the shape of the curve is fixed and depends only on the material parameters.

For example, a given amplifier at a comparatively low pump power may see the local-Stokes-gain region marked "I" in Fig. 6.3 — the resulting total amplifier gain is the integral of the dashed curve over that region, which is negative due to the dominance of linear losses. The same amplifier at a slightly higher pump power may see the region marked "II" in Fig. 6.3, where the total gain is now positive. At even higher pump powers, the amplifier may see the region marked "III" in Fig. 6.3, where the total gain is now again negative due to the dominance of FCA. It is clear that for even higher pump powers, the total gain must decrease further. Thus, every amplifier of a fixed length L has a pump power at which the total amplifier gain is maximal, and beyond which the gain must decrease with increasing pump power.

6.2.3. Maximum possible gain

The dashed curve in Fig. 6.3 shows schematically how the local Stokes gain $\gamma(z)$ is distributed inside a silicon Raman amplifier. As the total amplifier gain is the integral over the dashed curve in Fig. 6.3, the maximum possible total gain is obtained when the

Stokes light "sees" exactly the positive region of the dashed curve between the points marked z_1 and z_2 in Fig. 6.3. Thus, the optimal waveguide length is $L_{\text{opt}} = z_2 - z_1$ and the optimal pump power is $P_{\text{opt}} = P_1$, where P_1 is the local pump power at z_1, see Fig. 6.3. We have derived explicit expressions for the optimal length L_{opt}, the optimal pump power P_{opt} and the resulting maximum possible gain $G_{\max}$ in terms of the material parameters, see Eqs. (6.13), (6.16) and (6.20); they have been published in [RK06].

Derivation

We start by rewriting the amplifier model Eqs. (6.1)–(6.3) in the form

$$\frac{1}{P}\frac{\mathrm{d}P}{\mathrm{d}z} = \frac{1}{H}\frac{\mathrm{d}H}{\mathrm{d}z} = -\alpha - B_p H - CH^2, \tag{6.8}$$

$$\frac{1}{S}\frac{\mathrm{d}S}{\mathrm{d}z} = -\alpha + B_s H - CH^2 = \gamma(z), \tag{6.9}$$

where we have defined the effective local pump intensity

$$H = \frac{P}{A_{\text{eff}}}, \tag{6.10}$$

furthermore $B_p = \beta_{pp}$, $B_s = g - 2\beta_{sp}$, and

$$C = \frac{\bar{\varphi}\lambda^2 \tau_{\text{eff}} \beta_{sp}}{2h\nu}. \tag{6.11}$$

In writing Eqs. (6.8)–(6.11), we have assumed that the linear losses for the pump and Stokes waves are equal, $\alpha_s = \alpha_p = \alpha$, and we have also neglected the difference in the pump and Stokes wavelengths and have simply set $\lambda_s = \lambda_p = \lambda$. Finally, we have assumed that all three effective areas occuring in the full model (6.1)–(6.3) are equal to A_{eff} and the confinement factors are unity, see the discussion in Sect. 5.3.1. These approximations often have an error of a few percent only and have the advantage of leading to particularly simple results. Explicit expressions for the general case can be written down, too, but they are lengthy, and the principal behavior remains the same [Ren].

We are interested in the region between z_1 and z_2, where the local Stokes gain is positive, see Fig. 6.3. Solving the quadratic equation $\gamma(H) = 0$, where γ is defined in Eq. (6.9), one finds that the local Stokes gain is positive for local pump intensities between H_1 and H_2, where

$$H_1 = H(z_1) = \frac{B_s + W_s}{2C}, \quad H_2 = H(z_2) = \frac{B_s - W_s}{2C}, \quad W_s = \sqrt{B_s^2 - 4\alpha C}. \tag{6.12}$$

If $\alpha C > B_s^2/4$, W_s is imaginary and the local Stokes gain is never positive, no matter what the local pump power is. In that case, no amplifier can be realized with the given waveguide technology. In the following we assume that $\alpha C \leq B_s^2/4$.

From Eq. (6.12) we immediately get the optimal input pump power required to achieve the maximal possible gain, namely (see Fig. 6.3)

$$P_{\text{opt}} = H_1 A_{\text{eff}} = \frac{B_s + W_s}{2C} A_{\text{eff}}. \tag{6.13}$$

The optimal length of the waveguide extends from z_1 to z_2, see Fig. 6.3:

$$L_{\text{opt}} = z_2 - z_1 = \int_{z_1}^{z_2} \mathrm{d}z. \tag{6.14}$$

The integral in Eq. (6.14) can not be solved directly, because we do not know z_2, which is the location where the pump power has decayed from its initial value H_1 to the desired value H_2; the decay of the pump power is governed by Eq. (6.8), which has no simple explicit solution. However, we can substitute $H(z)$ for z as the integration variable in Eq. (6.14). Then, using Eq. (6.8), one obtains

$$L_{\text{opt}} = \int_{H_1}^{H_2} \frac{1}{H(-\alpha - B_p H - CH^2)} \,\mathrm{d}H. \tag{6.15}$$

This integral can be solved in closed form as

$$L_{\text{opt}} = \frac{1}{2\alpha} \ln \left[\left(\frac{B_s + W_s}{B_s - W_s} \right) \left(\frac{4\alpha C + B_s B_p - W_s W_p}{4\alpha C + B_s B_p + W_s W_p} \right)^{B_p/W_p} \right], \tag{6.16}$$

where

$$W_p = \sqrt{B_p^2 - 4\alpha C}. \tag{6.17}$$

When the waveguide has the optimal length L_{opt} given by Eq. (6.16) and is pumped with the optimal pump power P_{opt} given by Eq. (6.13), we obtain the maximum possible gain,

$$G_{\max} = \exp \left[\int_{z_1}^{z_2} \gamma(z) \,\mathrm{d}z \right]. \tag{6.18}$$

Again, this integral can not be solved directly, because the longitudinal evolution of the pump intensity $H(z)$ is not known. However, substituting $H(z)$ for z as the integration variable in Eq. (6.18) and inserting Eqs. (6.8) and (6.9), we obtain

$$G_{\max} = \exp \left[\int_{H_1}^{H_2} \frac{-\alpha + B_s H - CH^2}{H(-\alpha - B_p H - CH^2)} \,\mathrm{d}H \right]. \tag{6.19}$$

This integral can now be evaluated explicitly, giving the maximum possible total gain

$$G_{\max} = \left(\frac{B_s - W_s}{B_s + W_s} \right) \left(\frac{4\alpha C + B_s B_p + W_s W_p}{4\alpha C + B_s B_p - W_s W_p} \right)^{(B_s + B_p)/W_p}. \tag{6.20}$$

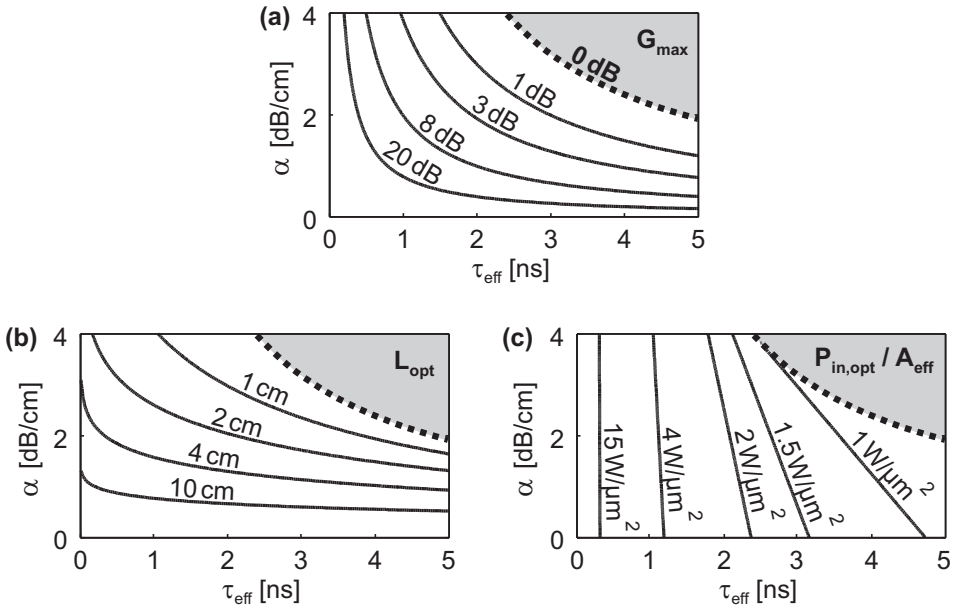

Figure 6.4.: (a) Maximal gain $G_{\max}$, (b) optimal length L_{opt} and (c) required input pump intensity $P_{\text{in,opt}}/A_{\text{eff}}$ for an optimal non-tapered Raman amplifier versus linear waveguide losses α and effective carrier lifetime τ_{eff}. Remaining parameters: $g = 20\,\text{cm/GW}$, $\beta = 0.7\,\text{cm/GW}$, $\lambda = 1550\,\text{nm}$, $\bar{\varphi} = 6 \times 10^{-10}$.

Discussion

The maximum possible gain of a silicon Raman amplifier, see Eq. (6.20), depends only on B_s, B_p and the product αC, where C is proportional to the effective carrier lifetime τ_{eff}. Both the effective carrier lifetime and the linear waveguide losses α depend strongly on how a waveguide is manufactured (see Table 5.3), whereas the remaining parameters contributing to B_s, B_p and C are material properties of bulk crystalline silicon, which are less accessible to deliberate modification. It is therefore interesting to consider the performance of silicon Raman amplifiers as a function of α and τ_{eff}.

Fig. 6.4a shows the maximum possible gain $G_{\max}$ as a function of the linear losses α and the effective carrier lifetime τ_{eff}. According to Eq. (6.20), the maximum possible gain depends only on the product of the two, $\alpha\tau_{\text{eff}}$, so that the curves of constant maximum possible gain in Fig. 6.4a are hyperbola. For $\alpha\tau_{\text{eff}} \sim \alpha C > B_s^2/4$, no amplifier can be realized, which is indicated as the shaded-gray area in Fig. 6.4a.

The fact that the maximum possible gain is determined only by the product $\alpha\tau_{\text{eff}}$ is relevant for deciding by which technological steps the performance of a silicon Raman amplifier is to be improved. Our result shows that the maximum possible gain can be increased equally well by decreasing the linear losses α (for example by waveguide-sidewall smoothing to reduce surface scattering [SSK05]), or by decreasing the effective

carrier lifetime τ_{eff} by the same factor (for example, by using a p-i-n structure [RJL+05], or by Helium implantation [LT06]). On the one hand, when decreasing the linear losses α, the maximum possible gain increases because the pump power can penetrate deeper into the waveguide before it gets so low that the linear losses dominate the Raman gain. The overall amplifier may thus be longer, and the total gain higher, see Fig. 6.4b. On the other hand, when decreasing the effective lifetime τ_{eff}, higher pump powers can be tolerated before FCA becomes significant, thus the Raman gain is more dominant which also increases the maximum possible total gain, see Fig. 6.4c.

Finally, the effective area A_{eff} has no influence on the maximum possible gain or the optimal length. It only scales the pump power necessary to achieve the maximum possible gain, see Eq. (6.13).

6.3. Tapered Raman amplifiers

In this section we introduce the concept of the tapered silicon Raman amplifier. While in the conventional amplifiers discussed in Sect. 6.2 the waveguide characteristics are invariant along the propagation direction, in a tapered amplifier they are allowed to vary, for example through a variation of the geometry of the waveguide. It will be shown that tapered Raman amplifiers can provide significantly more gain than conventional amplifiers.

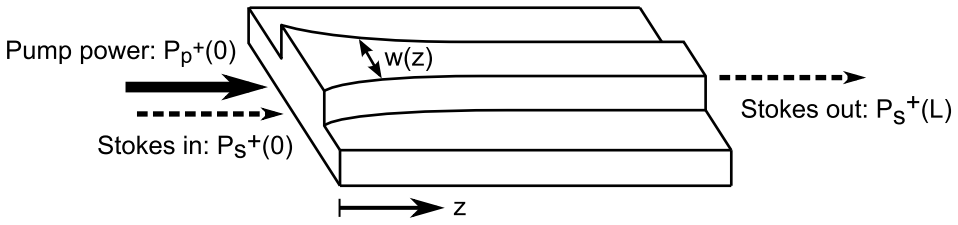

Figure 6.5.: Schematic of a tapered silicon Raman amplifier. The waveguide width w varies along the propagation direction z.

6.3.1. Principle

Model and geometry

Fig. 6.5 shows a schematic of a tapered silicon Raman amplifier as considered here. The pump power P_0 and the Stokes signal to be amplified are injected at the left-hand side of the waveguide at $z = 0$. As in the previous sections of this chapter, we consider amplifiers in the unsaturated regime, i. e., the Stokes powers are much smaller than pump powers,

$S \ll P$, such that the depletion of the pump wave due to SRS and non-degenerate TPA can be neglected. For an adiabatic taper $A_{\text{eff}}(z)$, the longitudinal evolution of the pump and Stokes powers is then governed by the equations

$$\frac{1}{P}\frac{\mathrm{d}P}{\mathrm{d}z} = -\alpha_p - \frac{\beta_{pp}}{A_{\text{eff}}}P - \bar{\varphi}\lambda_p^2 N_{\text{eff}}, \tag{6.21}$$

$$\frac{1}{S}\frac{\mathrm{d}S}{\mathrm{d}z} = -\alpha_s + \frac{g - 2\beta_{sp}}{A_{\text{eff}}}P - \bar{\varphi}\lambda_s^2 N_{\text{eff}} \quad =: \gamma(z), \tag{6.22}$$

$$N_{\text{eff}}(z) = \frac{\tau_{\text{eff}}\beta_{pp}}{2h\nu_p A_{\text{eff}}^2}P^2. \tag{6.23}$$

In writing Eqs. (6.21)–(6.22), we have neglected the difference between the effective areas for SRS and TPA, writing simply A_{eff} instead, and we have assumed that the confinement factors η_p and η_s for the pump and Stokes modes, respectively, are equal. This approximation is often made in the literature [CRDJ04, LRJ+06] and clarifies the following discussion while having an error of a few percent only for many waveguides, see, e. g., Fig. 5.3. The total amplifier gain is defined as

$$G = \frac{S(L)}{S(0)} = \exp\left[\int_0^L \gamma(z)\,\mathrm{d}z\right], \tag{6.24}$$

where L is the amplifier length.

The idea behind tapering

As discussed in Sect. 6.2.2, the local Stokes gain,

$$\gamma(z) = -\alpha_s + \frac{g - 2\beta_{sp}}{A_{\text{eff}}}P - \frac{\bar{\varphi}\lambda_s^2\tau_{\text{eff}}\beta_{pp}}{2h\nu_p A_{\text{eff}}^2}P^2, \tag{6.25}$$

can not be made arbitrary large merely by increasing the pump power P. Due to FCA (described by the third, quadratic term in Eq. (6.25)), there is an optimal local pump power P that maximizes the local Stokes gain. In a conventional non-tapered, longitudinally invariant waveguide, the maximum local Stokes gain is only obtained at a single waveguide position z_0, because the pump power P decays along z, see Fig. 6.3. Before and after z_0, the local Stokes gain will invariably be lower.

On the other hand, if the local Stokes gain could somehow be kept at a high level along the entire length of the amplifier, the total amplifier gain would evidently be increased; the right-hand side of Eq. (6.25) should be as large as possible at each position z inside the amplifier in order to make the total Stokes gain large. It can be seen that the FCA term in Eq. (6.25) dominates over the Raman-gain term at positions z inside the waveguide where the local pump power $P(z)$ is large, because the FCA term depends

on the square of the pump power. However, the FCA term also inversely depends upon the square of the effective area A_{eff}, whereas the Raman-gain term depends inversely upon A_{eff} only in the first power. Consequently, by changing the value of A_{eff}, we can shift the relative weighting between the Raman-gain and FCA-loss terms; if FCA is too large because of large pump powers, we should increase A_{eff}. This would result in an undesired reduction of the Raman gain according to $1/A_{\text{eff}}$ but simultaneously in a much stronger reduction of the FCA-loss term according to $1/A_{\text{eff}}^2$.

Consequently, if we allow the effective area to vary longitudinally, we should choose $A_{\text{eff}}(z)$ such that the right-hand side of Eq. (6.25) is maximal at each waveguide position z, according to the local pump power $P(z)$. Of course, the local-pump-power distribution $P(z)$ itself is also influenced by varying the effective-area distribution $A_{\text{eff}}(z)$, see Eq. (6.21). In general, the amplifier length L, the pump power P_0 and the effective-area taper $A_{\text{eff}}(z)$ have to be optimized such that total gain G, obtained from the solution of Eqs. (6.21)–(6.24), is maximal.

The effective-area taper $A_{\text{eff}}(z)$ can be realized, e. g., by varying the width $w(z)$ of the waveguide along the propagation direction, as suggested in Fig. 6.5. Of course, varying the waveguide width will also influence other waveguide parameters such as the linear losses $\alpha_{p,s}$ and the effective carrier lifetime τ_{eff}. In order to illustrate the basic principle of tapering, however, we will assume in the following that only the effective area $A_{\text{eff}}(z)$ varies along z, and other parameters remain fixed.

The typical shape for a taper is a decrease of A_{eff} toward regions of lower pump power: the latter is injected at the left-hand side ($z = 0$) and decreases towards the right-hand side because it loses power by TPA and FCA, see Eq. (6.21). Therefore, the optimal effective area typically will be larger at the pumped end of the waveguide and smaller at the opposite end. Before giving the optimal effective-area taper explicitly in Sect. 6.3.2, we will first illustrate the principle by means of a few examples.

Illustration of the effect of various tapers

The solid curve in Fig. 6.6b shows the gain as a function of the pump power for the optimal non-tapered amplifier, where we have chosen an effective area of $A_{\text{eff}} = 1.6\,\mu\text{m}^2$, which is shown as the solid curve in Fig. 6.6a. The choice of the effective area does not affect the maximum possible gain of a non-tapered amplifier but only scales the pump power necessary to achieve it, see Sect. 6.2.3. In this case, the maximal gain of 6 dB is obtained at a pump power of 2.5 W, and the entire amplifier is 4.7 cm long.

We now take the optimal non-tapered amplifier (solid curves) and arbitrarily increase the effective area at the beginning of the waveguide to twice its previous value, and the

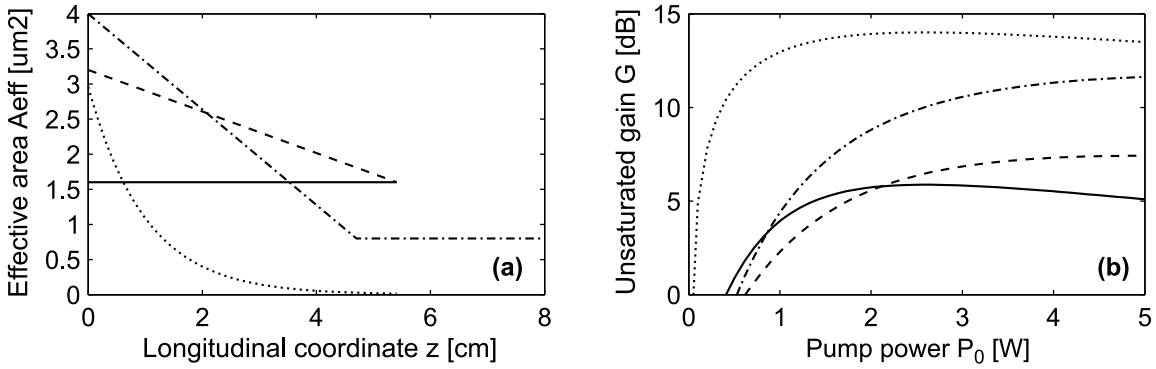

Figure 6.6.: Comparison of the effect of several different tapers on the amplifier characteristics. The left-hand figure shows four effective-area taper shapes, and the right-hand figure shows the corresponding amplifier gain as a function of the pump power. The solid curves correspond to the optimal non-tapered amplifier.

effective area is assumed to decay linearly to its original value at the end of the waveguide, see the dashed curve in Fig. 6.6a. The corresponding characteristics are shown as the dashed curve in Fig. 6.6b. The tapered amplifier can deliver more gain than the optimal non-tapered amplifier: it achieves a slightly higher gain of 7.2 dB at a pump power of 5 W. By making the effective area larger at the beginning of the waveguide, we have reduced FCA stronger than Raman gain, and the amplifier can tolerate more pump power and deliver more gain than the best non-tapered amplifier.

Finally, the dashed-dotted curves in Fig. 6.6 illustrate the case of another arbitrarily chosen taper. This time we have also increased the overall length of the amplifier. While such a length increase can only have a detrimental effect for a non-tapered amplifier (the optimal length of which was 4.7 cm), the tapered amplifier of length 8 cm achieves twice as much gain as the optimal non-tapered one.

6.3.2. Optimal effective-area taper and maximum possible gain

Suppose the length L of a silicon Raman amplifier is fixed, and the effective area $A_{\text{eff}}(z)$ is allowed to vary freely along z, while all other waveguide parameters are z-invariant. We have shown that then there is a maximum possible gain that can be achieved only when the effective-area taper $A_{\text{eff}}(z)$ has an exponential shape along z [RKB05].

To see this, we first define an effective local pump intensity,

$$H(z) = \frac{P(z)}{A_{\text{eff}}(z)}, \tag{6.26}$$

in terms of which Eqs. (6.21)–(6.23) can be written

$$\frac{1}{A_{\text{eff}}}\frac{\mathrm{d}A_{\text{eff}}}{\mathrm{d}z} + \frac{1}{H}\frac{\mathrm{d}H}{\mathrm{d}z} = -\alpha_p - B_p H(z) - C_p H^2(z), \tag{6.27}$$

$$\frac{1}{S}\frac{\mathrm{d}S}{\mathrm{d}z} = -\alpha_s + B_s H(z) - C_s H^2(z) = \gamma(z), \tag{6.28}$$

where $B_p = \beta_{pp}$, $B_s = g - 2\beta_{sp}$ and $C_{p,s} = \bar{\varphi}\lambda_{p,s}^2 \tau_{\text{eff}}\beta_{pp}/(2h\nu_p)$. The maximal gain G of the amplifier is obtained when the local Stokes gain $\gamma(z)$ attains its maximum possible value at each position z, see Eq. (6.24). As the local Stokes gain, Eq. (6.28), depends only on $H(z)$ (while α_s, B_s and C_s are fixed material parameters), the maximal local Stokes gain is obtained when $\mathrm{d}\gamma/\mathrm{d}H = B_s - 2C_s H = 0$. The optimal amplifier must therefore be designed such that the effective local pump intensity has the value

$$H(z) = H_{\text{opt}} = \frac{B_s}{2C_s} = \text{const} \tag{6.29}$$

along the entire waveguide. Then, the local Stokes gain is also constant along the waveguide,

$$\gamma(z) = \gamma_{\max} = -\alpha_s + \frac{B_s^2}{4C_s} = \text{const}. \tag{6.30}$$

Inserting Eq. (6.29) in Eq. (6.27), we obtain a differential equation describing the optimal shape of the effective-area taper,

$$\frac{1}{A_{\text{eff}}}\frac{\mathrm{d}A_{\text{eff}}}{\mathrm{d}z} = -\alpha_p - B_p H_{\text{opt}} - C_p H_{\text{opt}}^2. \tag{6.31}$$

Solving Eq. (6.31), we get the desired optimal effective-area taper,

$$A_{\text{eff}}(z) = A_{\text{eff}}(0)e^{-Kz}, \tag{6.32}$$

which has an exponential shape with the decay constant

$$K = \alpha_p + \frac{B_p B_s}{2C_s} + C_p\left(\frac{B_s}{2C_s}\right)^2. \tag{6.33}$$

The maximum possible total gain of the optimally tapered amplifier is obtained from Eqs. (6.24) and (6.30) as

$$G_{\max}(L) = e^{\gamma_{\max}L} = \exp\left\{\left(\frac{B_s^2}{4C_s} - \alpha_s\right)L\right\} = \exp\left\{\left[\frac{h\nu_p(g-2\beta_{sp})^2}{2\bar{\varphi}\lambda_s^2\tau_{\text{eff}}\beta_{pp}} - \alpha_s\right]L\right\}. \tag{6.34}$$

Eq. (6.34) shows that an amplifier with positive gain can only be realized as long as the material parameters satisfy the condition

$$\alpha_s C_s < \frac{B_s^2}{4}. \tag{6.35}$$

This is the same condition that must be fulfilled for conventional non-tapered amplifiers, see Eq (6.7). Thus, if the material parameters are such that it is impossible to realize a non-tapered amplifier with positive gain, it is also impossible to realize a tapered amplifier. If, however, condition (6.35) is fulfilled, then the advantage of the tapered amplifier is that its total gain can be made arbitrarily large simply by increasing its length L, see Eq. (6.34), whereas for non-tapered amplifiers, there is an upper limit to the achievable gain, which is obtained only for the optimal length given by (6.16).

The pump power required to achieve the maximum gain (6.34) of the optimally tapered amplifier is obtained from Eqs. (6.29) and (6.26) as

$$P_{\mathrm{opt}} = P(0) = H(0)A_{\mathrm{eff}}(0) = H_{\mathrm{opt}}A_{\mathrm{eff}}(0). \tag{6.36}$$

Depending on the amount of available pump power, the effective area at the beginning of the waveguide should be chosen according to Eq. (6.36). On the other hand, for a given effective area at the beginning of the waveguide, Eq. (6.36) gives the pump power at which the amplifier delivers its maximal gain given by Eq. (6.34). The effective-area distribution inside the amplifier is given in either case by Eq. (6.32).

The dotted curves in Figs. 6.6a and 6.6b show the longitudinal effective-area distribution and the amplifier characteristics for an optimally tapered silicon Raman amplifier. Its length is that of the optimal non-tapered one, $L = 4.7\,\mathrm{cm}$, and the effective area at the beginning of the waveguide, $A_{\mathrm{eff}}(0)$, has been chosen such that the tapered amplifier delivers its maximum gain at the same pump power as the optimal non-tapered one. Fig. 6.6 shows that by using the optimal taper instead of a longitudinally invariant effective area, the gain of the amplifier has increased from 6 dB to 14 dB.

In practice, the value down to which the effective area can be tapered is limited, such that the optimal taper derived in this section may not always be realizable. A taper that is optimal given the technological constraints for realizable effective areas would then have to be found through numerical optimization, see also Sect. 7.3. Finally, we have assumed in this section that the effective area can be changed independently from other waveguide characteristics. If, e. g., the effective carrier lifetime and the linear losses varied significantly with a change of the effective area, the optimal taper shape would differ from the exponential one derived here.

6.4. Cladding-pumped Raman amplifiers

In this section, we show that the maximum achievable total gain of silicon Raman amplifiers can be significantly increased by injecting the pump power into a surrounding cladding instead of directly into the silicon core.

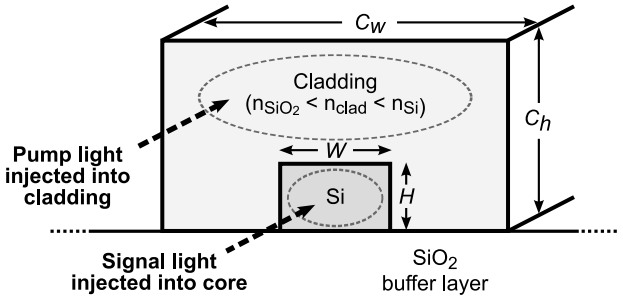

Figure 6.7.: Waveguide cross section for a cladding-pumped Raman amplifier. Pump power is injected into the upper cladding instead of directly into the silicon core.

The results of this section have been developed in collaboration with Jalali's group at the University of California in Los Angeles and have been published in [KRB+06b].

6.4.1. Geometry and principle

Fig. 6.7 shows a schematic view of the waveguide structure for a cladding-pumped silicon Raman amplifier. The proposed structure consists of a rectangular silicon waveguide core on top of a silica buffer layer. It is covered by a cladding whose refractive index lies between that of silica and silicon, i. e., $n_{\mathrm{SiO_2}} < n_{\mathrm{clad}} < n_{\mathrm{Si}}$. The signal light to be amplified at the Stokes wavelength is guided in the fundamental mode of the entire structure, which is highly confined to the silicon core. The pump light, however, is injected in a higher-order mode, the power of which is mainly guided in the cladding. Fig. 6.8 shows the mode-intensity profiles for a possible choice of the pump and Stokes modes.

The advantage of this arrangement is easily illustrated. A small part of the pump mode that extends into the silicon core amplifies the Stokes mode through SRS. It also generates free carriers through TPA, as in a simple core-pumped amplifier. The resulting FCA will affect both the Stokes and the pump mode. However, the pump mode is much less affected, because it is concentrated outside of the silicon and thus overlaps only slightly with the free carriers. If the cladding is large enough, the pump power can propagate without being significantly attenuated by FCA—the main effect limiting the efficiency of core-pumped amplifiers has thus been reduced.

Modeling

We numerically model the longitudinal propagation of the pump and Stokes powers along the waveguide shown in Fig. 6.7 using the model summarized in Sect. 5.5. We assume an undepleted amplifier, i. e., small Stokes powers.

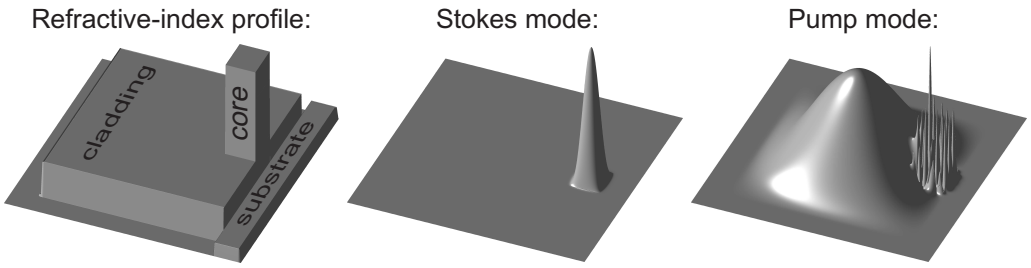

Figure 6.8.: A possible choice of the pump and Stokes modes for the cladding-pumped amplifier structure shown in Fig. 6.7. Shown is the refractive-index profile for comparison, and the mode-intensity profiles. The pump mode has a spiky structure inside the silicon core, because the latter is relatively large in this example ($2 \times 1.5\,\mu\mathrm{m}^2$) and the pump mode is thus a mode of the entire structure of very high order.

6.4.2. Results

We have analyzed different waveguides of the type shown in Fig. 6.7. For the Stokes mode, we have used the fundamental predominantly horizontally polarized mode of the structure. For the pump mode, we have used that mode of the structure which is predominantly horizontally polarized in the cladding and which has the largest effective index just below the cladding refractive index n_{clad}, i.e., the lowest-order cladding mode. That mode typically has a single large lobe inside the cladding and various small lobes inside the silicon and will be easy to excite practically, see Fig. 6.8. The modes were calculated using the full-vectorial mode solver described in the appendix.

We assume in the simulations that the linear pump and Stokes losses are $\alpha_p = 0.1\,\mathrm{dB/cm}$ and $\alpha_s = 1.0\,\mathrm{dB/cm}$, respectively. We choose a cladding index of $n_{\mathrm{clad}} = 2.0$, corresponding to, e. g., silicon oxynitride [BGO03], which can be integrated relatively easily with the processing of the rest of the structure.

Fig. 6.9a shows the behavior of the amplifier with cladding width and height of $C_w = C_h = 9\,\mu\mathrm{m}$, a silicon core width and height of $W = 2\,\mu\mathrm{m}$ and $H = 1.5\,\mu\mathrm{m}$, respectively, and an effective free-carrier lifetime of $\tau_{\mathrm{eff}} = 1\,\mathrm{ns}$. The gain for the signal light at 15.6 THz Raman shift is plotted versus pump wavelength in the lower part of Fig. 6.9 for pump powers of 5, 10 and 15 W. The highest gain for the signal light is reached when the pump wavelength is chosen around 1409 nm.

By modifying the waveguide geometry, the gain peak can be shifted to other wavelengths. For example, in Fig. 6.9b, another waveguide geometry was assumed: the cladding width and height are $C_w = 11\,\mu\mathrm{m}$ and $C_h = 9.3\,\mu\mathrm{m}$, respectively, and the silicon core width and height are $W = 2\,\mu\mathrm{m}$ and $H = 1.55\,\mu\mathrm{m}$, respectively. The optimized length is now 40 cm and the gain reaches even 42 dB if a pump power of 15 W is injected

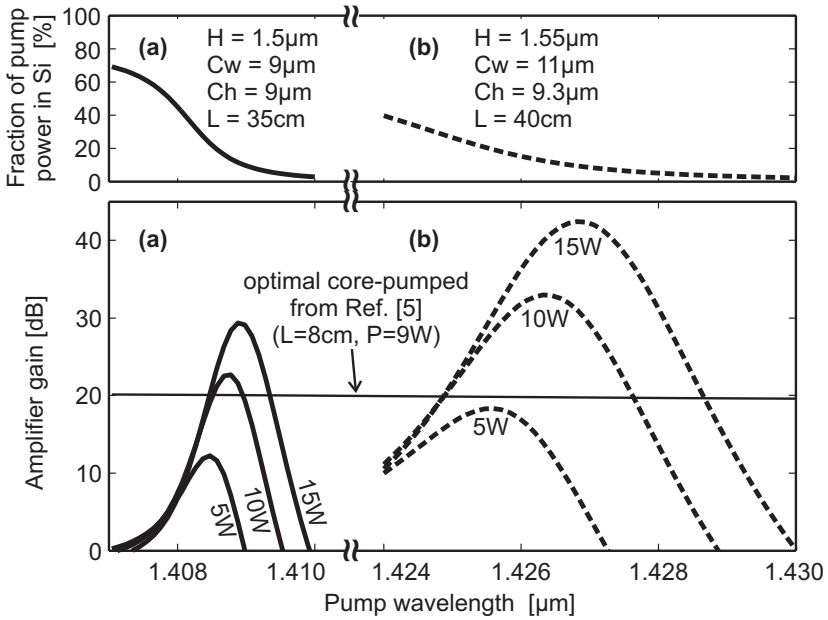

Figure 6.9.: Gain versus pump wavelength for cladding-pumped amplifiers based on the structure shown in Fig. 6.7 with an effective free-carrier lifetime of $\tau_{\text{eff}} = 1\,\text{ns}$. The maximum possible gain in a simple core-pumped amplifier is 20 dB.

at the wavelength of 1427 nm.

For comparison, the maximum gain achievable with a simple core-pumped structure (see section 6.2.3) with the same $\tau_{\text{eff}} = 1\,\text{ns}$ is limited to only 20 dB as indicated by the almost horizontal thin line.

Origin of spectral gain peaks

The pronounced spectral gain peaks in Fig. 6.9 occur due to a spatial re-distribution of the guided power within the pump mode field when varying the pump wavelength.

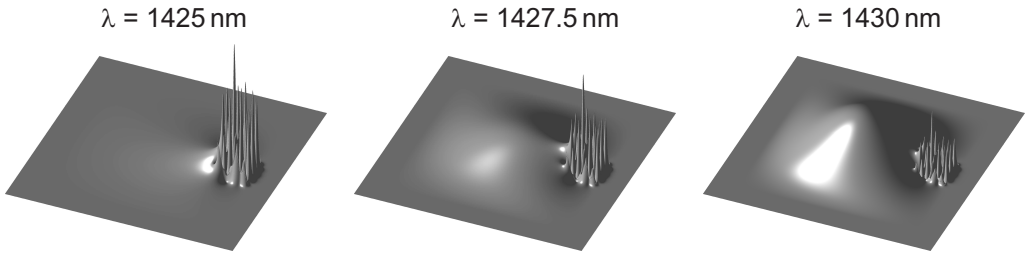

Figure 6.10.: Illustration of the spatial re-distribution of the power within the pump-mode field with varying wavelength. Shown is the mode-intensity profile for the pump mode of the structure of Fig. 6.9b at three different wavelengths.

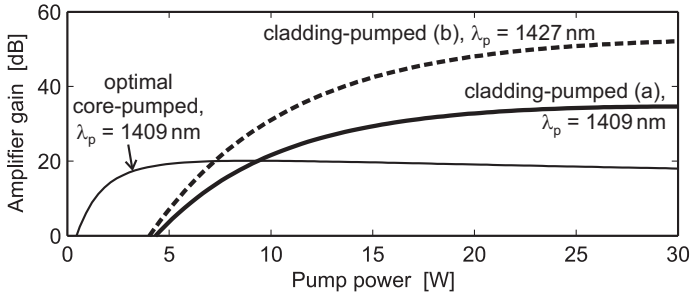

Figure 6.11.: Gain versus pump power for the optimal core-pumped amplifier (thin solid curve) and the cladding-pumped amplifiers from Fig. 6.9 (a) and (b).

For example, consider the case of our second example corresponding to the dashed curves in Fig. 6.9. At wavelengths larger than 1430 nm most of the pump power propagates in the big cladding lobe of the pump mode; the pump mode at $\lambda = 1430\,\text{nm}$ is plotted on the right-hand side of Fig. 6.10. The overlap with the silicon core is small and thus no significant total gain can be achieved with the limited available pump power of 15 W.

If the wavelength decreases, the pump power confines more and more to the silicon core: the dynamics of the intramodal power re-distribution within the pump mode is illustrated by the strong spectral dependence of the fraction of power in the core in the upper part of Fig. 6.9.[1] Additionally, the pump mode at $\lambda = 1425\,\text{nm}$ is shown on the left-hand side of Fig. 6.10. The increased pump intensity in the core at short wavelengths causes too large FCA and the total gain of the cladding-pumped amplifier is small again.

However, around 1427 nm the balanced distribution of the power within the pump mode field to both the core and the cladding is optimal (see the middle of Fig. 6.10), and the total gain can be raised up to 42 dB for an optimized length of 40 cm at a pump power of 15 W.

Effect of amplifier length and free-carrier lifetime

The dependence of the gain of the optimized amplifiers from Fig. 6.9 on the pump power is shown in Fig. 6.11. Despite the small overlap of the pump mode with the silicon core, even the gain of the cladding-pumped amplifier saturates with increasing pump power since FCA inavoidably predominates at sufficiently high pump intensities.

[1] For even shorter wavelengths, not shown in the figure, the mode eventually becomes entirely confined in the silicon—the mode's effective index surpasses the cladding index and the field inside the cladding becomes evanescent.

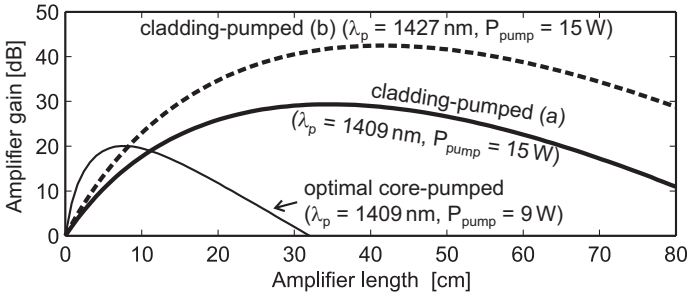

Figure 6.12.: Gain versus amplifier length for the optimal core-pumped amplifier (thin solid curve) and the cladding-pumped amplifiers from Fig. 6.9 (a) and (b).

Fig. 6.12 shows the dependence of the gain of the two cladding-pumped amplifiers designed in Fig. 6.9 on their length. Although they reach their maximal total gain of 29 and 42 dB at 35 and 40 cm length, respectively, the maxima are relatively flat and the choice of the length is not very critical. The simple core-pumped amplifier indicated by the thin solid line reaches its gain maximum of only 20 dB at a length of 8 cm, and any further increase of the length reduces the total gain. This illustrates the greater freedom for exploiting the Raman gain along a long waveguide if the pump is guided in a cladding without FCA.

Finally, we analyze the influence of the effective free-carrier lifetime on the amplifier performance. The designs of the cladding-pumped and core-pumped amplifiers shown in Fig. 6.9 have been made for an effective free-carrier lifetime of $\tau_{\text{eff}} = 1\,\text{ns}$. Fig. 6.13 now shows the gain of these amplifiers for various other lifetimes without any re-optimization. The cladding-pumped amplifiers perform better than the core-pumped amplifier in a wide range of effective free-carrier lifetimes.

It should be mentioned that the large optimal waveguide length maximizing the gain of cladding-pumped silicon Raman amplifiers can easily be realized on silicon-on-insulator chips on a small area by exploiting the extremely small bending radii made possible by the high index contrast, see section 6.5. Further, the shape of the gain spectrum at the Stokes wavelength will not be modified by the present cladding-pumped structure since the field of the fundamental mode used as the Stokes mode is already highly confined to the silicon core and does not change significantly with wavelength.

Conclusions

We have shown that cladding-pumped silicon Raman amplifiers can provide significantly more gain than their simple core-pumped counterparts. The underlying principle is that the pump power is guided primarily in an optically linear cladding surrounding the silicon

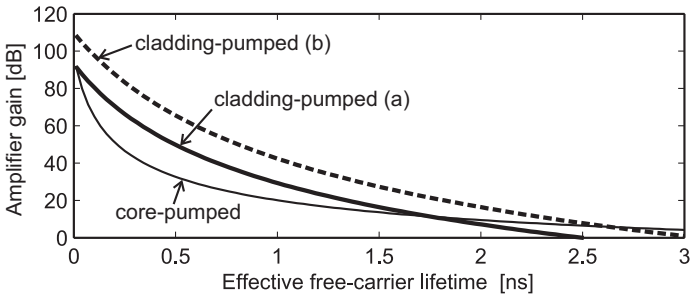

Figure 6.13.: Core-pumped and cladding-pumped amplifier gains versus free-carrier lifetime τ_{eff}.

core and thus propagates relatively unimpaired by FCA. This permits longer amplifier lengths and higher pump powers, which leads to a larger possible total gain.

The examples analyzed here showed maximal total gain up to 42 dB. The large number of geometric parameters leaves much freedom for further optimization. For example, a reduction of the effective areas by decreasing the core dimensions would permit a similar reduction of the required pump power.

6.5. Curvature loss in silicon waveguides

The analysis of the previous sections in this chapter has shown that optimally designed silicon Raman amplifiers can have lengths on the order of tens of centimeters, especially if they are based on waveguides with low linear propagation losses. In order to fit on one wafer, the amplifying waveguide will thus have to be, at least partly, curved.

We show that the curvature loss of silicon rib waveguides can vary by orders of magnitude, depending on the geometry (rib width W, rib height H, etch depth D, see the right-hand side of Fig. 5.1). We show in particular that the quasi-TM mode can experience significantly less curvature loss at the same bend radius than the quasi-TE mode. Integrated-optic devices making use only of the TM mode and a polarization-diversity scheme can thus profit from smaller possible bend radii and the resulting circuit-size reduction. The main loss mechanism for the quasi-TM rib mode can be coupling to the orthogonally polarized TE slab mode, which radiates power away from the waveguide. This is possible due to the slight hybridicity of the quasi-TM rib mode. Neglecting this hybridicity would lead to a significant underestimation of the curvature losses. Thus, accurate simulation of waveguides with low quasi-TM-mode curvature loss requires full-vectorial simulation models. The results of this section have been published in [KRB06a].

6.5.1. Modeling

The rib waveguides we analyze here are shown schematically on the right-hand side in Fig. 5.1. A central rib of height H and width W is surrounded by slab waveguides of height $H-D$, where D is the etch depth. All calculations are performed at a wavelength of $\lambda = 1.55\,\mu$m, where the substrate, the silicon core, and the top cladding have refractive indices $n_{\mathrm{SiO_2}} = 1.444$, $n_{\mathrm{Si}} = 3.477$, and $n_{\mathrm{Air}} = 1.0$, respectively.

We have used the full-vectorial finite-difference mode solver described in Appendix A in order to calculate the complex mode fields and propagation constants of guided and leaky modes of the rib waveguides.

6.5.2. Curvature loss in silicon rib waveguides

Survey of TE- and TM-mode losses

Fig. 6.14a shows the curvature loss of the fundamental quasi-TE mode (transverse E field predominantly along the y axis, see Fig. 5.1)) of silicon rib waveguides for a 90-degree bend section with a bend radius of $R = 48\,\mu$m. The rib height has been kept fixed at $H = 1.5\,\mu$m, and the rib width W and the etch depth D have been varied. None of the analyzed waveguides exhibit losses less than 1 dB per 90-degree bend. In contrast, the losses for the quasi-TM mode (transverse E field predominantly along the x axis) are much lower. They are shown in Fig. 6.14b at the same bend radius of $R = 48\,\mu$m. In a wide range of waveguide widths W and etch depths D, the curvature losses for the quasi-TM mode have acceptable values below $0.1\,\mathrm{dB}/90°$.

TM-mode loss mechanism

The reason for the fact that the TM mode experiences less curvature loss than the TE mode becomes clear when considering a simple effective-index model for the curved waveguide.

The thick solid curve in Fig. 6.15 shows schematically the equivalent index profile $n_{\mathrm{eq,TE}}(y)$ for TE modes of the rib waveguide shown on the right-hand side of Fig. 5.1, where the tilt of the profile represents the curvature of the rib waveguide [Vas91]. The thin solid line indicates the effective index $n_{\mathrm{eff,TE}}$ of the fundamental TE waveguide mode. According to a Wentzel-Kramers-Brillouin analysis, the curvature loss of this mode is mainly proportional to $\exp(-I)$, where

$$I = \frac{2\pi}{\lambda} \int_{W/2}^{y_{\mathrm{c,TE}}} \sqrt{n_{\mathrm{eff,TE}}^2 - n_{\mathrm{eq,TE}}(y)^2}\,\mathrm{d}y \tag{6.37}$$

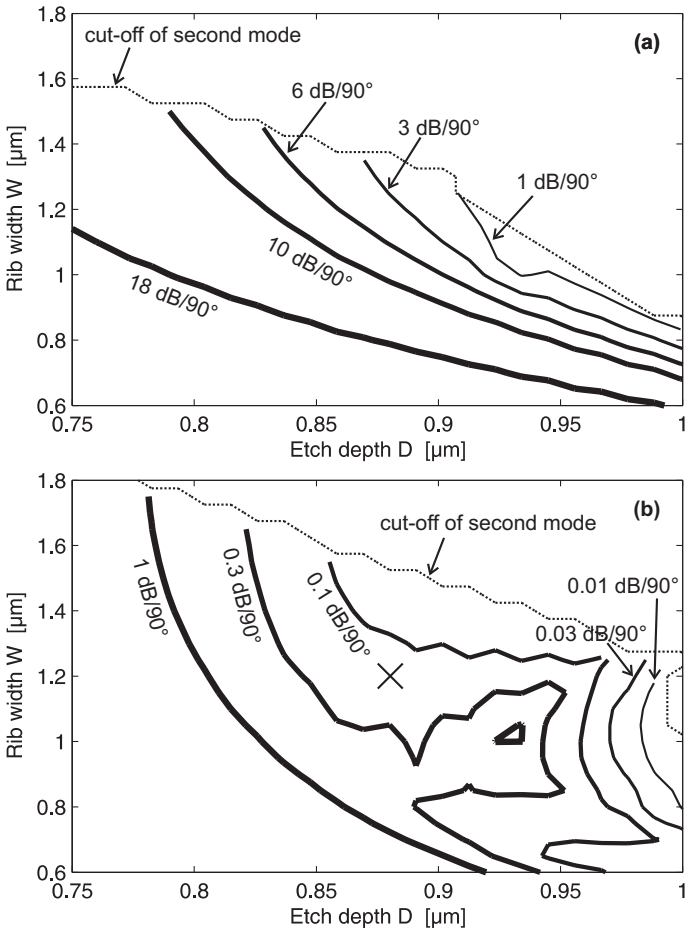

Figure 6.14.: Curvature loss for silicon rib waveguides with height $H = 1.5\,\mu$m in a 90-degree bend at a bend radius of $R = 48\,\mu$m. *(a)* TE mode, *(b)* TM mode.

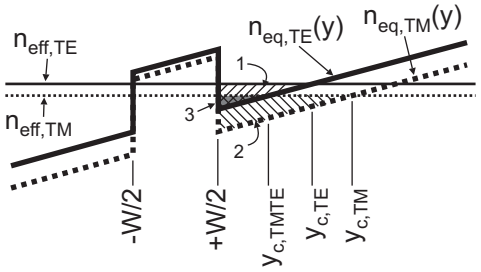

Figure 6.15.: Schematic effective-index model illustrating the three curvature-loss mechanisms. The three triangular areas (1: hatched along SW–NE, 2: hatched along NW–SE, and 3: their intersection marked in gray color) visualize the tunneling barriers for radiation, 1: from the TE rib mode to the TE slab mode, 2: from the TM rib mode to the TM slab mode, and 3: from the TM rib mode to the TE slab mode, respectively.

is an integral over the spatial region where the field is purely evanescent [Vas91]. This region extends from the core-cladding boundary at $y = W/2$ to the TE caustic at $y = y_{\mathrm{c,TE}}$. Light must tunnel through this barrier (the strength of which is characterized by I) into the oscillation region beyond the caustic. The tunnel barrier has been visualized as the triangular area labelled "1" in Fig. 6.15; it is enclosed by the effective-index line $n_{\mathrm{eff,TE}}$ and the equivalent index profile $n_{\mathrm{eq,TE}}(y)$.

Analogously, the thick dotted curve in Fig. 6.15 shows the equivalent index profile $n_{\mathrm{eq,TM}}(y)$ for TM modes, and the thin dotted line indicates the TM-mode effective index $n_{\mathrm{eff,TM}}$. Here, the curvature-loss tunnel barrier is the triangular area labelled "2", which is enclosed by the two curves between the core-cladding boundary and the TM caustic $y = y_{\mathrm{c,TM}}$. This area is larger than the corresponding TE area for the following reason. In the slab region ($|y| > W/2$), the equivalent index $n_{\mathrm{eq,TM}}(y)$ of TM modes is lower than the equivalent index $n_{\mathrm{eq,TE}}(y)$ of TE modes. The effective indices of TE and TM waveguide modes, however, are much closer together – in a zero-birefringence waveguide, they would even coincide. It is then clear geometrically that the tunnel barrier is usually both deeper and longer for TM modes, resulting in lower curvature loss for the TM mode at the same bend radius.

However, the above discussion is not complete. We have to take into account the fact that the modes in a rib waveguide are not perfectly uniformly polarized but slightly hybrid. The presence of an orthogonal field component permits a coupling of the TE waveguide mode to the TM slab mode and of the TM waveguide mode to the TE slab mode. The latter case is particularly important. Analogous to the two cases in the preceding paragraphs, the loss induced by radiation of the TM rib mode into the TE slab mode is related to the triangular area marked as "3" in Fig. 6.15, which is enclosed

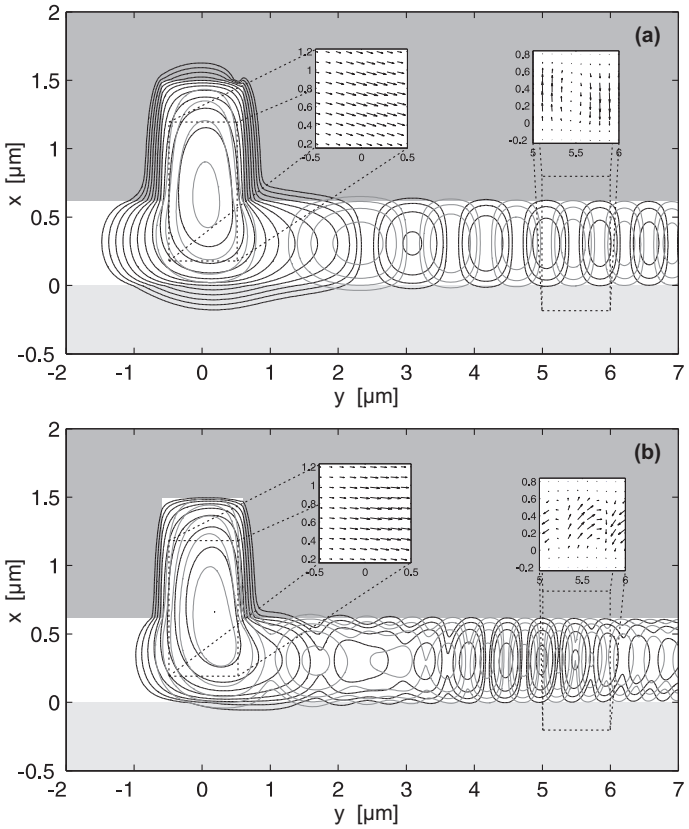

Figure 6.16.: Contours in steps of 2 dB of the transverse-H-field magnitude of the quasi-TM mode of the waveguide marked with a cross in Fig. 6.14b. Looking into the paper plane, the waveguide is curved to the left such that power is radiated towards the outer, right-hand slab waveguide. Dark and light contours correspond to real and imaginary parts of the field, respectively. The insets show the real part of the transverse-H-field vectors. *(a),* bend radius is $R = 80\,\mu$m; *(b),* bend radius is $R = 30\,\mu$m.

by the effective-index line $n_{\mathrm{eff,TM}}$ and the equivalent index profile $n_{\mathrm{eq,TE}}(y)$ between the core-cladding boundary and the caustic $y = y_{\mathrm{c,TETM}}$ (this area is simply the intersection of the other two areas "1" and "2"). It can be seen in Fig. 6.15 that this tunnel barrier is particularly small and thus enables an efficient radiation mechanism for the TM rib mode, even when the hybridicity of the rib mode is very small. The cross-polarization coupling from the TE waveguide mode to the TM slab mode can be neglected, because the corresponding tunnel barrier is much higher than that of the coupling to the TE slab mode.

Illustration of curvature loss mechanisms

In this section we illustrate the coupling of the curved TM waveguide mode to the TE slab mode. As an example, we pick the waveguide marked with a cross in Fig. 6.14b: $H = 1.5\,\mu$m, $D = 0.88\,\mu$m, $W = 1.2\,\mu$m.

That the coupling of the TM rib mode to the TE slab mode is indeed significant is shown in Fig. 6.16a, where the transverse H-field of the quasi-TM mode in the rib waveguide marked with a cross in Fig. 6.14b has been plotted for a bend radius of $R = 80\,\mu$m. The radiation of power into the slab waveguide can be clearly seen –

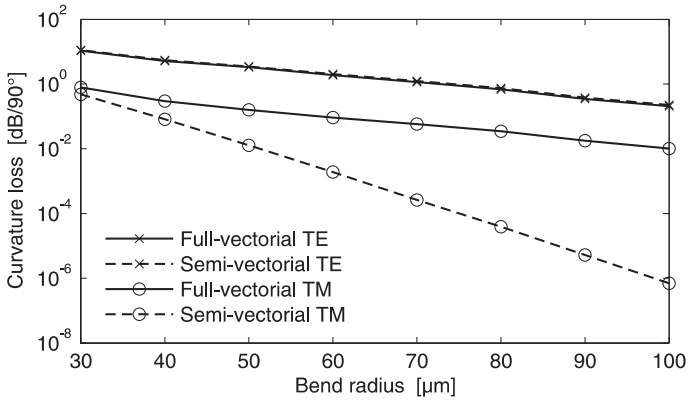

Figure 6.17.: 90-degree curvature loss versus bend radius for the waveguide marked with a cross in Fig. 6.14b. While TE-mode losses are described well by a semi-vectorial model, TM-mode losses require a full-vectorial description due to cross-polarization radiation.

towards the outside, the phase of the mode field increases, such that the phase fronts of the propagating wave lag behind those inside the core and power is radiated away. The insets in Fig. 6.16a show the vector character of the transverse H field in the core region and in the outer slab. Even though the core field is predominantly parallel to the y axis (quasi-TM mode), the slab carries away power mainly in the TE mode, which means that the main loss mechanism is coupling to the orthogonally polarized slab mode, as discussed in Sect. 6.5.2.

For shorter bending radii, the tunneling barrier to the TM slab mode becomes increasingly shorter, and eventually the TM slab mode also carries a substantial part of the radiated power. Fig. 6.16b shows the mode field of the same waveguide as in Fig. 6.16a for a bending radius of $R = 30\,\mu$m, where now the beating between the TE and TM slab modes can be clearly seen.

6.5.3. Insufficiency of semi-vectorial modeling

As another illustration of the significance of TE-slab-mode radiation for TM rib modes, we have plotted in Fig. 6.17 the curvature losses of the TE and TM rib modes versus the bending radius, calculated with both full-vectorial and semi-vectorial formalisms. For the TE mode, the difference between full-vectorial and semi-vectorial calculations is relatively small. However, the TM rib-mode losses are significantly underestimated by the semi-vectorial calculations. The reason for this is that the semi-vectorial TM calculation can not, by definition, take into account the coupling to the TE slab mode. Therefore, it does not allow for the main loss mechanism and yields much too low loss values.

Incidentally, this cross-polarization radiation is not the dominant loss mechanism in the GaAs/AlGaAs rib-waveguide structures from Refs. [Aus82, DH88] which are often used as benchmarks for curvature-loss calculations [GBM91, YK93, BG00, DH04]. The results for the curvature losses given in Refs. [GBM91, YK93, BG00, DH04] are accurately reproduced also by the mode solver used for the present analysis. However, there is practically no difference between semi-vectorial and full-vectorial simulations when applied to the waveguides of Refs. [GBM91, YK93, BG00, DH04], neither for the quasi-TE modes nor for the quasi-TM modes. In those rib waveguides, the quasi-TE rib mode radiates primarily into the TE slab mode and the quasi-TM rib mode radiates primarily into the TM slab mode, as opposed to the silicon-on-insulator structure analyzed in this section.

6.6. Chapter summary

We have shown in this chapter that the most basic form of silicon Raman amplifier as first demonstrated in [CDR$^+$03] has an upper limit on the total gain that can be achieved with a given waveguide technology. On the other hand, we have proposed a tapered SRA, which can deliver more gain by keeping the local pump intensity at its optimum value throughout the waveguide. As an alternative way of achieving an increased maximum possible gain in SRAs, we have analyzed cladding-pumped SRAs, in which the pump power is guided in an additional cladding surrounding the silicon core; this reduces the FCA seen by the pump and allows longer amplifiers with more gain than possible with conventional SRAs. The required long waveguide lengths can be realized on silicon chips by making use of tight bends made possible by the high index contrast of silicon waveguides; however, we have shown that the accurate design of curved silicon waveguides requires fully vectorial simulation tools.

7. Analysis and design of silicon Raman lasers

In the final chapter of this thesis, properties of conventional and new designs for silicon Raman lasers (SRLs) are discussed. Section 7.1 gives details on the modeling and basic characteristics of SRLs. New and more efficient SRL designs are presented in sections 7.2 (bidirectionally pumped SRL) and 7.3 (tapered SRL). The final section 7.4 shows that the principle of cascading known from RFLs (see Sect. 3.3) can be applied to SRLs to create silicon lasers with output wavelengths which have a large offset from the pump wavelength.

The results of this chapter have been published in [KRB04,KRB05a,KRB05c,KRB06c, KDRB06].

7.1. Basic characteristics of silicon Raman lasers

In this section we discuss the basic characteristics of Raman lasers in silicon waveguides. We show numerically that continuous-wave Raman lasing is possible in silicon waveguides, in spite of the detrimental presence of TPA and FCA. Shortly after the results of the study described in this section had been published [KRB04], the first continuous-wave silicon Raman laser could be demonstrated experimentally by Intel in 2005 [RJL+05].

7.1.1. Geometry and model

Fig. 7.1 shows the schematic of the silicon Raman laser setup we analyze in this section. It consists of a silicon waveguide of length L, into the left-hand side of which pump-laser light at the wavelength λ_p is coupled in. Inside the waveguide, Raman scattering generates optical power at the Stokes wavelength λ_s. The longitudinal evolution of the forward- (+) and backward-propagating (−) pump ("p") and Stokes ("s") powers $P_p^{\pm}$ and $P_s^{\pm}$ is described by the model summarized in Sect. 5.5. We only need to add suitable

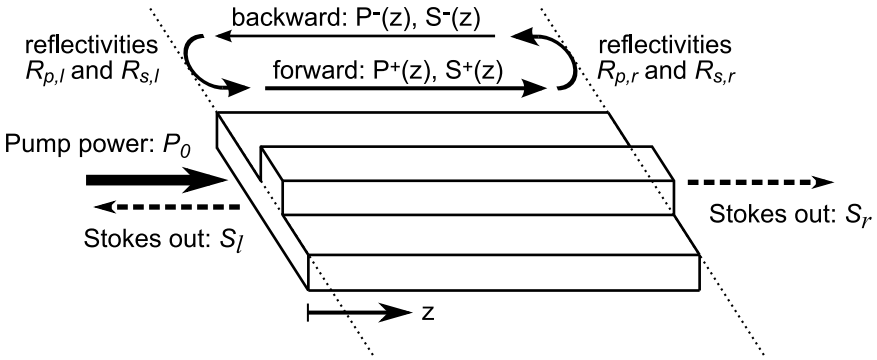

Figure 7.1.: Schematic of a basic silicon Raman laser. Pump power is injected at the left-hand side into a silicon waveguide. The Stokes (lasing-wavelength) cavity is formed by reflectivities $R_{s,l}$ and $R_{s,r}$ at the ends of the waveguide, while reflectivities at the pump wavelength $R_{p,l}$ and $R_{p,r}$ can be used to influence the longitudinal pump-power distribution.

boundary conditions at the left-hand ("l") and right-hand ("r") ends of the waveguide, where the pump and Stokes wavelengths see power reflectivities of $R_{p,l}$, $R_{p,r}$, $R_{s,l}$ and $R_{s,r}$, respectively. The reflectors could be formed by polished waveguide end surfaces, by thin-film coatings on the end surfaces, or by waveguide Bragg gratings.

The first two boundary conditions relate the powers of the forward- and backward-propagating Stokes waves $P_s^{\pm}$ at the waveguide end faces through the corresponding power reflectivities,

$$P_s^+(0) = R_{s,l} P_s^-(0), \qquad P_s^-(L) = R_{s,r} P_s^+(L). \tag{7.1}$$

The other two boundary conditions relate the forward- and backward-propagating pump waves $P_p^{\pm}$ as well as the injected pump power P_0 as

$$P_p^+(0) = T_p P_0 + R_{p,l} P_p^-(0), \qquad P_p^-(L) = R_{p,r} P_p^+(L), \tag{7.2}$$

where P_0 is the pump-laser power and T_p is the coupling efficiency into the waveguide. We assume lossless reflectors, i. e., $T_p = 1 - R_{p,l}$.

The left-hand one of Eqs. (7.2) assumes an incoherent superposition of the reflected backward-propagating pump wave and the externally injected pump power. This boundary condition is thus applicable whenever the pump-laser spectrum is so broad that it spans several free spectral ranges (FSRs) of the silicon-waveguide cavity. For example, the pump laser used in [CDR+03] is a Raman fiber laser with a spectral width of several tens of gigahertz, while a silicon-waveguide cavity with a length of 1 cm has an FSR of only $c/(2Ln) \approx 5\,\mathrm{GHz}$.

7.1.2. Lasing and shutdown thresholds

Simulation parameters

We initially concentrate on lasers with non-coated waveguide end-faces and assume that all reflectivities are due to the silicon/air interface, $R_{p,l} = R_{p,r} = R_{s,l} = R_{s,r} = 30\%$. We base our simulations on the waveguide structure shown on the right-hand side of Fig. 5.1, for which the various effective areas for SRS and TPA are shown in Fig. 5.3. At the wavelengths chosen here (pump and Stokes wavelengths of $\lambda_p = 1427\,\mathrm{nm}$ and $\lambda_s = 1542\,\mathrm{nm}$, respectively), the effective areas have values of about $1.6\,\mu\mathrm{m}^2$ and the confinement factors are close to unity. We choose conservative values for the bulk-silicon Raman-gain and TPA constants in order to avoid too optimistic results, see Sect. 5.5.

Numerical calculation of the threshold power

Around threshold, the Stokes powers are much smaller than the pump powers, $P_s^{\pm} \ll P_p^{\pm}$, and we can simplify the full model of Sect. 5.5 to

$$\pm\frac{1}{P_p^{\pm}}\frac{\mathrm{d}P_p^{\pm}}{\mathrm{d}z} = -\alpha_p - \beta_{pp}\frac{P_p^{\pm} + 2P_p^{\mp}}{A_{pp}^{(\mathrm{TPA})}} - \eta_p\bar{\varphi}\lambda_p^2\bar{N}, \tag{7.3}$$

$$\pm\frac{1}{P_s^{\pm}}\frac{\mathrm{d}P_s^{\pm}}{\mathrm{d}z} = -\alpha_s + g\left(\frac{P_p^{\pm}}{A_{\mathrm{co}}^{(\mathrm{SRS})}} + \frac{P_p^{\mp}}{A_{\mathrm{cntr}}^{(\mathrm{SRS})}}\right) - \beta_{sp}\frac{2P_p^{+} + 2P_p^{-}}{A_{sp}^{(\mathrm{TPA})}} - \eta_s\bar{\varphi}\lambda_s^2\bar{N} = \gamma^{\pm}(z), \tag{7.4}$$

$$\bar{N} = \frac{M}{2}\frac{\beta_{pp}}{h\nu_p A_{pp}^{(\mathrm{TPA})}}(P_p^{+2} + P_p^{-2} + 4P_p^{+}P_p^{-}). \tag{7.5}$$

The laser is at threshold when the Stokes round-trip net gain equals the losses due to outcoupling at the left-hand and right-hand end faces with reflectivities $R_{s,l}$ and $R_{s,r}$. From Eqs. (7.4) and (7.1) we can thus obtain the oscillation condition

$$R_{s,l}R_{s,r}\exp\left[2\int_0^L \bar{\gamma}(z)\,\mathrm{d}z\right] = 1, \tag{7.6}$$

where we have defined the local Stokes gain $\bar{\gamma}(z)$ as the average between the gains experienced by the forward- and backward-propagating Stokes waves,[1]

$$\begin{aligned}\bar{\gamma}(z) &= \frac{1}{2}\left[\gamma^{+}(z) + \gamma^{-}(z)\right] \\ &= -\alpha_s - \eta_s\bar{\varphi}\lambda_s^2\bar{N}(z) + \left(\frac{g}{2A_{\mathrm{co}}^{(\mathrm{SRS})}} + \frac{g}{2A_{\mathrm{cntr}}^{(\mathrm{SRS})}} - \frac{2\beta_{sp}}{A_{sp}^{(\mathrm{TPA})}}\right)\left[P_p^{+}(z) + P_p^{-}(z)\right]\end{aligned} \tag{7.7}$$

[1] If the effective areas for co- and counter-propagating SRS were equal, i. e., $A_{\mathrm{co}}^{(\mathrm{SRS})} = A_{\mathrm{cntr}}^{(\mathrm{SRS})}$, then $\bar{\gamma}(z) = \gamma^{+}(z) = \gamma^{-}(z)$.

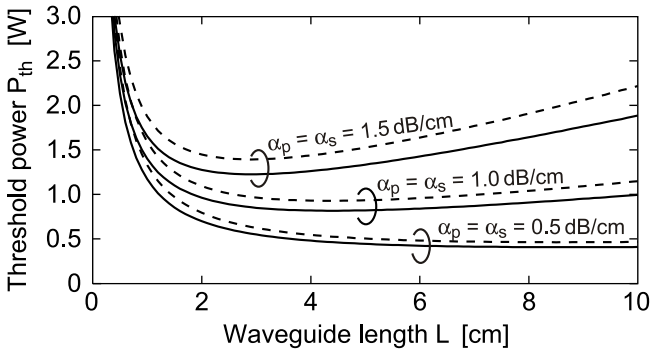

Figure 7.2.: Threshold pump power of silicon Raman lasers versus waveguide length L. End-face reflectivities are 30%, and free-carrier absorption is assumed to be negligible ($\tau_{\text{eff}} = 0$). *Solid curves:* No two-photon absorption ($\beta = 0$). *Dashed curves:* With two-photon absorption, $\beta = 0.7\,\text{cm/GW}$.

In order to find the threshold pump power P_{th}, we numerically calculate the longitudinal pump-power distribution from Eqs. (7.3) and (7.2) for varying pump powers P_0 until $P_p^+(z)$ and $P_p^-(z)$ fulfill Eq. (7.6). The corresponding pump power P_0 is then the threshold pump power P_{th}.

Lasing threshold

We first look at the imaginary case of a silicon Raman laser in which both TPA and FCA are absent, i. e., we artifically set $\beta_{pp} = \beta_{sp} = 0$ and $\tau_{\text{eff}} = 0$. The three solid curves in Fig. 7.2 show the threshold pump power of such a laser as a function of the waveguide length L, for three different loss coefficients $\alpha = \alpha_p = \alpha_s$. The results suggest that it should be possible to pump a silicon Raman laser beyond threshold by using a pump laser with only a few Watts of output power, provided the effects of TPA and FCA are negligible. In that case, the conversion efficiencies of the silicon Raman laser are comparable to those obtainable from Raman fiber lasers, see Sect. 3.1.4.

Next we look at the influence that TPA has on the threshold pump power. The dashed curves in Fig. 7.2 show the threshold power as a function of the waveguide length L, when the TPA coefficients have realistic non-zero values (see Sect. 5.5), yet FCA is still assumed to be absent, i. e., all charge carriers are assumed to recombine instantaneously after generation and thus $\tau_{\text{eff}} = 0$. TPA evidently increases the required threshold pump powers, but only relatively weakly.

In contrast to the slight effect of TPA, the effect of FCA ($\tau_{\text{eff}} > 0$) can be much more dramatic, which is illustrated in Fig. 7.3. The linear waveguide losses are now fixed at $\alpha_p = \alpha_s = 1.0\,\text{dB/cm}$. The dashed line again shows the threshold power as a function of the waveguide length for no TPA ($\beta_{pp} = \beta_{sp} = 0$) for comparison, whereas the solid lines show the threshold powers in presence of TPA (non-zero β_{pp} and β_{sp} as in Sect. 5.5) and several different charge-carrier lifetimes τ_{eff}. As expected, a larger τ_{eff} results in an increased threshold. Furthermore, there is a limited usable range of waveguide lengths

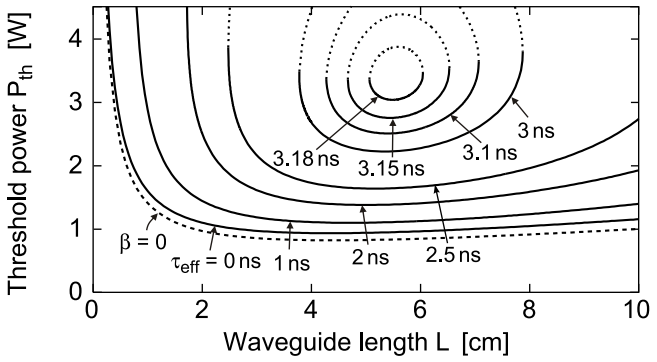

Figure 7.3.: Threshold pump power of silicon Raman lasers versus waveguide length L for several effective carrier lifetimes τ_{eff} and $\alpha_p = \alpha_s = 1.0\,\text{dB/cm}$. The solid and dotted curves show, for a given τ_{eff}, the lasing and shutdown thresholds, respectively. Dashed curve (included for comparison): threshold in the absence of TPA and FCA.

outside of which the laser has no threshold at all. Outside this range, the waveguide will never start lasing, no matter how large the pump power is (e. g., for $L = 80\,\text{mm}$ and τ_{eff} larger than approximately 3.0 ns, the device has no lasing threshold). For increasing τ_{eff}, the usable range becomes increasingly smaller, until at $\tau_{\text{eff}} \approx 3.2\,\text{ns}$, it vanishes completely. In other words, there is a maximum effective carrier lifetime that can be tolerated for lasing.

The origin of the limited usable waveguide-length range is the increase of the overall cavity losses with increasing pump power through the nonlinear absorption mechanisms TPA and FCA. If only linear losses were present, the overall cavity losses would remain constant with respect to the pump power, and for any given waveguide length L there would be a pump-power level above which the laser will start lasing [AY79].

7.1.3. Laser characteristics

Even for configurations inside the usable waveguide-length range, there is a continuing growth of the overall cavity losses when increasing the pump-laser power beyond threshold. This can be seen in Fig. 7.4, where the input-output characteristics of several lasers with various effective carrier lifetimes τ_{eff} are plotted. These characteristics were calculated from the full model described in Sect. 5.5, and we defined the output power of the laser as $P_{\text{out}} = P_s^+(L)(1 - R_{s,r})$. Directly above threshold, an increase of the pump power also increases the output power. However, there clearly exists a rollover point, i. e., a critical pump power beyond which a further increase of the pump power actually results in a decrease of the output power and, eventually, in a return to zero at the "shutdown threshold". Thus, an increase of the pump power not only increases the Raman gain, but also increases the losses for both the pump and the Stokes waves through the nonlinear loss mechanisms TPA and FCA. This eventually leads to the breakdown of lasing operation at the shutdown threshold. Furthermore, Fig. 7.4 shows that for

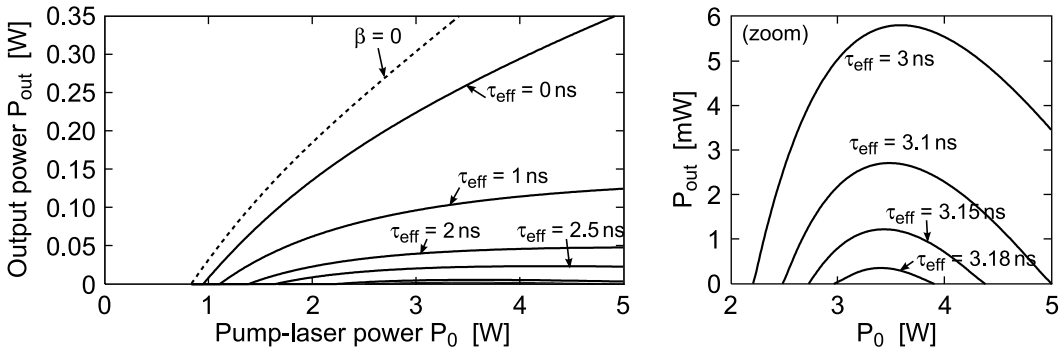

Figure 7.4.: *(left:)* Input-output characteristics of silicon Raman lasers with $L = 55\,\text{mm}$ and several values of the effective carrier lifetime τ_{eff}. The dashed curve corresponds to absence of TPA and FCA. *(right:)* Zoom into the characteristics corresponding to large τ_{eff}.

increasing τ_{eff}, the maximum conversion efficiency of the lasers dramatically decreases and the lasing and shutdown thresholds come closer to each other.

The shutdown-threshold power was in fact also obtained during the numerical threshold computations according to Sect. 7.1.2 – for every given waveguide length L, there is either no threshold at all or there are two threshold pump powers (in the presence of TPA and FCA). The solid curves in Fig. 7.3 show the lower of the two threshold powers (i. e., the lasing threshold), while the dotted curves show the upper threshold (i. e., the shutdown threshold). Lasing of the device can only take place between these two pump-power levels, with a maximum output power somewhere in between. The two solution branches merge at two limit points (the ends of the usable waveguide-length range), forming a closed egg-shaped curve, which narrows as τ_{eff} increases and eventually vanishes completely at the maximum tolerated effective carrier lifetime.

Increased end-face reflectivities

As a last example we consider what happens when we apply coatings to the ends of the silicon waveguide in order to increase the reflectivities. Specifically, we chose left-hand and right-hand Stokes reflecitivities of 80% and left-hand and right-hand pump reflectivities of 0 and 100%, respectively, such that $T_p = 100\%$ (a right-hand reflectivity of 100% for the pump wave is often used in Raman fiber lasers so that the pump power that is unused after a single pass is recycled and reflected back into the cavity).

Figure 7.5 shows the calculated threshold power versus waveguide length and the input-output characteristics of the high-reflectivity silicon Raman laser for various effective carrier lifetimes. The thresholds are much lower than in the first laser (see Fig. 7.3). We attribute this to the increased Stokes reflectivities which result in lower cavity losses,

and this together with the efficient pump-backreflection arrangement yields lower thresholds. Furthermore, the maximum tolerable carrier lifetime is now about twice as large as in Fig. 7.3, and the optimal waveguide length for minimum threshold power varies more strongly with τ_{eff}.

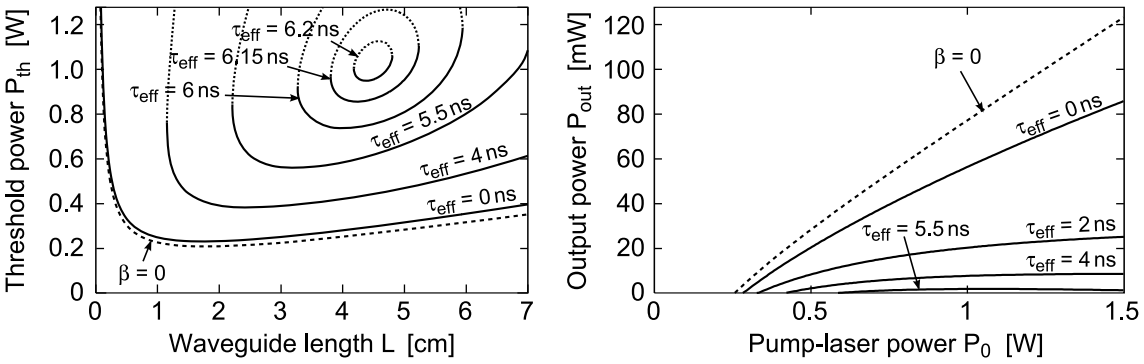

Figure 7.5.: Threshold pump power versus waveguide length L (*left*) and input-output characteristics at $L = 35\,\text{mm}$ (*right*) of silicon Raman lasers for several effective carrier lifetimes τ_{eff}. The only changes in the laser configuration against Figs. 7.3 and 7.4 are Stokes reflectivites of 80%, and left-hand and right-hand pump reflectivities of 0% and 100%, respectively.

7.2. Bidirectionally pumped silicon Raman lasers

In this section we introduce the bidirectionally pumped silicon Raman laser, where pump power is injected from both ends of the waveguide instead of only one end, see Fig. 7.6. This pumping scheme significantly increases the tolerance of silicon Raman lasers against FCA and leads to more efficient lasing [KRB05c].

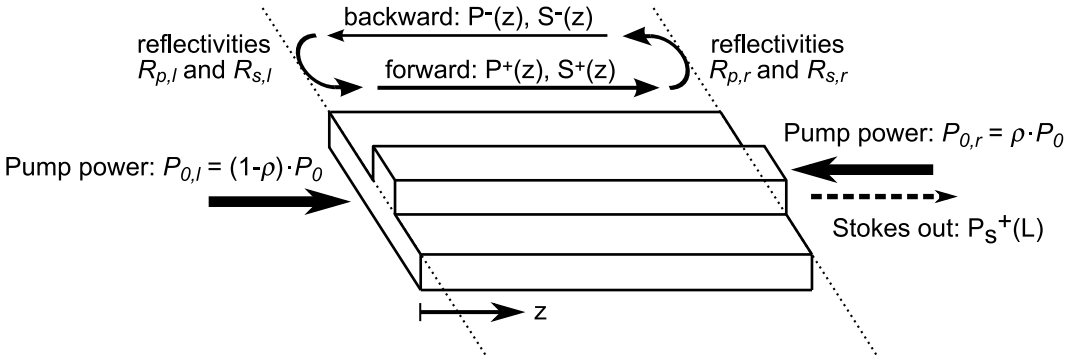

Figure 7.6.: Schematic of a bidirectionally pumped silicon Raman laser.

7.2.1. Model

Our model for bidirectionally pumped silicon Raman lasers is essentially that which we have used in Sect. 7.1 to analyze single-side-pumped lasers. The only change is a straightforward modification of the boundary conditions: the reflection of the waves at the two end faces of the silicon waveguide (at $z = 0$ and $z = L$) with the reflectivities $R_{\{p,s\},\{l,r\}}$ and the input coupling of the left-hand and right-hand pump powers $P_{0,\{l,r\}}$ with efficiencies $T_{p,\{l,r\}}$ are taken into account by the new boundary conditions (see also Fig. 7.6),

$$P_p^+(0) = T_{p,l}P_{0,l} + R_{p,l}P_p^-(0), \qquad P_s^+(0) = R_{s,l}P_s^-(0), \tag{7.8}$$

$$P_p^-(L) = T_{p,r}P_{0,r} + R_{p,r}P_p^+(L), \qquad P_s^-(L) = R_{s,r}P_s^+(L). \tag{7.9}$$

The output power of the laser is $P_{\text{out}} = P_s^+(L)(1 - R_{s,r})$. We will consider only lasers which have been prepared such that they have a left-hand Stokes reflectivity of $R_{s,l} = 100\%$ (i. e., we want to have all the laser output power on the right-hand side), whereas the other reflectivities have the Si–air Fresnel-reflectivity value of $R_{p,l} = R_{p,r} = R_{s,r} = 30\%$.

In practice, bidirectional pumping of the Raman laser could be achieved by the use of two separate pump-laser diodes at the left-hand and right-hand ends of the silicon waveguide, the power of which could be controlled independently. For clarity, however, we choose to present our results for a situation where we have only one pump laser, the output power P_0 of which is split between the left-hand and right-hand ends according to the splitting ratio ρ, i. e., the left-hand and right-hand pump powers are $P_{0,l} = (1-\rho)P_0$ and $P_{0,r} = \rho P_0$. Thus, the case $\rho = 0$ corresponds to conventional single-side pumping.

7.2.2. Lasing and shutdown thresholds

We start by demonstrating the effect of the introduction of bidirectional pumping on the threshold powers of the laser. Fig. 7.7a shows the lasing and shutdown thresholds for single-side pumping ($\rho = 0$) as a function of the laser length for various carrier lifetimes τ_{eff}. For a given τ_{eff}, lasing is possible only inside the corresponding closed egg-shaped curve delimited by the two thresholds as discussed in Sect. 7.1.2. For example, for $\tau_{\text{eff}} = 4.0\,\text{ns}$, lasing is only possible for waveguide lengths between 2.5 and 8.1 cm (marked with dots in Fig. 7.7a). In particular, the laser with $L = 7\,\text{cm}$ (marked with a vertical arrow in Fig. 7.7a) starts lasing at a pump power of 1.8 W, and stops lasing again at the shutdown threshold of 4.7 W due to excessive FCA, delivering maximum output power somewhere in between. For increasing τ_{eff}, the range where lasing is possible

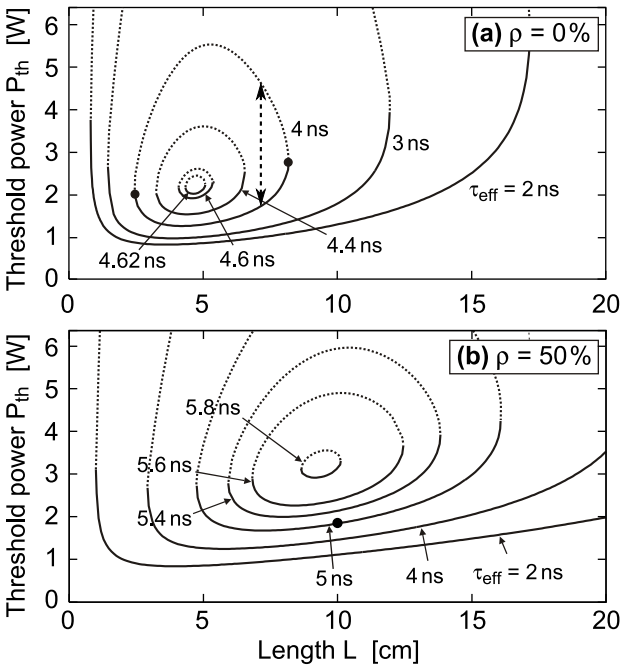

Figure 7.7.: Threshold pump-laser powers for lasing (solid) and shutdown (dotted) versus laser length L for several effective lifetimes τ_{eff}. *(a)* single-side-pumped lasers ($\rho = 0$), *(b)* lasers are bidirectionally pumped with a pump-power splitting ratio of $\rho = 50\%$, i. e., the pump-laser power is split equally between the two waveguide ends.

shrinks, and it closes completely at the maximum tolerable lifetime of about 4.65 ns. Fig. 7.7b shows the corresponding curves for the case where the pump power is split equally between the left-hand and right-hand ends, i. e., the pump-power splitting ratio is $\rho = 50\%$. The maximum tolerable lifetime is now about 5.82 ns, which is higher by 25% as compared to the single-side-pumped case, an indication of higher tolerance against FCA. For shorter lifetimes, the laser length can now be chosen more freely.

The reason for the improved tolerance against FCA is easily illustrated. Consider the laser with $\tau_{\text{eff}} = 5\,\text{ns}$ and $L = 10\,\text{cm}$ at a pump-laser power of $P_0 = 1.8\,\text{W}$. When bidirectionally pumped with $\rho = 50\%$, the laser is exactly at threshold (marked with a thick dot in Fig. 7.7b). The corresponding pump-power distribution is plotted as the thick solid and dashed lines in Fig. 7.8a, and the thick line in Fig. 7.8b shows the distribution of the resulting net Stokes gain (defined in Eq. (7.7)). Its integral along the waveguide amounts to 2.6 dB. In contrast, the thin curves in Figs. 7.8a and 7.8b correspond to the case of single-side-pumping. It can be seen that here the pump power drops more rapidly at the left-hand side of the waveguide due to higher FCA than in the bidirectionally pumped case. As a consequence, the net Stokes gain is lower: its integral is only $-0.077\,\text{dB}$, meaning net loss. Thus, bidirectional pumping is more efficient in providing Stokes gain for the same pump-laser power.

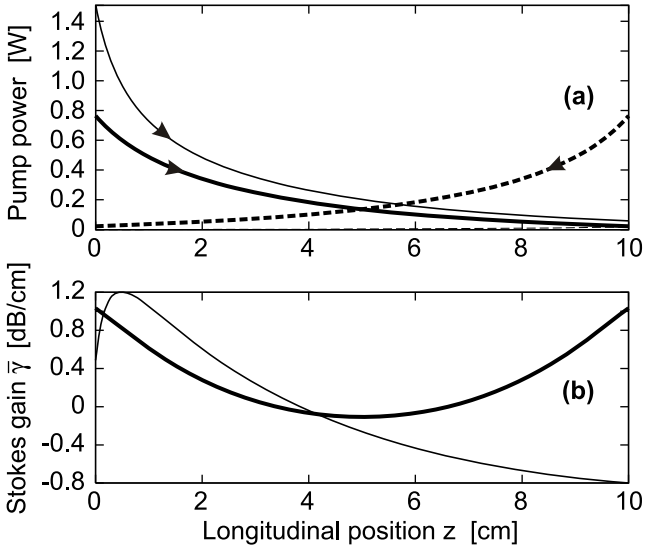

Figure 7.8.: Comparison between single-side-pumped (thin) and bidirectionally pumped (thick) waveguides at the same total pump power P_0. *(a)* longitudinal distribution of pump powers (solid: forward, dashed: backward), *(b)* local Stokes gain $\bar{\gamma}$.

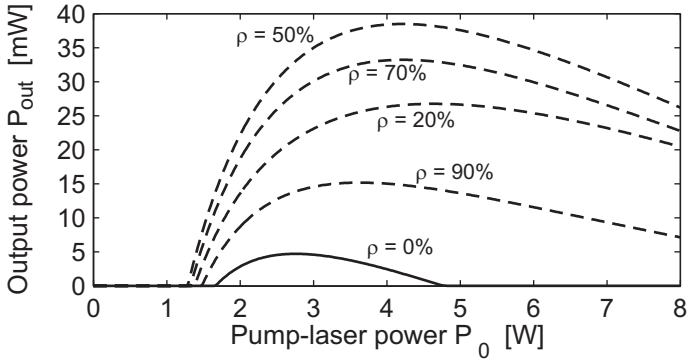

Figure 7.9.: Input-output characteristics of the laser marked with a vertical arrow in Fig. 7.7a for several values of the pump-power splitting ratio ρ.

Input-output characteristics

Now we look at the influence of bidirectional pumping on the laser characteristics. Consider the laser configuration marked with a vertical arrow in Fig. 7.7a, i. e., the laser with $L = 7\,\mathrm{cm}$, $\tau_{\mathrm{eff}} = 4\,\mathrm{ns}$ and single-side pumping ($\rho = 0$). Its characteristic is shown as the solid curve in Fig. 7.9. The dashed curves in the same figure show the characteristics when the same laser is bidirectionally pumped with the same total pump power but several different splitting ratios. All of these lasers are more efficient than their single-side-pumped counterpart, the most dramatic efficiency increase by a factor of 2.7 occuring at a pump-power splitting ratio of $\rho = 50\%$.

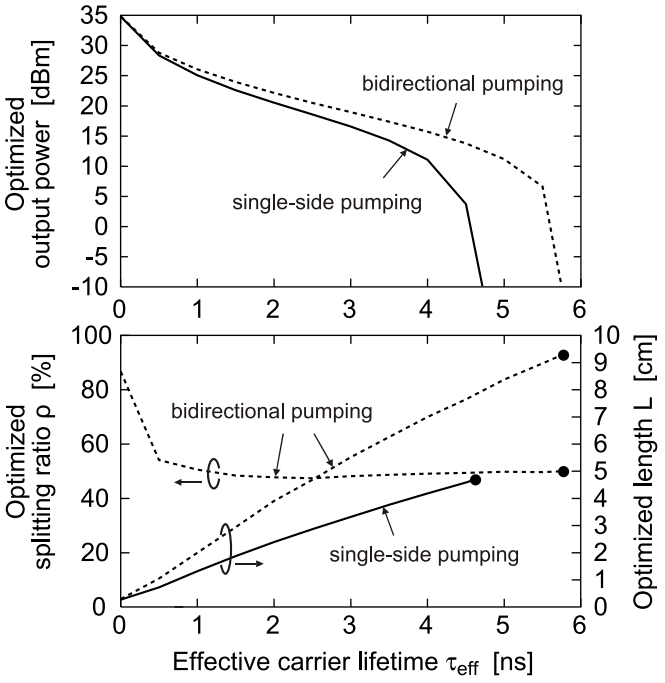

Figure 7.10.: *(a):* Maximum output powers of single-side-pumped (solid) and bidirectionally pumped (dashed) silicon Raman lasers as a function of the effective carrier lifetime τ_{eff}. Length L and pump-power splitting ratio ρ have been varied to find the maximum output power for each τ_{eff}. The optimization results for L and ρ are plotted in part *(b)*.

Optimization for various lifetimes

In this section we investigate how the laser-efficiency increase provided by bidirectional pumping depends on the effective carrier lifetime τ_{eff}. For each value of τ_{eff}, we first optimize the length L of a single-side-pumped laser such that it produces the maximum possible output power. Simultaneously, we optimize the length L and the pump-power splitting ratio ρ of a bidirectionally pumped laser. We assume that the available pump-laser power is limited to 8 W. The resulting maximum output powers for both laser types are shown in Fig. 7.10a as a function of τ_{eff}. As expected, bidirectionally pumped lasers are more efficient than single-side-pumped lasers, and the lasing efficiency is improved the more dramatically the larger τ_{eff} is. For example, when the lifetime is $\tau_{\text{eff}} = 3\,\text{ns}$, bidirectional pumping increases the maximum output power by 2.3 dB, whereas at $\tau_{\text{eff}} = 4.5\,\text{ns}$, the increase is already 10 dB. It can also be seen, in agreement with Fig. 7.7a, that single-side-pumped configurations do not lase as τ_{eff} exceeds 4.6 ns. Fig. 7.10a also shows that this maximum tolerable lifetime is larger for bidirectionally pumped lasers.

Fig. 7.10b shows the laser lengths and splitting ratios ρ corresponding to the optimized lasers from Fig. 7.10a. For large τ_{eff}, the optimized bidirectionally pumped lasers have a splitting ratio of 50%. The reason for this is as follows: because the Stokes powers are low, they nearly see the undepleted-pump gain which in turn is maximal when the left-hand and right-hand pump powers are kept as low as possible, i. e., when the pump power is equally split between both ends ($\rho = 50\%$, see Fig. 7.8). The optimal device

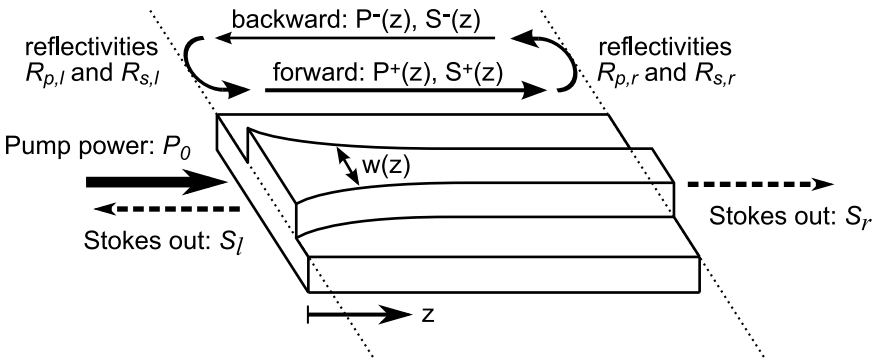

Figure 7.11.: Schematic of a tapered silicon Raman laser.

lengths increase with τ_{eff} until the maximum tolerable lifetimes of 4.65 and 5.82 ns, respectively, are reached (see Sect. 7.2.2). The optimal device lengths at those values of τ_{eff} correspond to the points towards which the closed threshold curves in Figs. 7.7a and 7.7b contract for increasing τ_{eff}.

7.3. Tapered silicon Raman lasers

It will be shown now that the concept of tapering introduced for silicon Raman amplifiers in Sect. 6.3 can also be successfully applied to silicon Raman lasers to enhance their efficiency. The results of this section have been published in [KRB05a]. A tapered silicon Raman laser is shown schematically in Fig. 7.11.

7.3.1. Modeling

The model we use to describe the longitudinal evolution of the pump and Stokes powers inside the silicon Raman laser is summarized in Sect. 5.5. The only additional simplification we make in this section is to approximate all effective areas for SRS and TPA occurring in Eqs.(5.50)–(5.52) by the same value and simply write A_{eff}. Also, we assume all confinement factors are unity. We have already made these simplifications in our analysis of tapered silicon Raman amplifiers. They are well justified for large waveguides, such as the rib waveguide whose effective areas have been plotted in Fig. 5.3.

In all simulations of tapered silicon Raman lasers, we will restrict ourselves to waveguides without any end-face coatings, i. e., $R_{p,l} = R_{p,r} = R_{s,l} = R_{s,r} = 30\%$ (only Fresnel reflection), $T_p = 1 - R_{p,l}$ (ideal input coupling). These reflectivities enter the model through the boundary conditions which are the same as for a non-tapered laser, see Sect. 7.1.1. The output power of the laser is defined as $P_{\text{out}} = P_s^+(L)(1 - R_{s,r})$.

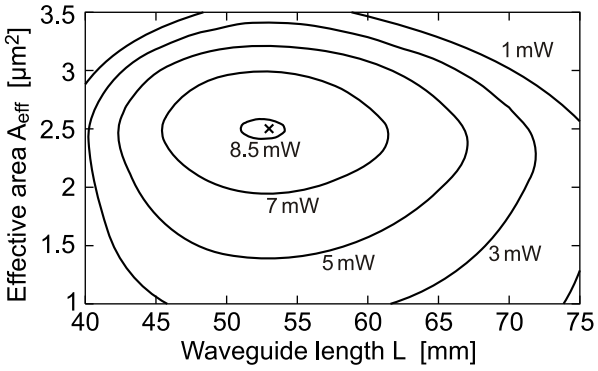

Figure 7.12.: Maximum output power for various lasers with non-tapered effective area A_{eff}, when pump power is limited to 5 W.

Throughout this section, we assume that the available pump-laser power is limited to 5 W, and we will look for silicon Raman lasers that yield maximum output power given these constraints by considering the dependence of the lasing characteristics on the waveguide length L and on the longitudinal variation of the effective area A_{eff}. We will show how the introduction of tapered effective areas can result in more efficient lasers for a given τ_{eff}, compared with the non-tapered lasers discussed in Sect. 7.1.

7.3.2. Optimal non-tapered laser

To start, we consider lasers in a non-tapered waveguide, i. e., the effective area A_{eff} is constant along z. Fig. 7.12 shows the maximum output power obtainable in such non-tapered lasers as a function of the waveguide length L and the effective area A_{eff} when a maximum pump power of 5 W is available. The effective free-carrier lifetime is assumed to be $\tau_{\text{eff}} = 3.0\,\text{ns}$. This is very close to the maximum tolerated effective carrier lifetime of 3.2 ns, above which no non-tapered laser can be realized.[2] Because of the closeness of the chosen $\tau_{\text{eff}} = 3.0\,\text{ns}$ to this critical value, the output powers obtainable from the analyzed silicon lasers are rather low—the best non-tapered laser ($A_{\text{eff}} = 2.5\,\mu\text{m}^2$ and $L = 53\,\text{mm}$, marked with a cross in Fig. 7.12) produces about 8.6 mW of Stokes output power.

Note from Fig. 7.12 that a decrease of the effective area does not necessarily result in more efficient lasers. The reason is that the relative weighting of FCA and Raman gain depends on the effective area: as can be seen from Eqs. (5.50)–(5.52), halving the effective area doubles the Raman gain, but at the same time increases the impact of FCA by a factor of four—loss increases faster than gain when decreasing A_{eff}, thus reducing the laser efficiency. On the other hand, an effective area that is too large throughout the laser is not advisable either – even though FCA is then suppressed much stronger

[2] The lifetime limit of 3.2 ns is obvious from Fig. 7.3 only for an effective area of $1.6\,\mu\text{m}^2$, but is in fact independent of the effective area, as a scaling of the differential equations shows.

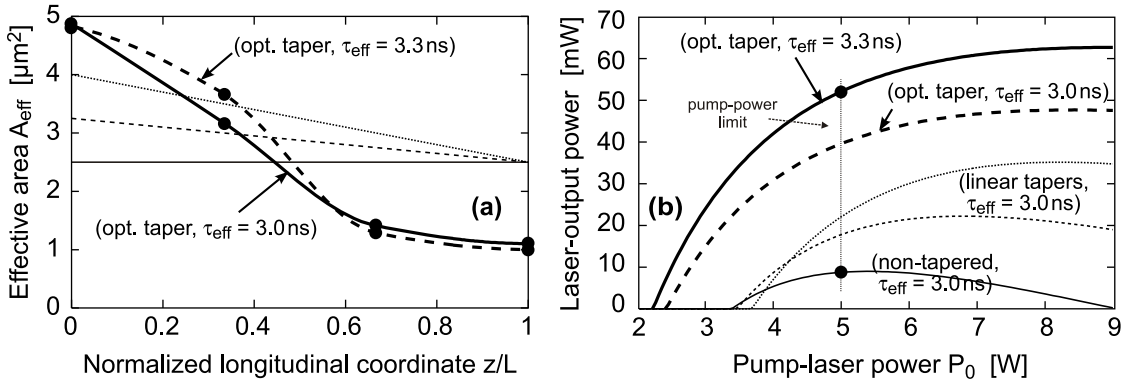

Figure 7.13.: Comparison of various tapered silicon Raman lasers. *(a):* longitudinal effective-area distribution $A_{\text{eff}}(z)$, where the longitudinal coordinate z has been normalized to the laser length L, *(b):* corresponding laser characteristics. The thick curves correspond to optimized tapers, while the thin solid curves correspond to the best non-tapered laser.

than Raman gain, we would also need more pump power at large effective areas, and we have set a limit of 5 W here. Therefore, there is an optimal (non-tapered) effective area in Fig. 7.12.

7.3.3. Tapered lasers

We now introduce an additional degree of freedom by allowing different effective areas at different positions inside the laser, for example by varying the width of the waveguide as suggested in Fig. 7.11. We have already discussed the principle for silicon Raman amplifiers in Sect. 6.3 – in regions where the total guided power is large (i. e., towards the pumped end of the silicon waveguide), FCA dominates over Raman gain. This dominance can be diminished by choosing a larger effective area $A_{\text{eff}}(z)$ only in that region: this results in a linear reduction of the local Raman gain, but in a quadratic reduction of FCA. On the other hand, in regions where relatively low amounts of power are guided, the effective area $A_{\text{eff}}(z)$ should be chosen smaller to increase the Raman gain.

The thin solid curve in Fig. 7.13b shows the input-output characteristics of the best non-tapered laser (marked with a cross in Fig. 7.12) with a constant $A_{\text{eff}} = 2.5\,\mu$m. Now we consider a tapered-waveguide laser: the other two thin curves in Fig. 7.13b show the characteristics when the effective area varies linearly along the waveguide with a fixed $A_{\text{eff}}(L) = 2.5\,\mu$m at the waveguide end according to the thin curves in Fig. 7.13a. At a pump power of 5 W, both tapered lasers yield a higher output power than the best laser in a non-tapered waveguide, in accordance with the discussion in the previous

paragraph. Even by a simple linear tapering of $A_{\text{eff}}(z)$, we have reduced the impact of FCA, and we have more than doubled the laser efficiency.

The thick solid curve in Fig. 7.13b shows the result of a simple optimization of the taper. We did not restrict ourselves to a linear taper but considered a more general taper instead, where we picked four values of $A_{\text{eff}}(z)$ at equidistant points along z (see thick dots in Fig. 7.13a) and interpolated with a piecewise cubic polynomial in between. Those four values of A_{eff} and the waveguide length L have been varied so as to find optimal values where the output power at $P_0 = 5\,\text{W}$ is maximal. When requiring that A_{eff} stay between 1 and $5\,\mu\text{m}^2$, the optimized laser has an output power of 51 mW, which is six times higher than the maximum output power of the best non-tapered laser (8.6 mW).

7.3.4. Lasing and shutdown thresholds

The characteristics in Fig. 7.13b show that the introduction of an effective-area taper strongly influences the threshold powers: while the lasing (lower) threshold is only slightly influenced, the shutdown (upper) threshold is shifted to significantly larger pump powers. This is also illustrated in Fig. 7.14, where the two thresholds are plotted for various waveguide lengths and several linear tapers. The shutdown threshold (dotted lines) grows with increasing effective area at the pumped side of the waveguide, showing that tapered lasers can be more tolerant against large free-carrier lifetimes τ_{eff}. Of course, the laser with an optimized non-linear taper and waveguide length (thick solid curve in Fig. 7.13a) is even more tolerant than all linear tapers shown in Fig. 7.14; its lasing and shutdown thresholds are 2.2 W and 52 W, respectively, the latter being far beyond the range plotted in Fig. 7.14.

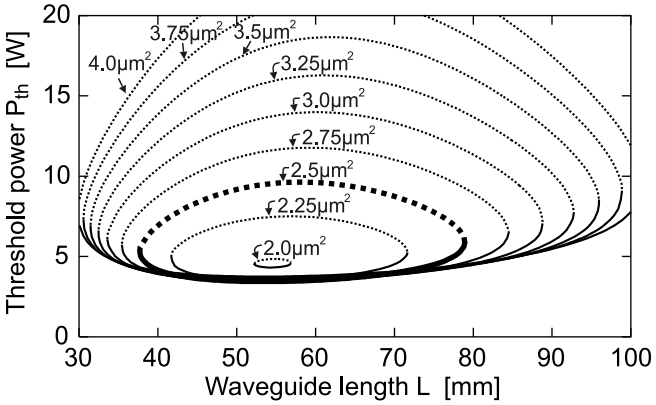

Figure 7.14.: Thresholds for lasing (solid) and shutdown (dotted) versus waveguide length L for linear effective-area tapers from indicated value at $z = 0$ to $2.5\,\mu\text{m}^2$ at $z = L$. The thick curve corresponds to the optimal non-tapered laser marked in Fig. 7.12.

The longitudinal variation of the effective area $A_{\text{eff}}(z)$ may be achieved practically by varying the waveguide geometry along the waveguide. However, a variation of the waveguide geometry may not only change A_{eff}, but also other parameters of the waveguide, for example the waveguide losses α and the effective charge-carrier lifetime τ_{eff}. A simple calculation shows that our principle still works even if τ_{eff} increases due to tapering: the thick dashed curve in Fig. 7.13a shows the characteristics corresponding to an optimized effective-area taper in a waveguide with an increased τ_{eff} of 3.3 ns. Again, the obtained output power of 39 mW is much higher than that of the best non-tapered laser with $\tau_{\text{eff}} = 3.0\,\text{ns}$. Note that a non-tapered laser with $\tau_{\text{eff}} = 3.3\,\text{ns}$ would never lase at all for any L or A_{eff}, see the discussion in Sect. 7.3.2. This shows that an effective-area taper increases the tolerance of the lasing characteristics against long charge-carrier lifetimes and significantly increases the efficiency of the silicon Raman laser.

7.4. Cascaded silicon Raman lasers as mid-infrared sources

In this final section, we show that the concept of *cascading*, which is well-known from Raman fiber lasers, can be successfully applied to silicon Raman lasers. We have published the results of this section in [KDRB06].

It will be shown that cascaded silicon Raman lasers, in which the pump light undergoes multiple Stokes shifts in a silicon waveguide, can efficiently convert near-infrared to mid-infrared radiation. The use of silicon waveguides for this purpose is particularly interesting, since TPA vanishes for wavelengths above 2.2 μm, such that FCA becomes insignificant if all wavelengths are large enough, and very efficient lasing should become possible. If the pump wavelength lies significantly below 2.2 μm, however, the effects of TPA and FCA becomes increasingly significant, and the question arises what is the shortest pump wavelength that can be used for a given waveguide.

7.4.1. Applications

Lasers emitting in the mid-infrared spectral region beyond 2 μm are of technological relevance because the fundamental vibrational and rotational absorption lines of many types of molecules fall into this region. For example, in the wavelength region around 3 μm, water exhibits very strong absorption [WWQ89], which suggests applications of 3-μm lasers in spectroscopy and in medicine [SV03]. Much research interest is directed towards realizing 3-μm sources in the form of solid-state, semiconductor and fiber lasers

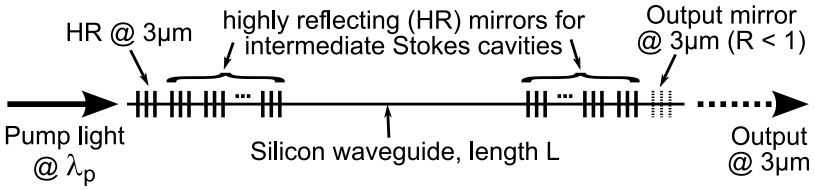

Figure 7.15.: Schematic view of a cascaded silicon Raman laser.

[SV03]. In this section, we investigate the possibility of using cascaded Raman cavities in a silicon waveguide in order to generate 3-μm radiation. The principle is to use stimulated Raman scattering (SRS) to shift the light of available near-IR pump sources to the desired output wavelength in the mid-IR through several intermediate Stokes shifts. Such a mid-IR source could be compactly realized in the entire transparency window of silicon (up to nearly 7 μm), without requiring the introduction of dopants with their fixed emission spectra.

Given the high efficiency of fiber-based cascaded Raman lasers, see Sect. 3, the use of cascaded Raman cavities in a silicon waveguide seems promising. However, the efficiencies that can be obtained and their dependence on the various technological and design parameters have not been analyzed so far. In particular, TPA and FCA must be taken into account in silicon waveguides but are not significant for Raman fiber lasers.

Fig. 7.15 illustrates the principle of a cascaded silicon Raman laser. The pump power of an external pump laser at wavelength λ_p is injected into the silicon waveguide, and Stokes light whose optical frequency is lower by the Raman shift of 15.6 THz is generated by Raman scattering. This first-order Stokes light circulates inside an intermediate cavity formed by highly reflecting elements (HR) such as Bragg gratings or dielectric coatings and acts itself as the pump source for the second-order Stokes line generated in the same waveguide. This cascading process is continued until the desired wavelength is reached (here, we design lasers with 3-μm wavelength output). Part of that light is allowed to leave the waveguide on the other end through an output reflector with power reflectivity $R < 1$.

7.4.2. Model

The parameters used in our simulations are based on the rib-waveguide structure from [LRJ+06], which is shown on the right-hand side of Fig. 5.1. We assume that the pump light and all Stokes lines propagate in the fundamental quasi-TE mode of the waveguide. In practice, this can be enforced, e. g., by making use of waveguide birefringence such that only the quasi-TE-mode reflection spectrum of the Bragg gratings lies inside the

Raman-gain spectrum.

The longitudinal evolution of the pump line and the various Stokes lines is governed by differential equations that are a straightforward extension of the model summarized in Sect. 5.5 to an arbitrary number of Stokes lines. As in that section, we assume that the waveguide is dispersive enough that four-wave mixing between the various laser lines plays no significant role. As the wavelengths occuring in the analyzed cascaded lasers vary in a wide range ($1.5 \ldots 3.0\,\mu$m, i. e., by a factor of two), it is essential that we take into account the wavelength dependence of the mode fields (and thus the effective areas, see Fig. 5.3, part of which is reproduced in Fig. 7.16) and of the bulk TPA and Raman-gain coefficients.

Our model for the TPA spectrum has already been summarized in Sect. 5.3 — we use the model of [Din03], which we calibrate such that the degenerate-TPA coefficient at a wavelength of 1427 nm has one of the higher values reported, 0.7 cm/GW [CRDJ04], in order not to underestimate the effects of nonlinear absorption, see Table 5.2. The degenerate TPA coefficient is plotted versus wavelength as the thick solid curve in Fig. 7.16. It vanishes for $\lambda > 2.2\,\mu$m, where the photon energy is less than half the indirect band gap of silicon.

As for the spectral dependence of the Raman-gain coefficient, we assume that the Raman-tensor components [GC80] and the Raman linewidth of silicon are constant in the wavelength range of interest, so that the Raman-gain constant scales essentially inversely with the Stokes wavelength [SB65, Boy03]. The thick dotted curve in Fig. 7.16 shows the peak Raman gain as a function of the pump wavelength, assuming that $g(\lambda_p = 1427\,\text{nm}) = 20\,\text{cm/GW}$ as in [JBD$^+$05], see Table 5.1. As realistic models for the wavelength dependence of the linear waveguide losses $\alpha(\lambda)$ in such a wide wavelength range are not available to the best of the author's knowledge, we will simply consider the effect of various different choices of constant loss coefficients. Potentially large losses caused by OH impurities in the silica cladding beyond $2\,\mu$m could be circumvented by undercutting of the silicon waveguide [JBD$^+$05].

For the numerical solution of the boundary-value problem describing the laser, we use the methods described in section 3.3.3 in the context of widely tunable cascaded RFLs.

7.4.3. Conversion efficiency versus lifetime and pump wavelength

In order to obtain Raman-laser output at $3.0\,\mu$m, one must choose a shorter pump wavelength whose corresponding optical frequency is offset from the desired output frequency

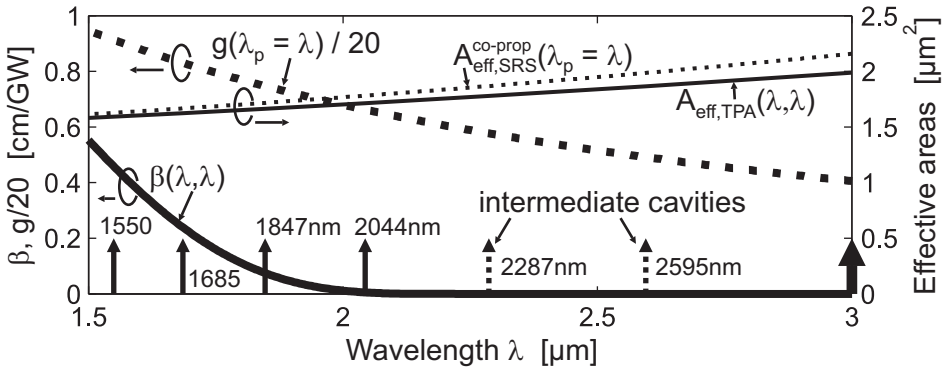

Figure 7.16.: Spectral dependence of the bulk coefficients (thick) and effective areas (thin) for degenerate Two-Photon Absorption (solid) and co-directional Stimulated Raman Scattering (dotted). The arrows indicate wavelengths offset by 15.6 THz from the desired output wavelength of 3.0 μm.

by an integer multiple of the silicon Raman shift of 15.6 THz. The solid upright arrows in Fig. 7.16 represent four possible choices that we have analyzed in the following. Intermediate cavities (dashed upright arrows) are needed in all these four arrangements. For each of the four pump-wavelength choices, we have optimized the laser length L in the range $0.5 \ldots 30$ cm, the output-coupler reflectivity R in the range $1 \ldots 90\%$ and the pump power in the range $0 \ldots 4$ W so that the output power of the cascaded laser is maximal. All other reflectivities have been fixed at 99%. This optimization was repeated for several effective carrier lifetimes τ_{eff}. Fig. 7.17 plots the optimized output power at 3.0 μm against the effective carrier lifetime.

We first consider the solid curve (a) in Fig. 7.17, which corresponds to a cascaded laser pumped at $\lambda_p = 2044$ nm, where we have assumed linear waveguide losses of 0.3 dB/cm [LRJ+06]. Even for the comparatively large effective carrier lifetime of $\tau_{\text{eff}} = 10$ ns, the output power of the cascaded silicon laser exceeds 1 W at a pump power of 4 W and thus has a conversion efficiency comparable to that of fiber-based cascaded Raman lasers [SV03, HBM+02]. The reason for this is that the TPA coefficient at the pump wavelength of 2044 nm is so small (see Fig. 7.16) that the rate of carrier generation by TPA is relatively low, and thus FCA becomes significant only for very long effective carrier lifetimes $\tau_{\text{eff}} > 10$ ns. Curve (b) in Fig. 7.17 shows the optimization results for higher linear losses of 1.0 dB/cm. Even for this value, which is rather high for the type of waveguide considered here, the achievable output powers still exceed 0.5 W.

Now we use shorter pump wavelengths. The nonlinear absorption effects will become progressively stronger, because the TPA coefficient increases towards shorter wavelengths (see thick solid curve in Fig. 7.16), and consequently the efficiency of cascaded

lasers will decrease. Curve (c) in Fig. 7.17 shows the maximal output power as a function of the effective carrier lifetime for a laser pumped at 1847 nm, i. e., one more cascade than for curve (a) and otherwise unchanged parameters. The output power exceeds 0.25 W for effective carrier lifetimes $\tau_{\text{eff}} < 1\,\text{ns}$. For $\tau_{\text{eff}} = 10\,\text{ns}$, however, it is not possible to obtain lasing at 3 μm at all.

For lasers with even shorter pump wavelengths, we found that waveguides with sub-nanosecond effective carrier lifetimes are necessary. Curves (d) and (e) in Fig. 7.17 correspond to pumping at 1685 nm. We had to assume slightly more favourable simulation parameters than for curve (c): for (d), we assumed lower linear losses of only 0.1 dB/cm, whereas for (e), we assumed a more optimistic value for the Raman-gain coefficient of $g(\lambda_p = 1427\,\text{nm}) = 30\,\text{cm/GW}$ [EDRMO+04]. We obtain output powers larger than 100 mW for effective carrier lifetimes $\tau_{\text{eff}} < 0.3\,\text{ns}$. Finally, curves (f) and (g) show the maximal output power versus effective carrier lifetime for pumping at 1550 nm. Both curves correspond to an optimistic choice for the linear losses of $\alpha = 0.1\,\text{dB/cm}$, and the Raman-gain coefficients for curves (f) and (g) are 20 and 30 cm/GW, respectively. The laser produces significant output power only for effective carrier lifetimes well below 1 ns.

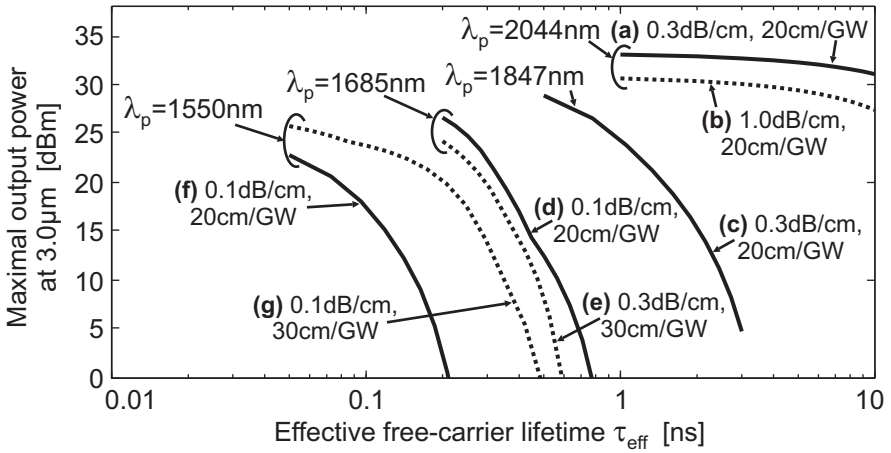

Figure 7.17.: Maximal output power of cascaded silicon Raman lasers emitting at 3.0 μm versus effective carrier lifetime τ_{eff} for four different pump wavelengths. Length L and output reflectivity R have been optimized.

In conclusion, we have shown that a cascaded silicon Raman laser can be used to efficiently convert light from near-IR wavelengths to 3 μm. For example, when pumped with 4 W at 2044 nm, one can obtain output powers of more than 0.5 W at 3 μm even for waveguides with a rather large effective carrier lifetime of 10 ns. The advantage of the cascaded silicon Raman laser for generation of mid-IR radiation is that the output

wavelength can be designed to lie anywhere in the mid-IR, provided the lasing silicon waveguide is transparent in the relevant spectral range and suitable pump sources are available.

7.5. Chapter summary

In this chapter, we have shown by numerical simulations that continuous-wave Raman lasing is possible in silicon waveguides. However, we have found that silicon Raman lasers have a roll-over point in their characteristics beyond which the output power decreases again, and a shutdown threshold at which lasing stops completely due to the increasing influence of FCA. We have then shown that in a bidirectionally pumped SRL, FCA is mitigated because the pump power is distributed more equally along the waveguide. Furthermore, the concept of tapering introduced in section 6.3 was applied to SRLs, showing that tapered SRLs can be significantly more efficient than non-tapered SRLs. Finally, we have shown that cascaded SRLs can be used to realize efficient mid-infrared sources based on near-IR pump lasers.

8. Conclusions

The nonlinear effect of stimulated Raman scattering is finding an increasing number of interesting applications in optical communications. For example, Raman amplifiers in optical fibers have recently gained in attractiveness as a spectrally flexible, low-noise alternative or add-on to conventional erbium-doped fiber amplifiers in long-haul optical communication systems, and they are starting to appear as key elements in modern commercial fiber-optic communications equipment. Raman fiber lasers, which too are based on the nonlinear effect of stimulated Raman scattering, are often used to pump these amplifiers. Finally, a quite novel application of stimulated Raman scattering is in Raman amplifiers and lasers based on silicon waveguides. These devices have been researched for a few years only, but they have the potential of being employed in future telecommunications equipment.

In this thesis, several new concepts for Raman amplifiers and lasers both in optical fibers and silicon waveguides with a strong potential of increasing the performance of fiber-optic communication systems have been developed, modeled and optimized. Alternative applications, especially for silicon-based designs operating in the mid-infrared region beyond 2 μm, may be found in spectroscopy and medicine.

In the first part of the thesis, Raman fiber lasers (RFLs) have been designed for the use as pump sources for Raman fiber amplifiers. Double-cavity RFLs have been proposed, in which the threshold pump power and the conversion efficiency at large pump powers can be optimized independently of each other, thereby improving the overall power efficiency of Raman-amplified transmission spans in which the pump power must be dynamically switched. Widely tunable RFLs have been analyzed, and a practical design tunable over the entire optical-communications wavelength range has been developed, which can be used, e. g., as an adaptive pump source for Raman amplifiers in which the channel load may change over time.

The stability of RFLs used as pump sources for optical communications is an important characteristic, as any fluctuations of the output power of the RFL are subsequently transferred to the signal inside a Raman amplifier, especially in co-pumped transmission

spans. A model describing the transfer of relative intensity noise (RIN) from the RFL's pump laser to the output of this RFL has been developed, which can qualitatively explain the measured RIN of an RFL. Based on that model, single-cavity RFLs have been optimized such that the bit-error-rate degradation of a Raman-amplified transmission span due to noise on the RFL is minimized. Furthermore, the concept of the double-cavity RFL introduced at the beginning can be used to realize lasers with characteristics exhibiting a conversion maximum, at which fluctuations of the pump-laser power are not transferred to the RFL output, thus stabilizing the RFL. Finally, it has been found that the power-dependent Stokes line broadening which is known to occur in RFLs can stabilize multi-wavelength RFLs against pump-power variations, while the conventional models of RFLs predict a significant instability.

In the second part of the thesis, fundamental properties and limitations of silicon Raman amplifiers and lasers have been analyzed, and novel designs with increased efficiency have been proposed. Compared to the case of fibers, additional nonlinear effects occur in silicon, namely Two-Photon Absorption (TPA) and Free-Carrier Absorption (FCA). These effects compete with the desired Raman amplification, and the design of efficient amplifiers or lasers consists in suitably balancing the various nonlinear effects. The basis of all these investigations is formed by a newly developed comprehensive mathematical model describing the propagation of the pump and Stokes waves inside a silicon waveguide under the influence of nonlinear effects. The model takes into account the high refractive-index contrast of silicon waveguides and the resulting fully vectorial character of the mode fields. Based on available material data, the nonlinear effects of stimulated Raman scattering and TPA between co- and counterpropagating waves have been formulated in terms of compact formulas for the effective areas, while FCA is represented by overlap integrals of the mode fields with the steady-state free-carrier distribution resulting from a carrier-diffusion process.

The nonlinear absorption effects TPA and FCA lead to a significantly different behavior of Raman-active devices based on silicon as compared to their fiber-optic counterparts. In particular, it has been shown that FCA sets an upper limit to the pump power that can be usefully injected in such devices, thus limiting amplifier gains and lasing efficiencies. The characteristics of silicon Raman lasers have been shown to have a roll-over point above which a further increase of the pump power actually decreases the laser output power. Eventually, at the shutdown threshold, lasing even stops completely. Explicit design rules for optimal silicon Raman amplifiers have been derived.

Aiming at increasing the maximum possible gain of silicon Raman amplifiers, it has been shown that tapering the modal effective area along the propagation direction keeps

the local pump intensity optimal at each position along the waveguide and thus increases the achievable total gain. The same principle has been shown to be useful for significantly increasing the output power of silicon Raman lasers. On the other hand, bidirectional pumping, where the pump power is injected from both sides, reduces the pump-power peaks at the waveguide ends and avoids excessive FCA by distributing the pump power more equally along the waveguide, leading to more efficient lasing. Furthermore, in a cladding-pumped silicon waveguide the pump power is partially removed from the silicon and guided in an additional cladding surrounding the silicon, thus mitigating the effect of FCA on the pump power. Optimal designs find a trade-off between this FCA mitigation and the concomitant Raman-gain reduction such that the total gain of the cladding-pumped amplifier is larger than that possible with core-pumped amplifiers. For optimal amplifiers or lasers, waveguide lengths on the order of tens of centimeters can be required. In order to realize these on a silicon chip, the waveguide needs to be at least partly curved. It was found that the curvature losses of silicon waveguides can vary in a wide range dependending on the waveguide geometry. Due to the hybrid leakage in curved silicon rib waveguides, fully vectorial simulation tools such as the finite-difference mode solver written in this thesis are indispensible for an accurate modeling of the polarization-dependent curvature loss and the practical design of curved silicon waveguides.

Finally, it has been shown that the concept of cascaded cavities known from Raman fiber lasers can be used successfully for spectrally cascading silicon Raman lasers to realize wavelength converters from near-infrared to mid-infrared radiation (such as $3\,\mu$m). As TPA becomes increasingly more severe for decreasing wavelengths, the achievable conversion efficiencies depend on the choice of the pump wavelength. If the latter is above $2\,\mu$m, the conversion efficiencies can approach those of RFLs.

In summary, new designs for Raman-based components for use in optical communications have been presented. In particular the proposed silicon-based Raman amplifiers and lasers have the potential of increasing the practicability of Raman amplification in future silicon-based telecommunications, where up to now a continuous-wave gain of at most 3 dB has been experimentally achieved. Together with ongoing technological improvements on the materials and processing side, such as a further reduction of the linear waveguide losses and the free-carrier lifetime of silicon waveguides, the presented concepts should help bringing silicon-based Raman amplification closer to practical applicability and commercial maturity.

A. Finite-difference mode solver

Motivation

An accurate, full-vectorial computation of the mode fields of optical waveguides was useful in various parts of this thesis for obtaining quantitative results. For example, in section 6.4 where we have discussed the cladding-pumped silicon Raman amplifier, the pump mode is a higher-order mode of the structure (see Fig. 6.8), which has a complicated vectorial structure inside the silicon, where it would be a very coarse approximation to assume that the field is uniformly polarized; none of the cartesian field components are negligible, and without a numerical tool it would have been difficult to obtain a realistic estimate for the mode field.

Furthermore, in section 6.5, we show that full-vectorial computations are essential for the design of silicon rib waveguides with low TM-mode curvature loss. Scalar [YK93], semi-vectorial [GBM91, DH04] or effective-index models [BG00] can significantly underestimate the curvature losses of the quasi-TM mode, because they do not allow for coupling of the quasi-TM rib mode to the radiating TE slab modes, which may be the principal curvature-loss mechanism.

Design of the mode solver

In order to allow for curved waveguides, the Helmholtz equation is written in cylindrical coordinates, where the angular coordinate corresponds to the propagation direction in the curved waveguide. The waveguide cross-section is described by regions of piecewise constant refractive index n. The eigenvalue problem for the waveguide modes is formulated in terms of the two transverse H-field components of the modes:

$$H^x_{xx} + H^x_{yy} + \frac{c}{1+cy} H^x_y + \left[\frac{\gamma^2}{(1+cy)^2} + k^2 n^2 \right] H^x = 0, \tag{A.1}$$

$$H^y_{xx} + H^y_{yy} + \frac{c}{1+cy} (3H^y_y + 2H^x_x) + \left[\frac{\gamma^2 + c^2}{(1+cy)^2} + k^2 n^2 \right] H^y = 0, \tag{A.2}$$

where $k = 2\pi/\lambda$, and x and y are the vertical and lateral coordinates, respectively, as in Fig. 5.1. The curvature c is the inverse of the radius of curvature R. The center

of revolution is at $y = -R$. These equations, together with appropriate boundary conditions at the interfaces between two regions of different refractive index n, constitute an eigenvalue problem for the magnetic field $H^{x,y}$ and the complex field-amplitude gain constant γ. The modes of a straight waveguide can be obtained from the formulation simply by assuming zero curvature, $c = 0$.

Perfectly Matched Layers (PMLs) are introduced through a complex coordinate transform [CM98] in order to allow for outgoing radiation, which always occurs in curved waveguides but may also occur for the leaky modes of a straight waveguide. At the interfaces between two regions of different refractive index n, the boundary conditions for the electromagnetic field have to be incorporated when discretizing the transverse cross section. To this aim, the method described in [CCC02] was used to derive first-order (six-point) finite-difference expressions for the differential operators. The formulas for four different choices of the six grid points are then averaged in order to obtain a symmetric formulation.

Finally, the resulting matrix eigenvalue problem is solved using the ARPACK package [LSY98], where we use the shift–invert mode which enables us to selectively calculate modes in the neighborhood of a given effective index. The loss per 90° bend is calculated from the imaginary part of the complex propagation constant. The remaining field components (the longitudinal H field, the E-field and the Poynting vector) are calculated from the two transverse H-field components through Maxwell's equations.

We have verified that the software yields results that agree with known exact solutions, for example for the step-index fiber. Also, the results for the curvature losses of rib waveguides given in [GBM91,YK93,BG00,DH04] are accurately reproduced by our mode solver; see the discussion in section 6.5.3.

List of publications

[CKRB03] S. Cierullies, M. Krause, H. Renner, and E. Brinkmeyer. Widely Tunable CW Raman Fiber Laser Supported by Switchable FBG Resonators. In *European Conference on Optical Communication (ECOC)*, pages 224–225, 2003. Paper Tu3.2.3.

[CKRB04] S. Cierullies, M. Krause, H. Renner, and E. Brinkmeyer. Switching dynamics of Raman fiber lasers. In *Conference on Lasers and Electro-Optics (CLEO)*, May 2004. Paper CMD2.

[CKRB05] S. Cierullies, M. Krause, H. Renner, and E. Brinkmeyer. Experimental and Numerical Study of the Switching Dynamics of Raman Fiber Lasers. *Appl. Phys. B*, 80(2):177–183, February 2005.

[HKM05] A. Harke, M. Krause, and J. Mueller. Low-loss single-mode amorphous silicon waveguides. *Electron. Lett.*, 41:1377–1379, December 2005.

[KCR03] M. Krause, S. Cierullies, and H. Renner. Stabilizing effect of line broadening in Raman fiber lasers. *Opt. Commun.*, 227(4–6):355–361, November 2003.

[KCRB03] M. Krause, S. Cierullies, H. Renner, and E. Brinkmeyer. Design of widely tunable Raman fibre lasers supported by switchable FBG resonators. *Electron. Lett.*, 39(25):1795–1797, December 2003.

[KCRB04] M. Krause, S. Cierullies, H. Renner, and E. Brinkmeyer. Pump-to-Stokes transfer of relative intensity noise in Raman fiber lasers. In *Conference on Lasers and Electro-Optics (CLEO)*, May 2004. Paper CMD5.

[KCRB06] M. Krause, S. Cierullies, H. Renner, and E. Brinkmeyer. Pump-to-Stokes RIN transfer in Raman fiber lasers and its impact on the performance of co-pumped Raman amplifiers. *Opt. Commun.*, 260(2):656–661, April 2006.

[KDRB06] M. Krause, R. Draheim, H. Renner, and E. Brinkmeyer. Cascaded silicon Raman lasers as mid-infrared sources. *Electron. Lett.*, 42(21):1224–1226, October 2006.

[KR04] M. Krause and H. Renner. Double-cavity Raman fibre lasers with suppressed pump-to-Stokes transfer of low-frequency RIN. *Electron. Lett.*, 40(11):656–657, May 2004.

[KR05a] M. Krause and H. Renner. Numerical calculation of the linewidth of Raman fiber lasers due to spontaneous Raman scattering. *AEÜ Int. J. Electron. Commun.*, 59(8):502–509, December 2005.

[KR05b] M. Krause and H. Renner. Theory and design of double-cavity Raman fiber lasers. *J. Lightwave Technol.*, 23(8):2474–2483, August 2005.

[KRB04] M. Krause, H. Renner, and E. Brinkmeyer. Analysis of Raman lasing characteristics in silicon-on-insulator waveguides. *Opt. Express*, 12(23):5703–5710, November 2004.

[KRB05a] M. Krause, H. Renner, and E. Brinkmeyer. Efficiency increase of silicon-on-insulator Raman lasers by reduction of free-carrier absorption in tapered waveguides. In *Conference on Lasers and Electro-Optics (CLEO)*, 2005. Paper CThB1.

[KRB05b] M. Krause, H. Renner, and E. Brinkmeyer. Incorporation of free-carrier diffusion into the modeling and design of a silicon strip-waveguide Raman laser. In *Messung und Modellierung in der Optischen Nachrichtentechnik (MMONT)*, 2005. Paper Do 4.

[KRB05c] M. Krause, H. Renner, and E. Brinkmeyer. Mitigation of Free-Carrier Absorption and Efficiency Increase in Silicon Waveguide Lasers by Bidirectional Pumping. In *2nd International Conference on Group IV Photonics*, 2005. Paper P15.

[KRB06a] M. Krause, H. Renner, and E. Brinkmeyer. Polarization-Dependent Curvature Loss in Silicon Rib Waveguides. *IEEE J. Sel. Top. Quantum Electron.*, 12(6):1359–1362, Nov/Dec 2006. (Part II, Special Issue on Silicon Photonics).

[KRB+06b] M. Krause, H. Renner, E. Brinkmeyer, S. Fathpour, D. Dimitropoulos, V. Raghunathan, and B. Jalali. Efficient Raman Amplification in Cladding-Pumped Silicon Waveguides. In *3rd International Conference on Group IV Photonics (GFP)*, 2006. Paper P6.

[KRB06c] M. Krause, H. Renner, and E. Brinkmeyer. Efficient Raman lasing in tapered silicon waveguides. *Spectroscopy*, 21(1):26–32, January 2006.

[KRH+05] M. Krause, H. Renner, A. Harke, J. Müller, and E. Brinkmeyer. Leakage Loss in Trench-Bulge Waveguides. *J. Lightwave Technol.*, 23(5):1890–1895, May 2005.

[KSC+05] M. Krause, R. Stanslovaityte, S. Cierullies, H. Renner, and E. Brinkmeyer. Double-Cavity Raman Fiber Laser with Improved Tolerance against High-RIN Pump Lasers. In *European Conference on Optical Communication (ECOC)*, 2005. Paper We4.P.25.

[RCK03] H. Renner, S. Cierullies, and M. Krause. Scaling rules for Raman fiber lasers. In *Optical Fiber Communication Conference (OFC)*, 2003. Paper MF25.

[RK06] H. Renner and M. Krause. Maximal total gain of non-tapered silicon-on-insulator Raman amplifiers. In *Optical Amplifiers and Their Applications (OAA) Topical Meeting*, 2006. Paper OMD2.

[RKB05] H. Renner, M. Krause, and E. Brinkmeyer. Maximal Gain and Optimal Taper Design for Raman Amplifiers in Silicon-on-Insulator Waveguides. In *Integrated Photonics Research and Applications Topical Meeting (IPRA)*, 2005. Paper JWA3.

Bibliography

[Agr01] G. P. Agrawal. *Nonlinear Fiber Optics*. Academic Press, 3rd edition, 2001.

[AMR88] U. M. Ascher, R. M. M. Mattheij, and R. D. Russell. *Numerical solution of boundary value problems for ordinary differential equations*. Prentice Hall, 1988.

[APT+01] F. Ahmed, M. Prabhu, A. Taniguchi, N. Kim, K. Ueda, and N. Kishi. Numerical Modeling and Experimental Confirmation of an Efficient Phosphosilicate-Fiber Raman Laser. *Jap. J. of Appl. Phys.*, 40(11):6411–6414, November 2001.

[Aus82] M. W. Austin. GaAs/GaAlAs Curved Rib Waveguides. *IEEE J. Quantum Electron.*, QE-18(4):795–800, April 1982.

[AY79] J. AuYeung and A. Yariv. Theory of cw Raman oscillation in optical fibers. *J. Opt. Soc. Am.*, 69(6):803–807, June 1979.

[BBR+02] J.-C. Bouteiller, K. Brar, S. Radic, J. Bromage, Z. Wang, and C. Headley. Dual-order Raman pump providing improved noise figure and large gain bandwidth. In *Optical Fiber Communications Conference (OFC)*, 2002. Post-Deadline Paper FB3.

[BBT+03] J.-C. Bouteiller, J. Bromage, H.-J. Thiele, K. Brar, and L. E. Nelson. Design Rules for Raman–amplified Long-Span Transmission. In *European Conference on Optical Communications (ECOC)*, 2003.

[BCF+05] S. A. Babin, D. V. Churkin, A. A. Fotiadi, S. I. Kablukov, O. I. Medvedkov, and E. V. Podivilov. Relative Intensity Noise in Cascaded Raman Fiber Lasers. *IEEE Photon. Technol. Lett.*, 17(12):2553–2555, December 2005.

[BCI+06] S. A. Babin, D. V. Churkin, A. E. Ismagulov, S. I. Kablukov, and E. V. Podivilov. Spectral broadening in raman fiber lasers. *Opt. Lett.*, 31:3007–3009, 2006.

[BCK05a] S. A. Babin, D. V. Churkin, and S. I. Kablukov. Longitudinal Mode Structure of the Two-Stage Raman Fiber Laser. *Laser Phys.*, 15(2):300–305, 2005.

[BCK+05b] S. A. Babin, D. V. Churkin, S. I. Kablukov, E. V. Podivilov, O. I. Medvedkov, and A. A. Fotiadi. Pump-to-Stokes relative intensity noise (RIN) transfer in Raman fiber lasers: observations and modeling. In *Optical Fiber Communication Conference (OFC)*, 2005. Paper OTuN6.

[BDB+00] I. A. Bufetov, E. M. Dianov, M. M. Bubnov, M. V. Grekov, S. A. Vasiliev, O. I. Medvedkov, A. V. Shubin, A. N. Guryanov, V. F. Khopin, and M. V. Yashkov. CW highly efficient 1.24 μm Raman laser based on low-loss phosphosilicate fiber. *Advances in Fiber Optics, Proceedings of SPIE*, 4083:111–117, 2000.

[BDJ+05] W. Bogaerts, P. Dumon, P. Jaenen, J. Wouters, S. Beckx, V. Wiaux, D. V. Thourhout, D. Taillaert, B. Luyssaert, and R. Baets. Silicon-on-insulator nanophotonics. In T. Pustelny, P. V. Lambeck, and C. Gorecki, editors, *Integrated Optics: Theory and Applications, Proc. SPIE*, volume 5956, pages 181–195, 2005.

[BFC+06] G. Bolognini, S. Faralli, A. Chiuchiarelli, F. Falconi, and F. D. Pasquale. High-Power and Low-RIN Lasers for Advanced First- and Higher Order Raman Copumping. *IEEE Photon. Technol. Lett.*, 18(15):1591–1593, August 2006.

[BG00] W. Berglund and A. Gopinath. WKB Analysis of Bend Losses in Optical Waveguides. *J. Lightwave Technol.*, 18(8):1161–1166, August 2000.

[BGL04] B. Burgoyne, N. Godbout, and S. Lacroix. Transient regime in a nth-order cascaded CW Raman fiber laser. *Opt. Express*, 12(6):1019–1024, March 2004.

[BGL05] B. Burgoyne, N. Godbout, and S. Lacroix. Theoretical analysis of nth-order cascaded continuous-wave Raman fiber lasers. I. Model and resolution. *J. Opt. Soc. Am. B*, 22(4):764–771, April 2005.

[BGO03] G.-L. Bona, R. Germann, and B. J. Offrein. SiON high-refractive-index waveguide and planar lightwave circuits. *IBM J. Res. & Dev.*, 47(2/3):239–249, March/May 2003.

[BJ04] O. Boyraz and B. Jalali. Demonstration of a silicon Raman laser. *Opt. Express*, 12(21):5269–5273, October 2004.

[Boy03] R. W. Boyd. *Nonlinear Optics*. Academic Press, 2nd edition, 2003.

[Car82] M. Cardona. *Light Scattering in Solids II*, volume 50 of *Topics in Applied Physis*, chapter 2, pages 19–178. Springer-Verlag, 1982.

[CCC02] Y.-C. Chiang, Y.-P. Chiou, and H.-C. Chang. Improved Full-Vectorial Finite-Difference Mode Solver for Optical Waveguides With Step-Index Profiles. *J. Lightwave Technol.*, 20(8):1609–1618, August 2002.

[CDHJ02] R. Claps, D. Dimitropoulos, Y. Han, and B. Jalali. Observation of Raman emission in silicon waveguides at 1.54μm. *Opt. Express*, 10(22):1305–1313, November 2002.

[CDJ02] R. Claps, D. Dimitropoulos, and B. Jalali. Stimulated Raman scattering in silicon waveguides. *Electron. Lett.*, 38(22):1352–1354, October 2002.

[CDR+03] R. Claps, D. Dimitropoulos, V. Raghunathan, Y. Han, and B. Jalali. Observation of stimulated Raman amplification in silicon waveguides. *Opt. Express*, 11(15):1731–1739, July 2003.

[CHB04] M. M. Clifford Headley and J.-C. Bouteiller. *Raman Amplifiers for Telecommunications 2*, chapter 11, Raman Fiber Lasers, pages 353–382. Springer, 2004.

[Cie05] S. Cierullies. *Abstimmbarkeit und Schaltverhalten kaskadierter Raman-Faserlaser*. PhD thesis, Technische Universität Hamburg-Harburg, 2005. Cuvillier Verlag, Göttingen.

[CLJ+00] D. I. Chang, D. S. Lim, M. Y. Jeon, H. K. Lee, and K. H. Kim. Dual-wavelength cascaded Raman fiber laser. In *IEEE LEOS Annual Meeting*, pages 395–396, 2000. Paper WA1.

[CM98] F. Collino and P. Monk. The Perfectly Matched Layer in Curvilinear Coordinates. *SIAM J. Sci. Comput.*, 19(6):2061–2090, November 1998.

[CPL+05] S. P. Chan, C. E. Png, S. T. Lim, G. T. Reed, and V. M. N. Passaro. Single-Mode and Polarization-Independent Silicon-on-Insulator Waveguides With Small Cross Section. *J. Lightwave Technol.*, 23(6):2103–2111, June 2005.

[CPO06] X. Chen, N. C. Panoiu, and R. M. Osgood, Jr. Theory of Raman-Mediated Pulsed Amplification in Silicon-Wire Waveguides. *IEEE J. Quantum Electron.*, 42(2):160–170, February 2006.

[CRB03] S. Cierullies, H. Renner, and E. Brinkmeyer. Numerical Optimization of Multi-Wavelength and Cascaded Raman Fiber Lasers. *Opt. Commun.*, 217(1-6):233–238, February 2003.

[CRDJ04] R. Claps, V. Raghunathan, D. Dimitropoulos, and B. Jalali. Influence of nonlinear absorption on Raman amplification in Silicon waveguides. *Opt. Express*, 12(12):2774–2780, June 2004.

[D+05] E. M. Dianov et al. Raman fibre lasers based on heavily GeO2-doped fibres. *Quantum Electron.*, 35(5):435–441, 2005.

[DH88] R. J. Deri and R. J. Hawkins. Polarization, scattering and coherent effects in semiconductor rib waveguide bends. *Opt. Lett.*, 13(10):922–924, October 1988.

[DH04] D. Dai and S. He. Analysis of characteristics of bent rib waveguides. *J. Opt. Soc. Am. A*, 21(1):113–121, January 2004.

[DHCJ03] D. Dimitropoulos, B. Houshmand, R. Claps, and B. Jalali. Coupled-mode theory of the Raman effect in silicon-on-insulator waveguides. *Opt. Lett.*, 28(20):1954–1956, October 2003.

[Din03] M. Dinu. Dispersion of Phonon-Assisted Nonresonant Third-Order Nonlinearities. *IEEE J. Quantum Electron.*, 39(11):1498–1503, November 2003.

[DJC+05] D. Dimitropoulos, R. Jhaveri, R. Claps, J. C. S. Woo, and B. Jalali. Lifetime of photogenerated carriers in silicon-on-insulator rib waveguides. *Appl. Phys. Lett.*, 86:071115, 2005.

[DQG03] M. Dinu, F. Quochi, and H. Garcia. Third-order nonlinearities in silicon at telecom wavelengths. *Appl. Phys. Lett.*, 82(18):2954–2956, May 2003.

[EDRMO+04] R. L. Espinola, J. I. Dadap, J. Richard M. Osgood, S. J. McNab, and Y. A. Vlasov. Raman amplification in ultrasmall silicon-on-insulator wire waveguides. *Opt. Express*, 12(16):3713–3718, August 2004.

[EMN00] Y. Emori, S.-I. Matsushita, and S. Namiki. Cost-effective depolarized diode pump unit designed for C-band flat-gain Raman amplifiers to control EDFA gain profile. In *Optical Fiber Communication Conference (OFC)*, 2000. Paper FF4.

[FBC+05] A. A. Fotiadi, S. A. Babin, D. V. Churkin, S. I. Kablukov, and E. V. Podivilov. Origin of uniform pump-to-Stokes relative intensity noise (RIN) transfer in Raman fiber lasers. In *Proc. Symposium IEEE/LEOS Benelux Chapter, Mons, Belgium*, pages 209–212, 2005. Paper P.31.

[FHM01] C. R. S. Fludger, V. Handerek, and R. J. Mears. Pump to Signal RIN Transfer in Raman Fiber Amplifiers. *J. Lightwave Technol.*, 19(8):1140–1148, August 2001.

[Fli91] N. Fliege. *Systemtheorie*. Teubner, 1991.

[GBM91] J.-S. Gu, P.-A. Besse, and H. Melchior. Method of Lines for the Analysis of the Propagation Characteristics of Curved Optical Rib Waveguides. *IEEE J. Quantum Electron.*, 27(3):531–537, March 1991.

[GC80] M. Grimsditch and M. Cardona. Absolute Cross-Section for Raman Scattering by Phonons in Silicon. *phys. stat. sol. (b)*, 102:155–161, 1980.

[GEM+94] S. G. Grubb, T. Erdogan, V. Mizrahi, T. Strasser, W. Y. Cheung, W. A. Reed, P. J. Lemaire, A. E. Miller, S. G. Kosinski, G. Nykolak, and P. C. Becker. 1.3 μm Cascaded Raman Amplifier in Germanosilicate Fibers. In *Optical Amplifiers and their Applications Topical Meeting, Postconference Edition*, pages 187–190, 1994. Paper PD3.

[HA05] C. Headley and G. P. Agrawal, editors. *Raman Amplification in Fiber Optical Communication Systems*. Elsevier, 2005.

[HBM+02] C. Headley, J.-C. Bouteiller, M. Mermelstein, K. Brar, and C. Horn. Raman fiber lasers as pumps for Raman amplification. In *Active and Passive Optical Components for WDM Communications II, Proc. SPIE*, volume 4870, pages 191–205, 2002.

[Hea05] C. Headley. *Raman Amplification in Fiber Optical Communication Systems*, chapter 7, Cascaded Raman Resonators, pages 303–366. Elsevier, 2005.

[Hel77] R. W. Hellwarth. Third-order optical susceptibilities of liquids and solids. *Prog. Quant. Electr.*, 5:1–68, 1977.

[HKJ76] K. O. Hill, B. S. Kawasaki, and D. C. Johnson. Low-threshold cw Raman laser. *Appl. Phys. Lett.*, 29(3):181–183, August 1976.

[HW94] D. C. Hutchings and B. S. Wherrett. Theory of anisotropy of two-photon absorption in zinc-blende semiconductors. *Phys. Rev. B*, 49(4):2418–2426, January 1994.

[JBD+05] B. Jalali, O. Boyraz, D. Dimitropoulos, V. Raghunathan, R. Claps, and P. Koonath. Silicon Raman Amplifiers, Lasers, and Their Applications. In *Conference on Group IV Photonics (GFP)*, 2005. Paper ThA1.

[JLSA77] R. K. Jain, C. Lin, R. H. Stolen, and A. Ashkin. A tunable multiple Stokes cw fiber Raman oscillator. *Appl. Phys. Lett.*, 31(2):89–90, July 1977.

[JM01] S. D. Jackson and P. H. Muir. Theory and numerical simulation of nth-order cascaded Raman fiber lasers. *J. Opt. Soc. Am. B*, 18(9):1297–1306, September 2001.

[JPR06] B. Jalali, M. Paniccia, and G. Reed. Silicon photonics. *IEEE Microwave Magazine*, pages 58–68, 2006.

[JRDB06] B. Jalali, V. Raghunathan, D. Dimitropoulos, and Ö. Boyraz. Raman-Based Silicon Photonics. *IEEE J. Sel. Top. Quantum Electron.*, 12(3):412–421, May/June 2006.

[JRL+05] R. Jones, H. Rong, A. Liu, A. W. Fang, M. J. Paniccia, D. Hak, and O. Cohen. Net continuous wave optical gain in a low loss silicon-on-insulator waveguide by stimulated Raman scattering. *Opt. Express*, 13(2):519–525, January 2005.

[JYY+98] B. Jalali, S. Yegnanarayanan, T. Yoon, T. Yoshimoto, I. Rendina, and F. Coppinger. Advances in Silicon-on-Insulator Optoelectronics. *IEEE J. Sel. Top. Quantum Electron.*, 4(6):938–947, 1998.

[KCDP00] V. I. Karpov, W. R. L. Clements, E. M. Dianov, and S. B. Papernyi. High-power 1.48μm phosphoro-silicate-fiber-based laser pumped by laser diodes. *Can. J. Phys.*, 78(5–6):407–413, May–June 2000.

[KEN+01] S. Kado, Y. Emori, S. Namiki, N. Tsukiji, J. Yoshida, and T. Kimura. Broadband flat-noise Raman amplifier using low-noise bi-directionally pumping sources. In *European Conference on Optical Communications (ECOC)*, pages 38–39, 2001. Post-Deadline Papers, Vol. 6.

[KFH02] H. H. Kee, C. R. S. Fludger, and V. Handerek. Statistical Properties of Polarisation Dependent Gain in Fibre Raman Amplifiers. In *Optical Fiber Communication Conference (OFC)*, 2002. Paper WB2.

[KSS+88] P. N. Kean, B. D. Sinclair, K. Smith, W. Sibbett, C. J. Rowe, and D. C. J. Reid. Experimental evaluation of a fibre Raman oscillator having fibre grating reflectors. *J. Mod. Opt.*, 35(3):397–406, 1988.

[KST+01] N. Kurukitkoson, H. Sugahara, S. K. Turitsyn, O. N. Egorova, A. S. Kurkov, V. M. Paramonov, and E. M. Dianov. Optimisation of two-stage Raman converter based on phosphosilicate core fibre: modelling and experiment. *Electron. Lett.*, 37(21):1281–1283, October 2001.

[LA03] Q. Lin and G. P. Agrawal. Vector theory of stimulated Raman scattering and its application to fiber-based Raman amplifiers. *J. Opt. Soc. Am. B*, 20(8):1616–1631, August 2003.

[LBL+02] F. Leplingard, S. Borne, L. Lorcy, T. Lopez, J.-J. Guérin, C. Moreau, C. Martinelli, and D. Bayart. Six output wavelength Raman fibre laser for Raman amplification. *Electron. Lett.*, 38(16):886–887, August 2002.

[LDVS00] M. Loncar, T. Doll, J. Vuckovic, and A. Scherer. Design and Fabrication of Silicon Photonic Crystal Optical Waveguides. *J. Lightwave Technol.*, 18(10):1402–1411, October 2000.

[LMB+05] F. Leplingard, C. Martinelli, S. Borne, L. Lorcy, D. Mongardien, and D. Bayart. Up to 22dB Reduction of the Relative Intensity Noise of a Raman Fiber Laser. In *European Conference on Optical Communications (ECOC)*, 2005. Post-Deadline Paper 4.4.6.

[Lou75] R. Loudon. The Raman Effect in Crystals. *Advances in Physics*, 13(52):423–482, 1975. Erratum in vol. 14, no. 56, pp. 621.

[LRJ+06] A. Liu, H. Rong, R. Jones, O. Cohen, D. Hak, and M. Paniccia. Optical Amplification and Lasing by Stimulated Raman Scattering in Silicon Waveguides. *J. Lightwave Technol.*, 24(3):1440–1455, March 2006.

[LRP+04] A. Liu, H. Rong, M. Paniccia, O. Cohen, and D. Hak. Net optical gain in a low loss silicon-on-insulator waveguide by stimulated Raman scattering. *Opt. Express*, 12(18):4261–4268, September 2004.

[LSY98] R. B. Lehoucq, D. C. Sorensen, and C. Yang. *ARPACK Users' Guide: Solution of Large-Scale Eigenvalue Problems with Implicitly Restarted Arnoldi Methods*. Society for Industrial & Applied Mathematics, 1998.

[LT04] T.-K. Liang and H.-K. Tsang. Nonlinear Absorption and Raman Scattering in Silicon-on-Insulator Optical Waveguides. *IEEE J. Sel. Top. Quantum Electron.*, 10(5):1149–1153, 2004.

[LT06] Y. Liu and H. K. Tsang. Nonlinear absorption and Raman gain in helium-ion-implanted silicon waveguides. *Opt. Lett.*, 31(11):1714–1716, June 2006.

[LWS80] P. Labudde, H. Weber, and R. H. Stolen. Bandwidth Reduction in CW Fiber Raman Lasers. *IEEE J. Quantum Electron.*, QE-16(2):115–117, February 1980.

[MBH03] M. D. Mermelstein, K. Brar, and C. Headley. RIN Transfer Measurement and Modeling in Dual-Order Raman Fiber Amplifiers. *J. Lightwave Technol.*, 21(6):1518–1523, June 2003.

[McK66] J. P. McKelvey. *Solid state and semiconductor physics*. Harper & Row, 1966.

[MHB+01] M. D. Mermelstein, C. Headley, J.-C. Bouteiller, P. Steinvurzel, C. Horn, K. Feder, and B. J. Eggleton. Configurable Three-Wavelength Raman Fiber Laser for Raman Amplification and Dynamic Gain Flattening. *IEEE Photon. Technol. Lett.*, 13(12):1286–1288, December 2001.

[MHB02] M. D. Mermelstein, C. Headley, and J.-C. Bouteiller. RIN transfer analysis in pump depletion regime for Raman fibre amplifiers. *Electron. Lett.*, 38(9):403–405, April 2002.

[Mil98] D. L. Mills. *Nonlinear Optics*. Springer, 2nd edition, 1998.

[MLB+04] C. Martinelli, F. Leplingard, S. Borne, D. Bayart, F. Vanholsbeeck, S. Coen, and T. Sylvestre. Stability enhancement for dual-order raman fiber lasers. *IEEE Photon. Technol. Lett.*, 16(9):2018–2020, 2004.

[MMV03] S. J. McNab, N. Moll, and Y. A. Vlasov. Ultra-low loss photonic integrated circuit with membrane-type photonic crystal waveguides. *Opt. Express*, 11:2927–2939, 2003.

[MTS+05] A. Martínez Rios, I. Torres Gómez, R. Selvas Aguilar, G. Anzueto Sanchez, and A. N. Starodumov. Analytical approach for the design of cascaded raman fiber lasers. *Revista Mexicana de Física*, 51(4):391–397, August 2005.

[Nay73] A. H. Nayfeh. *Perturbation methods*. John Wiley & Sons, 1973.

[PKC01] S. B. Papernyi, V. I. Karpov, and W. R. L. Clements. Efficient dual-wavelength Raman fiber laser. In *Optical Fiber Communication Conference (OFC)*, 2001. Paper WDD15.

[PKJU00] M. Prabhu, N. Kim, L. Jianren, and K.-I. Ueda. Output Characteristics of High-Power Continuous Wave Raman Fiber Laser at 1484 nm using Phosphosilicate Fiber. *Opt. Rev.*, 7(5):455–461, 2000.

[PKU00] M. Prabhu, N. Kim, and K.-I. Ueda. Output Characteristics of High-Power Continuous Wave Raman Fiber Laser at 1239 nm Using Phosphosilicate Fiber. *Opt. Rev.*, 7(4):297–302, 2000.

[PL04] L. Pavesi and D. J. Lockwood, editors. *Silicon Photonics*. Springer-Verlag Berlin Heidelberg, 2004.

[PL06] V. M. N. Passaro and F. D. Leonardis. Space-Time Modeling of Raman Pulses in Silicon-on-Insulator Optical Waveguides. *J. Lightwave Technol.*, 24(7):2920–2931, July 2006.

[PV86] C. Pask and A. Vatarescu. Spectral approach to pulse propagation in a dispersive nonlinear medium. *J. Opt. Soc. Am. B*, 3(7):1018–1024, July 1986.

[PW02] V. E. Perlin and H. G. Winful. Optimal Design of Flat-Gain Wide-Band Fiber Raman Amplifiers. *J. Lightwave Technol.*, 20(2):250–254, February 2002.

[RBJ05] V. Raghunathan, O. Boyraz, and B. Jalali. 20 dB on-off Raman amplification in silicon waveguides. In *Conference on Lasers and Electro-Optics (CLEO)*, 2005. Paper CMU1.

[RC70] J. M. Ralston and R. K. Chang. Spontaneous-Raman-Scattering Efficiency and Stimulated Scattering in Silicon. *Phys. Rev. B*, 2(6):1858–1862, September 1970.

[RCD00] M. Rini, I. Cristiani, and V. Degiorgio. Numerical Modeling and Optimization of Cascaded CW Raman Fiber Lasers. *IEEE J. Quantum Electron.*, 36(10):1117–1122, October 2000.

[Ren] H. Renner. private communication.

[RHT01] P. C. Reeves-Hall and J. R. Taylor. Wavelength tunable CW Raman fibre ring laser operating at 1486–1551nm. *Electron. Lett.*, 37(8):491–492, April 2001.

[RJL+05] H. Rong, R. Jones, A. Liu, O. Cohen, D. Hak, A. Fang, and M. Paniccia. A continuous-wave Raman silicon laser. *Nature*, 433:725–727, February 2005.

[RK98] K. Rottwitt and H. D. Kidorf. A 92 nm bandwidth Raman amplifier. In *Optical Fiber Communication Conference (OFC)*, 1998. Post-Deadline Paper PD6.

[RLJ+05] H. Rong, A. Liu, R. Jones, O. Cohen, D. Hak, R. Nicolaescu, A. Fang, and M. Paniccia. An all-silicon Raman laser. *Nature*, 433:292–294, January 2005.

[RLN+04] H. Rong, A. Liu, R. Nicolaescu, M. Paniccia, O. Cohen, and D. Hak. Raman gain and nonlinear optical absorption measurement in a low-loss silicon waveguide. *Appl. Phys. Lett.*, 85(12):2196–2198, September 2004.

[RM73] J. F. Reintjes and J. C. McGroddy. Indirect Two-Photon Transitions in Si at 1.06um. *prl*, 30(19):901–903, May 1973.

[RSSJ06] V. Raghunathan, R. Shori, O. M. Stafsudd, and B. Jalali. Nonlinear absorption in silicon and the prospects of mid-infrared silicon Raman lasers. *Phys. Stat. Sol. (a)*, 203(5):R38–R40, 2006.

[RVY04] G. W. Rieger, K. S. Virk, and J. F. Young. Nonlinear propagation of ultrafast 1.5 um pulses in high-index-contrast silicon-on-insulator waveguides. *Appl. Phys. Lett.*, 84(6):900–902, February 2004.

[SB65] Y. R. Shen and N. Bloembergen. Theory of Stimulated Brillouin and Raman Scattering. *Phys. Rev. A*, 137(6):1787–1805, March 1965.

[SB86] R. A. Soref and B. R. Bennett. Kramers-kronig analysis of electro-optical switching in silicon. In *Proc. SPIE*, volume 704, 1986.

[SB87] R. A. Soref and B. R. Bennett. Electrooptical Effects in Silicon. *IEEE J. Quantum Electron.*, QE-23(1):123–129, January 1987.

[SdSE02] J. E. Sipe, C. M. de Sterke, and B. J. Eggleton. Rigorous derivation of coupled mode equations for short, high-intensity grating-coupled, co-propagating pulses. *J. Mod. Opt.*, 49(9):1437–1452, 2002.

[See91] K. Seeger. *Semiconductor Physics*. Springer, 5th edition, 1991.

[SF03] T. Suhara and M. Fujimura. *Waveguide nonlinear-optic devices*. Springer-Verlag Berlin Heidelberg, 2003.

[SL83] A. W. Snyder and J. D. Love. *Optical Waveguide Theory*. Chapman and Hall, 1983.

[SM04] R. Salem and T. E. Murphy. Polarization-insensitive cross correlation using two-photon absorption in a silicon photodiode. *Opt. Lett.*, 29(13):1524–1526, July 2004.

[SSK05] D. K. Sparacin, S. J. Spector, and L. C. Kimerling. Silicon Waveguide Sidewall Smoothing by Wet Chemical Oxidation. *J. Lightwave Technol.*, 23(8):2455–2461, August 2005.

[SSP91] R. A. Soref, J. Schmidtchen, and K. Petermann. Large Single-Mode Rib Waveguides in GeSi-Si and Si-on-SiO_2. *IEEE J. Quantum Electron.*, 27(8):1971–1974, August 1991.

[Sta06] R. Stanslovaityte. Rauschverhalten von Single- und Double-Cavity-Raman-Faserlasern. Diplomarbeit an der Technischen Universität Hamburg-Harburg, 2006.

[Sto80a] R. H. Stolen. Fiber Raman Lasers. *Fiber and Integrated Optics*, 3(1):21–51, 1980.

[Sto80b] R. H. Stolen. Nonlinearity in Fiber Transmission. *Proc. IEEE*, 68(10):1232–1236, October 1980.

[Sto04] R. H. Stolen. *Raman Amplifiers for Telecommunications 1, Physical Principles*, chapter Fundamentals of Raman Amplification in Fibers, pages 35–59. Springer-Verlag, 2004.

[SV03] I. T. Sorokina and K. L. Vodopyanov, editors. *Solid-State Mid-Infrared Laser Sources*, volume 89 of *Topics in Applied Physics*. Springer Berlin / Heidelberg, 2003.

[SWR05] E. Schulze, A. Warnke, and F. Raub. 40 Gb/s WDM-Transmission with EDFAs in Comparison to Raman Amplified Transmission with Raman Fiber Lasers as First-Order and Second-Order Pump. In *Optical Fiber Communication Conference (OFC)*, 2005. Paper OThF2.

[TPT05] J. C. Travers, S. V. Popov, and J. R. Taylor. Efficient continuous-wave holey fiber Raman laser. *Appl. Phys. Lett.*, 87:031106, 2005.

[TWL+02] H. K. Tsang, C. S. Wong, T. K. Liang, I. E. Day, S. W. Roberts, A. Harpin, J. Drake, and M. Asghari. Optical dispersion, two-photon absorption and self-phase modulation in silicon waveguides at 1.5 um wavelength. *Appl. Phys. Lett.*, 80(3):416–418, January 2002.

[TYF+05] T. Tsuchizawa, K. Yamada, H. Fukuda, T. Watanabe, J. Takahashi, M. Takahashi, T. Shoji, E. Tamechika, S. Itabashi, and H. Morita. Microphotonics Devices Based on Silicon Microfabrication Technology. *IEEE J. Sel. Top. Quantum Electron.*, 11(1):232–240, 2005.

[Vas91] C. Vassallo. *Optical waveguide concepts*. Elsevier, 1991.

[VM04] Y. A. Vlasov and S. J. McNab. Losses in single-mode silicon-on-insulator strip waveguides and bends. *Opt. Express*, 12(8):1622–1631, April 2004.

[WSZ02] P. J. Winzer, K. Sherman, and M. Zirngibl. Time-Division Multiplexed Raman Pump Experiment Using a Tunable C-Band Laser. *IEEE Photon. Technol. Lett.*, 14(6):789–791, June 2002.

[WWQ89] D. M. Wieliczka, S. Weng, and M. R. Querry. Wedge shaped cell for highly absorbent liquids: infrared optical constants of water. *Appl. Opt.*, 28(9):1714–1719, May 1989.

[XAL05] Q. Xu, V. R. Almeida, and M. Lipson. Demonstration of high Raman gain in a submicrometer-size silicon-on-insulator waveguide. *Opt. Lett.*, 30(1):35–37, January 2005.

[YC05] P. Y. Yu and M. Cardona. *Fundamentals of Semiconductors*. Springer, 3rd, corrected edition, 2005.

[YK93] T. Yamamoto and M. Koshiba. Numerical Analysis of Curvature Loss in Optical Waveguides by the Finite-Element Method. *J. Lightwave Technol.*, 11(10):1579–1583, October 1993.

[YSC+05] H. Yamada, M. Shirane, T. Chu, H. Yokoyama, S. Ishida, and Y. Arakawa. Nonlinear-optic silicon-nanowire waveguides. *Jpn. J. Appl. Phys.*, 44:6541–6545, 2005.

[YXJ+05] W. N. Ye, D.-X. Xu, S. Janz, P. Cheben, M.-J. Picard, B. Lamontagne, and N. G. Tarr. Birefringence Control Using Stress Engineering in Silicon-on-Insulator (SOI) Waveguides. *J. Lightwave Technol.*, 23(3):1308–1318, March 2005.